

# **Scale-bridging investigation into edge cracking of multiphase steels**

Von der Fakultät für Georesourcen and Materialtechnik der  
Rheinisch-Westfälischen Technischen Hochschule Aachen

zur Erlangung des akademischen Grades einer

**Doktorin der Ingenieurwissenschaften**

genehmigte Dissertation

vorgelegt von

**Niloufar Habibi, M. Sc.**

**Berichter:** Univ.-Prof. Dr.-Ing. Sebastian Münstermann

Prof. Dr.-Ing. Junhe Lian

Tag der mündlichen Prüfung: 03.07.2024

Diese Dissertation ist auf den Internetseiten der Universitätsbibliothek online verfügbar



---

## Declaration on publications

---

This dissertation includes the following research articles that have been published in international peer-reviewed journals. The candidate has conducted the study as well as written all the papers.

**Chapter II** - Numerical investigation into effects of fracture behavior on edge cracking sensitivity

**N Habibi**, M Zhou, J Lian, M Koenemann, S Muenstermann

<https://doi.org/10.1016/j.jmatprotec.2023.117965>

**Chapter III** - Effects of Microstructural Properties on Damage Evolution and Edge Crack Sensitivity of DP1000 Steels

**N Habibi**, S Mathi, T Beier, M Könemann, S Münstermann

<https://doi.org/10.3390/cryst12060845>

**Chapter IV** - Effects of damage evolution on edge crack sensitivity in dual-phase steels

**N. Habibi**, T. Beier, J. Lian, B. Tekkaya, M. Koenemann, S. Muenstermann

<https://doi.org/10.1002/srin.202400178>

**Chapter V** - Numerical quantification of damage accumulation resulting from blanking in multi-phase steel

**N Habibi**, F Pütz, M Könemann, V Brinnel, S Münstermann, M Feistle, W Volk

<https://doi.org/10.1088/1757-899X/418/1/012058>

**Chapter VI** - Deformation and damage assessments of Two DP1000 steels using a micromechanical modelling method

**N Habibi**, N Vajragupta, S Münstermann

<https://doi.org/10.3390/cryst1107080>





---

## Acknowledgments

---

I would like to express my most sincere gratitude to Prof. Sebastian Münstermann, for providing me with this unique opportunity to work in his group and also for his constant support of my work and research. I have benefited significantly from his immense knowledge and wisdom, as well as continuous encouragement and recognition. I would like also to express my gratitude to Prof. Junhe Lian from Aalto University for his scientific support, constructive comments, and inspiration in my dissertation as well as my papers.

Moreover, I am very grateful to all my colleagues in IMS group at IBF and IEHK. I will never forget the help from you and the happy moments shared with you. I would like to thank specially Fuhui, Berk, Dongsong, David, Yannik, and Zhen for all the support and kindness. In addition, I would like to thank Ms. Martina Sparrer, Ms. Marion Köster, Ms. Ulrike Groß-Schwarzbauer, Ms. Julia Bürke, Ms. Nicole Olles, Ms. Kirsten Heinrichs, Dr. Michael Dölz and Dr. Markus Könemann for taking care of many administrative issues. I am also grateful to our technicians, Mr. Wilhelm Meier, Mr. Sebastian Seibel, Mr. Jürgen Dartenne, Mr. Dietmar Sodar, Mr. Horst Tschammer, Mr. Marc Grümmer, Mr. Wieslaw Tupiec, Ms. Angela Sommer, Ms. Heidi Mercks de Espinoza, Ms. Doris Horst, Mr. Frank Flesch, and all colleagues in administration and IT group for the support in the administrative issues.

I would like to appreciate the effort of all my students, Amin, Ayzhat, Santhosh, Mengya, Xie, Radhey, Moritz, Milad, Navich, Talha, Tianqi, Meng, and Qing. Your motivation, resilience, and intelligence significantly facilitated my work. I am thankful to all my project partners, who worked with me and supported me a lot. I would like to acknowledge RWTH Aachen University for granting computing resources under project <rwth0306>, <rwth0459>, and <rwth1234>.

My special thanks to the female circle around. My inspiring group leader, Dr. Victoria Brinnel, my supportive strong colleagues, Barbara, Jinshan, Wenqi, Boyu, and Sophie, my lovely friends, Stefanie, Radita, Ekin, Farzaneh, Marieh, and Narges. Your strong, supportive, and independent personality inspired me to strive for greater success and confidence in my own journey.

Last but not least, I would like to say thank you to my parents, Maryam Geransayeh and Gholamhossein Habibi. Without your unconditional love and support, nothing would be possible.

تقدیم به مادر و پدر عزیزم، که بدون عشق و پشتیبانی همیشگی شما هیچ یک از موفقیت‌های من امکان پذیر نبود. به یاد برادر عزیزم امیرحسین، و دایی مهربانم، دایی محمود عزیز، که خاطرشان همواره و تا ابد در دلهایمان زنده و گرامی خواهد ماند

Niloufar Habibi  
Berlin, 2024



---

## Abstract

---

Edge cracking is one of the main challenges in widespread applications of dual-phase (DP) steel sheets. It does not only restrict the formability at component edges during forming processes but also cannot be anticipated by the conventional forming limits, which makes the design of a successful forming process possible only by trial and error approaches. To overcome this issue, a thorough understanding of this phenomenon is required. Therefore, a scale-bridging investigation was conducted in the present dissertation to study the potential reasons for edge cracking, such as materials properties, edge quality, and edge forming processes. However, all these reasons could be summed up as damage evolution in the material throughout the applied complicated deformation condition. For the macro-scale study, a phenomenological uncoupled damage criterion along with a kinematic hardening model was developed to describe the plasticity and fracture behavior of the examined steels. To cover a wide range of stress states, various experiments were designed, which underwent mostly proportional loading. For the meso-scale, Tresca fracture model, maximum shear stress, was applied to predict the damage initiation in the generated representative volume elements (RVEs). These RVEs were constructed according to the actual microstructural features, like grain size, phase fraction, and texture, as well as mechanical properties of individual phases, which were derived using nano-indentation and an inversely calibrated crystal plasticity model. The results of both scales showed that when microstructural and mechanical properties of the ferrite and martensite phases are more similar in a DP steel, the deformation is distributed more homogeneously throughout the material, which leads the local formability to increase, damage initiation to be retarded, and consequently edge cracking sensitivity to decrease. Moreover, it was revealed that the data of available experimental methods for edge cracking evaluation cannot be directly used in complex edge forming processes. The hole expansion test (HET) applies distinct stress states at different locations on the specimen, which could cause crack initiation was even far from the edges. Edge-fracture-tensile testing (EFTT) method could be successful for the comparison of edge crack resistance between different materials, however it considers only one stress state at the edge. While finite element modeling of edge manufacturing and the subsequent edge deforming process along with a proper plasticity-damage model was reported as a promising method for investigation of edge cracking in different materials and deformation processes.

---

## Kurzfassung

---

Die Kantenrissbildung ist eine der größten Herausforderungen bei der Anwendung von Dualphasen-Stahlblechen (DP). Sie schränkt nicht nur die Umformbarkeit an den Bauteilkanten während des Umformprozesses ein, sondern kann auch nicht durch die konventionellen Umformgrenzen antizipiert werden, so dass die Gestaltung eines erfolgreichen Umformprozesses nur durch Trial-and-error möglich ist. Um dieses Problem zu überwinden, ist ein gründliches Verständnis dieses Phänomens erforderlich. Daher wurde in der vorliegenden Arbeit eine skalenübergreifende Untersuchung durchgeführt, um die Gründe für die Kantenrisse zu untersuchen, wie z. B. Materialeigenschaften, Kantenqualität und Kantenumformverfahren. Alle diese Gründe können jedoch als Schädigungsentwicklung im Material unter den angewandten komplizierten Verformungsbedingungen zusammengefasst werden. Für die Makroskala-Studie wurde ein phänomenologisches ungekoppeltes Schädigungskriterium zusammen mit einem kinematischen Verfestigungsmodell entwickelt, um das Plastizitäts- und Bruchverhalten der untersuchten Stähle zu beschreiben. Um ein breites Spektrum an Spannungszuständen abzudecken, wurden verschiedene Experimente konzipiert, die überwiegend proportional belastet wurden. Für die Mesoskala wurde das Tresca-Versagensmodell mit maximaler Scherspannung angewandt, um die Schädigungsinitierung in den erzeugten repräsentativen Volumenelementen (RVEs) vorherzusagen. Diese RVEs wurden entsprechend den tatsächlichen mikrostrukturellen Merkmalen wie Korngröße, Phasenanteil und Textur sowie den mechanischen Eigenschaften der einzelnen Phasen konstruiert, die mithilfe von Nanoindentation und einem invers kalibrierten Kristallplastizitätsmodell abgeleitet wurden. Die Ergebnisse beider Skalen zeigten, dass sich die Verformung homogener über das gesamte Material verteilt, wenn die mikrostrukturellen und mechanischen Eigenschaften der Ferrit- und Martensitphasen in einem DP-Stahl ähnlich sind. Dies führt zu einer Erhöhung der lokalen Verformbarkeit, einer Verzögerung der Schädigungsinitierung und folglich zu einer Verringerung der Kantenrissempfindlichkeit. Darüber hinaus wurde festgestellt, dass die Daten verfügbarer experimenteller Methoden zur Bewertung der Kantenrisse bei komplexen Kantenumformprozessen nicht direkt verwendet werden können. Beim Lochaufweitungsversuch (HET) treten an verschiedenen Stellen der Probe unterschiedliche Spannungszustände auf, was dazu führen kann, dass der Riss auch weit entfernt von den Kanten beginnt. Das EFTT-verfahren könnte sich für den Vergleich der Kantenrissbeständigkeit verschiedener Werkstoffe eignen, berücksichtigt jedoch nur einen Spannungszustand an der Kante. Die Finite-Elemente-Modellierung der Kantenherstellung und des anschließenden Kantenverformungsprozesses in Verbindung mit einem geeigneten Plastizitäts-Schadensmodell wurde als vielversprechende Methode zur Untersuchung der Kantenrisse in verschiedenen Materialien und Verformungsprozessen beschrieben.

---

## Table of Contents

---

Chapter I: Introduction.....	1
1.1 Introduction.....	1
1.2 Outline of the thesis .....	2
1.3 Fundamentals .....	2
1.4 Objectives and scope of the study.....	14
1.5 References.....	15
Chapter II: Numerical investigation into effects of fracture behavior on edge cracking sensitivity.....	18
Chapter III: Effects of microstructural properties on damage evolution and edge crack sensitivity of DP1000 steels.....	37
Chapter IV: Effects of damage evolution on edge crack sensitivity in dual-phase steels.....	61
Chapter V: Numerical quantification of damage accumulation resulting from blanking in multi-phase steel .....	92
Chapter VI: Deformation and damage assessments of two DP1000 steels using a micromechanical modelling method .....	102
Chapter VII: Summary, discussion, and outlook .....	126
7.1 Macro-scale investigation .....	126
7.2 Meso-scale investigation.....	128
7.3 Multi-scale integration .....	129
7.4 Outlook .....	129



---

## Chapter I: Introduction

---

### 1.1 Introduction

Increasing environmental concerns and safety standards oblige the automotive industry to develop lightweight designs. In this regard, advanced high strength steels (AHSSs) offer promising possibilities of manufacturing lightweight components. Their excellent combination of strength and formability allows for sheet components to be created with thinner thickness while maintaining the desired safety factor and minimizing overdesigning [1]. Nevertheless, their forming limits need to be determined to design a successful manufacturing process as well as to ensure its performance during the service. The forming limit diagram (FLD) is a conventional tool to predict failure occurrence in the sheets under various loading conditions. However for AHSSs, crackings appear at the some manufactured edges, which are not expected by using FLD evaluation. The mechanism of this so called “edge cracking” phenomenon has not been fully understood and still remains as an unsolved challenge for widespread usage of these steels [2].

Sheared cut edges are more prone to edge cracking. The shear cutting techniques are commonly used in the sheet metal processing industry, as they provide easy implementation and high-volume manufacturing, and favor high economic efficiency. These techniques apply severe hardening, damage, and roughness during creating the edges. Therefore, the sheared edge cracking in AHSSs turns into an urged topic for the industry with different desirable solutions, including material improvement, optimization of shear cutting processes, and designing of proper evaluation methods.

It could be possible to consider all the aforementioned aspects by using an integrated computational materials engineering (ICME) tool. ICME integrates materials information at different scales into the analysis of component performance and production processes. Using this multiscale computational approach not only increases time and cost efficiency for engineers, but also for the optimization of production processes according to the material properties. Additionally, it allows for the development of new materials with customized properties.

Aiming to gain a better understanding of edge cracking in this work by employing ICME method, three high strength dual-phase (DP) steels with distinct microstructural features are investigated. The complex microstructure of DP steels makes them more sensitive to edge cracking and favorite for the regarding study. As the materials are subjected to non-proportional loading conditions during shear cutting and the following edge deforming processes, the materials’ mechanical and failure responses to various stress states should be considered. By aiding the finite element method, the meso- and macro-scales observation are discussed in detail. For meso-scale, representative volume elements (RVEs) are generated based on microstructural features and mechanical properties of each phase in the materials. Various stress states are applied on RVEs by defining proper periodic boundary conditions to determine the damage initiation in addition to deformation distribution for each condition. For macro-scale investigation, assorted edge manufacturing and subsequent forming processes along with parallel simulations are used to expose the edge cracking phenomenon. For this purpose, a powerful plasticity-coupled damage model is developed,

which considers the Bauschinger effect on plasticity as well as stress state dependency and non-proportional loading influences on damage. These characteristics enable the model to properly describe the material response through the complicated multi-steps forming processes. To conclude, this dissertation reveals edge cracking challenge and provides promising solutions by applying an ICME approach.

### **1.2 Outline of the thesis**

This thesis consists of seven chapters and can be mainly divided into four parts. The first part, Chapters 1, represents the structure of the thesis, required fundamental knowledge, and the objective and scope of this study. Therefore, edge cracking is defined, the origins of this phenomenon are explained in terms of material properties (Dual phase steels) and tool design, and the common and promising evaluation methods are described. Since all the reasons originated from damage evolution in the material and through the specific processes, the study is conducted through multi-scale perspectives. Chapters 2, 3 (partially), 4, and 5 (mostly) discuss macro-level aspects (the second part), while Chapters 3 (partially), 4 (slightly) and 6 focus on the meso-scale study (the third part). Chapter 2 reveals the important stress states that a metal sheet experiences through shear-cutting and subsequent hole expansion forming, which is vital for designing reasonable and practical experimental and numerical approaches. Also, the effects of fracture strain levels at different stress states on the material's damage behavior are studied throughout these processes by defining various imaginary fracture loci in this chapter. Afterwards, various experimental tests were conducted on different high strength dual phase steels to cover a wide range of stress states, which are explained in Chapter 3. Note that these tests showed locally proportional loading under global deformation, which promoted the study of damage behavior for each stress state. The local strains were measured using digital image correlation technique (macro-scale) and damage micro-mechanisms (meso-scale) were observed using scanning electron microscopy micrographs at the fracture sites. By aiding the experimental data from this chapter in Chapter 4, the contributing factors that influence the edge cracking, including materials, edge quality, and edge forming process are disclosed. Various shear-cutting/hole expansion set-up conditions were applied, and the edge crack sensitivity was evaluated. As the results of the hole expansion test are heavily dependent on the tool design, a brand-new method was also considered in Chapter 5 for assessing edge crack sensitivity, Edge-Fracture-Tensile-Test. To elaborate the study on damage micro-mechanisms, the numerical meso-scale method was employed, and the results are explained in Chapter 6. Hence, the representative volume elements were constructed based on the microstructural and micromechanical features of the studied materials and underwent various loading conditions. Note that a crystal plasticity model was calibrated to describe the plasticity behavior of the materials. The macro-scale study is presented in the fourth part. Considering the contents of Chapters 2-6 are presented as individual publications, the last part of this thesis, Chapter 7, discloses the link between the chapters and summarizes the remarkable conclusions and outlooks.

### **1.3 Fundamentals**

#### *1.3.1 Edge cracking phenomenon*

In component production, manufacturing edges is one of the first steps. However, any mechanical cutting operation such as shearing, piercing, blanking, slitting, or trimming reduces the ductility of the sheet



material near the manufactured edges, since during cutting they experience high plastic deformation. Therefore, some cracks from the edges could appear through further deformation steps. Studies [3–5] have shown advanced high strength steels are more prone to edge cracking, figure 1. This figure represents the strong correlation between ultimate tensile strength (UTS) and hole expansion ratio (HER) of various conventional and advanced high strength steels. HER is a quantified parameter to evaluate edge crack sensitivity according to ISO 16630 standard [6], which is described in section 1.3.2.3. Higher HER value stands for larger formability at the edge, i.e., lower edge cracking sensitivity. Although figure 1 illustrated a drastic decrease in HER by increasing in UTS, particularly for dual phase (DP) steels, some exceptions like DP980 are observed. This implies the edge cracking is independent from global formability but caused by local ductility potential [3,7]. Materials global formability is defined as the capability of undergoing plastic deformation without any localized necking, namely the uniform strain distribution. Whereas local formability signifies material's ability to endure plastic deformation in a local area without fracturing. Heibel et al [8] measured true thickness strain at fracture as an indicator for local formability and reported its proportional correlation with HER, figure 2. Local formability is directly controlled by microstructural features, like grain size, morphology, texture, and strength of each phase in addition to phase and deformation distribution throughout the material. Since DP steels contain complex microstructure, their global and local properties could vary by any microstructural changes and represent distinguish mechanical and damage behaviors. In addition to intrinsic materials' properties, poor edge quality and improper edge deforming processes can accelerate edge cracking occurrence. Different edge manufacturing techniques apply different amounts of hardening, damage, roughness, and shape irregularities on the material at edge and even close to it, which can diversify further forming limits. Also, the edge can experience various stress states considering the forming process design, which might be critical for that particular edge and failure occurrence. The following sections summarize the most important studies and findings about each of these contributory factors.

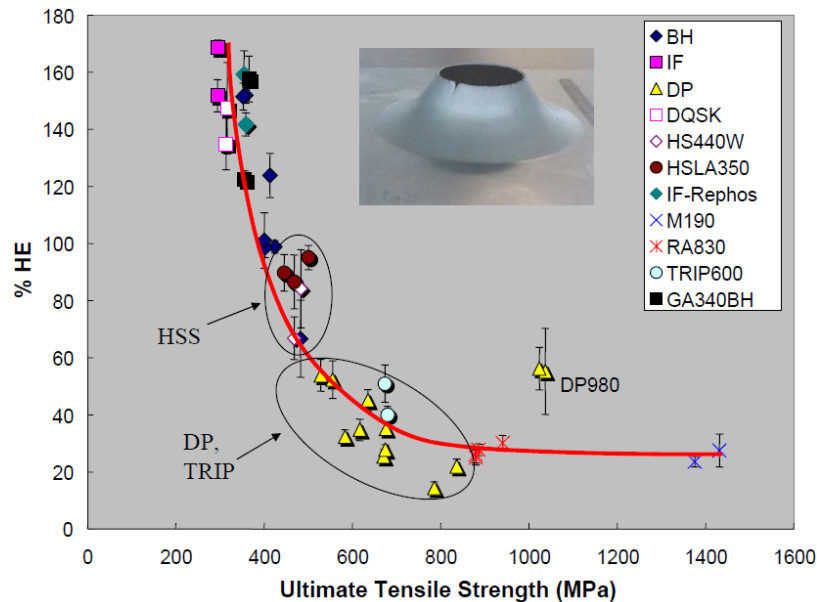


Figure 1. Dependency of the sheared edge stretching limits on the ultimate tensile strength [3].

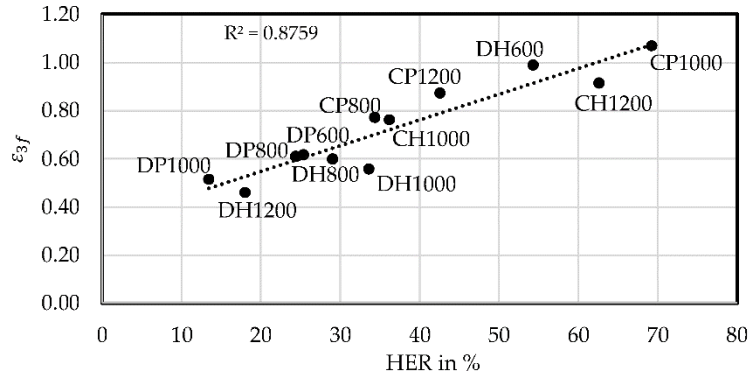


Figure 2. Proportional relation between true thickness strain at fracture and hole expansion ratio [8].

### 1.3.2 Contributing factors

#### 1.3.2.1 Material (DP steel)

DP steels offer good combination of strength, formability, and toughness, which makes them highly desirable for a wide range of applications in various industries, particularly in automotive and structural engineering. These unique properties appear as a result of their complex microstructure, containing soft ferritic matrix and scattered hard martensitic islands. This heterogeneous microstructure leads to incompatible strain distribution between the phases and stress concentration due to morphological irregularities, which detain the local formability and trigger damage initiation. Ghadbeigi et al [9] performed an in-situ micro-tensile test along with a digital image correlation (DIC) technique on a DP1000 grade steel to measure the local plastic strain distributions and observe damage nucleation and evolution. Results represented a non-uniform strain distribution within the microstructure, which induced various damage micro-mechanisms, including martensite cracking, ferrite-martensite interface decohesion and localization and deformation bands in coarse ferrite grains, figure 3.

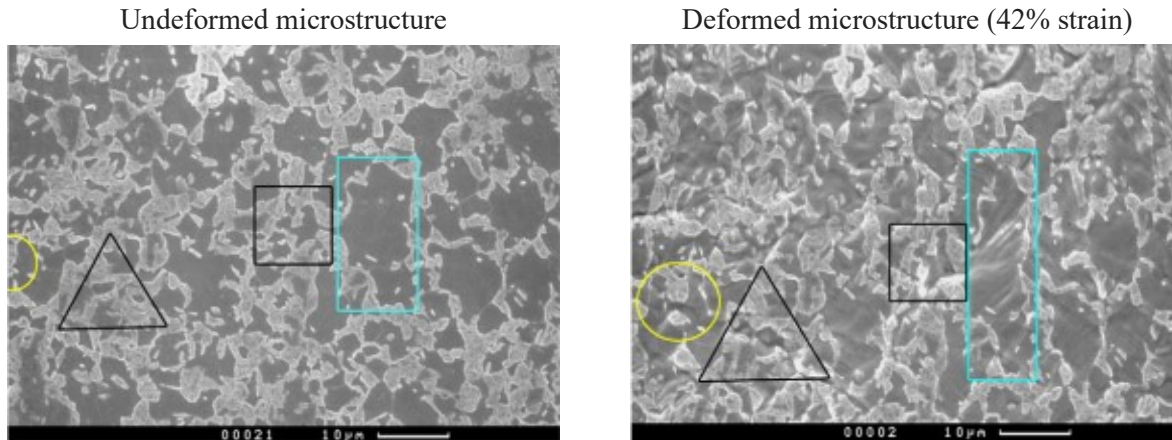


Figure 3. Analyzed area under in-situ tensile test, before and after deformation [9]. Various damage mechanisms were observed, circle: martensite cracking, triangle and square: damage at ferrite-martensite interface, and rectangular: deformation bands in a coarse ferrite grain.

Pathak et al [10] showed the importance of microstructural homogeneity of multi-phase steels on the local formability. They compared the behavior of a ferritic-martensitic dual phase (DP) steel with a complex phase (CP) ferritic-bainitic steel, DP780 versus CP800, under various stress states and studied damage evolution using 3D micro-tomography and quantitative stereology to collect voids information and digital image correlation (DIC) technique to measure the local strain during the tests. The results indicated a significant number of scattered void nucleation in CP800 before formation of macro-cracks. While extensive coalescence happened in DP780 corresponding to martensite bandings in the as-received sheet. The number of voids per unit volume as well as volume fraction of void through applied strains were plotted for different stress states, figure 4. DP780 represented a higher rate of damage accumulation in comparison to CP800, as a result of higher strength differential between its phases and non-uniform deformation distribution. Figure 5 illustrates the ductile damage evolution under uniaxial and biaxial tension. Moreover, in another work [11], they proved the roll of local formability of these materials on edge crack sensitivity by measuring equivalent failure strain for hole expansion tests and hole tension tests, figure 6. The microstructural heterogeneity level can be changed by varying chemical composition, thermomechanical manufacturing processes, and post processing heat treatments, which alter phase strength, phase volume fraction, phase distribution, grain size, grain morphology, and texture.

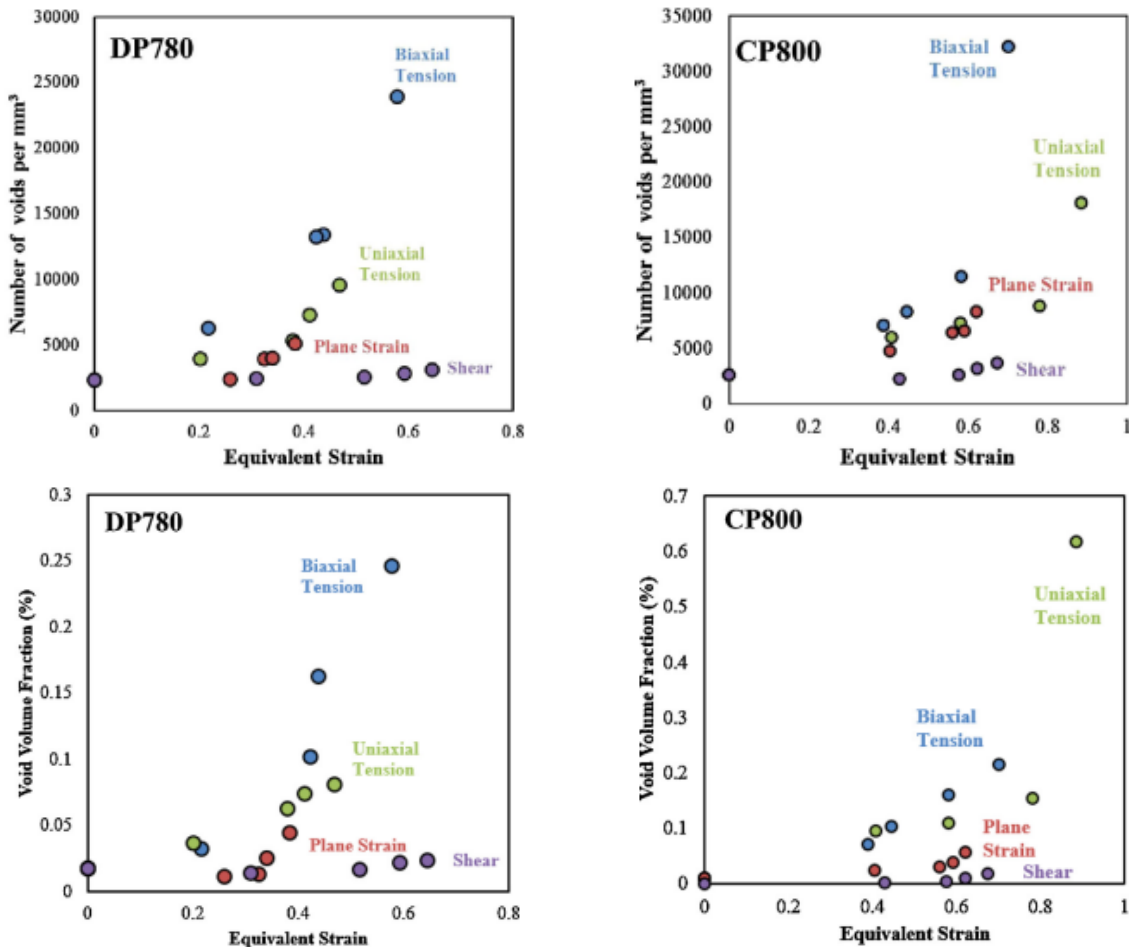


Figure 4. Evolution of normalized number and void volume fraction for different loading conditions [10].

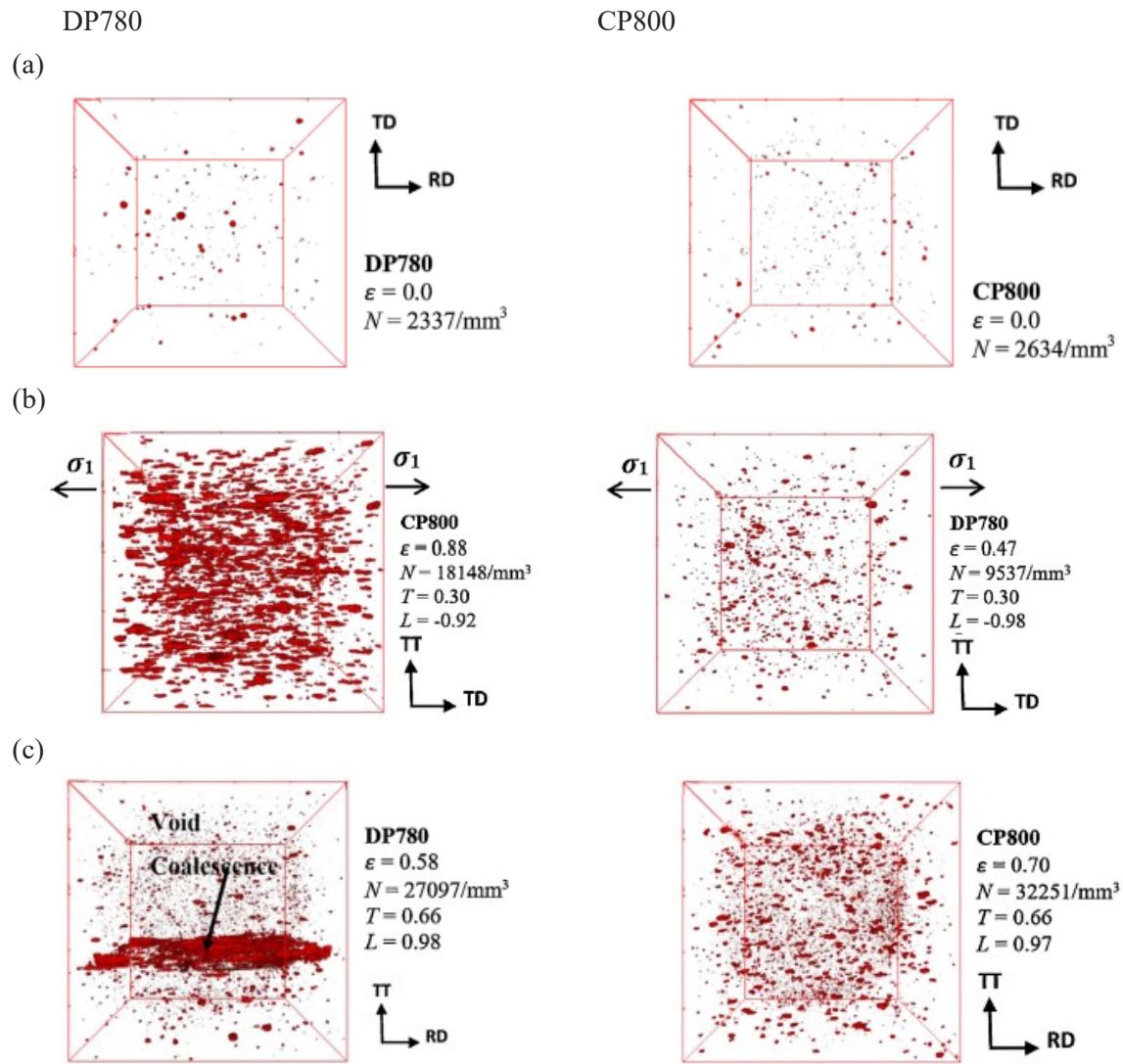


Figure 5. 3D views of damage within (a) undeformed, (b) hole tension , and (c) biaxial tension specimens [10].

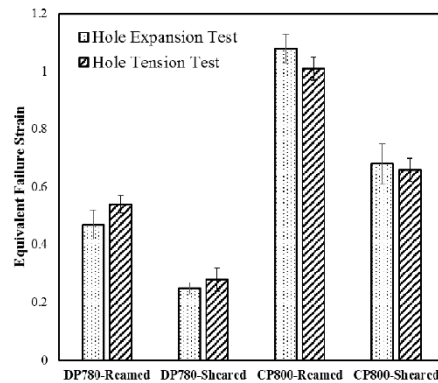


Figure 6. Equivalent failure strains hole tension and hole expansion tests for various edge manufacturing for the studied AHSSs. [11].

Thus, several researchers studied the effects of these changes to improve the edge sensitivity of DP steels. Pan et al [12] decrease the heterogeneity of a DP780 steel by adding 0.02 wt% Nb alloying element and decreasing 0.055 wt% C. The former increased the strength of ferrite as a solid solution effect and the latter decreased the strength of martensite. Therefore, the mean nano-hardness difference between the phases decreased from 2.494 to 1.347 GPa and the average HER increased from 20% to 30%. Madrid et al [13] showed the increase in carbon content of martensite in DP steels decreased the HER. Hu et al [14] reduced the phase strength differentials of a DP980 steel by tempering for several hours at 300 °C, which resulted into some carbides precipitation and losing tetragonality of martensite, i.e. tempering make martensite properties closer to the softer ferrite matrix. They calculated flow curves of individual phases by a combined high energy x-ray diffraction (HEXRD) and crystal plasticity modelling approach, figure 7. The results disclosed, although the general formability decreased by tempering, the local fracture strains increased and HER rose relatively four times higher.

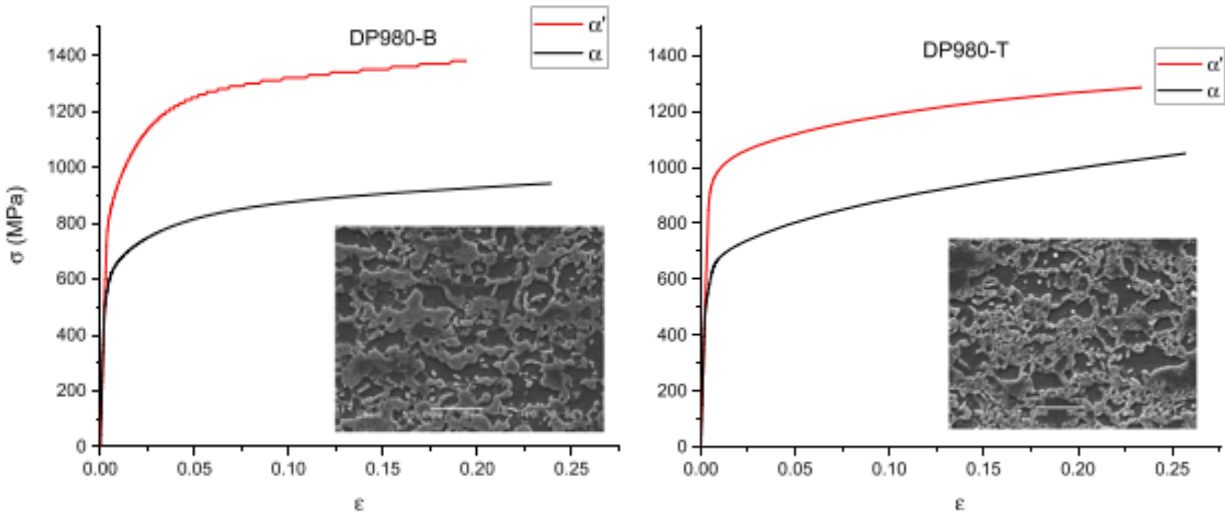


Figure 7. The stress-strain curves of individual phases for the DP980 steel: (a) DP980-B (as received sheet) and (b) DP980-T (tempered at 300 °C), where  $\alpha'$  denotes martensite and  $\alpha$  denotes ferrite [14].

Terrazas et al [15] investigated the effects of martensite size and distribution in five commercial DP steels with the UTS about 1000 MPa. They reported a reasonable correlation of HER with combined parameter of martensite colony size, contiguity fraction of martensite-martensite interface, and mean free distance between martensite colonies, figure 8. This parameter could represent the homogeneity of the microstructure and its key role in ductile damage evolution. Note that generally increasing volume fraction and size of martensite particles reduces carbon content of martensite. Park et al [16] studied the effects of the martensite distribution in the DP structure on formability and damage development, by applying four different thermomechanical processes on a hot-rolled steel sheet with ferrite-pearlite initial microstructure, figure 9. They observed, by forming a chain-like network between martensite grains around the ferrite grains, the strain hardening of the DP steel is significantly increased with negligible loss of total elongation in comparison the DP steels with isolated scattered martensite throughout the ferritic matrix. However, it drastically decreased the localized formability, figure 9. By utilizing in-situ tensile test along with DIC

method, they observed lower strain partitioning between martensite and ferrite in the chained-type microstructure, which could be the reason for strain hardening improvement. SEM micrograph analysis from the fracture surfaces and close to the fracture site revealed that damage initiated by formation of microvoids at ferrite-martensite interfaces in the isolated-type martensite, which could grow as large as a ferrite grain. Whereas in chained type martensite microstructure, damage appeared at the martensite joints. Although these voids grew relatively slowly, their number increased rapidly throughout the microstructure and suppressed local forming, figure 9. Pütz et al [17] also numerically revealed the adverse effects of martensite banding structures on damage evolution. By using statistically representative volume elements (sRVE) method along with a critical principal stress criterion for damage initiation, they stated that banded microstructure reaches 2.5% damaged elements 20% earlier than the microstructure with no bands.

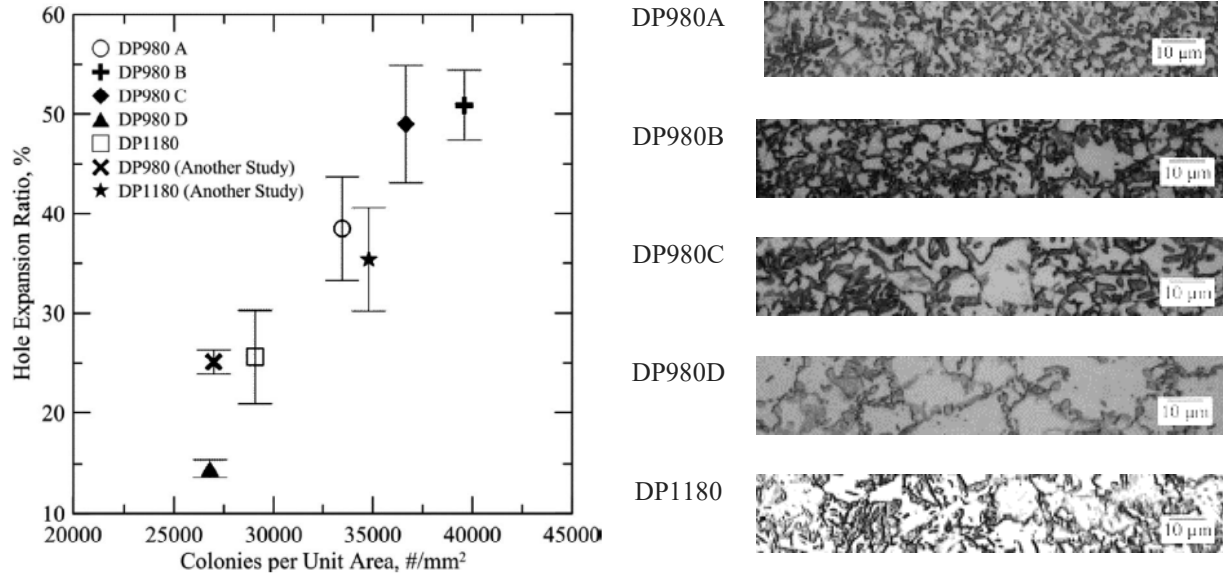


Figure 8. Effects of martensite size and distribution in commercial high strength DP steels on hole expansion ratio [15]



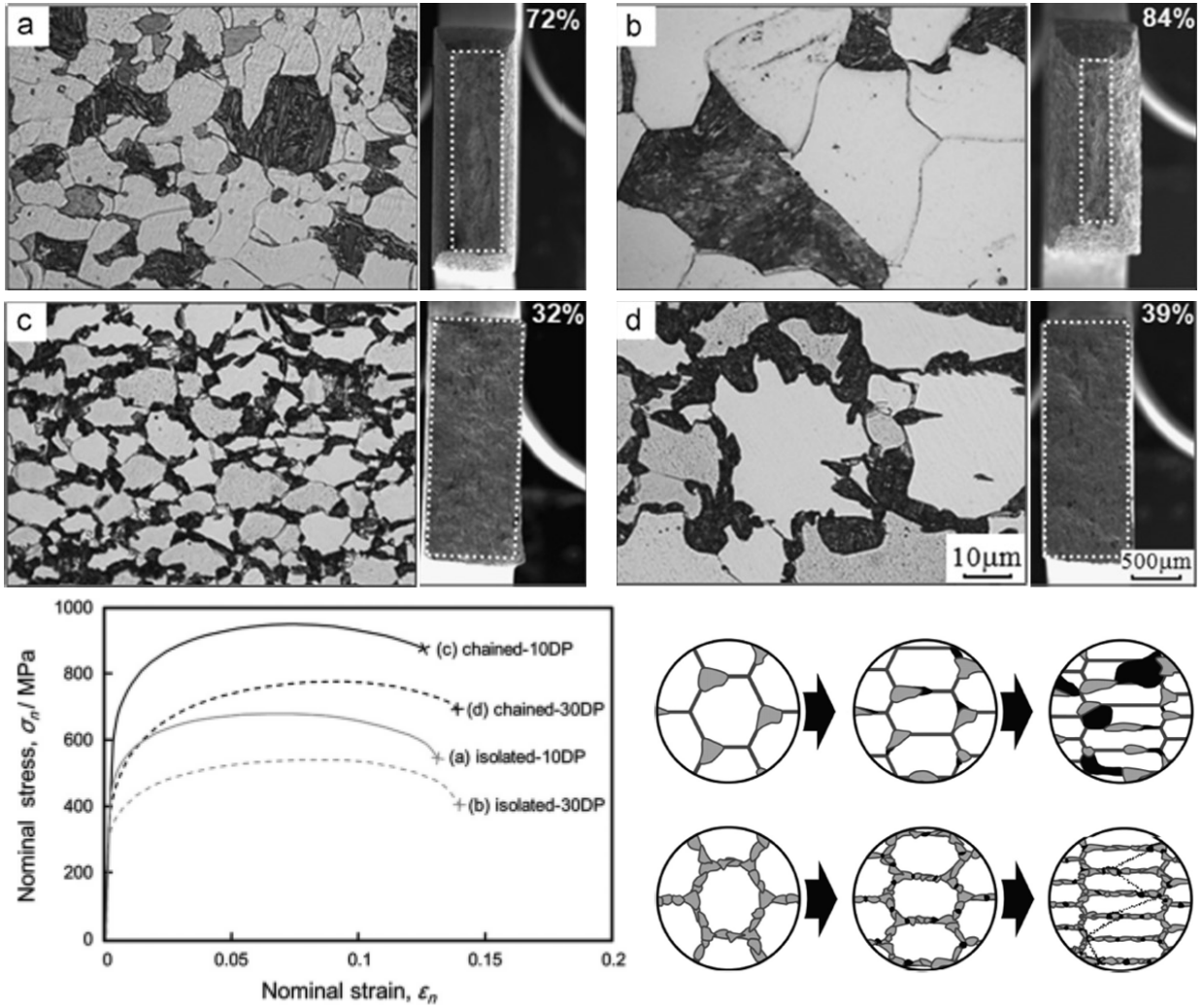


Figure 9. Effects of the martensite distribution in the DP structure on formability and damage development [16]

Although ferrite grain can considerably blunt the microcracks in DP steels and restrain brittle catastrophic failure, damage-induced softening contributes substantially to the formability of DP steels with high martensite content [18]. Hasegawa et al. [19] compared the HER of DP980 steels with different martensite volume fractions, A: 34%, B: 49%, and C: 100% (a martensitic steel). Surprisingly, the HER increased with increasing in martensite volume fraction, so  $HER_A$ : 35%,  $HER_B$ : 58%, and  $HER_C$ : 90%. They concluded that the applied hardening and damage during the punching is not the main factor of edge formability. Since, for example, although the cracks appeared at the edge for the martensitic steel (steel C), they propagated very slowly through the sheet plane in comparison to the other steels, figure 10.

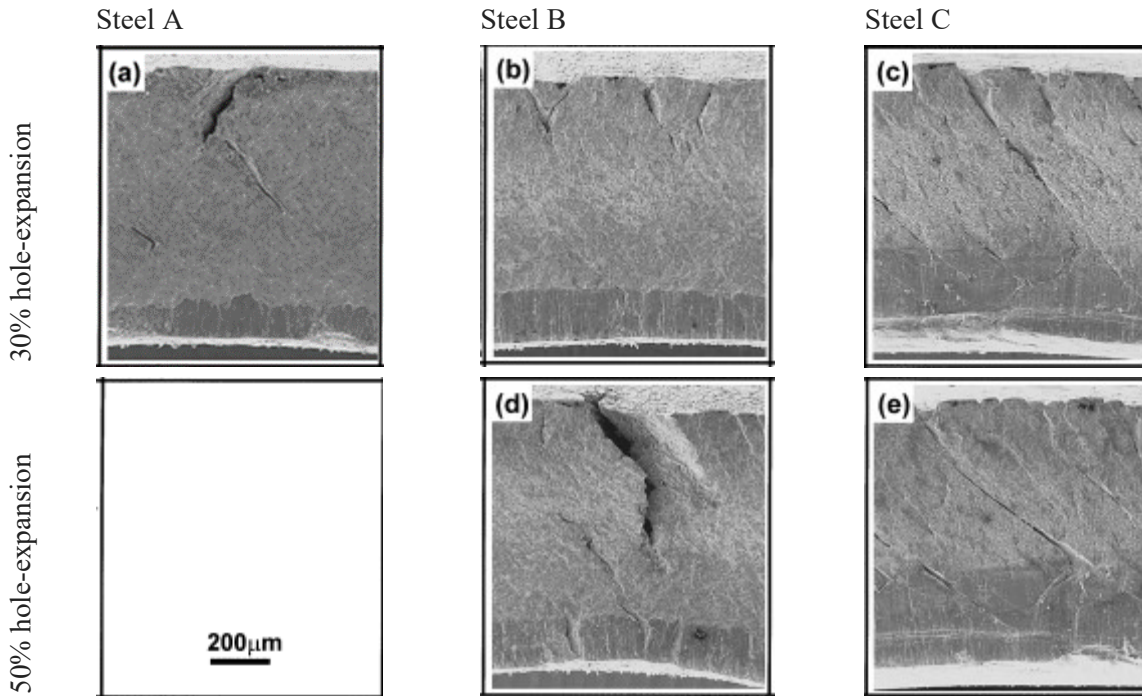


Figure 10. Crack propagation during hole expansion test [19]

#### 1.3.2.2 Edge manufacturing process

Besides material properties, edge manufacturing techniques have a crucial influence on edge cracking in sheet metals. The way sheet edges are formed, finished, or treated during the manufacturing process can affect their structural integrity and sensitivity to cracking. Although shear cutting is the most common and widely used method for cutting sheet metal, due to its cost-efficient and high-rate production, it could apply severe local hardening and damage at the cut edges as well as the adjacent material, which is known as the “shear affected zone” or in brief “SAZ” [20]. Figure 11 compares the maximum engineering strain between different edge manufacturing and edge forming methods and implies the higher sensitivity of the sheared cut edges to cracking [21]. To minimize the adverse effects of shear-cutting at the edge, the cutting tools and process should be optimized, such as die clearance, tool edges, friction, shearing angle, punching speed, temperature, etc. Shear cutting creates a rough surface with different characteristics, figure 12, including roll-over, clean-shear/burnish, fracture, and burr parts. Roll-over is the result of bending effect before the punch penetrates through the sheet. Clean-shear or burnish part is produced by penetration of the punch through the sheet until a crack initiates. Fracture part is called for the part which creates due to crack propagation through the rest of sheet thickness. Burr part appears due to the support of bottom die which delays in fracture. As long as the process produces a smoother surface with lower deformation and fewer micro-cracks, the edge cracking resistance improves. For example, reducing cutting clearance could reduce the burr size and improve the edge quality [22], figure 13. Cutting clearance is the gap between the punch and die, which is normalized by the sheet thickness. However, for very small clearance, the crack cannot propagate easily through the narrow path and a secondary burnish appears from the bottom, which is not aligned with the first crack. Therefore, the edge quality deteriorates [23]. Note that the minimum clearance



that a secondary burnish could occur is material and tool design dependent. Moreover, punching speed and the consequent adiabatic heating could influence the material behavior at the edge. Hartmann et al [24] evaluated experimentally the strain rate evolution a quasi-static punching (10 mm/s) by using high resolution- high speed optical measurements along with DIC techniques. They reported the strain rate could increase up to 50 1/s.

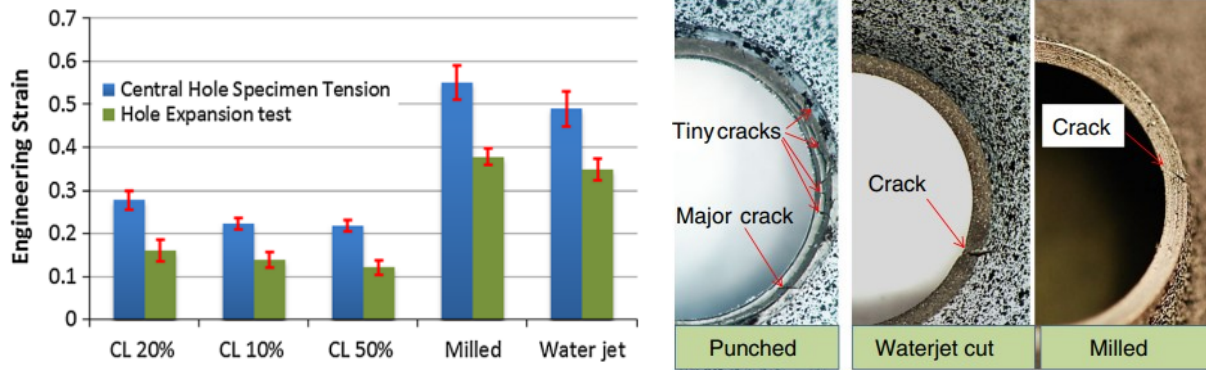


Figure 11. Local surface strain and cracking behavior for different types of edge [21].

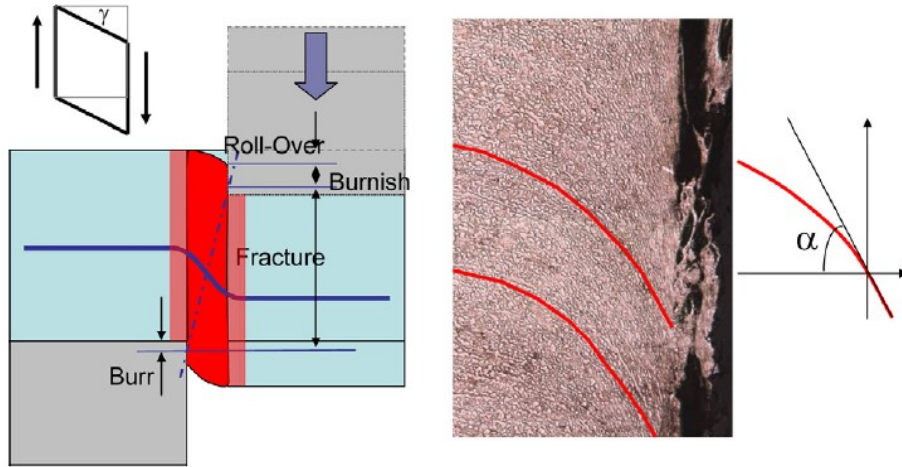


Figure 12. Schematic of simple shear process. The shear deformation resulted in tilting of metal flow lines that were originally horizontal from rolling and tilted to an angle which can be used for shear strain measurement [23].

### 1.3.2.3 Edge deforming process

Edge cutting is one of the initial steps in component manufacturing. Afterwards, the sheet undergoes several forming processes to obtain the final complex shape. As the material in SAZ has experienced severe deformation, its formability potential decreases, which is not considered in the conventional forming limit curves (FLCs) of sheet materials and edge cracking happens unexpectedly, figure 14. Thus, proposing new experimental or numerical methods for prediction of edge cracks becomes the main challenge in forming of AHSS, which is briefly summarized below.

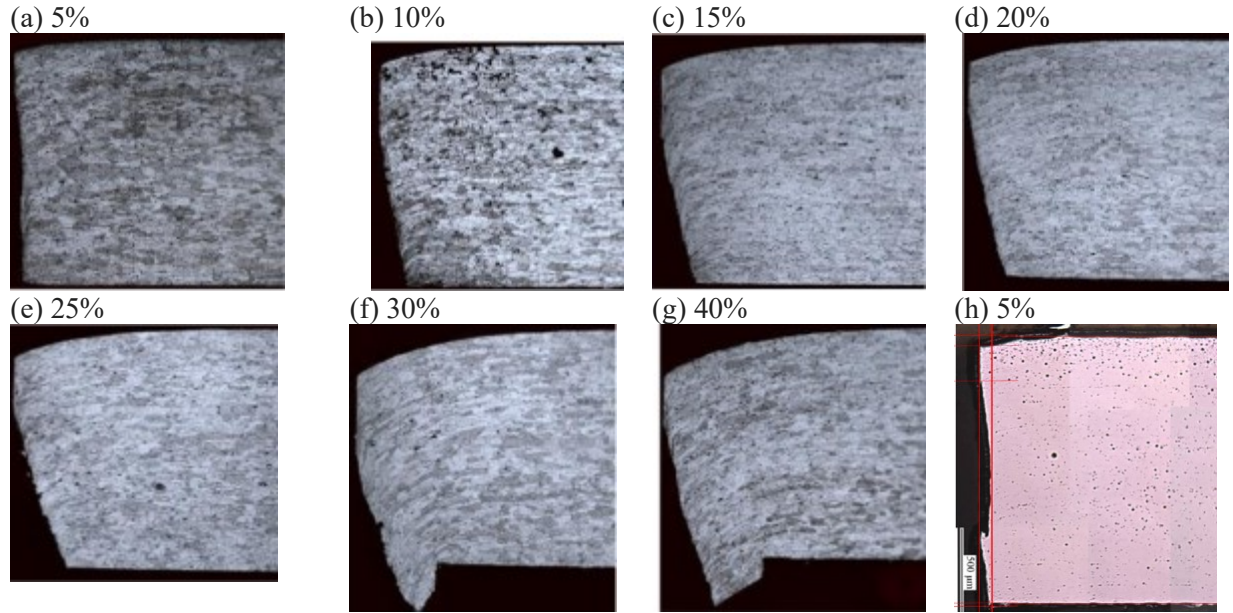


Figure 13. (a) to (g) Comparison between different cutting clearances (from 5% to 40%) for an AA6111T4 aluminum alloy (0.9 mm thick) using a punch with 10 mm diameter [22]. (h) secondary burnish happening in DP780 steel sheet (1.6 mm thick) using a punch with 15.8 mm diameter [23].

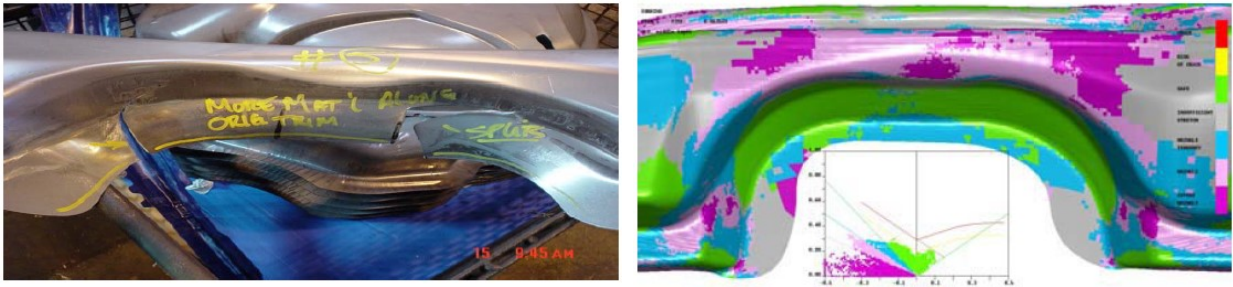


Figure 14. Edge cracking appeared during the forming process of an automotive underbody structural part made by DP780 steel (left). While FLC predicted the safe forming design for the sheet and all strains remained below the FLC(right) [25].

Hole expansion test (HET) is the only standardized method, ISO 16630 [6], to quantify the edge cracking sensitivity of metal sheets with the thickness range of 1.2-6.0 mm. In this method, a pierced hole is formed by a conical punch with the angle of  $60 \pm 1^\circ$  until a crack propagates throughout the whole thickness. Afterwards, hole expansion ratio (HER) is calculated as the ratio of the changes in diameter after hole expansion ( $D_h - D_0$ ) to the diameter of the initial hole ( $D_0$ ), figure 15. Choi et al [26] also proposed a crack inspection algorithm to automatize HER calculation in addition to increase the accuracy. In this regard, a monochrome CCD camera with 5 M pixels was utilized to detect the crack initiation and propagation. Their work consisted of several steps including binarization, blob detection, background deletion, selection of regions of interest, image linearization, and crack identification with the captured images during the HER test, figure 16. In addition to this standard HET, some similar experimental methods are also used for defining HER, such as KWI with cylindrical punch [27], HET with using Nakajima punch [28], collar

forming test (CFT) by applying drawing loading [29,30], Diabolo test with a diabolo shape punch [31]. The results of all these methods are highly controlled by the process parameters like tool geometries and frictional condition. Furthermore, the specimens experience various loading modes at the edge [32]. Moreover, some other testing techniques have been designed using tensile machine, such as open hole tensile tests (OHTT) with a strip sheet with a hole inside [33], and edge fracture tensile tests (EFFT) [34] with a tensile specimen with one sheared-cut edge and one milled edge. These methods apply the tension loading at the edges.

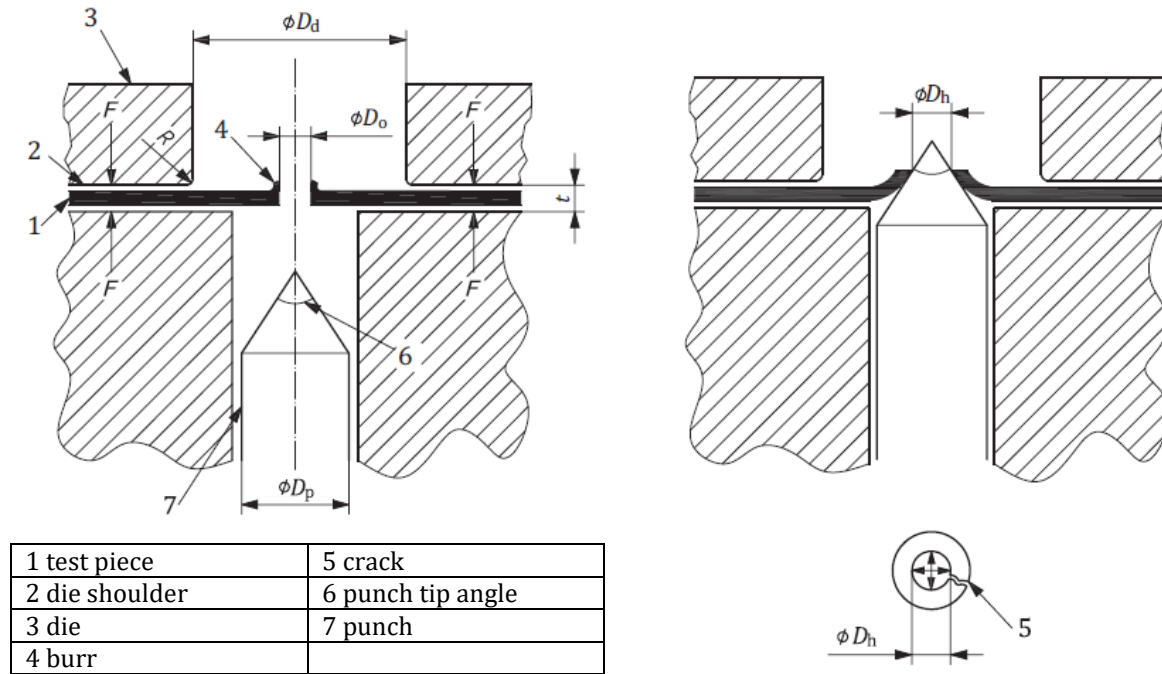


Figure 15. Schematic diagram of hole expansion test, (left) before and (right) after deformation process [6].

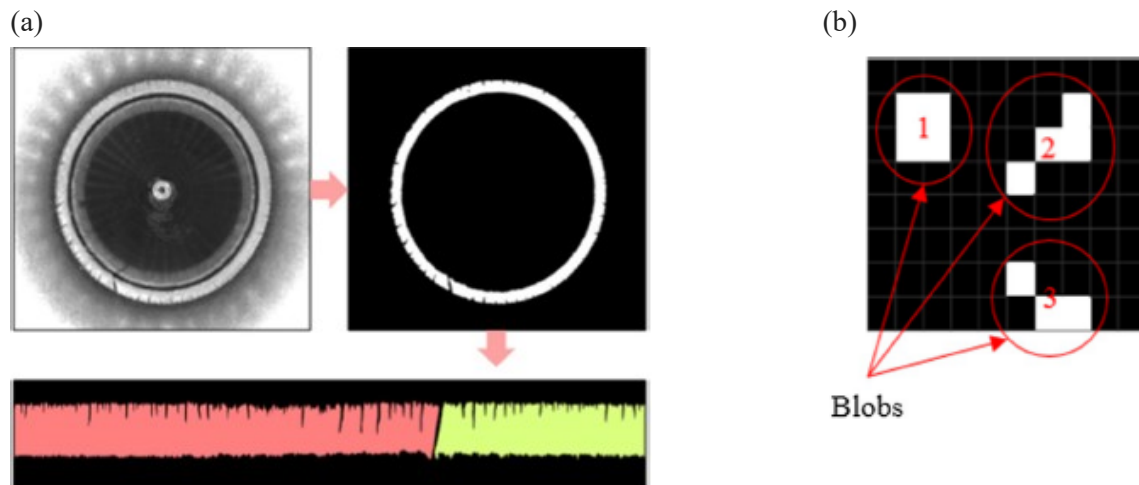


Figure 16. Automated hole expansion ratio measurement experimental method [26]

A proper method for prediction of edge cracking should satisfy the essential requirements, as listed below:

- Independent from tooling design and specimen geometries
- No frictional effect
- Homogenous stress distribution and avoidance of forced cracking
- Reproducible results
- Easy handling
- High cost, resource, and effort efficiency
- Employing wide range of stress states at the edge in mostly proportional loading condition

Despite several proposed experimental techniques, none could satisfy all the requirements and anticipate edge cracking in different forming conditions. Therefore, using computation technologies and employing finite element analysis and other numerical methods draw attention. Researchers develop numerical models that incorporate material mechanical properties, forming conditions, and the geometrical constraints of the component. By analyzing the stress and strain distribution, deformation history, and potential failure criteria, numerical simulations could help identify areas prone to edge cracking. Various uncoupled fracture models have been applied in this regard, such as Modified Mohr–Coulomb (MMC) [35,36], Rice-Tracey [14], Cockcroft-Latham [37], and Johnson-Cook [38]. However, very few studies considered the effect of strain rate and temperature on the hardening behavior and fracture limits of the materials through punching and the subsequent edge forming [24]. Habibi et al [39] proved considering the applied hardening and damage during shear-cutting is vital for correct prediction of edge cracking occurrence. Therefore, they should be calculated accurately. Nevertheless, local formability is highly influenced by the microstructural features of the materials [40]. Therefore, coupling their effects in the simulations is essential for material selection as well as edge crack prediction. However, the direct implementations of microstructural models in macroscale simulations are mightily restricted by their computational efficiency.

### 1.4 Objectives and scope of the study

Edge cracking phenomenon in AHSS restricts their widespread application. Despite many investigations on this topic, several open questions remain regarding the reasons for its occurrence and characteristics of a reliable approach for its prediction. Since, it is still challenging and critical to understand loading conditions throughout shear-cutting and subsequent forming processes. Also, how materials, the main root of edge cracking, respond to under these loading conditions. In this regard, the following scientific questions are addressed in the present dissertation.

- How to accurately predict edge cracking from macro-scale viewpoints? What are the most important parameters to consider? How can this complex multi-step process be simplified?
- Which loading conditions does a sheet metal experience under the shear cutting and subsequent forming processes? How does the damage evolve?
- Which microstructural features could improve or restrict local formability of DP steels under various stress states? Which damage micro-mechanisms can appear in different microstructures?

In order to achieve these objectives, experimental and numerical investigations have been conducted using three high strength dual phase steels with distinct microstructural features both macro- and meso-scale point of views. The main scientific contribution of this dissertation can be summarized as follows.

- A two-surface isotropic-kinematic plasticity model is coupled with a powerful phenomenological damage model.
- An elaborate experimental-numerical methodology is proposed for prediction of crack initiation through complex forming processes, which is able to anticipate edge cracking as well. This method considers the effects of strain rate and temperature (due to adiabatic heating) on plasticity and fracture.
- The stress states during shear-cutting and hole expansion tests are derived from the 3D simulations, which eliminates the misunderstanding about these processes according to 2D investigations.
- The effects of microstructural features on local formability and strain limits are investigated experimentally and numerically.
- The interaction between macro- and meso-scale are discussed by using the concept of damage initiation and evolution under various loading conditions.

## 1.5 References

- [1] C.C. Tasan, M. Diehl, D. Yan, M. Bechtold, F. Roters, L. Schemmann, C. Zheng, N. Peranio, D. Ponge, M. Koyama, An overview of dual-phase steels: advances in microstructure-oriented processing and micromechanically guided design, *Annual Review of Materials Research* 45 (2015) 391–431.
- [2] D. Raabe, B. Sun, A. Da Kwiatkowski Silva, B. Gault, H.-W. Yen, K. Sedighiani, P. Thoudend Sukumar, I.R. Souza Filho, S. Katnagallu, E. Jäggle, Current challenges and opportunities in microstructure-related properties of advanced high-strength steels, *Metallurgical and Materials Transactions A* 51 (2020) 5517–5586.
- [3] S. Sadagopan, D. Urban, C. Wong, M. Huang, B. Yan, Formability characterization of a new generation high strength steels, United States, 2003, <https://doi.org/2172/1001171>.
- [4] A. Dalloz, J. Besson, A.-F. Gourgues-Lorenzon, T. Sturel, A. Pineau, Effect of shear cutting on ductility of a dual phase steel, *Engineering Fracture Mechanics* 76 (2009) 1411–1424.
- [5] H. Wu, D. Li, C. Niu, J. Chen, Investigations on the flanging characteristics of advanced high-strength sheet metals with different sheared edge quality, *The International Journal of Advanced Manufacturing Technology* 125 (2023) 5591–5603.
- [6] ISO 16630, Metallic materials—Sheet and strip—Hole expanding test, ISO-International Organization for Standardization Geneva, 2009.
- [7] S. Westhäuser, M. Schneider, M. Teschner, I.A. Denks, Local ductility—key parameter for predicting formability of AHSS, *IOP Conf. Series: Materials Science and Engineering* 651 (2019) 12049.
- [8] S. Heibel, T. Dettinger, W. Nester, T. Clausmeyer, A.E. Tekkaya, Damage mechanisms and mechanical properties of high-strength multiphase steels, *Materials* 11 (2018) 761.
- [9] H. Ghadbeigi, C. Pinna, S. Celotto, Yates JR, Local plastic strain evolution in a high strength dual-phase steel, *Materials Science and Engineering: A* 527 (2010) 5026–5032.

- [10] N. Pathak, J. Adrien, C. Butcher, E. Maire, M. Worswick, Experimental stress state-dependent void nucleation behavior for advanced high strength steels, *International Journal of Mechanical Sciences* 179 (2020) 105661.
- [11] N. Pathak, C. Butcher, M.J. Worswick, E. Bellhouse, J. Gao, Damage evolution in complex-phase and dual-phase steels during edge stretching, *Materials* 10 (2017) 346.
- [12] L. Pan, J. Xiong, Z. Zuo, W. Tan, J. Wang, W. Yu, Study of the stretch-flangeability improvement of dual phase steel, *Procedia Manufacturing* 50 (2020) 761–764.
- [13] M. Madrid, C.J. van Tyne, S. Sadagopan, E.J. Pavlina, J. Hu, K.D. Clarke, Effects of testing method on stretch-flangeability of dual-phase 980/1180 steel grades, *Jom* 70 (2018) 918–923.
- [14] X. Hu, X. Sun, K. Raghavan, R.J. Comstock, Y. Ren, Linking constituent phase properties to ductility and edge stretchability of two DP 980 steels, *Materials Science and Engineering: A* 780 (2020) 139176.
- [15] O.R. Terrazas, K.O. Findley, C.J. van Tyne, Influence of martensite morphology on sheared-edge formability of dual-phase steels, *ISIJ international* 57 (2017) 937–944.
- [16] K. Park, M. Nishiyama, N. Nakada, T. Tsuchiyama, S. Takaki, Effect of the martensite distribution on the strain hardening and ductile fracture behaviors in dual-phase steel, *Materials Science and Engineering: A* 604 (2014) 135–141.
- [17] F. Pütz, N. Fehleemann, V. Göksu, M. Henrich, M. Könemann, S. Münstermann, A data driven computational microstructure analysis on the influence of martensite banding on damage in DP-steels, *Computational Materials Science* 218 (2023) 111903.
- [18] A.-P. Pierman, O. Bouaziz, T. Pardoen, P.J. Jacques, L. Brassart, The influence of microstructure and composition on the plastic behaviour of dual-phase steels, *Acta Materialia* 73 (2014) 298–311.
- [19] K. Hasegawa, K. Kawamura, T. Urabe, Y. Hosoya, Effects of microstructure on stretch-flange-formability of 980 MPa grade cold-rolled ultra high strength steel sheets, *ISIJ international* 44 (2004) 603–609.
- [20] X.M. Chen, C. Du, X. Wu, Zhu X, S.D. Liu, Sheet metal shearing and edge characterization of dual phase steels, *IDDRG International Conference* (2009).
- [21] K. Wang, M. Luo, T. Wierzbicki, Experiments and modeling of edge fracture for an AHSS sheet, *International Journal of Fracture* 187 (2014) 245–268.
- [22] X.H. Hu, X. Sun, S.F. Golovashchenko, An integrated finite element-based simulation framework: From hole piercing to hole expansion, *Finite Elements in Analysis and Design* 109 (2016) 1–13.
- [23] X. Wu, H. Bahmanpour, K. Schmid, Characterization of mechanically sheared edges of dual phase steels, *Journal of Materials Processing Technology* 212 (2012) 1209–1224.
- [24] C. Hartmann, H.A. Weiss, P. Lechner, W. Volk, S. Neumayer, J.H. Fitschen, G. Steidl, Measurement of strain, strain rate and crack evolution in shear cutting, *Journal of Materials Processing Technology* 288 (2021) 116872.
- [25] M.F. Shi, X. Chen, Prediction of stretch flangeability limits of advanced high strength steels using the hole expansion test, 2007.
- [26] S. Choi, K. Kim, J. Lee, S.H. Park, H.-J. Lee, J. Yoon, Image processing algorithm for real-time crack inspection in hole expansion test, *International Journal of Precision Engineering and Manufacturing* 20 (2019) 1139–1148.
- [27] E. Siebel, A. Pomp, Ein neues Prüfverfahren für Feinbleche, Verlag Stahleisen, 1929.



- 
- [28] E. Atzema, Different aspects of formability in AHSS, Forming in Car Body Engineering, 26À27 September (2012).
- [29] L.I. Besong, J. Buhl, M. Bambach, Increasing formability in hole-flanging through the use of punch rotation based on temperature and strain rate dependent forming limit curves, *International Journal of Material Forming* 15 (2022) 37.
- [30] F. Stachowicz, Estimation of hole-flange ability for deep drawing steel sheets, *Archives of Civil and Mechanical Engineering* 8 (2008) 167–172.
- [31] C. Held, M. Liewald, M. Sindel, Erweiterte Werkstoffprüfverfahren zur Charakterisierung von Leichtbaublechwerkstoffen im Hinblick auf die Kantenriss sensitivität, *Materials Testing* 52 (2010) 596–602. <https://doi.org/10.3139/120.110166>.
- [32] M. Schneider, A. Geffert, I. Peshekhodov, A. Bouguecha, B.-A. Behrens, Overview and comparison of various test methods to determine formability of a sheet metal cut-edge and approaches to the test results application in forming analysis: Überblick und Vergleich von Testmethoden für die Bewertung der Umformbarkeit einer geschnittenen Blechkante sowie Ansätze zur Nutzung der Versuchsergebnisse in der Umformsimulation, *Materialwissenschaft und Werkstofftechnik* 46 (2015) 1196–1217.
- [33] K. Watanabe, M. Tachibana, K. Koyanagi, K. Motomura, Simple prediction method for the edge fracture of steel sheet during vehicle collision (1st report). Evaluation of fracture limit from the edge using small-sized test pieces, 2006.
- [34] M. Feistle, I. Pätzold, R. Golle, W. Volk, Predicting edge cracks on shear-cut high-strength steels by modified uniaxial tensile tests, *Key Engineering Materials* 703 (2016) 49–55.
- [35] L. Qian, W. Ji, C. Sun, G. Fang, J. Lian, Prediction of edge fracture during hole-flanging of advanced high-strength steel considering blanking pre-damage, *Engineering Fracture Mechanics* 248 (2021) 107721.
- [36] K. Wang, L. Greve, T. Wierzbicki, FE simulation of edge fracture considering pre-damage from blanking process, *International Journal of Solids and Structures* 71 (2015) 206–218.
- [37] S. Han, Y. Chang, C.Y. Wang, H. Dong, A comprehensive investigation on the damage induced by the shearing process in DP780 steel, *Journal of Materials Processing Technology* 299 (2022) 117377.
- [38] I. Pätzold, J. Stahl, R. Golle, W. Volk, Reducing the shear affected zone to improve the edge formability using a two-stage shear cutting simulation, *Journal of Materials Processing Technology* 313 (2023) 117872.
- [39] N. Habibi, T. Beier, H. Richter, M. Könemann, S. Münstermann, The effects of shear affected zone on edge crack sensitivity in dual-phase steels, *IOP Conf. Series: Materials Science and Engineering* 651 (2019) 12073.
- [40] S. Park, W. Cho, B.-S. Jeong, J. Jung, S. Sung, H. Na, S.-I. Kim, M.-G. Lee, H.N. Han, A dual-scale FE simulation of hole expansion test considering pre-damage from punching process, *International Journal of Solids and Structures* 236 (2022) 111312.

---

## **Chapter II: Numerical investigation into effects of fracture behavior on edge cracking sensitivity**

---

**Niloufar Habibi, Meng Zhou, Junhe Lian, Markus Könemann and Sebastian Münstermann**

Journal of Materials Processing Technology 2023, 316 (117965)

<https://doi.org/10.1016/j.jmatprotec.2023.117965>

### **Highlights:**

- An elaborate study on stress-state evolution during shear-cutting and subsequent hole expansion process was conducted.
- Response of different fracture behaviors throughout these processes was studied numerically.
- A guidance to improve calibration strategy of fracture models for edge cracking prediction was provided.



## Numerical investigation into effects of fracture behavior on edge cracking sensitivity

Niloufar Habibi<sup>a,\*</sup>, Meng Zhou<sup>a</sup>, Junhe Lian<sup>b</sup>, Markus Koenemann<sup>a</sup>, Sebastian Muenstermann<sup>a</sup>

<sup>a</sup> Steel Institute, RWTH Aachen University, Aachen, Germany

<sup>b</sup> Department of Mechanical Engineering, Aalto University, Espoo, Finland

\* niloufar.habibi@iehk.rwth-aachen.de

### Abstract

Deep insight into fracture evolution throughout shear cutting and the subsequent deformation process plays a crucial role in successful experimental and numerical prediction of edge cracking. It allows not only to apply an appropriate strategy for experimental comparison between different materials but also to select a proper fracture criterion and calibration method for numerical simulations. The present work aims to provide this knowledge by simulation of shear cutting and the following hole expansion process for various imaginary fracture loci of the Bai-Wierzbicki model. This uncoupled fracture model was modified to consider influences of deformation history, in addition to stress states. The new fracture loci were artificially designed to uncover the individual effects of fracture resistance of four distinct stress states, which are pure shear, plane strain, uniaxial tension, and biaxial tension. The results reveal clear changes in the crack initiation and evolution throughout each deformation process, which are discussed by deriving the loading history at different points of the created edge. The gained knowledge is applied to the experimental results of two different dual-phase steel sheets to explain their behaviors.

### Keywords

Edge cracking, fracture locus, stress state, finite element method

### 1. Introduction

Shear cutting is widely acclaimed as one of the fundamental and irreplaceable initial manufacturing processes in industry, due to its simple operation, easy assembly, and low cost. However, the accumulated damage at the produced edge through this process is gradually considered a challenge in the automotive industry, where using high-strength sheet materials is drastically increased for body-in-white parts. Despite the good general formability of the utilized new-generation metals, like dual-phase (DP) steels, their poor local formability suppresses further deformation at an edge, especially a shear-cut one (Tasan et al., 2015). Therefore, edge cracking happens, which cannot be predicted by conventional numerical or analytical tools, such as the forming limit diagram. Since experimental trial and error is not a feasible method for designing a successful forming process, many studies have been conducted to introduce promising numerical approaches for edge cracking anticipation. For this purpose, the main characteristics of a manufactured edge, which are edge quality and accumulated damage, should be perfectly understood and considered (Feistle et al., 2022; Yu et al., 2016; Zhao et al., 2022).

Edge quality refers to the roughness and shape of the edge which is controlled by the assigned wear between the material and manufacturing tools. Wechsuanmanee et al (Wechsuanmanee et al., 2021) investigated

the effects of edge quality on the subsequent hole expansion deformation. They analyzed the surface topography of a wire-cut edge by a confocal microscope and constructed a 3D sub-model of the hole expansion test with an edge that represented the real roughness data in Abaqus finite element (FE) software. The results showed that this method reduced the discrepancy between experimental and simulation prediction of hole expansion ratio (HER), as the quantitative parameter for edge crack sensitivity, from 24.4% to 13.3%. Han et al (Han et al., 2022a) simulated various shear-cutting processes of hot stamping steel by employing six well-known simple fracture criteria, including Rice-Tracey, Freudenthal, Cockcroft-Latham, Brozzo, Oh, and Oyane models, which all contain a maximum of two material constants. The models were calibrated by minimizing differences between experimental and simulated force-displacement curves for shear cutting through an iterative method (Han et al., 2016). They concluded that the Cockcroft-Latham model can predict the sizes and shapes of different shear-cut zones better than the other models. Furthermore, they stated that the stress triaxiality constantly increased as the cutting punch penetrated deeper into the material. Gutknecht et al (Gutknecht et al., 2016) implemented a fully coupled Lemaitre-type stress-triaxiality-dependent damage model for a 2D simulation of a shear-cutting process and claimed that two main different mechanisms appeared: first, the dominant shearing during the formation of the burnished zone, and second, gradual increase of stress triaxiality under the tension mode during fracturing. Sandin et al (Sandin et al., 2022) showed that the stress state during shear-cutting is not fully supported by using plane stress specimens for calibration of the modified Mohr-Coulomb fracture locus, and proper prediction of shear-cut edge shape required precise information of the plane strain valley. Therefore, they proposed a tuning method by local calibration of the fracture surface for obtaining more accurate predictions.

Although comparison of the shape of a shear-cut edge between simulation and experiment has been mostly used for claiming accurate numerical prediction, the effects of extreme induced work-hardening and damage at the shear-affected zone (SAZ) play a significant role in edge cracking during the following deformation processes. Note that severe flow of materials (Cui et al., 2019; Casellas et al., 2017), micro-cracks, and micro-voids formation (Han et al., 2022b) at SAZ have been proved experimentally in numerous reports. Moreover, Habibi et al (Habibi et al., 2019) disclosed numerically that adding the effect of shape at a shear-cut edge to accumulated damage can improve the predicted HER by only about 5% while taking the roughness individually without any residual damage into account could not even correctly predict the site of crack initiation during the hole expansion test. Thus, even transferring only the damage properties of SAZ to the simulation of a subsequent forming could be sufficient for assessing edge cracking occurrence (Wang et al., 2015; Mu et al., 2017). In this regard, the accurate damage value and distribution of SAZ could be calculated by using a 2D finite element simulation of cutting, while a very fine mesh pattern is applied at this zone. Then, this accurate data could be transferred to a 3D model of a hole-forming process, while using a coarser mesh pattern to reduce the calculation time. Although it seems a promising method, the mapping technique is very important to representing the damage properly and achieving correct results (Lingbeek et al., 2022).

In addition, the material microstructural properties have a major impact on edge crack sensitivity, by controlling the damage micro-mechanisms and local formability. This holds true, especially for high-

strength steels which mostly contain very complex multiphase microstructures (Heibel et al., 2018; Pathak et al., 2017). Therefore, scale-bridging methods have been recently applied for edge cracking prediction. In these methods, representative volume elements (2D or 3D) were constructed according to the microstructural features of the material and the mechanical behavior of individual phases was defined using a crystal plasticity approach, which was calibrated using experimental data from nano-indentation techniques (Habibi et al., 2021; Park et al., 2021; Park et al., 2022) or high energy X-ray diffractions (Hu et al., 2020). As materials undergo complicated non-proportional loading paths through shear-cutting and hole-forming processes, assigning correct boundary conditions is vital.

The above showed a glimpse of the current numerical methods for edge cracking prediction and its obstacles. Therefore, the present paper aims to expose the actual physical mechanism through a shear-cutting and a successive hole expansion process, to promote material selection and simulation strategies, including fracture models calibration, mapping technique, and boundary conditions assignment. Hence, various stress state dependent fracture loci were designed and implemented in the simulations. The results disclosed the influences of fracture strains of the materials on their behavior through the cutting and hole expansion processes.

## 2. Methodology

To investigate the effect of fracture locus on edge cracking sensitivity, several imaginary fracture loci were designed in various shapes and fracture strain levels. In other words, new materials were invented with the same plasticity but different fracture behaviors. Afterwards, the response of the new fracture loci under shear cutting and the subsequent hole expansion tests were assessed.

### 2.1. Design of new fracture loci

For creating new fracture loci, Bai-Wierzbicki (BW) (Bai and Wierzbicki, 2008) strain-based phenomenological damage model was used to describe the fracture behavior of the materials.

$$D = \int_0^{\varepsilon^p} \frac{d\varepsilon^p}{(C_1 e^{-C_2 \eta_{avg}} - C_3 e^{-C_4 \eta_{avg}}) \bar{\theta}_{avg}^2 + C_3 e^{-C_4 \eta_{avg}}}, \quad \eta_{avg} > -1/3 \quad \text{Eq. 1}$$

where  $D$  is the scalar failure indicator,  $\varepsilon^p$  represents equivalent plastic strain. This version of the damage model considers the influences of stress state and loading condition, in terms of stress triaxiality ( $\eta = \frac{\sigma_m}{\bar{\sigma}}$ )

and normalized Lode angle parameter ( $\bar{\theta} = 1 - \frac{2}{\pi} \cos^{-1} \left( \frac{3\sqrt{3}}{2} \frac{J_3}{J_2^{3/2}} \right)$ ), where  $\sigma_m$  and  $\bar{\sigma}$  are the mean stress and von Mises equivalent stress,  $J_2$  and  $J_3$  are the deviatoric stress invariants, respectively. Also, it takes the effects of non-proportional loading paths into account (by using integration formulation), which is a crucial factor in such a complicated multi-step deformation process in the present study. Therefore, the average values of stress states for each increment should be used as well ( $\bar{\theta}_{avg} = \frac{1}{\varepsilon^p} \int_0^{\varepsilon^p} \bar{\theta}(\varepsilon^p) d\varepsilon^p$  and  $\eta_{avg} = \frac{1}{\varepsilon^p} \int_0^{\varepsilon^p} \eta_{avg}(\varepsilon^p) d\varepsilon^p$ ).

Compared to the original formulation, a cut-off of stress triaxiality at  $-1/3$  is introduced following the research by (Bao and Wierzbicki, 2005), who conducted a large number of mechanical tests and proposed the cut-off value of  $-1/3$  for metals, under which failure is suppressed in deformation. This concept is later

confirmed and applied by (Teng and Wierzbicki, 2006) and also implemented to other failure criteria, e.g., the ductile fracture model by (Lou et al., 2012). Therefore, in the current model, it is also assumed that damage does not develop under multiaxial compression loadings (Bao and Wierzbicki, 2005), and  $D$  is calculated here only for  $\eta_{\text{avg}} > -1/3$ . It is also noted that there is a discontinuity in the current formulation when the failure strains are approaching the cut-off stress triaxiality from higher values. This results in a sudden increase of the failure strain from a finite value to infinity at a stress triaxiality of  $-1/3$ . Physically, a smooth transition shall be more physical for this process, as demonstrated in the fracture model by (Lou et al., 2012). However, the BW model formulation does not introduce these smooth transition features, and therefore, the discontinuous formulation here is a simplified form for the smooth process, which can be proven to show negligible impact only to stress triaxiality very close to  $-1/3$  (Lou et al., 2012; Park et al., 2017).

The parameters  $C_{1-4}$  are material constants that should be calibrated using at least four experimental tests with different stress states. In this formulation, fracture happens when  $D$  reaches the value of one. In this state,  $\epsilon^P$  becomes the equivalent plastic strain at fracture ( $\epsilon_f^P$ ). Here, the parameters of the reference material are listed in table 1 as Ref., which were taken from reference (Pütz et al., 2020) for a DP1000 steel sheet with a thickness of 1.5 mm. The parameters were calibrated using several different plane-strain, central-hole, and notched dog-bone tensile tests along with parallel simulations. Note that since the damage initiation of this material was reported (Münstermann et al., 2017; Liu et al., 2020) very close to the fracture, the damage initiation point is negligible; hence an uncoupled model could be applied successfully. The calibrated fracture locus is illustrated in figure 1 in the space of stress triaxiality, normalized lode angle parameter, and equivalent plastic strain.

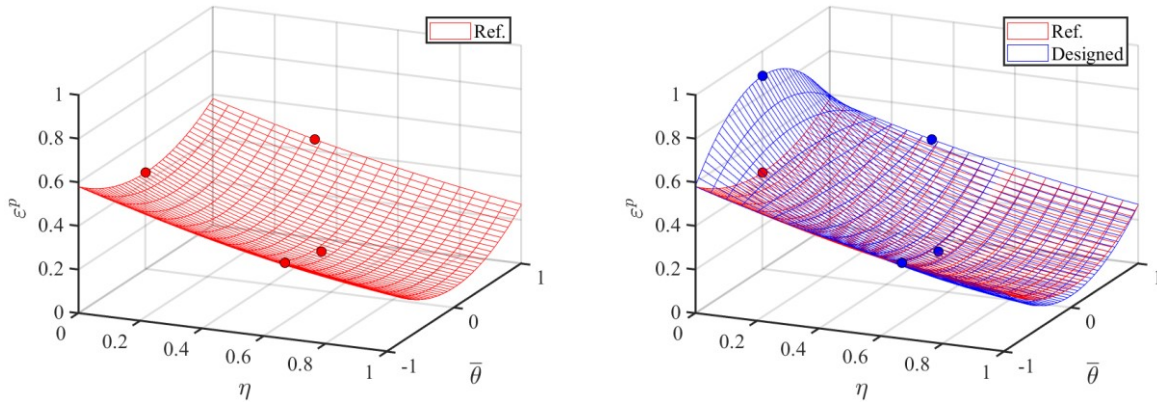


Figure 1. The provided points and fitted fracture loci for the Ref. (left) and designed (right) materials illustrate the applied method.

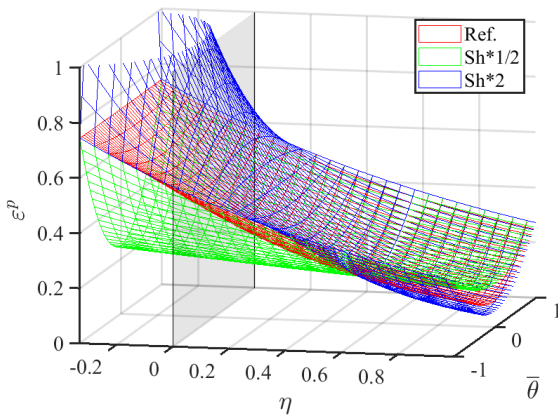
As this model contains four constants, only four new points were required for plotting a new fracture locus. Therefore, at first, four points at different stress states were extracted from the reference material. These stress states included shear ( $\eta=0$ ,  $\bar{\theta}=0$ ), plane strain ( $\eta=0.57$ ,  $\bar{\theta}=0$ ), uniaxial tension ( $\eta=0.33$ ,  $\bar{\theta}=1$ ), and biaxial tension ( $\eta=0.67$ ,  $\bar{\theta}=-1$ ), and the corresponding fracture strains ( $\epsilon_f^P$ ) for the Ref. material are 0.443,

0.181, 0.451, and 0.349, respectively. In other words, by using these points, in fact, the surface shape is controlled by varying two lines of  $C_1 e^{-C_2 \eta_{avg}}$ , when  $\bar{\theta} = \pm 1$ , and  $C_3 e^{-C_4 \eta_{avg}}$ , when  $\bar{\theta} = 0$ .

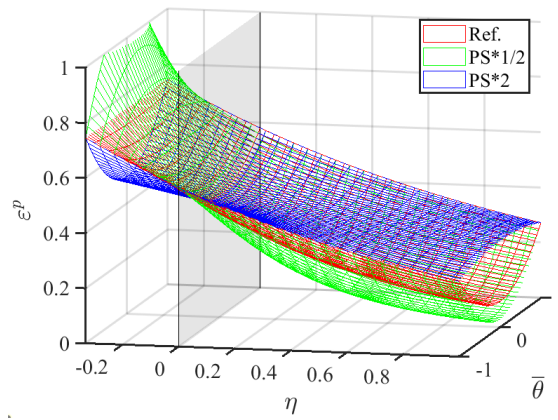
Table 1. The material constants of the BW fracture model used in this study.

	Ref. (Pütz et al., 2020)	Sh*1/2	Sh*2	PS*1/2	PS*2	UT*1/2	UT*2	BT*1/2	BT*2
$C_1$	0.580	0.580	0.580	0.580	0.580	0.148	2.273	1.137	0.296
$C_2$	0.760	0.760	0.760	0.760	0.760	-1.279	2.799	2.799	-1.279
$C_3$	0.443	0.222	0.886	0.443	0.443	0.443	0.443	0.443	0.443
$C_4$	1.570	0.354	2.786	2.786	0.354	1.570	1.570	1.570	1.570

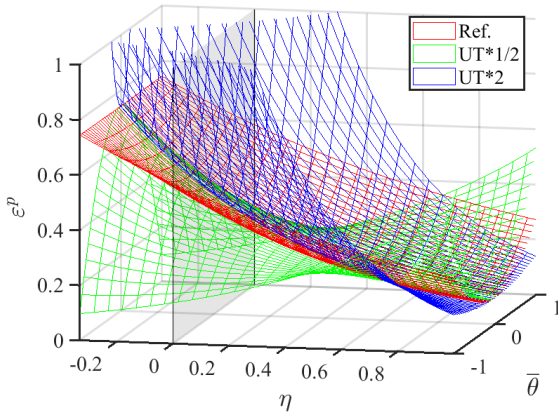
Shear



Plane strain



Uniaxial tension



Biaxial tension

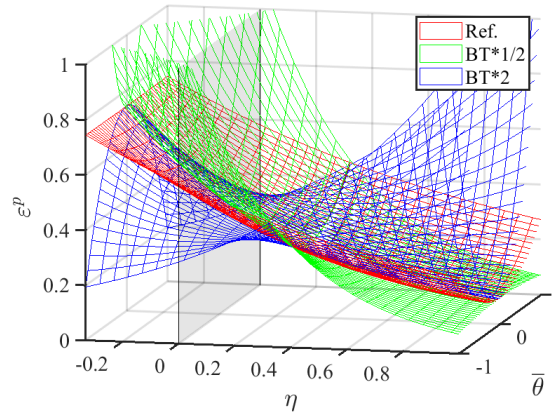


Figure 2. The fracture loci of the Ref. and new materials.

Then, the extracted fracture strain of only one stress state was individually multiplied by 2 while the fracture strains of the other mentioned stress states remained the same, and the new fracture locus was fitted with the model equation, figure 1. The same procedure was also employed for multiplying the fracture strains individually by 0.5. Finally, eight new fracture loci were designed, figure 2. To clarify the method, the new material constants are also listed in table 1. Abbreviations of Sh, PS, UT, and BT individually stand for

shear, plane strain, uniaxial tension, and biaxial tension stress states.  $Sh^{*1/2}$  and  $Sh^{*2}$  refer to the new loci, in which the fracture strains at shear stress state became half and double, respectively. Note that among these artificial fracture loci  $UT^{*1/2}$  and  $BT^{*2}$  show a negative slope for stress triaxiality versus normalized Lode angle parameter through some stress states, since  $C_2 < 0$ . Therefore, although the results are presented in the following, no specific discussion is being held in the following sections.

## 2.2. Simulation model

To assess the impacts of the hypothetical fracture loci on edge crack sensitivity, finite element Abaqus 2019/Explicit software was used to simulate a shear-cutting process which was followed by a hole expansion process. A two-step 3D model was created. The assembly scheme, boundary conditions, and mesh pattern are displayed in figure 3. The first step of the simulation was the cutting process, where a deformable solid sheet with a thickness of 1.5 mm was cut using a punch with a diameter of 29.6 mm. Note that the sheet was clamped between a die with a diameter of 30 mm and a holder, and an optimal clamping force was applied to constrain the sheet and prevents it from drawing or tearing throughout the cutting. Therefore, the die clearance regarding the sheet thickness is 13.3%. Additionally, all the tool parts were modeled as discrete rigid bodies with an edge radius of 0.05 mm. After the hole was cut in the sheet, it underwent an expansion simulation using a conical punch with an angle of  $50^\circ$  through the second step. To decrease the computation time and by considering the symmetric axes, only  $5^\circ$  of the set-up was modeled. Friction between the tools and the sheet was considered as the Coulomb model with a coefficient of 0.1 (Wang et al., 2015). Since new surfaces were created during the cutting process, the contact pairs were defined by a node-to-surface algorithm. A very fine mesh size of  $0.025 \text{ mm} \times 0.025 \text{ mm} \times 0.025 \text{ mm}$  with the element type of eight-node brick element with reduced integration (C3D8R) was employed for the critical regions, where the deformation was concentrated. The Mises plasticity and BW fracture model were applied by a VUMAT subroutine, in which the crack initiation and propagation were visualized by element deletion. The flow curve was extrapolated to high strains using the Hollomon-Voce hardening model, as shown in reference (Pütz et al., 2020). Furthermore, the edge crack sensitivity was quantified by calculation of the hole expansion ratio, when an edge crack propagated into the material RD-TD plane. Note that this local implementation approach of damage with mesh size concerns could influence the results of crack initiation and propagation, and also HER values.

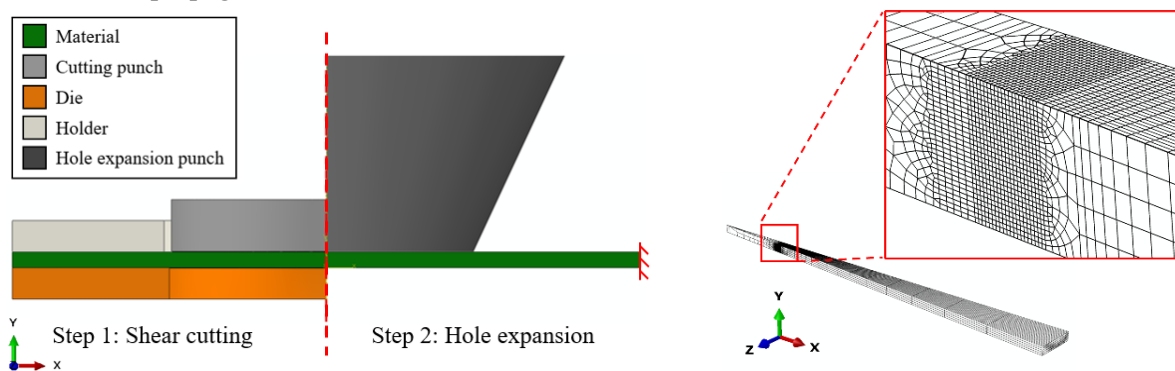


Figure 3. The assembly (left) and mesh pattern (right) of the created model.

The findings of material behavior regarding its fracture strains were verified by comparing the experimental results of an exact similar shear cutting and hole expansion test on other two different DP1000 steel sheets, CR590Y980T-DP and CR700Y980T-DP, with a thickness of 1.5 mm. The chemical, mechanical, and damage properties of these materials were thoroughly studied in Ref. (Habibi et al., 2022).

### 3. Results and discussion

In order to elaborate discussion, the results are demonstrated in two sections: 1. Shear cutting process, and 2. subsequent hole expansion process. In each section, first, the stress state evolution is discovered throughout the process at the critical regions, which could provide a good grasp of the effects of the forming steps. Afterwards, the influences of the new fracture loci are shown and discussed based on the stress state evolution and in comparison to the reference material.

#### 3.1. Step 1: Shear-cutting process

The cut edge of the reference material is depicted in figure 4 regarding the distribution of failure indicator (D) at the final separation frame. As expected, the D parameter is high at the cut edge and decreases gradually with increasing distance from the edge. Like any cut edge, the edge represents four parts:

- Roll-over part: Result of bending effects before the punch penetrates the sheet.
- Burnished/clean-shear part: Penetration consequence of the punch through the sheet until the crack initiation.
- Fracture part: Propagation of the crack through the rest of the sheet thickness.
- Burr part: Result of the bottom die support and delay in fracture.

The stress state evolution versus the failure indicator was derived for the first element of each edge region. These elements were selected from the deleted elements, which are highlighted in figure 4 on the undeformed view. The extracted stress state history indicates that all the critical elements experienced the deformation with  $\bar{\theta}$  very close to 0 through the whole shear cutting. Therefore, consideration of this parameter in the fracture model is vital. Otherwise, the stress state could be mistakenly interpreted, as uniaxial tension in some parts, which has been already reported vastly before, such as Ref. (Gutknecht et al., 2016; Han et al., 2022b). Hence, the information of only tensile tests or biaxial tests is not sufficient for the prediction of materials response in shear cutting. The elements from roll-over and burr (number 1 and 4) parts underwent low stress triaxialities at the beginning of deformation to very high ones (close to plane strain) at  $D=1$ . This obviously implies that bending happened. The element from the burnished part (number 2) experienced a pure shear stress state all over the cutting process, as correctly also named the clean-shear part. Furthermore, the fracture part was formed after the crack was initiated and the element at this region (number 3) went from compression ( $-0.33 \approx \eta$ ) at the beginning of deformation (before the crack was initiated) to medium stress triaxiality ( $\eta \approx 0.33$ ) when it was deleted as the crack propagated. Note that the stress triaxiality at each region increased almost constantly while the loading was applied.

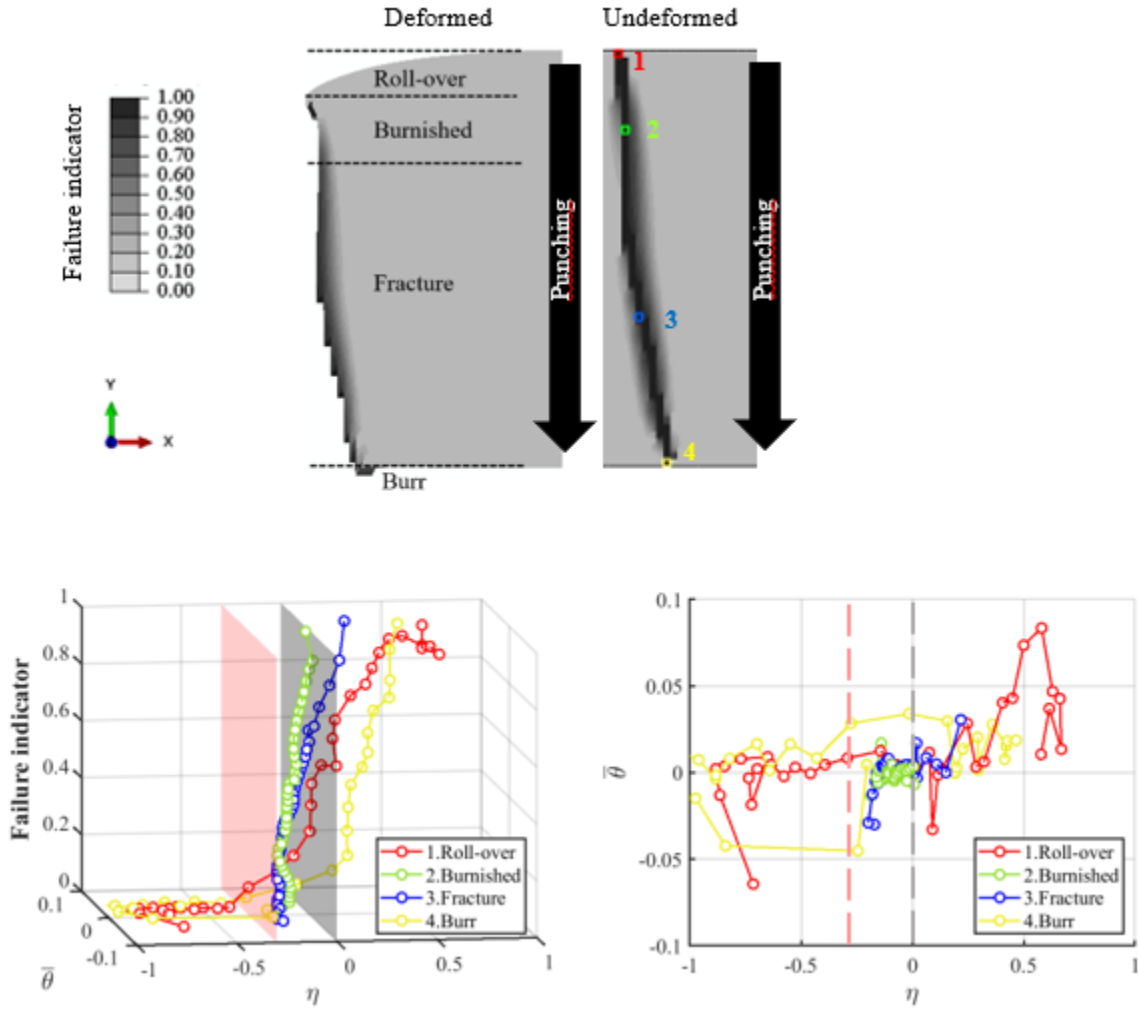


Figure 4. The stress state evolution through cutting process for elements at different regions of the cut edge.

Cut edges of the designed materials are shown in figure 5, and the sizes of different parts are summarized in the diagram. In addition, the force-displacement curves of the cutting process and the deformation energy (area under the force-displacement curve) are compared in figure 6, which can be divided into two components, energy for crack initiation (marked with red triangles on force-displacement curves and dashed columns in the energy diagrams) and energy for crack propagation (the solid parts of energy columns). Since by changing fracture strains for uniaxial tension or biaxial tension, the fracture strains throughout  $\bar{\theta}=0$  remained the same for these new fracture loci (UT\* $\frac{1}{2}$ , UT\*2, BT\* $\frac{1}{2}$ , and BT\*2), they showed very negligible influence on the cutting process. Therefore, the discussion in this section is only focused on Sh\* $\frac{1}{2}$ , Sh\*2, PS\* $\frac{1}{2}$ , and PS\*2 loci.



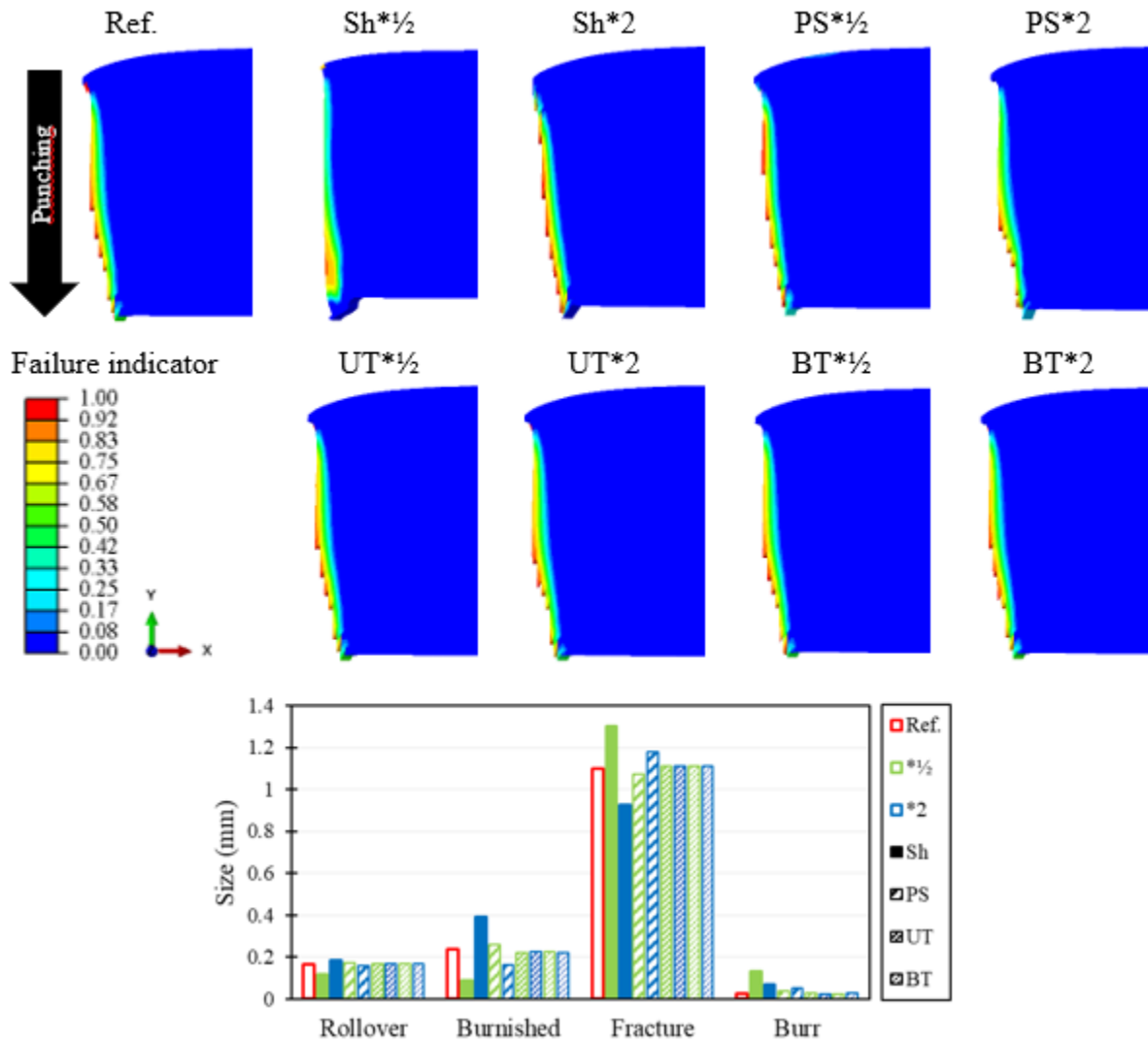


Figure 5. The distribution of accumulated damage at the cut edge and size of different regions for designed materials.

Clear changes appeared at the cut edge of the new materials in comparison to the reference material, which can be explained by the so far achieved knowledge of stress state evolution at different parts of the cut edge. These changes include the size of each part, deformation energy for crack initiation as well as crack propagation, edge shape (or surface irregularity), amount and distribution of damage from cutting at the created edge. All these parameters were influenced by the crack initiation moment and its propagation rate at each edge part. As mentioned, the elements at each part of the edge experienced a specific range of stress states and whenever the crack propagates faster, because of the lower level of fracture strain at that range of stress state, the size of the region became smaller, and the amount of applied damage was lower. The deformation of the roll-over part was stopped by the deletion of element 1, in figure 4. The burnished part started from element 1 to element 2. The former element underwent  $-1 < \eta < 0.57$  and the latter experienced  $-0.33 < \eta < 0$ . The average fracture strain values for both ranges of stress triaxialities were higher for new

materials Sh\*2 and PS\* $\frac{1}{2}$  than the reference material, while they remained lower for Sh\* $\frac{1}{2}$  and PS\*2. Therefore, part size and amount of residual damage at the roll-over and burnished parts were higher for Sh\*2 and PS\* $\frac{1}{2}$ . As the thickness of the sheet remains almost the same, when these two parts were larger, the fracture part became smaller. Note that the vertical separation at the edge may not represent only the burnished part in the FE simulation, but depends on the crack growth pace, and could include the fracture part as well. The complete separation happened when element 4 was deleted. This element underwent  $-1 < \eta < 0.5$ , and whenever the fracture strain for a material is higher in this range, a bigger burr part has to be expected, like for Sh\*2 and PS\*2 conditions. However, a very large burr appeared for Sh\* $\frac{1}{2}$ , which is explained in the following using figure 9. This figure shows the crack did not grow through exactly the same path as the maximum damage accumulated. The comparison of failure evolution between the marked red and blue elements for Sh\* $\frac{1}{2}$  and reference material reveals the damage was accumulating at both elements from the beginning of deformation while the stress triaxiality of red and blue elements are  $\eta < -0.2$  (compression) and  $-0.1 < \eta < 0.57$  (bending), respectively. But after more deformation (punch displacement), the stress triaxiality at the red element rose and became  $\eta > 0.3$  (uniaxial tension), while the blue element almost stopped further deformation and only was pushed by the punch. Therefore, no more damage accumulates in the blue element, while it constantly increases for the red element until the fracture indicator reaches 1. If the crack reaches element 4 very fast due to low fracture strains at the other parts, like for Sh\* $\frac{1}{2}$ , while the red element is still under compression and the amount of accumulated damage is negligible, the crack will propagate towards the blue element, and it will be deleted. For the record, the fracture indicator does not increase if the stress triaxiality is less than the cut-off value.

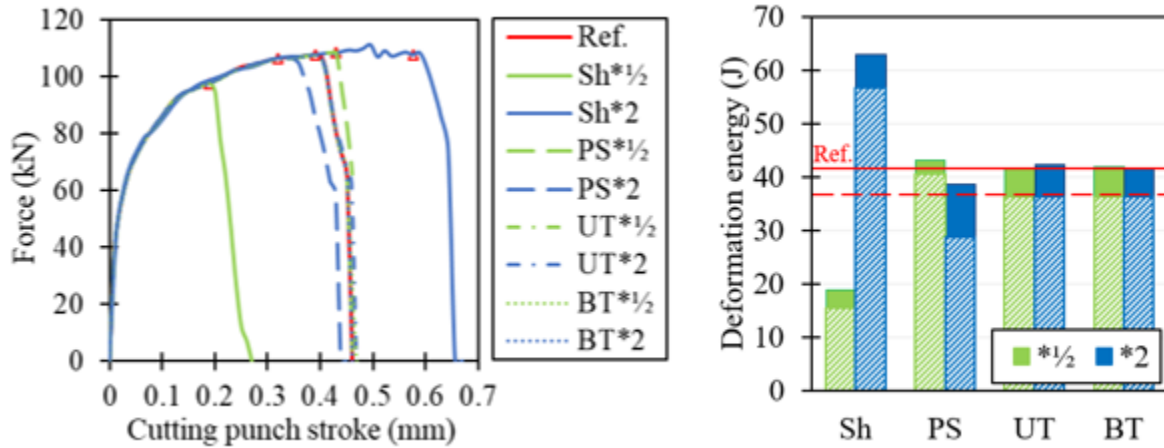


Figure 6. The force-displacement responses of different materials during the cutting process. The red triangles show the crack initiation for each case. The deformation energy was calculated and divided into before and after crack initiation, dashed, and solid parts, respectively.

The deformation energy was determined before and after the first element deletion by calculation of the area under the force-displacement curve of the cutting process. The former expresses crack initiation energy, i.e. formation of roll-over and burnish parts, and the latter states crack propagation energy, creation of fracture and burr parts. The investigation shows the crack initiation energy has proportional relation with

the slope of  $\bar{\theta}=0$  (i.e.  $\epsilon_{Sh}-\epsilon_{PS}$ ), and crack propagation energy relates to the average fracture strain of  $\bar{\theta}=0$ , in other words, the integration of fracture strain for the aforementioned range, figure 9.

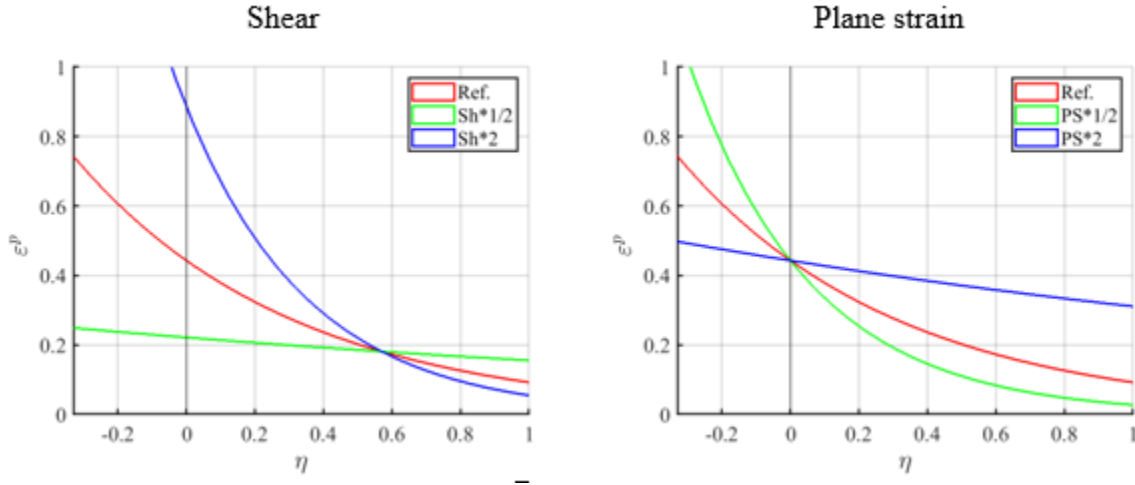


Figure 7. The employed fracture loci at  $\bar{\theta}=0$ .

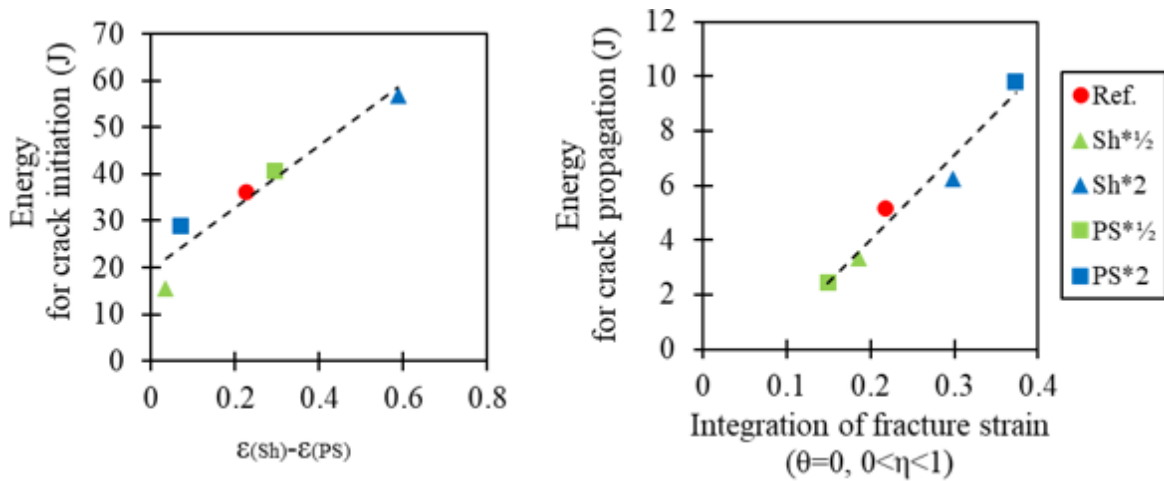


Figure 8. The relation between energy of crack initiation and propagation with the fracture locus slope at  $\bar{\theta}=0$  (left) and average fracture strain (right), respectively.

### 3.2. Step 2: Subsequent hole expansion process

Following the shear-cutting process, the manufactured hole underwent the hole expansion process with a conical punch. Figure 10 shows the edge of reference material at the frame when a crack propagated into the plane RD-TD (orthogonal to the cut-edge). The damage and stress state evolution were extracted from three elements which were deleted simultaneously at different parts of the edge at the mentioned frame. Element 1 (red) is located at the burr region but in the second column of elements far from the edge, hence its deletion is considered as crack propagation into the RD-TD plane. Due to the location, it encountered a low amount of damage over the previous step. Through this step, the element experienced the stress state of  $\bar{\theta} \approx -0.65$  and  $\eta \approx 0.07$  at the beginning which rose continually and reached  $\bar{\theta} \approx 0.4$  and  $\eta \approx 0.9$  at the end. Element 2 (green) is located at the fracture region of the edge, where the elements endured the highest

damage accumulation during the first step. This element underwent roughly uniaxial tension throughout the hole expanding ( $\bar{\theta} \approx 0.8$  and  $0.25 < \eta < 0.4$ ), as the cracks also showed up along the loading direction in this region. The third element (blue) is located at the burnished part with 0.8 pre-damage. During hole expansion, this element experienced uniaxial tension at the beginning which evolved to shearing at the end. Therefore, the cracks in this region formed at  $45^\circ$  regarding the loading direction. The results indicate that throughout the hole expansion test, higher damage was applied to the upper elements, thus  $D_1^{HE} > D_2^{HE} > D_3^{HE}$ , while the order of the amount of residual damage from the cutting step is  $D_2^{Cut} > D_3^{Cut} > D_1^{Cut}$ .

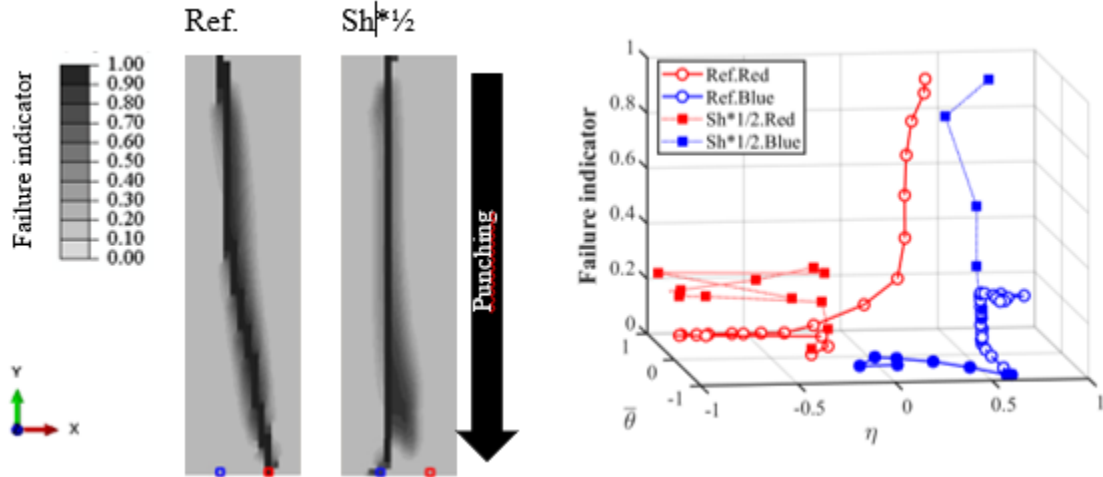


Figure 9. The explanation of different crack propagation for Sh\*1/2 condition, using the stress state history of two elements with high failure potential.

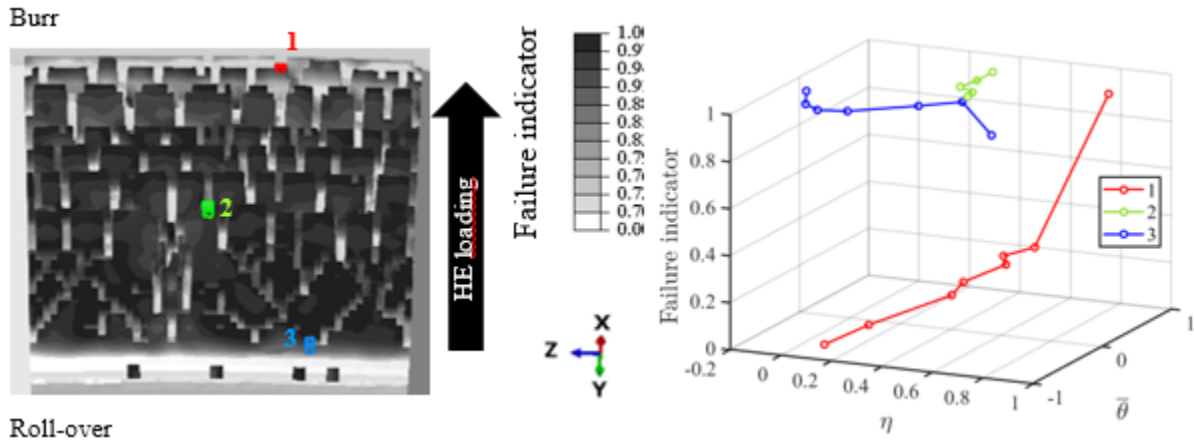


Figure 10. Comparison of the evolution of failure and stress triaxiality through the hole expansion process for 3 elements that failed simultaneously at the frame of crack propagation through the sheet plane. The blue and green elements were at the edge and the red one was the first deleted element at the sheet plane. Note that the initial failure values were inherited from the shear-cutting step and the last failure values for all the selected elements were 1, which means failure happened and the element was deleted.

The new materials reacted distinctively, figure 11. Note that the cracks can occur along two directions, along the cut-edge and orthogonal to the cut-edge, which is shown by y and x in figure 12, respectively. As the residual damage is high along the edge, the crack appeared there at first, not in the bulk material. However, the number of cracks along the y direction until a crack is initiated in the x direction is dependent on how easily the crack can be formed in each direction. The crack in the former direction is similar to element 2 and 3 of the reference material and the latter is like element 1. The hole expansion ratio was also calculated as a crack propagated orthogonally to the cut-edge (x direction), figure 12. Since the red element, which represents this crack, experienced wide ranges of stress state, increasing average fracture strain ( $-1 < \bar{\theta} < 1$  and  $0 < \eta < 1$ ) could rise the HER. Hence, many cracks were formed along the edge in PS\*2 condition before any crack was initiated orthogonally. However, no specific relation between these two parameters could be found, since the results are also affected by the first deformation step. Furthermore, when the fracture strain at shear was low, the cracks at the edge were inclined to propagate diagonally, like in Sh\* $\frac{1}{2}$ . Whereas only vertical cracks in Sh\*2 were created. The condition PS\* $\frac{1}{2}$  was not able to undergo this step, as the fracture strain of plane strain was defined as very low, it cannot stand more bending at the roll-over part at the beginning deformation of hole expansion.

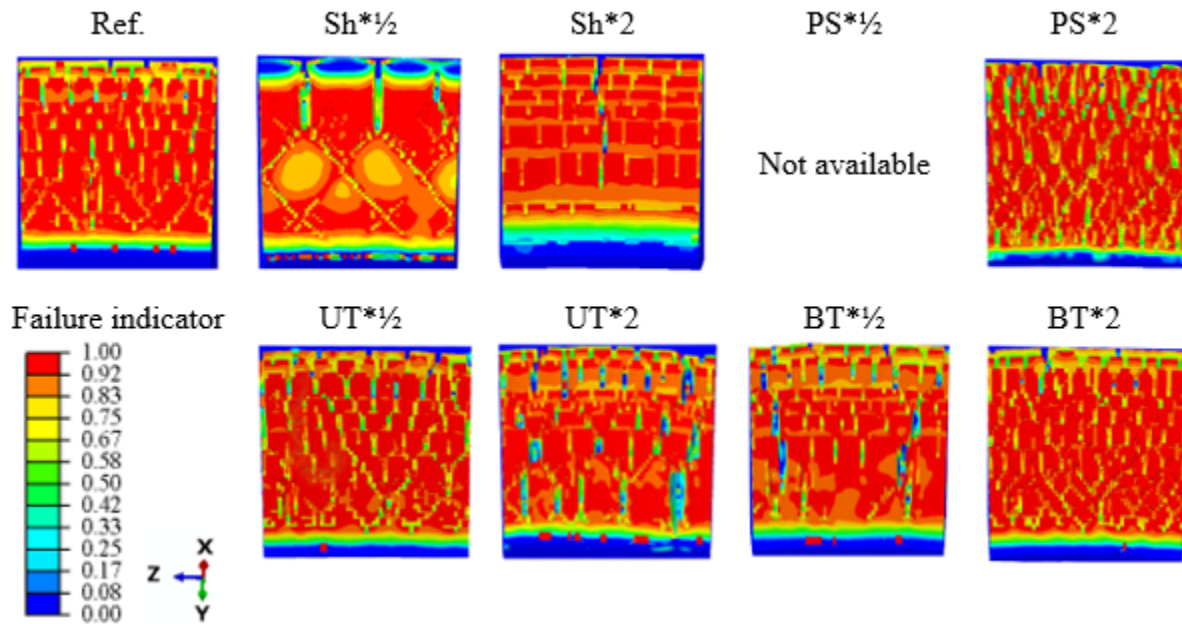


Figure 11. The behavior of the edges for designed materials through the subsequent hole expansion process. The photos were taken at the frame when a crack propagated orthogonally to the edge.

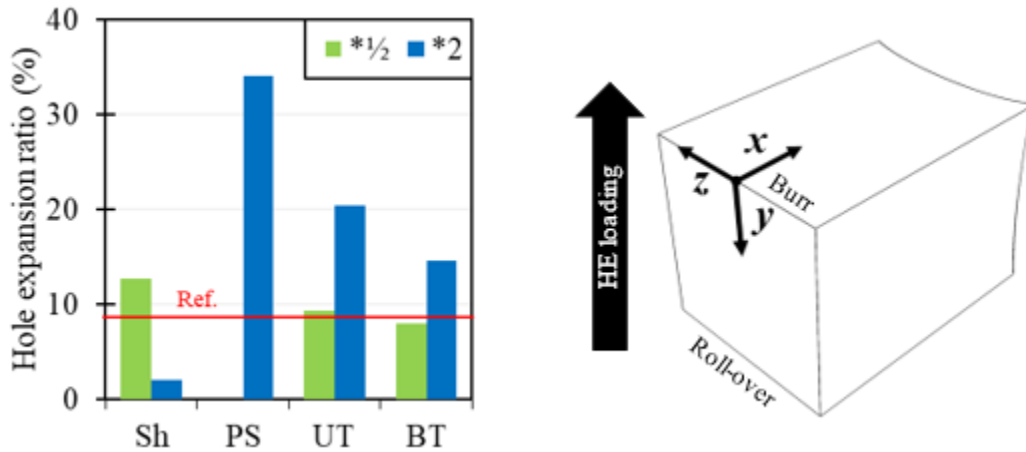


Figure 12. Hole expansion ratio at the moment that a crack is initiated along the x-direction.

The obtained knowledge is evaluated in the following by examining two other DP1000 steel sheets under the same experiments as the aforementioned simulation model. The fracture loci, figure 13, were roughly plotted based on local strains taken by digital image correlation method for uniaxial tensile, plane strain (R7.5), shear (torsion), and biaxial tension (bulge test) in Ref. (Habibi et al., 2022). CR700Y980T-DP represents substantially higher fracture strains than CR590Y980T-DP. The difference is about 100% for low stress triaxiality (like  $\eta=0$  for shear stress state) and 33% for higher stress triaxiality (like  $\eta=0.6$  for plane strain condition). As expected for the material with higher fracture strains (CR700Y980T-DP), especially for  $\eta \leq 0$ , a larger burnished part was formed during the shear cutting and the separation occurred diagonally from the punch position to the die position. Furthermore, in the hole-expanding process, multiple cracks were initiated at the edge before a crack was able to diffuse in the bulk material. The crack initiation and propagation took place rather slowly which led to an average HER value of 21.5%. While for the other material (CR590Y980T-DP) with remarkably lower fracture strains, the separation started after creating a smaller burnished part and propagated into the thickness. It seems a second crack from the bottom also initiated and met the first crack in the middle of the fracture region, as marked with a yellow arrow in figure 14. Therefore, complete separation happened faster and vertically, and no burr was created. The initiation site of the second crack was located far from the die, where the material experienced bending (plane strain condition), equal to the blue element in figure 9. These happenings appeared as this material represented very low fracture strain throughout  $\bar{\theta}=0$ , the same as Sh $*1/2$  condition. Unlike the former material, only one crack was created at the edge during the hole expansion test, which propagated through a shear path like the condition of Sh $*1/2$ , and it happened fast resulting in an HER value of 7.5% which is related to the low average fracture strain. Note that the marked crack at the edge in figure 13, can also play a significant role in low stretch flangeability (Han et al., 2022b).



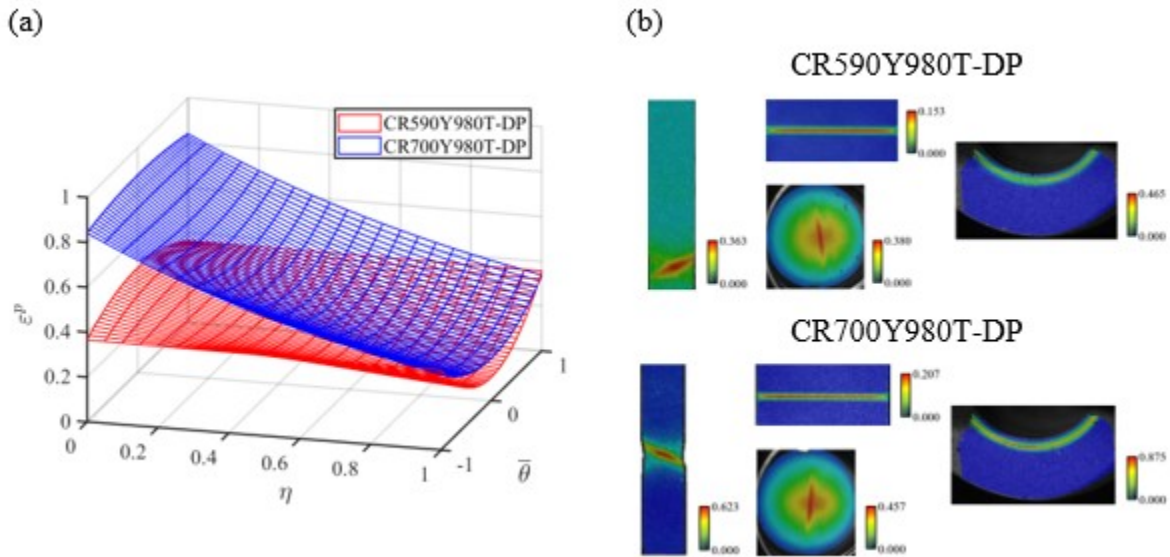


Figure 13. (a) Fracture loci of two DP1000 steels, which were calibrated using fracture strains at the different stress state experiments in (b) from Ref. (Habibi et al., 2022).

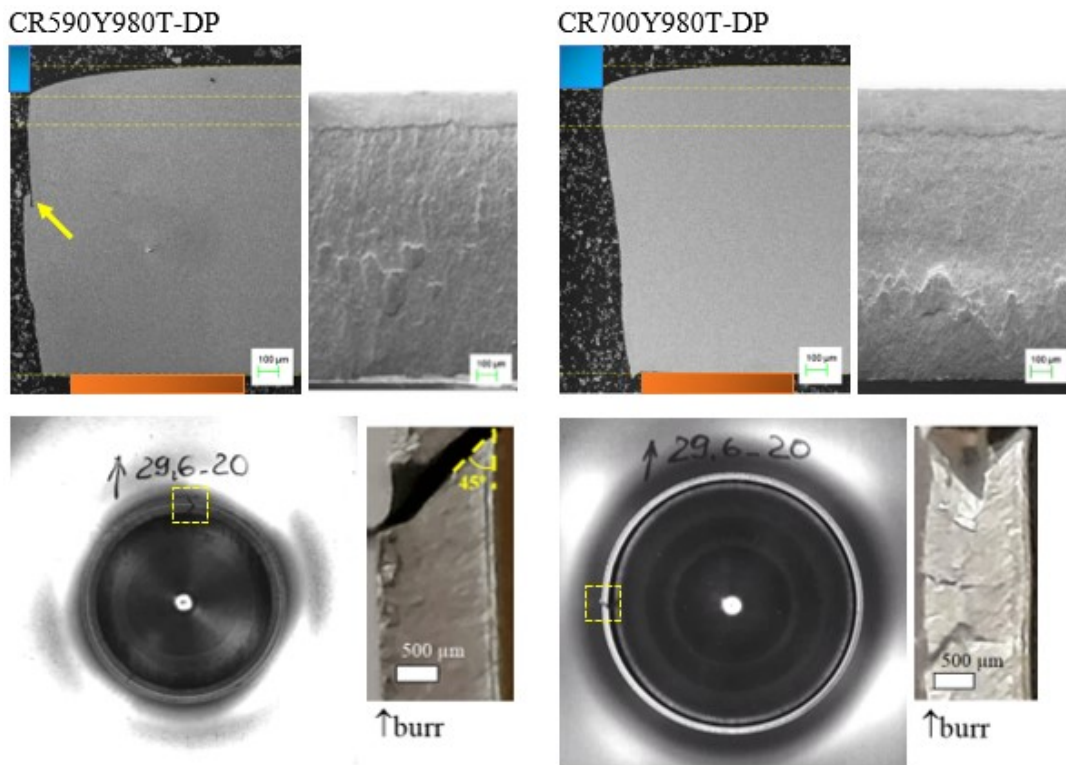


Figure 14. Top: The side and fracture view of cut edges for the studied steels after shear cutting.

The gray and orange rectangles illustrate the relative position of the cutting punch and die, respectively. Bottom: The behavior of cut edge for the studied steels after shear cutting and hole expansion tests.

### 4. Conclusion

The present paper aimed to provide a vision into shear cutting and edge crack sensitivity, by focusing on applied loading conditions and fracture behavior of materials. In this regard, eight different artificial fracture loci were created based on the reference fracture behavior of a DP1000 steel sheet, which underwent a shear cutting and a subsequent hole expansion test. The following conclusions can be drawn:

- The material experienced normalized Lode angle parameter of 0 throughout the whole shear cutting process. Therefore, precise information of fracture strains through this path is vital for correct simulations and predictions, which is possible by considering pure shear and tensile plane strain tests.
- When the fracture strain is low in a pure shear stress state, the crack propagates fast and the path is vertical. Whereas, for high fracture strains, the crack propagates slowly and diagonally from the punch towards the die.
- The occurrence of rapid crack can lead to different crack paths and formation of a large burr.
- Through the hole expansion, the edge of material experienced uniaxial tension to shear stress states, while the sheet plane underwent biaxial to plane strain tension modes. Whenever the crack in a material can propagate easier through the sheet plane than the reference material, fewer cracks were formed at the edge until the failure.
- The trends in both mentioned processes were also observed in the experimental tests of two different DP1000 sheets.

### Declaration of competing interest

The authors declare that they have no known competing financial interests or personal relationships that could have appeared to influence the work reported in this paper.

### CRedit authorship contribution statement

**Niloufar Habibi:** Writing – original draft, Data curation, Investigation. **Meng Zhou:** Investigation, Writing – Review & Editing. **Junhe Lian:** Writing – Review & Editing, **Markus Koenemann:** Writing – Review & Editing, **Sebastian Muenstermann:** Supervision, Funding acquisition, Writing – Review & Editing.

### Acknowledgement

The simulations were performed with computing resources granted by RWTH Aachen University under project <rwth0459>.

### References

- Bai, Y., Wierzbicki, T., 2008. A new model of metal plasticity and fracture with pressure and Lode dependence. *International Journal of Plasticity*, vol. 24, 1071–1096.
- Bao, Y., Wierzbicki, T., 2005. On the cut-off value of negative triaxiality for fracture. *Engineering fracture mechanics*, vol. 72, 1049–1069.
- Casellas, D., Lara, A., Frómeta, D., Gutiérrez, D., Molas, S., Pérez, L., Rehrl, J., Suppan, C., 2017. Fracture toughness to understand stretch-flangeability and edge cracking resistance in AHSS. *Metallurgical and Materials Transactions A*, vol. 48, 86–94.



- Cui, Z., Bhattacharya, S., de Green, Alpas, A.T, 2019. Mechanisms of die wear and wear-induced damage at the trimmed edge of high strength steel sheets. *Wear*, vol. 426, 1635–1645.
- Feistle, M., Golle, R., Volk, W., 2022. Edge crack test methods for AHSS steel grades: A review and comparisons. *Journal of Materials Processing Technology*, 117488.
- Gutknecht, F., Steinbach, F., Hammer, T., Clausmeyer, T., Volk, W., Tekkaya, A.E, 2016. Analysis of shear cutting of dual phase steel by application of an advanced damage model. *Procedia Structural Integrity*, vol. 2, 1700–1707.
- Habibi, N., Beier, T., Richter, H., Könemann, M., Münstermann, S. (Eds.), 2019. The effects of shear affected zone on edge crack sensitivity in dual-phase steels, IOP Publishing.
- Habibi, N., Mathi, S., Beier, T., Könemann, M., Münstermann, S., 2022. Effects of Microstructural Properties on Damage Evolution and Edge Crack Sensitivity of DP1000 Steels. *Crystals*, vol. 12, 845.
- Habibi, N., Vajragupta, N., Münstermann, S., 2021. Deformation and Damage Assessments of Two DP1000 Steels Using a Micromechanical Modelling Method. *Crystals*, vol. 11, 805.
- Han, S., Chang, Y., Wang, C., Han, Y., Dong, H., 2022a. Experimental and Numerical Investigations on the Damage Induced in the Shearing Process for QP980 Steel. *Materials*, vol. 15, 3254.
- Han, S., Chang, Y., Wang, C.Y, Dong, H., 2022b. A comprehensive investigation on the damage induced by the shearing process in DP780 steel. *Journal of Materials Processing Technology*, vol. 299, 117377.
- Han, X., Yang, K., Ding, Y., Tan, S., Chen, J., 2016. Numerical and experimental investigations on mechanical trimming process for hot stamped ultra-high strength parts. *Journal of Materials Processing Technology*, vol. 234, 158–168.
- Heibel, S., Dettinger, T., Nester, W., Clausmeyer, T., Tekkaya, A.E, 2018. Damage mechanisms and mechanical properties of high-strength multiphase steels. *Materials*, vol. 11, 761.
- Hu, X., Sun, X., Raghavan, K., Comstock, R.J, Ren, Y., 2020. Linking constituent phase properties to ductility and edge stretchability of two DP 980 steels. *Materials Science and Engineering: A*, vol. 780, 139176.
- Lingbeek, R.A., Schalk-Kitting, D., Gruschka, P., Uurike, M., Peetsalu, P., Blome, P. (Eds.), 2022. Modelling stamped edges in FEM breakage analyses of high-strength steel safety components, IOP Publishing.
- Liu, W., Lian, J., Münstermann, S., Zeng, C., Fang, X., 2020. Prediction of crack formation in the progressive folding of square tubes during dynamic axial crushing. *International Journal of Mechanical Sciences*, vol. 176, 105534.
- Lou, Y., Huh, H., Lim, S., Pack, K., 2012. New ductile fracture criterion for prediction of fracture forming limit diagrams of sheet metals. *International Journal of Solids and Structures*, vol. 49, 3605–3615.
- Mu, L., Wang, Y., Zang, Y., Araujo Stemler, P.M, 2017. Edge fracture prediction using uncoupled ductile fracture models for DP780 sheet. *Journal of Failure Analysis and Prevention*, vol. 17, 321–329.
- Münstermann, S., Lian, J., Pütz, F., Könemann, M., Brinnel, V. (Eds.), 2017. Comparative study on damage evolution during sheet metal forming of steels dp600 and dp1000, IOP Publishing.
- Park, N., Huh, H., Lim, S.J, Lou, Y., Kang, Y.S, Seo, M.H, 2017. Fracture-based forming limit criteria for anisotropic materials in sheet metal forming. *International Journal of Plasticity*, vol. 96, 1–35.
- Park, S., Cho, W., Jeong, B.-S., Jung, J., Sung, S., Na, H., Kim, S.-I., Lee, M.-G., Han, H.N, 2022. A dual-scale FE simulation of hole expansion test considering pre-damage from punching process. *International Journal of Solids and Structures*, vol. 236, 111312.

- Park, S., Jung, J., Cho, W., Jeong, B.-S., Na, H., Kim, S.-I., Lee, M.-G., Han, H.N., 2021. Predictive dual-scale finite element simulation for hole expansion failure of ferrite-bainite steel. *International Journal of Plasticity*, vol. 136, 102900.
- Pathak, N., Butcher, C., Worswick, M.J., Bellhouse, E., Gao, J., 2017. Damage evolution in complex-phase and dual-phase steels during edge stretching. *Materials*, vol. 10, 346.
- Pütz, F., Shen, F., Könnemann, M., Münstermann, S., 2020. The differences of damage initiation and accumulation of DP steels: a numerical and experimental analysis. *International Journal of Fracture*, vol. 226, 1–15.
- Sandin, O., Hammarberg, S., Parareda, S., Frómeta, D., Casellas, D., Jonsén, P. (Eds.), 2022. Prediction of sheared edge characteristics of advanced high strength steel, IOP Publishing.
- Tasan, C.C, Diehl, M., Yan, D., Bechtold, M., Roters, F., Schemmann, L., Zheng, C., Peranio, N., Ponge, D., Koyama, M., 2015. An overview of dual-phase steels: advances in microstructure-oriented processing and micromechanically guided design. *Annual Review of Materials Research*, vol. 45, 391–431.
- Teng, X., Wierzbicki, T., 2006. Evaluation of six fracture models in high velocity perforation. *Engineering fracture mechanics*, vol. 73, 1653–1678.
- Wang, K., Greve, L., Wierzbicki, T., 2015. FE simulation of edge fracture considering pre-damage from blanking process. *International Journal of Solids and Structures*, vol. 71, 206–218.
- Wechsuwanmanee, P., Lian, J., Münstermann, S., 2021. 3D Multilevel Modeling of Surface Roughness Influences on Hole Expansion Ratios. *steel research international*, vol. 92, 2100449.
- Yu, X., Chen, J., Chen, J., 2016. Interaction effect of cracks and anisotropic influence on degradation of edge stretchability in hole-expansion of advanced high strength steel. *International Journal of Mechanical Sciences*, vol. 105, 348–359.
- Zhao, C., Wang, T., Li, Z., Liu, J., Huang, Z., Huang, Q., 2022. Prediction of magnesium alloy edge crack in edge-constraint rolling process by using a modified GTN model. *International Journal of Mechanical Sciences*, 107961.

---

## **Chapter III: Effects of microstructural properties on damage evolution and edge crack sensitivity of DP1000 steels**

---

**Niloufar Habibi, Santhosh Mathi, Thorsten Beier, Markus Könemann and Sebastian Münstermann**

Crystals 2022, 12(6), 845

<https://doi.org/10.3390/cryst12060845>

### **Highlights:**

- Damage evolution and fracture behavior of different DP steels were investigated under wide range of stress states.
- For this purpose, various fracture tests with local proportional loading were performed along with DIC measurement.
- Microstructural features and evolution were studied using SEM, EBSD, and nano-indentation methods.
- A clear correlation of the local formability and damage micro-mechanism with microstructural features was found.
- The more homogenous microstructure and lower phase strength differential led to higher local formability and resistance to edge cracking.

## Effects of microstructural properties on damage evolution and edge crack sensitivity of DP1000 steels

Niloufar Habibi<sup>1,\*</sup>, Santhosh Mathi<sup>1</sup>, Thorsten Beier<sup>2</sup>, Markus Könemann<sup>1</sup> and Sebastian Münstermann<sup>1</sup>

<sup>1</sup> Integrity of Materials and Structures, Steel Institute, RWTH Aachen University, Intzestr. 1, 52072 Aachen, Germany; niloufar.habibi@iehk.rwth-aachen.de: santhosh.mathi@rwth-aachen.de: markus.koenemann@iehk.rwth-aachen.de: sebastian.muenstermann@iehk.rwth-aachen.de

<sup>2</sup> Thyssenkrupp Steel Europe AG, Kaiser-Wilhelm-Str. 100, 47166 Duisburg, Germany; thorsten.beier@thyssenkrupp.com

\* Correspondence: niloufar.habibi@iehk.rwth-aachen.de

### Abstract:

In the present work, microstructural damage behavior of two DP1000 steels through various stress states was studied to thoroughly learn the interaction between microstructure, damage evolution, and edge stretchability. In addition, microstructural changes at the fracture sites and fracture surfaces were observed using scanning electron microscope. The distinctive mechanical and damage behaviors of the materials were revealed, however the steels were slightly different from chemical composition, microstructural characteristics, and yield stress. The results showed that when microstructural and mechanical properties of phases were more similar, i.e. the microstructure was more homogenous, damage was initiated by cracking at ferrite-martensite interfaces, and it propagated along the loading direction. This allowed the material to represent high local formability and significant necking. In contrast, by increasing the dissimilarity between ferrite and martensite phases, damage propagated by shear linking of the voids, which hindered local deformation of the material and led it to sudden fracture after negligible necking. These distinct damage evolutions noticeably influenced on the materials' edge stretchability. Since higher local formability favors the edges with higher resistance to cracking, the hole expansion ratio increases which was clearly observed throughout the current study.

### Keywords:

Dual phase steels, damage micro-mechanisms, stress states, local formability, edge crack sensitivity

### 1. Introduction

Dual phase (DP) steels are widely used in automotive industry as they represent good combination of strength and formability. This behavior is caused by simultaneous existence of ductile ferrite matrix and hard martensite islands. The state of each phase, like their chemical composition, volume fraction, spatial distribution, size and morphology, and the interaction between them impose the mechanical properties and appears distinct types of these steels to satisfy requirements of different applications [1, 2]. However, this complexity makes researchers baffle how damage initiation and evolution mechanisms can restrict the formability and cause new challenges like edge cracking [3-5].

Edge cracking is sensitive to quality of the manufactured edge. Some widely used manufacturing processes, such as shearing cutting technique, induce high amount of damage and roughness at the edge and make

further formation of the edge problematic [6]. By controlling and designing the microstructural features of DP steels, their damage mechanisms and sensitivity to edge cracking can be improved. The previous researches showed that lower strength differential between the phases, by tempering heat treatment [7] or by adding some alloying elements like Nb [8] can increase the hole expansion ratio (HER). Furthermore, lowering martensite content [9], smaller grain size [10], and more homogeneous microstructure [11] can improve HER. Obviously, these microstructure changes can vary the damage behavior and mechanism in DP steels as well.

Different damage micro-mechanisms have been reported in different DP steels [12-18]. Cheloe Darabi et al. [19, 20] observed damage initiation at low strains in the middle of large ferrite phase, at the interfaces between phases, and at the trapped ferrite phase surrounded by martensite. Also, the micro-crack initiation was detected at higher strains at thin martensite phase, due to strain or shear band growth, and at boundary between the phases. Sun et al. [21] mainly investigated the effects of martensite volume fraction on damage using microstructure modeling. The study showed that DP steels with less than 15% martensite phase caused damage predominantly due to pre-existing micro-voids in ferrite phase and materials with more than 40% martensite was due to incompatibility between hard and soft phases, while the influence of pre-existing voids no longer mattered. Lai et al. [22] also studied on martensite volume fraction and reported when the martensite volume increased, the tensile strength increased but fracture strain decreased. When the martensite volume was less, the interface decohesion was the main void nucleation mechanism and predominantly occurred at triple junctions and propagated to ferrite grain boundaries. In contrast, when the martensite volume was high, initiation of fracture was majorly happening at the edge of martensite phases. They also concluded that the failure of DP steels mainly occurred due to ductile fracture and partially due to brittle fracture at the last stages of failure process, especially when the martensite volume was sufficiently high. Kusche et al. [23, 24] statistically studied the dominant deformation-induced-damage mechanisms in DP800 by using panoramic imaging technique and machine learning methods. They reported damage initiated by cracking in brittle martensite and propagated rapidly into bordering ferrite grains

The present work aims to expose the profound influence of damage behavior dictated by microstructural features on the effective materials performance, especially in a complicated deformation process. In this regard, the deformation and damage micro-mechanisms of two DP1000 steels under various stress states were compared. Moreover, damage evolution throughout edge manufacturing and further deforming was studied as the effective materials performance in a complicated deformation process.

## 2. Materials and Methods

### 2.1. Material characterization

Two different steels of DP1000 grade with a thickness of 1.5 mm were examined in this study. Their chemical compositions are given in table 1. The initial microstructures in rolling direction (ND-RD) were characterized by scanning electron microscopy (SEM). Figure 1 indicates that CR590Y980T-DP contained 65% ferrite matrix (the darker phase) and 35% martensite islands (the brighter phase), while CR700Y980T-DP contains 55% ferrite and 45% martensite phases. Note that the phase fractions were estimated based on several SEM photos and Digimizer image analysis software. Also, some non-metallic particles and

inclusions were detected using energy dispersive X-ray tool of SEM machine. Moreover, electron backscatter diffraction (EBSD) method was operated on an area of  $100 \times 100 \mu\text{m}^2$ , at 15 kV and using a step size of 50 nm, to analyze texture of the materials as crystallographic orientation distribution in figure 2 (a), inverse pole figures in figure 2 (b), and grain size distribution for each phase in figure 3. This data implies that for CR700Y980T-DP, the grain sizes of both ferrite and martensite phases were finer, the texture was more homogeneous, and martensite islands distributed more randomly (no martensite bands) than in the other material. The general material hardness was measured by Vickers hardness tests with load of 98 N, figure 4 (a). Also, cube-corner nano-indentation tests were carried out at loading rate of 1 nm/s for depth of 100 nm on ferrite grains with crystallographic orientations close to  $\{100\}$ ,  $\{110\}$ , and  $\{111\}$  fibers parallel to the investigated direction, figure 4 (b). As expected, the hardness of ferrite grains was higher in CR700Y980T-DP, since its higher amount of Mn caused solid-solution strengthening in the ferrite phase. Therefore, the hardness for martensite and ferrite phases was closer in this material, as shown in figure 4.

**Table 1.** Chemical compositions of the investigated steels (wt.%).

Steel grade	C	Si	Mn	P	S	Al	Ti
CR590Y980T-DP	0.043	0.301	1.807	0.012	0.007	0.037	0.048
CR700Y980T-DP	0.080	0.293	2.813	0.011	0.002	0.291	0.075

## 2.2. Experimental procedure

The effects of different stress states on damage behavior of the studied DP1000 steels were investigated. In this regard, tensile tests were applied on different geometries, figure 5, by stroke speed of 0.005 mm/s. Note that a measured gauge length of 50 mm was considered for all the samples. The biaxial deformation mode was applied through hydraulic bulge test with stroke speed of 0.02 mm/s, figure A1. In addition, grooved in-plane torsion tests were carried out in Institute of Forming Technology and Lightweight Construction at TU Dortmund University. The details of this test were presented by Yin et al. [25]. All the tests were performed along with 3D digital correlation image (DIC) technique using camera frequency of 5 s, in order to track the local deformation. The stress triaxiality of the conducted tests were calculated [26-28] and summarized in table A1, which claims that various stress states were studied in the present work. In order to examine damage evolution in different stress states for each material, fracture sites were examined by scanning electron microscope. For this purpose, the crack initiation sites were observed from normal and side views, as shown for an example of uniaxial tensile specimen in figure 5. Moreover, hole expansion tests were performed to investigate the effects of damage mechanisms on the edge crack sensitivity of the materials. In this regard, a 50° conical punch was applied on wire-cut and punched holes with a diameter of 39.67 mm. Note that the punched holes were manufactured with 10% clearance of the punching die. According to the standard ISO 16630:2017 [29], hole expansion ratios were calculated as a through-thickness edge crack appeared.

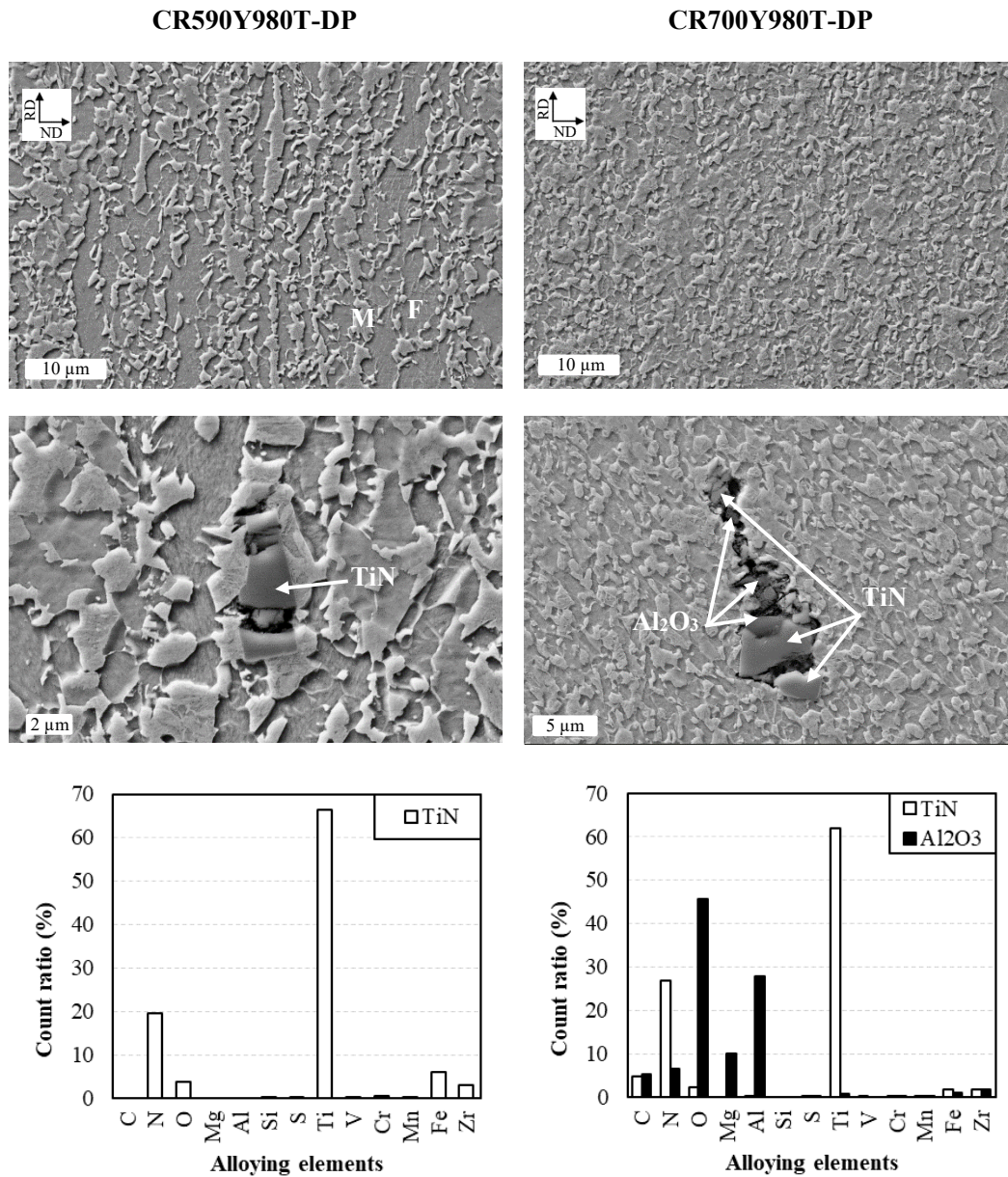


**Figure 1.** SEM study on the initial microstructures in ND-RD plane, which shows distribution of ferrite (F) and Martensite (M) in the materials. TiN and Al<sub>2</sub>O<sub>3</sub> particles were also detected.



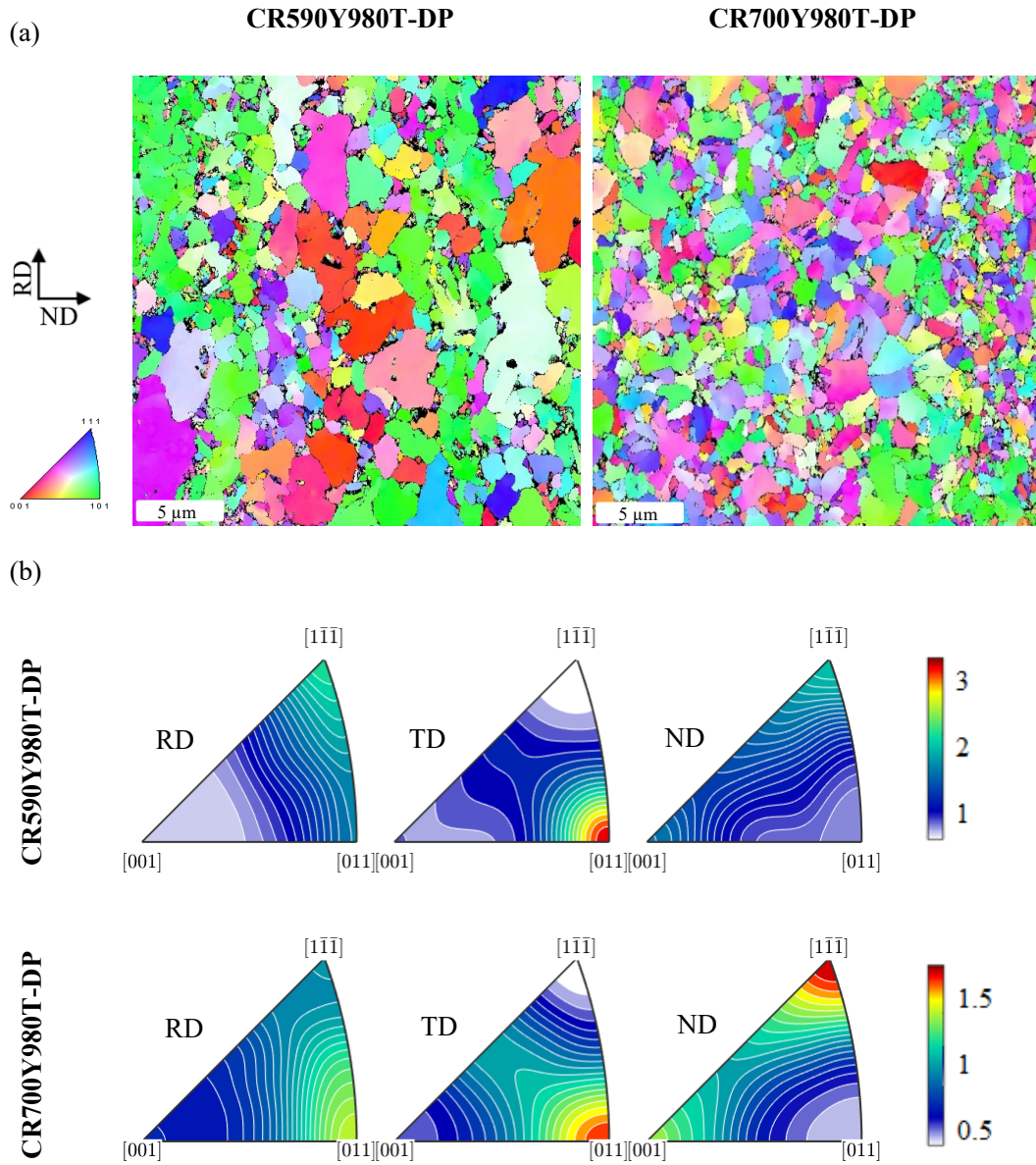


**Figure 2.** The texture analysis using EBSD for as-received materials; (a) crystallographic misorientation of grains, (b) inverse pole figures.



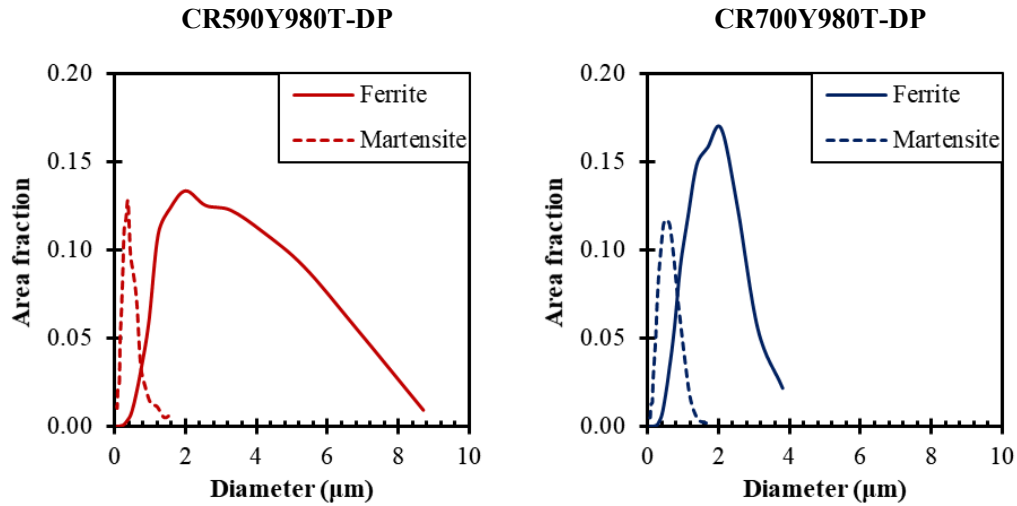
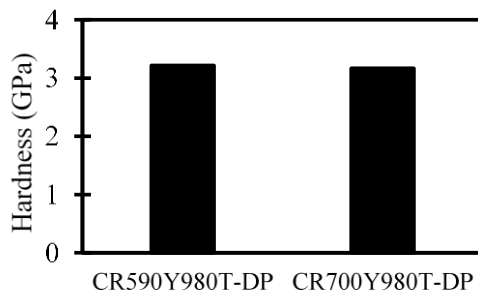


**Figure 3.** Comparison of grain size distribution of ferrite and martensite phases for each studied steel alloy.

(a) Vickers hardness test



(b) Nano-indentation on ferrite grains

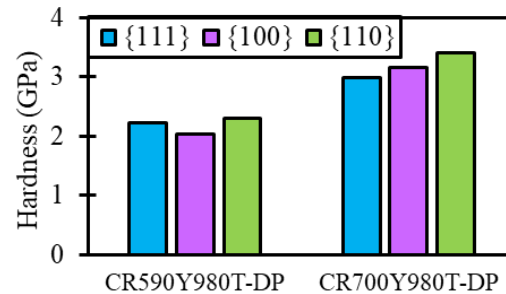


**Figure 4.** Comparison of Hardness between the studied steels; (a) standard Vickers hardness, and (b) Nano-indentation on ferrite grains with crystallographic orientations close to  $\{111\}$  (in blue),  $\{100\}$  (in purple), and  $\{110\}$  (in green).

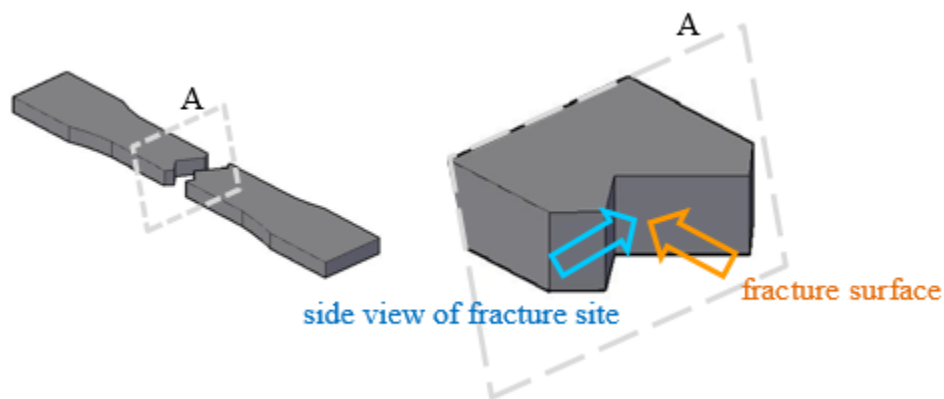


**Figure 5.** Damage evolution was studied at the crack initiation site from different views by SEM.

### 3. Results and discussion

#### 3.1. Mechanical behavior under various stress-states

Mechanical and damage behaviors of the materials through different stress states are presented, compared, and discussed below in terms of force-displacement and local strains. By using DIC method, the local major strains were taken just before any crack appeared at the surface. With the help of a rainbow-color map of major strain, distribution and localization of deformation were indicated. Thus, the deformation concentration and crack initiation were displayed by red spots. Figure 6 illustrates responses of the materials through uniaxial tensile tests. As expected, the yield stress and ultimate tensile stress for CR590Y980T-DP were almost 600 and 1020 MPa, and for CR700Y980T-DP were about 700 and 970 MPa. The strain hardening rate and homogenous elongation were higher in CR590Y980T-DP. Although, the post necking elongation and local strain before fracture were higher in CR700Y980T-DP, which led to pronounced localized necking and fracture with an angle of about  $53^\circ$ , i.e. ductile fracture occurred. Whereas, CR590Y980T-DP represented a fracture perpendicular to the loading direction, small localized necking, and lower local strain by DIC, which indicates less ductile fracture manner. This evidence was also detected by an SEM study on the side and normal views of fracture initiation sites, figure 7. The thickness of CR590Y980T-DP was reduced from 1.50 mm to 1.28 mm and failed by shearing through the thickness with negligible necking. While in the other material the thickness was reduced dramatically to 0.68 mm and the thinning was more pronounced. The fracture surfaces in figure 7 (b) illustrate the relatively smooth surface for CR590Y980T-DP and rough dimple like fracture surface for CR700Y980T-DP. However, at the higher magnification in figure 7 (c), ductile fracture mechanisms are revealed for both materials with bimodal dimple sizes, fine dimples and big voids which contained non-metallic impurities and inclusions such as TiN and  $Al_2O_3$ . Note that the voids seem finer and deeper in CR700Y980T-DP and the number of huge voids caused by inclusions was considerable in comparison to the other steel, figure 7 (b).

The same trends were also indicated for the other samples, which represent different stress states. The detailed results are shown in appendix B, figures B1-B8. It can be concluded that steel CR590Y980T-DP showed difficulties to maintain localized plastic deformation without developing damage and fracture. Thus, its local formability is lower than that of steel CR700Y980T-DP. The reasons of these behaviors are discussed in the following section according to the microstructural features and damage micro-mechanisms of the studied steels.

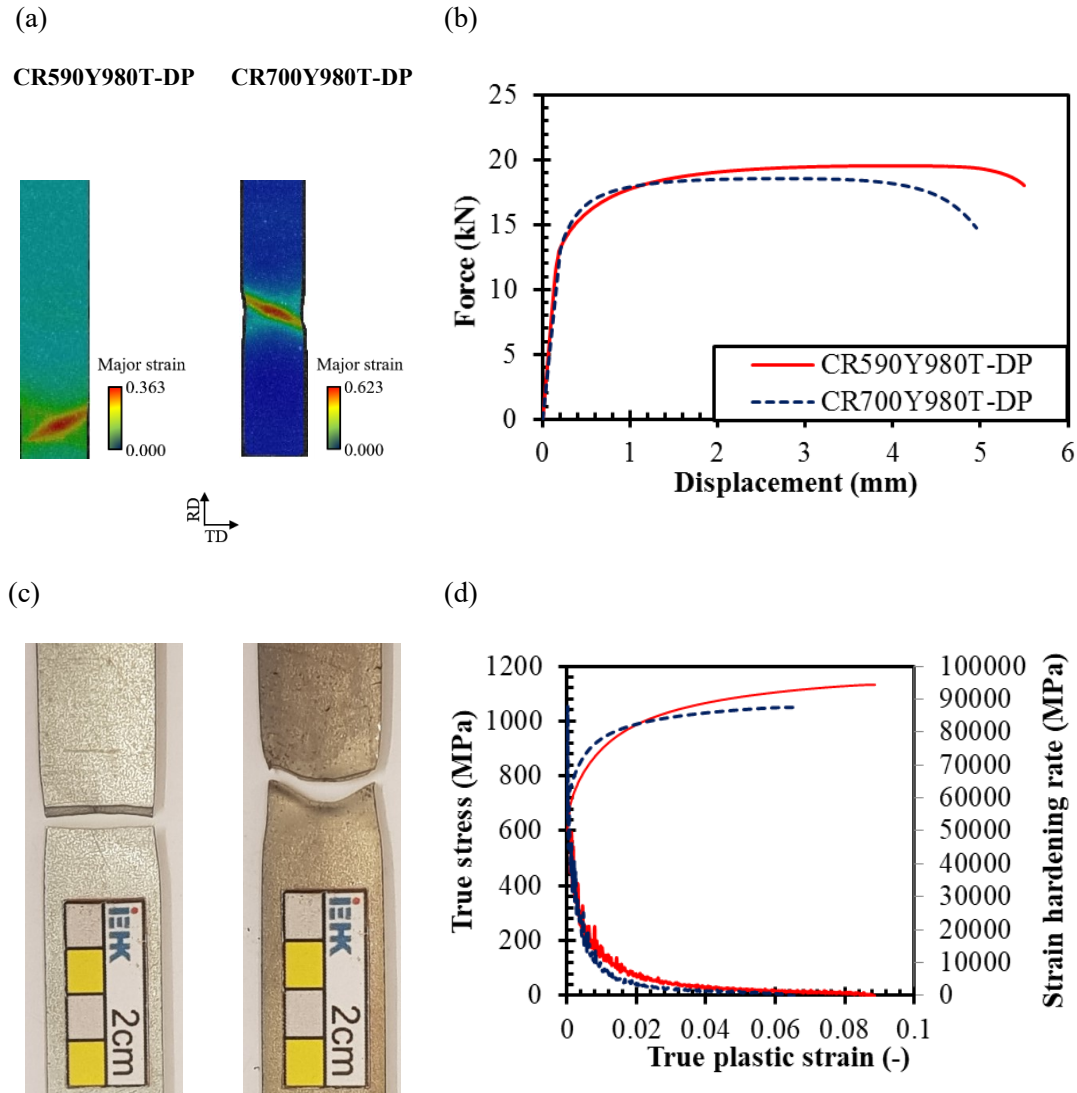


**Figure 6.** Responses of the materials through uniaxial tensile tests ( $\eta=0.33$ ); (a) strain distribution by DIC at the fracture moment, (b) force-displacement curves, (c) fracture positions, and (d) Stress-strain and strain hardening rate curves of the studied materials through homogenous plastic elongation.

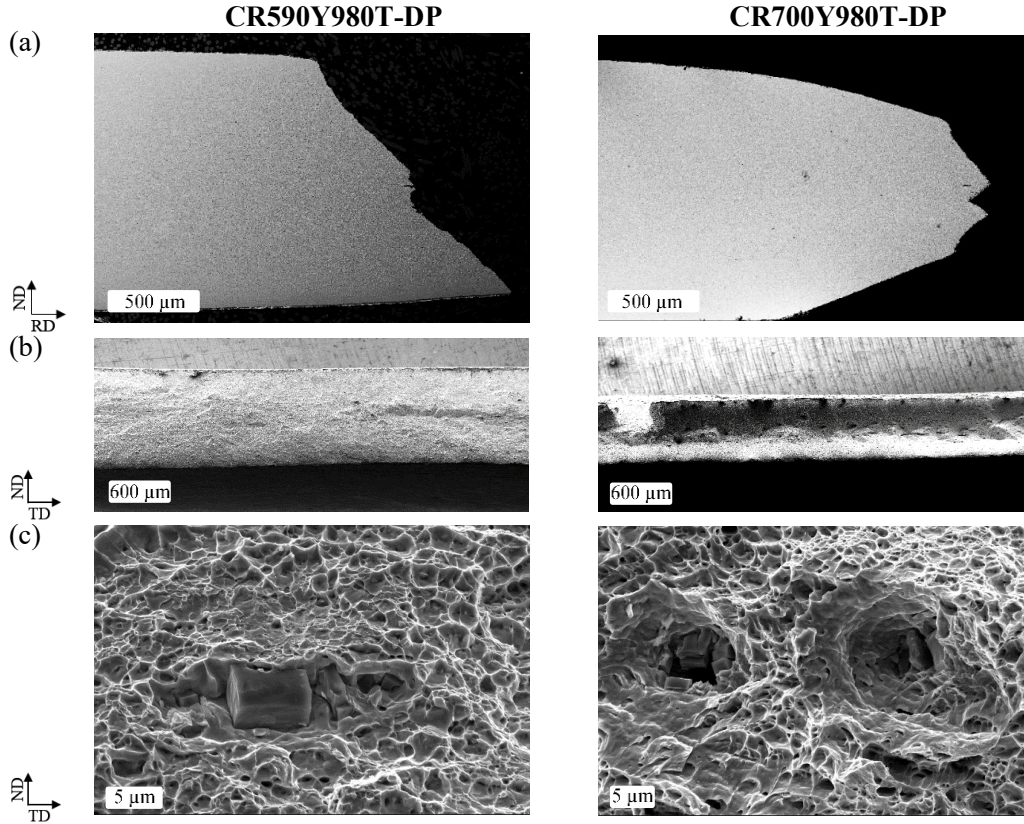
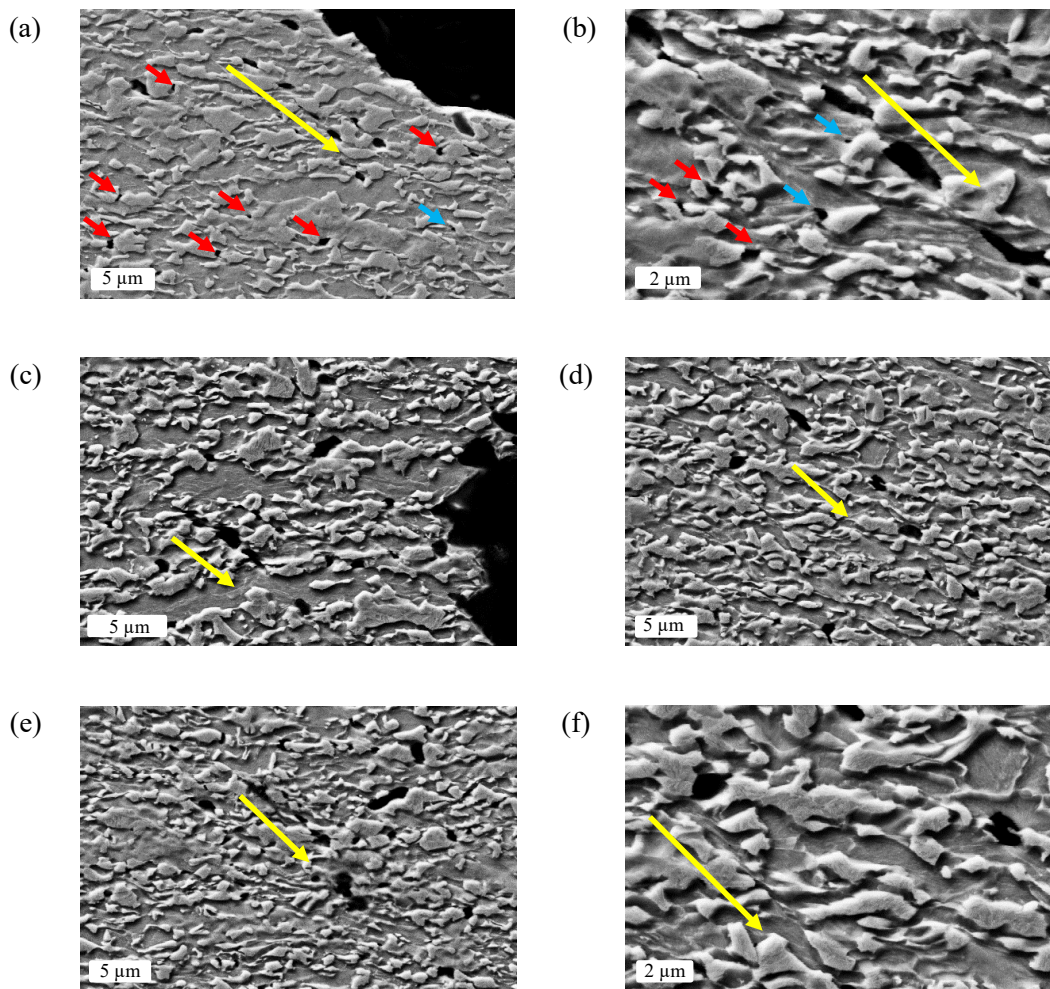


**Figure 7.** SEM study at fracture sites of uniaxial tensile tests ( $\eta=0.33$ ) for the materials; (a) thickness views, (b) and (c) fracture surfaces.

### 3.2. Damage micro-mechanisms

The damage micro-mechanisms were also investigated by SEM, figures 8 to 10. The previous studies [18, 30] discovered that damage in DP steels nucleates as martensite cracking, decohesion of ferrite-martensite interfaces, failure in a ferrite grain, and cavity formation at TiN particles. Figure 8 illustrates the microstructural changes at the fracture site in CR590Y980T-DP for different stress states. The small voids reveal that the most prominent damage initiation mechanism in this material is martensite cracking. The grown voids imply that the voids caused the separation in martensite islands, passed through the ferrite phase, and coalesced through shear bands which formed in the ferrite phase. Several shear bands are marked in figure 8 by arrows, which induced higher localization and stress triaxiality at the area and led to rapid voids growth and coalescence [31]. This shear linking of voids was also clear in the fracture surface view, figure 10 (a), where the voids represented shallow depth and inclined with respect to the main loading direction.

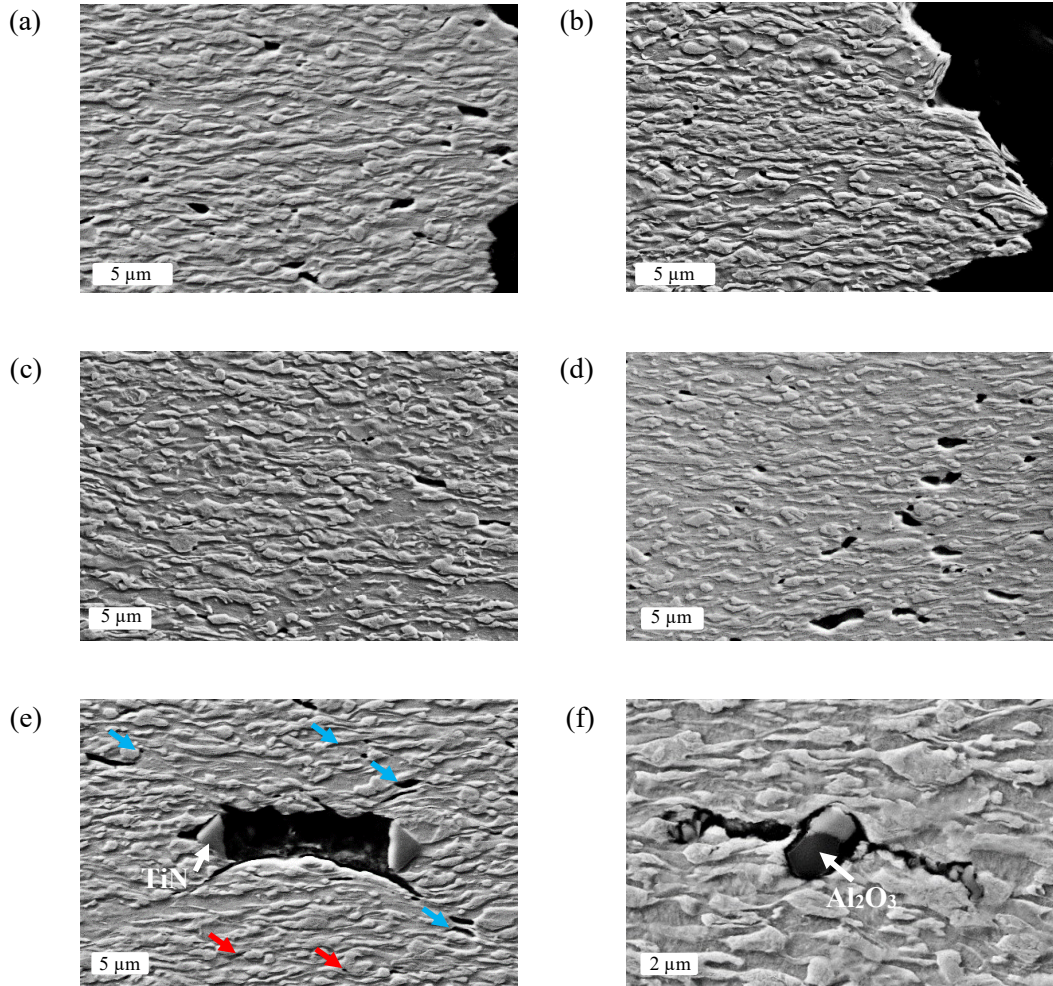




**Figure 8.** Damage mechanisms in CR590Y980T-DP steel in different stress states; (a) and (b) uniaxial tensile test, (c) U-notched tensile test, (d) plane strain tensile test, (e) and (f) bulge test. The arrows show some damage micro mechanisms: Yellow=shear bands and shear linking of the voids, Red=martensite cracking, Blue=decohesion between ferrite and martensite phases. As the number of voids in the figures are significant, only few of them were marked to avoid covering the pictures details.

In contrast, a different dominant damage micro-mechanism can be detected for CR700Y980T-DP in figure 9. Evidently, damage initiated by decohesion of ferrite-martensite interfaces which later propagated and elongated along the phase boundaries parallel to the loading direction. Note that no shear bands were formed, which accelerate the damage process. Since the strength differential between ferrite and martensite in this material was very low, based on hardness measurement in figure 4, the strain partitioning became more even between the phases and the grain boundaries became the favorable sites of void nucleation. Therefore, the void propagation and coalescence occurred along the grain boundaries towards the loading direction. Furthermore, due to the lower mismatch in strength and morphology (like grain size and shape) throughout this material compared to the other one, amount of void nucleation and propagation was lower, despite the higher strain it experienced at the fracture zone. In addition, it was observed [3] that the damage initiation mechanism for DP steels with large ferrite grains is caused by strain localization inside of the

phase, like for CR590Y980T-DP. While for DP steels with fine ferrite grains, like for CR700Y980T-DP, it happens due to strain localization at the phase boundaries.



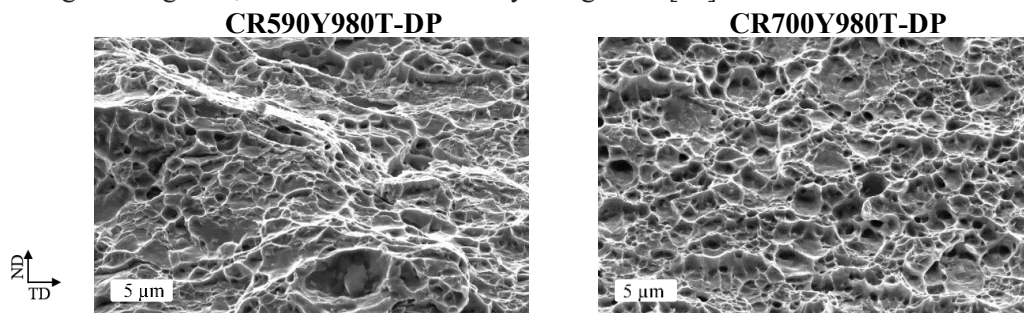
**Figure 9.** Damage mechanisms in CR700Y980T-DP steel in different stress states; (a) uniaxial tensile test, (b) U-notched tensile test, (c) plane strain tensile test, (d) bulge test. Cracking around the non-metallic inclusions (e) TiN and (f)  $\text{Al}_2\text{O}_3$ . The arrows show some damage micro mechanisms: Red=martensite cracking, Blue=decohesion between ferrite and martensite phases.

Figure 10 (b) also shows that the voids seem deeper in this material, and they are located towards the normal axis of the fracture surface which was the loading direction as well. It is worth mentioning that the number of very fine voids is noticeable, which determines that the damage initiated constantly and homogeneously at several potential sites, which are the grain boundaries. Note that for this material, numerous huge voids were also observed around the inclusion even far away from the fracture edges, since it contained higher amount of Ti and Al. As this material represented quite ductile manner in both deformation and failure, it seems inclusions played minor role in overall damage development.

In brief, the differences in damage mechanisms for these studied steels could be explained by considering the microstructural features and mechanical properties of individual microstructural constituents, which were described previously in section 2.1. The material was able to experience higher post-localized



deformation when the ferrite and martensite grains were finer, their hardness were closer, and the texture was more similar, i.e. the microstructure and mechanical properties were more homogenous. This phenomenon was also shown in micro-mechanical simulations of DP steels in Ref. [30]. For this material, the dominant damage mechanism was decohesion of ferrite-martensite interfaces, as the strength differential and strain partitioning were low between the phases. Whereas the coarser microstructure with high strength mismatch led damage to initiate by martensite cracking at few sites, which admitted by earlier studies as well, and afterward weaker martensites began to deform rapidly along the activated shear bands at the neighbouring ferrite grains, which also observed by Kang et al. [32].



**Figure 10.** Comparison of fracture surfaces for 7.5 plane strain tensile specimens clearly reveals different damage micro-mechanisms in these materials.

### 3.3. Edge crack sensitivity

The local formability behavior and damage mechanisms play significant roles on the bendability, fracture toughness and edge-cracking of the materials [33]. Since the studied material in this work represented different damage behaviors, their edge crack sensitivities were also investigated. In this regard, hole expansion ratio was measured for wire-cut and punched holes, figure 11 and 12. As expected, HER is higher for wire-cut holes, figure 12, as this cutting process applies lower damage than punching at the manufactured edges [34]. However, the HER value for wire-cut edges are about quintuple and double higher than punched edges for CR590Y980T-DP and CR700Y980T-DP, respectively. This indicates that CR590Y980T-DP is more prone to the edge quality and edge cracking. The final edge cracks are illustrated in figure 11, from the plane and thickness views. The photos were taken at the moment that a through-thickness crack appeared. In all conditions, CR700Y980T-DP sheets experienced more general thinning and deformation through HET than the other material. The cracks clearly prove the contrasting features between the materials, low HER and shearing through the thickness for CR590Y980T-DP, whereas high HER and significant localization for CR700Y980T-DP. It is worth mentioning that for wire-cut edge of CR700Y980T-DP, the crack initiates by plane strain necking far from the edge, at the contact site of HE-punch and the specimen. This implies that the residual damage from wire-cutting for this material was very low, which cannot trigger an edge cracking [35]. Furthermore, although several small cracks can be observed at the outer punched edge of CR700Y980T-DP, only one of them was successful to propagate across the thickness and then through the plane of the specimens, which can be explained by taking a look at the residual damage from punching for both materials, figure 13.

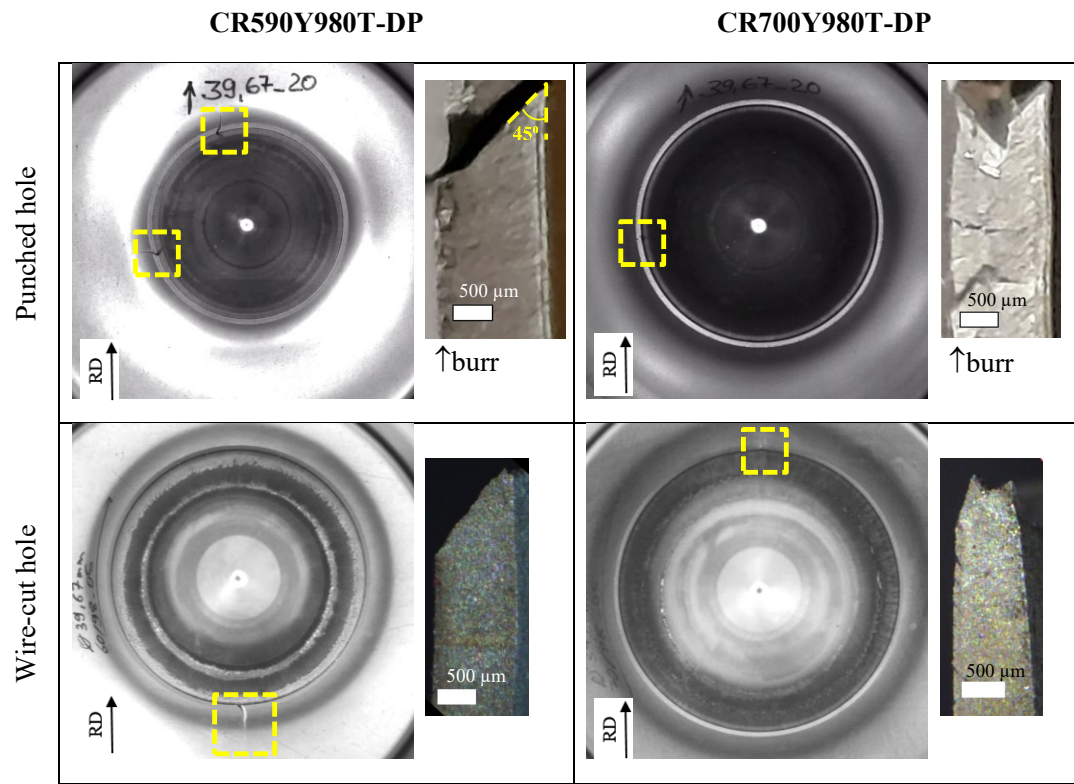


Figure 11. Comparison of edge-crack initiation in these steel for punched and wire-cut holes.

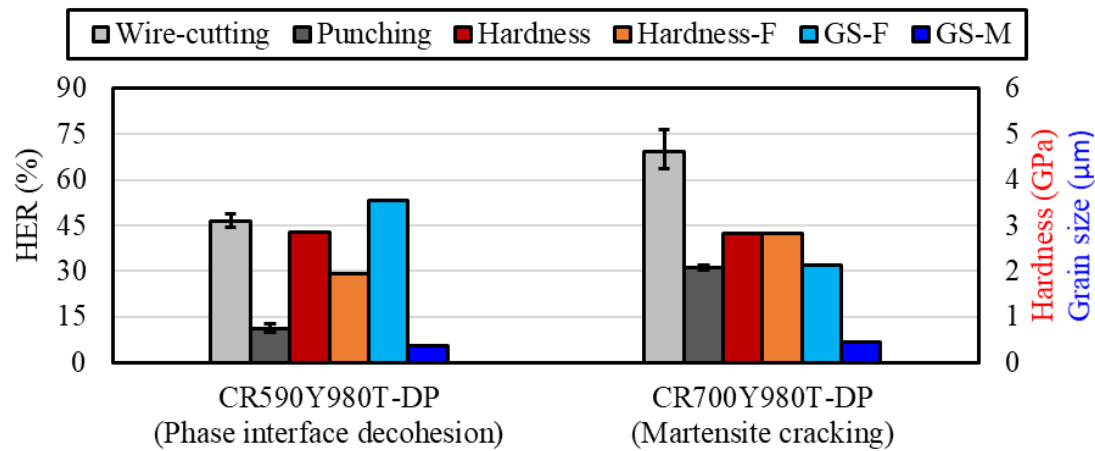
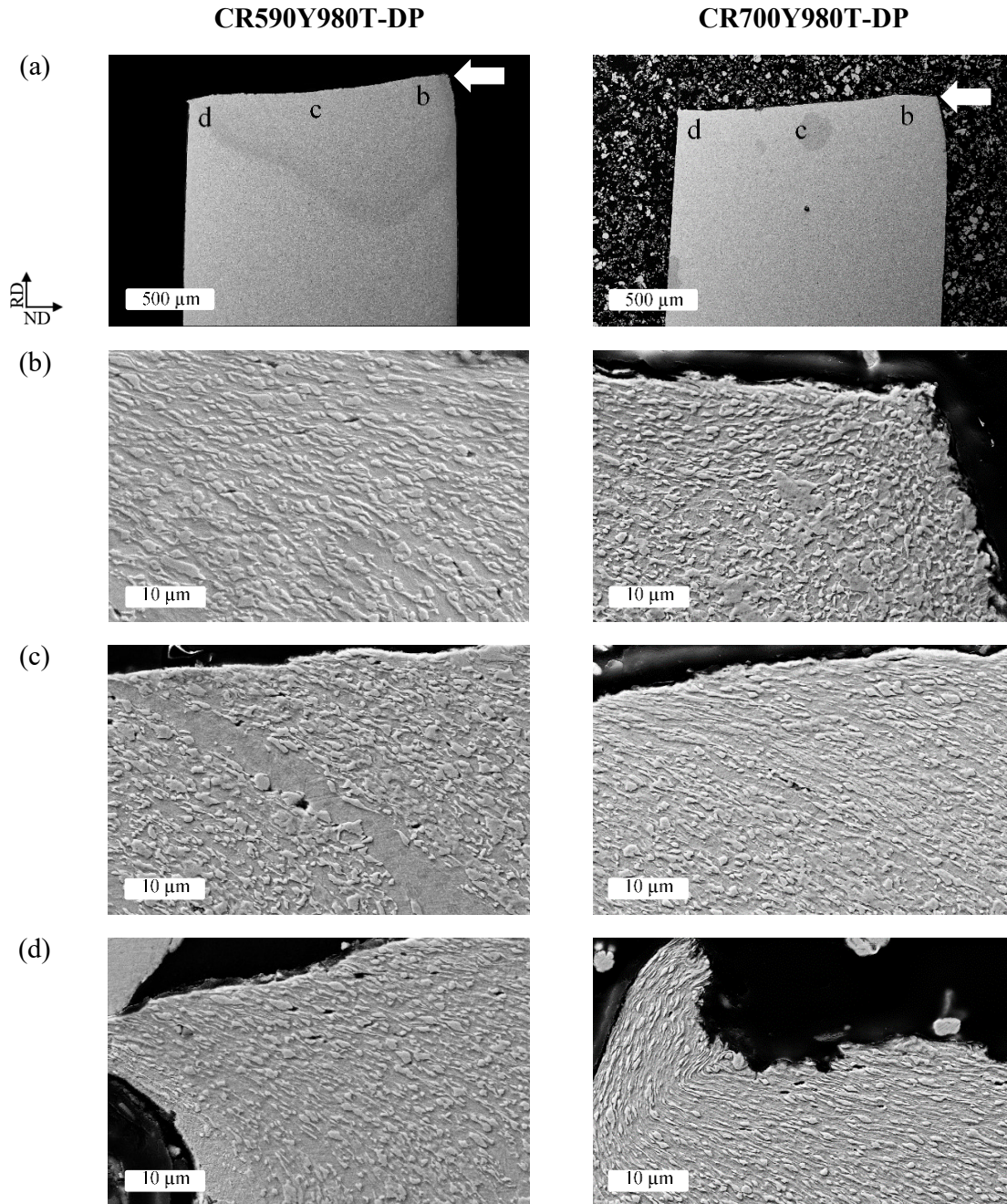


Figure 12. Comparison of the hole expansion ratio and microstructural characteristics of studied materials.





**Figure 13.** Induced damage through the punching process, (a) the punched edge, (b) the roll-over and burnished part, (c) the fracture part, and (d) the burr part.

Figure 13 compares the features and residual damage at the edges after punching process for the investigated materials. Although the sizes of both roll over and burnished parts are larger for CR700Y980T-DP, no micro-crack can be detected in these parts, even at high magnification. While several martensite crackings can be easily seen for the other material, figure 13 (b). As the stress state at the beginning for punching is pure shearing [36], this behavior was predictable, because of high fracture strain of this material in the pure shearing mode, figure B7. For both steels, the population of cracks increases in fracture part of shear-cut

edge and the highest can be observed at the lower part of fracture part, close to the burr part. The sizes of burr parts are very small, as reported for other DP steels [34]. Roughly speaking for CR700Y980T-DP at the punched edge, the observed cracks are fewer, smaller, and mostly took place very close the cut edge, i.e. lower residual damage from the cutting process. Due to the fact that the microstructural and mechanical properties of the phases are so close, figure 12, which made the material more homogenous. Note that, although few large cracks are observed at inclusions and impurities for this material, they are located far from the deformation and fracture sites. Therefore, they could not have any influence on the cut edge property and HER.

#### 4. Conclusion

According to the detailed analyses discussed above, the present study showed the effects of microstructural characteristics on both the macro- and micro-mechanical behaviors of DP steels under various stress state conditions. When the features of ferrite and martensite phases, in terms of grain sizes, morphology, and mechanical properties, were more similar and homogenous, the damage initiated by decohesion of ferrite-martensite interfaces simultaneously at several sites and induced higher local formability and local fracture strains. In contrast, for coarser and more uneven microstructure with higher strength mismatch, damage occurred by martensite cracking and rapid propagation through shear bands within adjacent ferrite grains, which significantly restricted the post localized deformation, i.e. the lower local formability. The results revealed that the damage behavior, which was dictated by the microstructural and micro-mechanical properties of the material, had noticeable effects on the edge cracking sensitivity, which was highly controlled by local ductility. The local formability influenced on both residual damage during the edge manufacturing and the edge formability itself. In case of similar global ductility of the materials, based on the extracted flow curves from conventional tensile tests, failure through thickness-shearing made rapid crack propagation, while deformation localization enabled the material to experience more deformation before the fracture. Therefore, HER is higher for the latter. In addition, the material with higher local formability experienced lower damage at the punched edge, in terms of number, size and location of the micro-cracks. Thus, this material was less sensitive to edge quality and the reduction of HER was lower.

**Author Contributions:** Conceptualization, N.H. and S.Mü.; methodology, N.H.; formal analysis, N.H. and S.Ma.; investigation, N.H., S.Ma. and T.B.; resources, S.Mü.; writing—original draft preparation, N.H. and S.Ma.; writing—review and editing: N.H., M.K. and S.Mü.; supervision, S.Mü.; funding acquisition, S.Mü. All authors have read and agreed to the published version of the manuscript.

**Acknowledgments:** The authors gratefully acknowledge Dr. Heinrich Traphoener from IUL, TU Dortmund for performing in-plane torsion tests.

**Conflicts of Interest:** The authors declare no conflict of interest. The funders had no role in the design of the study; in the collection, analyses, or interpretation of data; in the writing of the manuscript, or in the decision to publish the results.

## Appendix A

Wide range of stress states were applied in this study, using different geometries and testing techniques, figure A1. The approximate stress triaxiality of each specimen was calculated and listed in table A1.

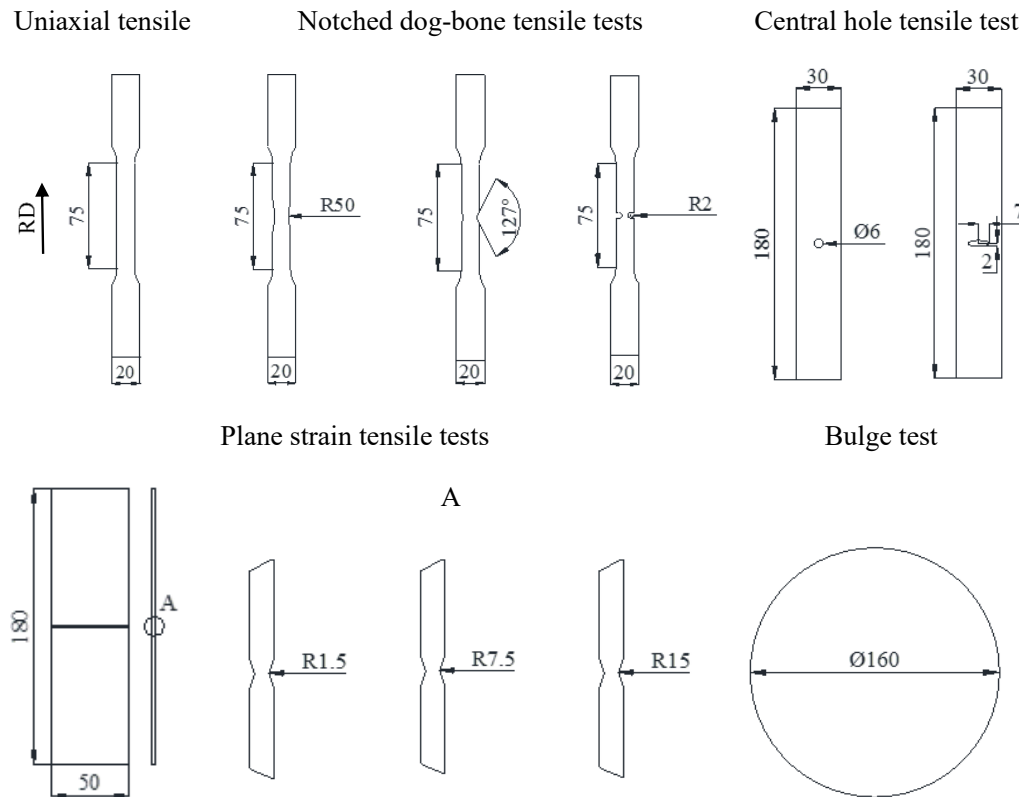


**Figure A1.** The geometries of specimens which were used for applying different stress states.

**Table A1.** This is a table. Tables should be placed in the main text near to the first time they are cited.

Geometry	Stress triaxiality ( $\eta$ )	Reference
Smooth dog bone uniaxial tension	0.33	[26]*
Notched dog bone uniaxial tension, R50	0.36	[26]*
Notched dog bone uniaxial tension, U-notched	0.48	[26]*
Central hole uniaxial tension, circle Ø6	0.33	[27]**
Central hole uniaxial tension, oval a2b7	0.40	[27]**
Flat grooved uniaxial tension, R1.5	0.74	[28]*
Flat grooved uniaxial tension, R7.5	0.61	[28]*
Flat grooved uniaxial tension, R15	0.59	[28]*
Bulge test, biaxial tension	0.67	[28]**
Torsion test	0.00	[25]**

The values of stress triaxiality are

\*calculated using the equations proposed in the references.

\*\*directly taken from the references which used the same geometry.

## Appendix B

In this appendix, the responses of the studied materials through different stress states are shown, figures B1-B8, i.e. the strain distribution captured by DIC and force-displacement curve. In addition, the fracture mechanisms were compared by observing the evolution of thinning at the fracture site and fracture surfaces of the materials using SEM method.

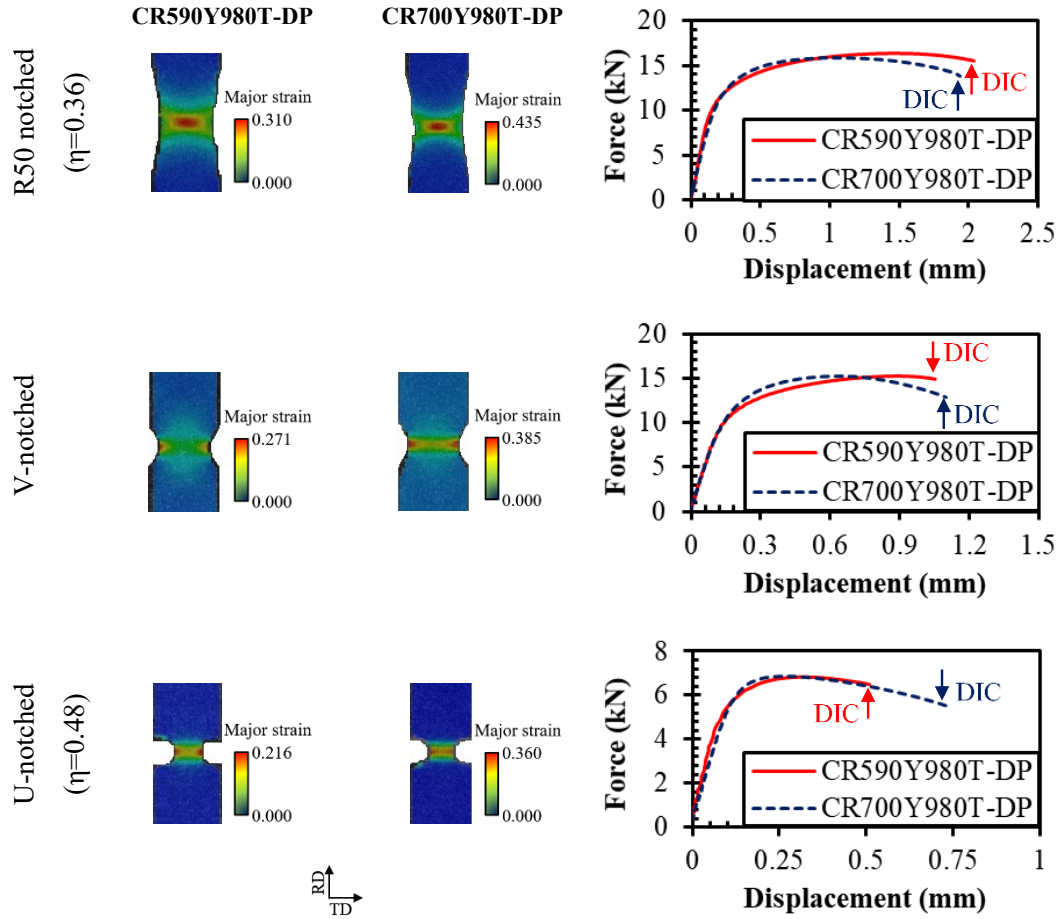


Figure B1. Responses of the materials for different notched dogbone specimens.

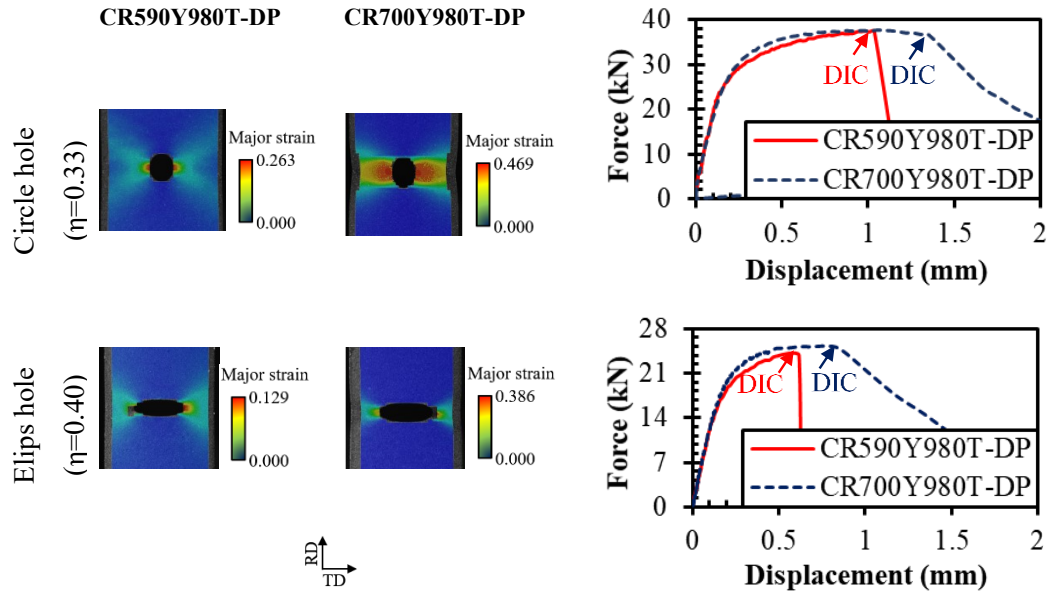


Figure B2. Responses of the materials for different central hole specimens.

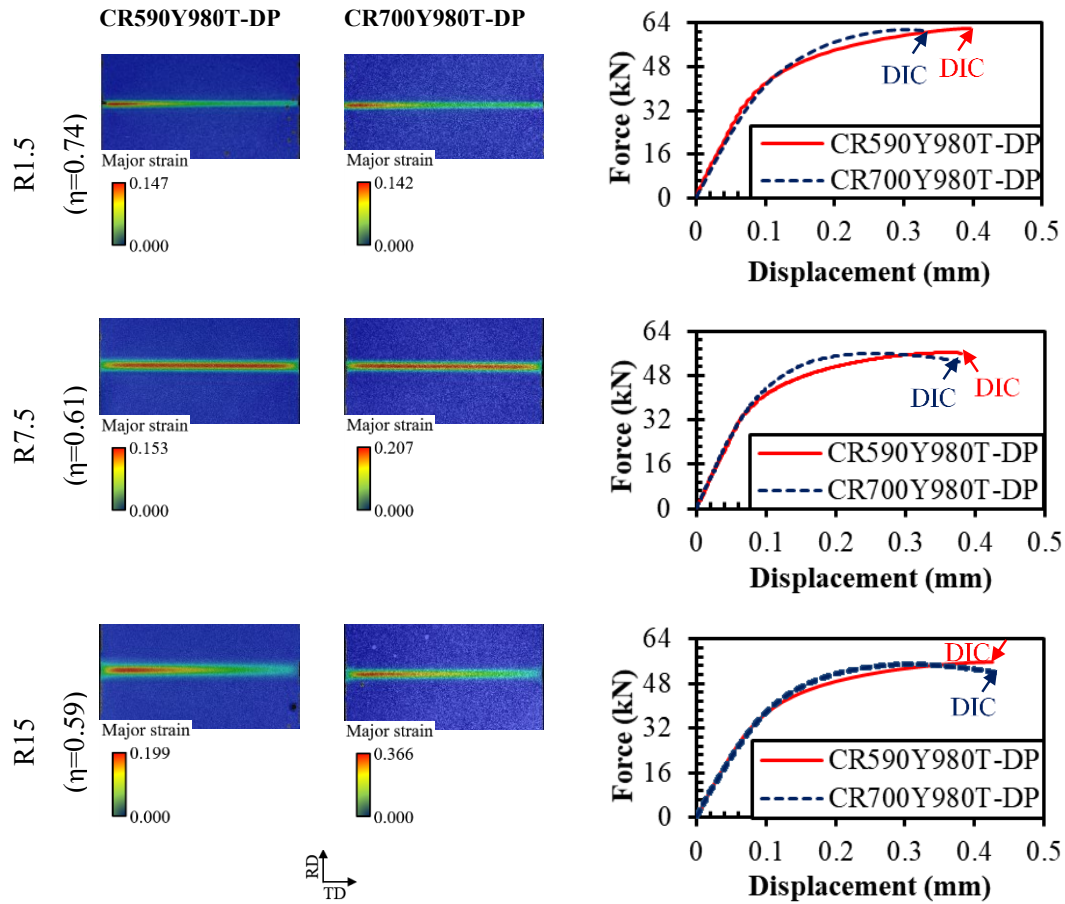
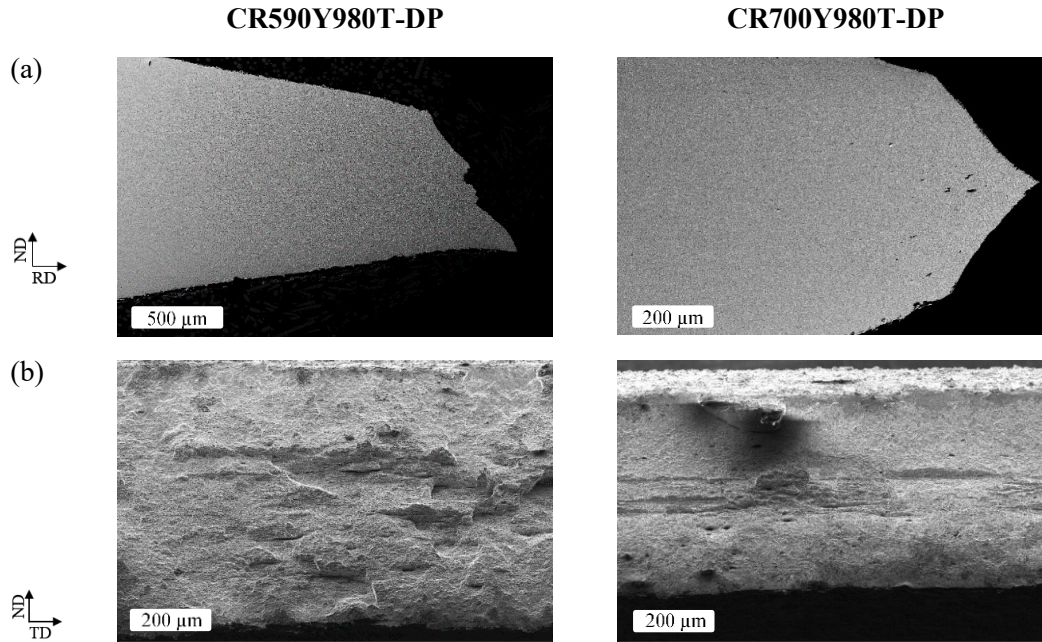
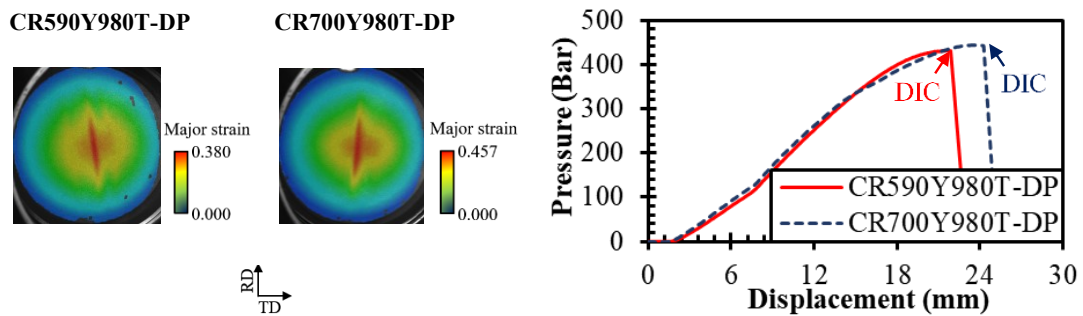


Figure B3. Responses of the materials for different plane strain specimens.





**Figure B4.** SEM study at fracture sites of R7.5 plane strain tensile tests ( $\eta=0.61$ ) for the materials; (a) thickness views, (b) fracture surfaces.



**Figure B5.** The strain distribution and materials response for hydraulic bulge test ( $\eta=0.67$ ).

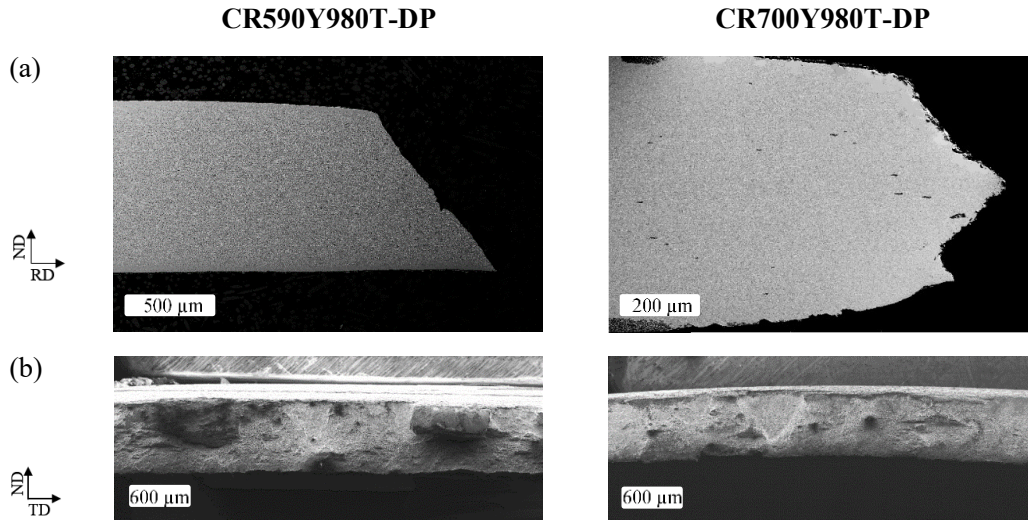


**Figure B6.** SEM study at fracture sites of hydraulic bulge tests for the materials; (a) thickness views, (b) fracture surfaces.

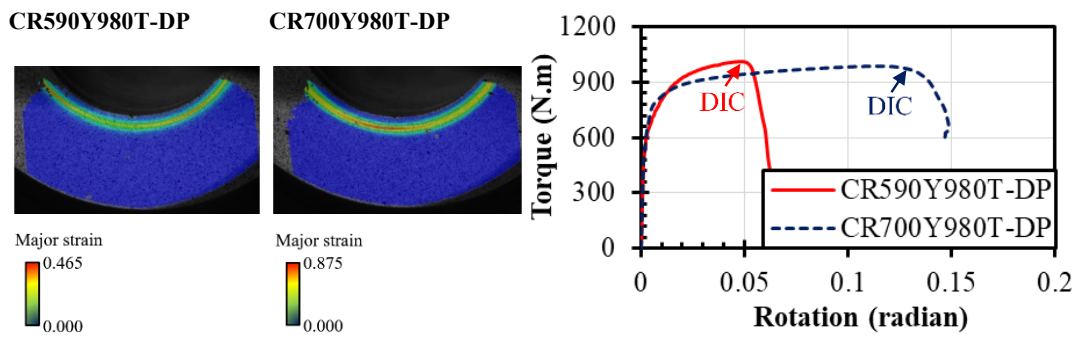


**Figure B7.** The strain distribution and materials response for grooved in-plane torsion test ( $\eta=0$ ).

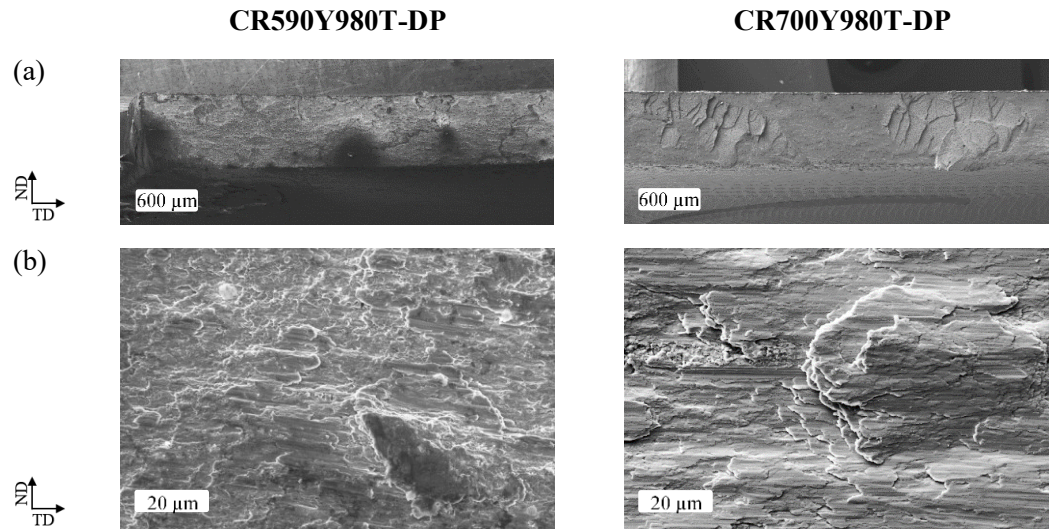


**Figure B8.** SEM study at fracture sites of in-plane torsion tests ( $\eta=0$ ) for the materials; (a) and (b) fracture surfaces.

## References

1. Rashid, M. Dual phase steels. *Annual Review of Materials Science* 1981, 11, 245-266. 1.
2. Tasan, C.C.; Diehl, M.; Yan, D.; Bechtold, M.; Roters, F.; Schemmann, L.; Zheng, C.; Peranio, N.; Ponge, D.; Koyama, M. An overview of dual-phase steels: advances in microstructure-oriented processing and micromechanically guided design. *Annual Review of Materials Research* 2015, 45, 391-431.
3. Darabi, A.C.; Chamani, H.; Kadkhodapour, J.; Anaraki, A.; Alaie, A.; Ayatollahi, M. Micromechanical analysis of two heat-treated dual phase steels: DP800 and DP980. *Mechanics of Materials* 2017, 110, 68-83.
4. Qin, S.; McLendon, R.; Oancea, V.; Beese, A.M. Micromechanics of multiaxial plasticity of DP600: Experiments and microstructural deformation modeling. *Materials Science and Engineering: A* 2018, 721, 168-178.
5. Zarei, S.; Nedoushan, R.J.; Atapour, M. The sources of the micro stress and strain inhomogeneity in dual phase steels. *Materials Science and Engineering: A* 2016, 674, 384-396.
6. Han, S.; Chang, Y.; Wang, C.Y.; Dong, H. A comprehensive investigation on the damage induced by the shearing process in DP780 steel, *Journal of Materials Processing Technology* 2022, 299, 117377.
7. Hu, X.; Sun, X.; Raghavan, K.; Comstock, R.; Ren, Y. Linking constituent phase properties to ductility and edge stretchability of two DP 980 steels. *Materials Science and Engineering: A* 2020, 780, 139176.
8. Pan, L.; Xiong, J.; Zuo, Z.; Tan, W.; Wang, J.; Yu, W. Study of the stretch-flangeability improvement of dual phase steel. *Procedia Manufacturing* 2020, 50, 761-764.
9. Balisetty, V.; Chakkingal, U.; Venugopal, S. Evaluation of stretch flangeability of dual-phase steels by hole expansion test. *The International Journal of Advanced Manufacturing Technology* 2021, 114, 205-217.
10. Moura, A.N.; Ferreira, J.L.; Martins, J.B.R.; Souza, M.V.; Castro, N.A.; Orlando, M.T.D.A. Microstructure, Crystallographic Texture, and Stretch-Flangeability of Hot-Rolled Multiphase Steel. *steel research international* 2020, 91, 1900591.
11. Terrazas, O.R.; Findley, K.O.; Van Tyne, C.J. Influence of martensite morphology on sheared-edge formability of dual-phase steels. *ISI International* 2017, ISIJINT-2016-2602.
12. Kadkhodapour, J.; Butz, A.; Rad, S.Z. Mechanisms of void formation during tensile testing in a commercial, dual-phase steel. *Acta Materialia* 2011, 59, 2575-2588.
13. Li, S.; Guo, C.; Hao, L.; Kang, Y.; An, Y. In-situ EBSD study of deformation behaviour of 600 MPa grade dual phase steel during uniaxial tensile tests. *Materials Science and Engineering: A* 2019, 759, 624-632.
14. Lian, J.; Yang, H.; Vajragupta, N.; Münstermann, S.; Bleck, W. A method to quantitatively upscale the damage initiation of dual-phase steels under various stress states from microscale to macroscale. *Computational materials science* 2014, 94, 245-257.
15. Münstermann, S.; Lian, J.; Pütz, F.; Könnemann, M.; Brinnel, V. Comparative study on damage evolution during sheet metal forming of steels dp600 and dp1000. In *Proceedings of the Journal of Physics: Conference Series*, 2017; p. 012074.
16. Ghassemi-Armaki, H.; Maaß, R.; Bhat, S.; Sriram, S.; Greer, J.; Kumar, K. Deformation response of ferrite and martensite in a dual-phase steel. *Acta Materialia* 2014, 62, 197-211.



17. Steinbrunner, D.L.; Matlock, D.; Krauss, G. Void formation during tensile testing of dual phase steels. *Metallurgical Transactions A* 1988, 19, 579-589.
18. Ghadbeigi, H.; Pinna, C.; Celotto, S. Failure mechanisms in DP600 steel: Initiation, evolution and fracture. *Materials Science and Engineering: A* 2013, 588, 420-431.
19. Darabi, A.C.; Guski, V.; Butz, A.; Kadkhodapour, J.; Schmauder, S. A comparative study on mechanical behavior and damage scenario of DP600 and DP980 steels. *Mechanics of Materials* 2020, 143, 103339.
20. Darabi, A.C.; Kadkhodapour, J.; Anaraki, A.P.; Khoshbin, M.; Alaie, A.; Schmauder, S. Micromechanical modeling of damage mechanisms in dual-phase steel under different stress states. *Engineering Fracture Mechanics* 2021, 243, 107520.
21. Sun, X.; Choi, K.S.; Liu, W.N.; Khaleel, M.A. Predicting failure modes and ductility of dual phase steels using plastic strain localization. *International Journal of Plasticity* 2009, 25, 1888-1909.
22. Lai, Q.; Bouaziz, O.; Gouné, M.; Brassart, L.; Verdier, M.; Parry, G.; Perlade, A.; Bréchet, Y.; Pardoën, T. Damage and fracture of dual-phase steels: Influence of martensite volume fraction. *Materials Science and Engineering: A* 2015, 646, 322-331.
23. Kusche, C.; Reclik, T.; Freund, M.; Al-Samman, T.; Kerzel, U.; Korte-Kerzel, S. Large-area, high-resolution characterisation and classification of damage mechanisms in dual-phase steel using deep learning. *PloS one* 2019, 14, e0216493.
24. Kusche, C.F.; Pütz, F.; Münstermann, S.; Al-Samman, T.; Korte-Kerzel, S. On the effect of strain and triaxiality on void evolution in a heterogeneous microstructure—A statistical and single void study of damage in DP800 steel. *Materials Science and Engineering: A* 2021, 799, 140332.
25. Yin, Q.; Tekkaya, A.E.; Traphöner, H. Determining cyclic flow curves using the in-plane torsion test. *CIRP Annals* 2015, 64, 261-264.
26. Selini, N.; Elmegueni, M.; Benguediab, M. Effect of the Triaxiality in Plane Stress Conditions. Triaxiality Effect in a PVC Material. *Engineering, Technology & Applied Science Research* 2013, 3, 373-380.
27. Lian, J.; Sharaf, M.; Archie, F.; Münstermann, S. A hybrid approach for modelling of plasticity and failure behaviour of advanced high-strength steel sheets. *International Journal of Damage Mechanics* 2013, 22, 188-218.
28. Bai, Y.; Teng, X.; Wierzbicki, T. Study on the effect of the third stress invariant on ductile fracture. Report, Cambridge 2006.
29. ISO16630:2017. Metallic materials—sheet and strip—hole expanding test. 2017.
30. Habibi, N.; Vajragupta, N.; Münstermann, S. Deformation and Damage Assessments of Two DP1000 Steels Using a Micromechanical Modelling Method. *Crystals* 2021, 11, 805.
31. He, X.; Terao, N.; Berghezan, A. Influence of martensite morphology and its dispersion on mechanical properties and fracture mechanisms of Fe-Mn-C dual phase steels. *Metal science* 1984, 18, 367-373.
32. Kang, J.; Ososkov, Y.; Embury, J.D.; Wilkinson, D.S. Digital image correlation studies for microscopic strain distribution and damage in dual phase steels. *Scripta Materialia* 2007, 56, 999-1002.
33. Heibel, S.; Dettinger, T.; Nester, W.; Clausmeyer, T.; Tekkaya, A.E. Damage mechanisms and mechanical properties of high-strength multiphase steels. *Materials* 2018, 11, 761.
34. Pathak, N.; Butcher, C.; Worswick, M.J.; Bellhouse, E.; Gao, J. Damage evolution in complex-phase and dual-phase steels during edge stretching. *Materials* 2017, 10, 346.

35. Krempaszký, C.; Larour, P.; Freudenthaler, J.; Werner, E. Towards more efficient hole expansion testing. In Proceedings of the IDDRG 2014 Conference, 2014; pp. 204-209.
36. Habibi, N.; Beier, T.; Richter, H.; Könemann, M.; Münstermann, S. The effects of shear affected zone on edge crack sensitivity in dual-phase steels. In Proceedings of the IOP Conference Series: Materials Science and Engineering, 2019; p. 012073.

---

## **Chapter IV: Effects of damage evolution on edge crack sensitivity in dual-phase steels**

---

**N. Habibi, T. Beier, J. Lian, B. Tekkaya, M. Koenemann, S. Muenstermann**

Steel Research International 2024

[https://doi.org/ 10.1002/srin.202400178](https://doi.org/10.1002/srin.202400178)

### **Highlights:**

- A method is derived to implement a coupled phenomenological damage model along with a two-surface isotropic-kinematic hardening model.
- The model is fully calibrated and validated by the lab-scale tests and successfully applied for prediction of edge cracking.
- Three high strength DP steels are studied through various shear-cutting and hole-expansion set-up conditions.
- Edge cracking is discussed based on the main contributing factors: material, edge quality, and edge forming process

## Effects of damage evolution on edge crack sensitivity in dual-phase steels

N. Habibi<sup>a</sup>, T. Beier<sup>b</sup>, J. Lian<sup>c</sup>, B. Tekkaya<sup>a</sup>, M. Koenemann<sup>a</sup>, S. Muenstermann<sup>a</sup>

<sup>a</sup> Institute of Metal Forming, RWTH Aachen University, Intzestraße 10, 52072 Aachen, Germany

<sup>b</sup> Thyssenkrupp Steel Europe AG, Kaiser-Wilhelm-Str. 100, 47166 Duisburg, Germany

<sup>c</sup> Advanced Materials and Manufacturing, Department of Mechanical Engineering, Aalto University, Puumiehenkuja 3, 02150 Espoo, Finland

### Abstract

The present study aims to thoroughly investigate the edge-cracking phenomenon in high-strength sheets. Hence, the edge crack sensitivity of three dual-phase steels was studied in various combinations of edge manufacturing and forming processes. Finite element simulations were performed to elaborate the study. In this regard, the Yoshida-Uemori kinematic hardening model was employed to describe the plasticity behavior of the materials under multi-step processes. A stress-state fracture model was coupled with this plasticity model to illustrate the distinguished local fracture strains of each material. Moreover, the effects of strain rate and the consequent temperature rise on hardening and damage were taken into account, which play significant roles during shear-cutting. The results showed although the shear-cutting processes were applied at very low speed, the strain rate and induced temperature were still high at the cutting area. The hole expansion results showed different fracture behaviors for different cases. In brief, cracking was initiated at a location, which showed the highest damage accumulation during edge manufacturing plus the subsequent forming process. Such a complicated situation can only be successfully predicted by using a computer-aided approach along with proper material modeling, like the applied model in this study.

### Keywords

Dual phase steels, Edge crack sensitivity, Finite element method, Fracture model, kinematic hardening

**Nomenclature\***

$b$	A material constant in YU model
$B$	Initial size of the bounding surface in YU model
$C$	A material parameter that controls the rate of kinematic hardening in YU model
$C_{1-6}$	Material parameters of damage initiation locus
$c_{1-3}^T$	Temperature correction function parameters
$c_{1-2}^{\dot{\epsilon}^p}$	Strain rate correction function parameters
$C_p$	Specific heat capacity (here is $C_p=466$ J/(kg.K) [1])
$D$	Damage variable
$D_0$	The initial hole diameter for hole expansion test
$D_{1-6}$	Material parameters of fracture locus
$D_h$	The average hole diameter after rupture during hole expansion test
$G_f$	A material constant based on energy dissipation theory
$I_{ddi}$	Ductile damage initiation indicator
$I_{df}$	Ductile fracture indicator
$k$	A material parameter that controls the rate of isotropic hardening in YU model
$K_0$	Bulk modulus
$\mathbf{n}$	Plastic flow direction tensor
$\mathbf{p}$	Hydrostatic pressure tensor
$R$	nonlinear Isotropic hardening component in YU model
$R_{sat}$	Saturated value of the isotropic hardening stress at infinitely large plastic strain
$\mathbf{s}$	Deviatoric stress tensor
$T$	Temperature
$T_0$	Reference temperature (here is $T_0=298$ K)
$Tr(.)$	Trace operator of $(.)$
$Y$	Initial yield stress
$\boldsymbol{\alpha}$	Back stress tensor
$\boldsymbol{\alpha}_*$	Position of the yield surface regarding to the center of the bounding surface
$\overline{\boldsymbol{\alpha}_*}$	Effective quantity of $\boldsymbol{\alpha}_*$
$\boldsymbol{\beta}$	Kinematic hardening of the bounding surface
$\beta_{TQ}$	Taylor–Quinney coefficient (here is $\beta_{TQ}=0.89$ [1])
$\gamma$	Effective plastic strain
$\Delta(.)$	Increment of $(.)$
$\boldsymbol{\epsilon}$	Total strain tensor

$\boldsymbol{\varepsilon}^e$	Elastic strain tensor
$\boldsymbol{\varepsilon}^p$	Plastic strain tensor
$\varepsilon^p$	Equivalent plastic strain
$\varepsilon_{ddi}^p$	Equivalent plastic strain at ductile damage initiation
$\varepsilon_{df}^p$	Equivalent plastic strain at ductile fracture
$\dot{\boldsymbol{\varepsilon}}^p$	Strain rate
$\dot{\varepsilon}_0^p$	Reference strain rate (here is $\dot{\varepsilon}_0^p=0.001 \text{ s}^{-1}$ )
$\eta$	Stress triaxiality
$\eta_c$	cut-off value for damage, (here is $\eta_c < -\frac{3-\bar{\theta}}{3\sqrt{\bar{\theta}^2+3}} + 1/3$ [2])
$\bar{\theta}$	Normalized Lode angle parameter
$\lambda$	Lame modulus
$\mu$	Shear modulus
$\rho$	Density (here is $\rho=7870 \text{ kg/m}^3$ )
$\boldsymbol{\sigma}$	Stress tensor
$\bar{\sigma}$	Equivalent stress
$\sigma_{di}^c$	Equivalent stress where damage initiates
$\bar{\sigma}_{vM}$	von Mises equivalent stress
$\sigma_y$	Yield stress
$\Phi$	Flow potential function
$(\cdot)_n$	$(\cdot)$ at the time $t_n$
$(\cdot)_{n+1}$	$(\cdot)$ at the time $t_{n+1}$
$(\dot{\cdot})$	Changes rate of $(\cdot)$

\* The bold symbols represent tensor parameters, while others are scalar quantities.

## 1. Introduction

The hostile global environmental and economic situations have compelled automotive manufacturers to develop lightweight components that meet stringent crash safety requirements [3]. In this pursuit, the continuous design and improvement of new advanced materials, such as dual-phase (DP) steels aim to achieve an optimal balance between strength and formability. However, the complex multi-step forming processes involved in creating the final product trigger several problems that hinder the widespread application of these materials. One of the unresolved challenges in sheet forming of high-strength materials is edge cracking, which appears despite conventional forming limits anticipating further deformation as a safe condition [4]. To overcome this problem, there is a need for new damage evaluation methods, that rely on a deep understanding of this phenomenon to successfully design highly efficient forming procedures. Casellas et al. [5] conducted experiments to measure the hole expansion ratios (HER) of various advanced high-strength steel (AHSS) sheets as a quantitative factor of edge crack sensitivity. Their HER results exhibited a similar trend as the materials' essential work of fracture. Heibel et al. [6] showed the relationship

between HER and local formability, which was defined by true thickness strain at fracture. Although these methods were successful in the studied cases, they should be verified under different stress states as well, since the cutting and subsequent forming processes are significantly influenced by loading modes. Therefore, employing hybrid testing and simulation methods could be a promising choice for considering various conditions even for various scales [7]. Complex microstructure in multi-phase steels causes different local formability behaviors and consequently edge crack sensitivity [8-11]. Namely, phase fraction, phase distribution, texture, individual morphological characteristics, and mechanical behavior of each phase could change the local formability of the materials. The role of these features has also been investigated through numerical approaches using representative volume element (RVE) models along with finite element (FE) simulations [12, 13]. These studies collectively suggest that a homogeneous strain distribution throughout the material can enhance local formability under various loading conditions. In addition to the materials' intrinsic properties, the tooling design plays a critical role in exacerbating the issue of edge-forming limitation. It encompasses the manufacturing technique utilized for edge creation and subsequent edge-forming processes. Punching is widely employed as an initial manufacturing process in the industry due to its great cost-effectiveness and efficiency. However, it applies severe hardening and damage to the shear-affected zone (SAZ). Consequently, a rough low-quality edge is produced, which facilitates premature failure from the edge. Wang et al. [14] have documented considerable dissimilarities in the HER of DP780 steel across varying hole expansion tests (HET). Their findings demonstrated HER of 38 and 35% for milled and waterjet cut holes, whereas 12% for the punched holes. In addition, the relationship between clearance and HER has garnered significant attention and various studies tried to unravel underlying mechanisms and optimize hole expansion performance [15- 17]. The clearance parameter directly impacts materials' flow and deformation behavior during plastic deformation. A larger clearance expands SAZ and produces a larger burr, which leads to higher edge cracking sensitivity. On the other hand, narrow clearance could also cause a secondary burnish which reduces HER. Wu et al. [18] argued a narrow clearance could suppress the main crack to develop throughout the thickness. Therefore, a secondary shearing as well as multiple sub-cracks form to separate the remaining thickness. These microcracks create rougher surfaces and lower edge quality [19]. Moreover, the influences of hole expansion punches with different shapes have been investigated. Wang et al. [14] showed conical, flat, and spherical punches apply different contact conditions and strain gradients. Conical punches maximize edge stretching, causing specimen rotation and non-uniform strain distributions. Flat punches cause minimal rotation near the edge leading to edge cracks occurring away from it. Spherical punches offer an intermediate loading condition with moderate strain gradients. Paul [20] observed that failure initiation occurs at the hole edge when employing a conical punch. However, in the case of hemispherical and flat-bottom punches, failure initiation was found to occur slightly away from that, i.e. inside of the sheet rather than at the edge. Krempaszky et al. [21] concluded that higher contact pressure, resulting from a smaller initial hole size and a smaller cone angle of the hole expansion punch, facilitates local necking formation. This phenomenon plays a key role in significant HER reduction. The explanation for this behavior lies in the concept of applied strain gradient [20, 22]. The presence of higher strain gradients suppresses plain strain necking at the punch-sheet contact site and allows edge cracking to happen. Prediction of various

edge manufacturing and following forming processes requires a powerful numerical tool to consider the effects of stress states, strain rates, adiabatic heating, and probable Bauschinger effect on hardening and damage behaviors. This study aims to propose a computer-aided approach to take all the aforementioned factors into account, unlike the existing studies which considered only part of them at the same time. In addition, its accuracy was verified successfully for different materials under various edge-cutting and forming procedures.

## 2. Materials and Methods

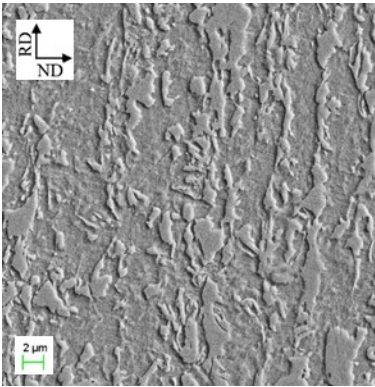
### 2.1 Materials

For this work, three different dual-phase (DP) steel sheets were studied with a thickness of 1.5 mm, and the commercial names of CR440Y780T-DP, CR590Y980T-DP, and CR700Y980T-DP. In these names, the first number addresses the yield stress and the second number stands for the ultimate tensile strength. The chemical compositions are listed in Table 1 and their as-received microstructures are shown in Figure 1. All the microstructures consist of ferrite and martensite phases. The phase fractions were calculated using Digimizer image analysis for several scanning electron microscope (SEM) images, while the relatively lighter and darker phases were marked as martensite and ferrite, respectively. To evaluate strength differences between the phases, the carbon contents were measured by electron probe microanalysis (EPMA) as 15- $\mu\text{m}$  line scans of the microstructures.

**Table 1.** Chemical composition of the studied DP steels.

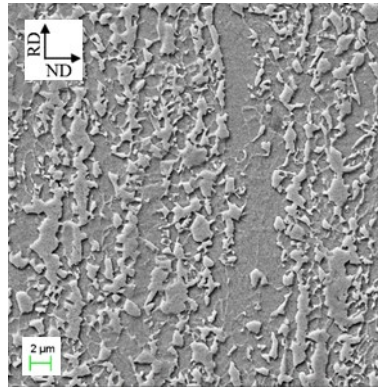
	C	Si	Mn	Al	Cr	Mo	Cu	Ti
<b>DP440/780</b>	0.149	0.212	1.670	0.049	0.733	0.011	0.044	0.031
<b>DP590/980</b>	0.074	0.301	1.830	0.048	0.387	0.061	0.023	0.048
<b>DP700/980</b>	0.074	0.294	2.498	0.037	0.693	0.118	0.123	0.076

**DP440/780**



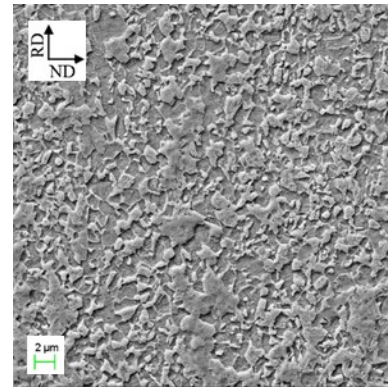
Ferrite: 65%  
Martensite: 35%

**DP590/980**



Ferrite: 65%  
Martensite: 35%

**DP700/980**



Ferrite: 55%  
Martensite: 45%

**Figure 1.** The initial microstructure and phase fraction for the studied materials.



## 2.2 Experimental procedure

### 2.2.1 Experiments for calibration of the models

The plasticity model was calibrated using cyclic in-plane torsion tests, which were described in Ref. [23]. Furthermore, the effects of a wide range of stress states on damage behavior were investigated for each material. In this regard, various testing methods were applied, including monotonic in-plane torsion, bulge, tensile tests with different notch geometries, and plane-strain tests, Figure 2. For detailed information about the technical drawings of specimens and experimental results see Ref. [10]. Furthermore, SEM was used to investigate the fracture surface and damage micro-mechanisms.

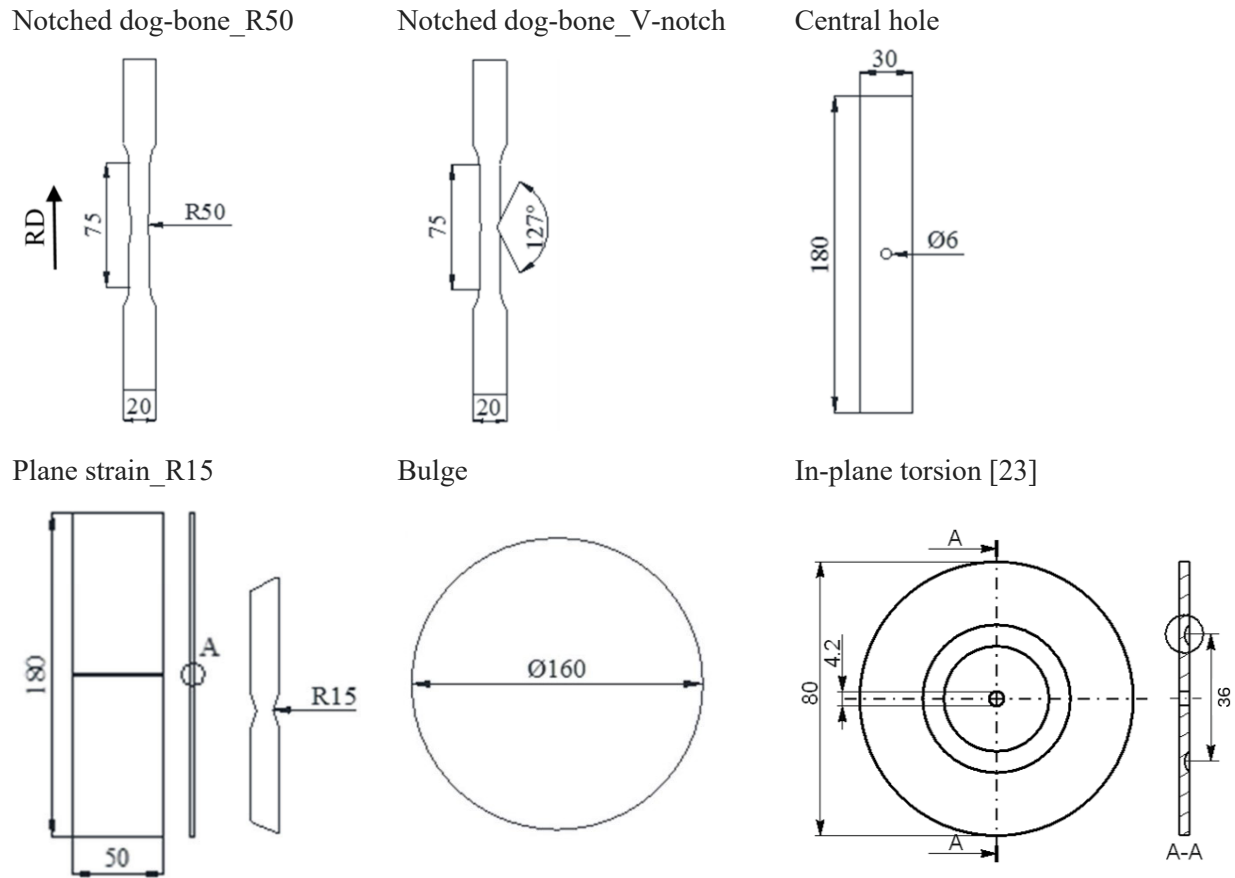


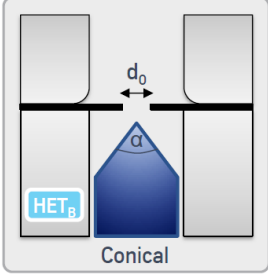
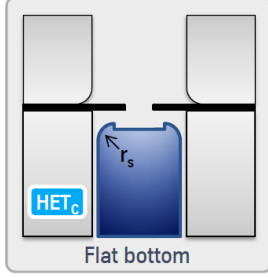
**Figure 2.** The specimen geometries of applied tests.

### 2.2.2 Shear-cutting and subsequent hole expansion test

In order to study the edge crack sensitivity, several edge conditions were manufactured through shear-cutting process and expanded with a conical or flat-bottom punch according to ISO 16630:2017 [24]. The tool conditions for each step are summarized in Table 2 and the speed of punches in both steps was 1 mm/s. The hole expansion ratios were measured as a quantitative parameter of edge cracking sensitivity. According to the aforementioned standard, HER should be calculated as a through-thickness edge crack occurs. This evaluation was assisted by video recording techniques which allowed precise results to be

extracted. Note that similar hole sizes were manufactured by wire-cutting as well to compare the potential of edge formability regards of pre-damage effects.

**Table 2.** Tool conditions of used cutting and hole expansion processes .

Shear-cutting tool			Hole expansion tool	
Ø Die	Ø Punch	Clearance	Conical 50°	Flat-bottom
30 mm	29.7 mm	10.0%	Ø 100 mm	Ø 100 mm; R <sub>s</sub> 15
	29.6 mm	13.3%		
39.97 mm	39.67 mm	10.0%		
	39.57 mm	13.3%		

## 2.3 Numerical procedure

### 2.3.1 Material model

Since the materials underwent complex multi-step deformation processes, shear-cutting followed by HET, changes in the yield stress should be considered. Therefore, a non-linear kinematic hardening model was used to describe the plasticity behavior more precisely. The damage behavior was also modeled using a stress state dependent phenomenological damage criterion which was coupled with the plasticity model. The models and implementation method are explained in the following. Note that all bold symbols show tensor variables and the rests are scalar variables.

#### 2.3.1.1 Plasticity model

The general yielding function ( $\Phi$ ) is described in stress space as follows:

$$\Phi = \bar{\sigma} - \sigma_y = 0 \quad \text{Eq. 1}$$

$\bar{\sigma}$  is equivalent stress and calculated according to von Mises yield criterion, equation 2.

$$\bar{\sigma} = \bar{\sigma}_{vM} = \sqrt{\frac{3}{2}} \|\mathbf{s} - \boldsymbol{\alpha}\| \quad \text{Eq. 2}$$

where  $\mathbf{s}$  and  $\boldsymbol{\alpha}$  are deviatoric stress tensor and back stress tensor, respectively.  $\sigma_y$  is yield stress. Since the strain rate could be high especially during shear-cutting and generate adiabatic heating, a multiplied function was used for yield stress calculation, equation 3.

$$\sigma_y = \sigma_{y(\dot{\varepsilon}^p, \dot{\varepsilon}_0^p, T_0)} \cdot \sigma_{y(\dot{\varepsilon}^p)} \cdot \sigma_{y(T)} \quad \text{Eq. 3}$$

$\sigma_{y(\dot{\varepsilon}^p, \dot{\varepsilon}_0^p, T_0)}$  shows the stress-strain curve under the reference strain rate ( $\dot{\varepsilon}_0^p$ ) and temperature ( $T_0$ ).

As The strain rate and temperature correction function are defined in equations 4 and 5, respectively.

$$\sigma_{y(\dot{\varepsilon}^p)} = c_1^{\dot{\varepsilon}^p} \cdot \ln \dot{\varepsilon}^p + c_2^{\dot{\varepsilon}^p} \quad \text{Eq. 4}$$

$$\sigma_{y(T)} = c_1^T \cdot \exp(-c_2^T \cdot T) + c_3^T \quad \text{Eq. 5}$$

The temperature changes ( $\Delta T$ ) due to adiabatic heating could be calculated as below [25, 26],

$$\Delta T = \frac{\beta_{TQ}}{\rho \cdot C_p} \cdot \sigma_y \cdot \Delta \epsilon^p \quad \text{Eq. 6}$$

where  $\beta_{TQ}$  is Taylor–Quinney coefficient,  $\rho$  is density, and  $C_p$  is specific heat capacity. They are all materials dependence. The increment of plastic strain ( $\Delta \epsilon^p$ ) is determined by applying the associated flow rule in the following equation:

$$\Delta \epsilon^p = \Delta \gamma \mathbf{n} \quad \text{Eq. 7}$$

where  $\mathbf{n}$  is the normal of yield surface and is  $\gamma$  effective plastic strain.

Yoshida-Uemori two-surface plasticity model [27] was employed in this work to satisfy the multi-step deformation requirements for capturing the Bauschinger effect. It contains two surfaces, the yield surface (the inner one) with radius of  $Y$  and the bounding surface (the outer one) with radius of  $B + R$ , Figure 3. The yield surface represents the plastic deformation occurrence by translating across the bounding surface while its size remains constant ( $Y$ ), therefore:

$$\sigma_{y(\epsilon^p, \epsilon_0^p, T_0)} = Y \quad \text{Eq. 8}$$

Whereas the bounding surface is able to both move and expand. The evolution of the yield surface is as:

$$\dot{\boldsymbol{\alpha}} = \dot{\boldsymbol{\beta}} + \dot{\boldsymbol{\alpha}}_* \quad \text{Eq. 9}$$

where  $\dot{\boldsymbol{\beta}}$  is kinematic hardening rate of the bounding surface:

$$\dot{\boldsymbol{\beta}} = k \left( \frac{b}{Y} (s - \boldsymbol{\alpha}) - \boldsymbol{\beta} \right) \dot{\gamma} \quad \text{Eq. 10}$$

And  $\dot{\boldsymbol{\alpha}}_*$  is the relative kinematic motion:

$$\dot{\boldsymbol{\alpha}}_* = C \left( \frac{B + R - Y}{Y} (s - \boldsymbol{\alpha}) - \sqrt{\frac{B + R - Y}{\bar{\alpha}_*}} \boldsymbol{\alpha}_* \right) \dot{\gamma} \quad \text{Eq. 11}$$

$C$ ,  $B$ , and  $Y$  are material constants.  $R$  is the nonlinear Isotropic hardening component of bounding surface and it evolves as:

$$\dot{R} = k(R_{sat} - R) \dot{\gamma} \quad \text{Eq. 12}$$

$k$  and  $R$  are material constants.

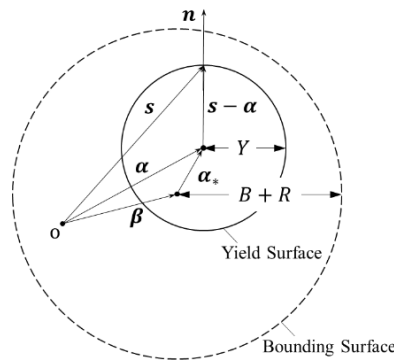


**Figure 3.** Schematic illustration of the Yoshida-Uemori model [27] Copyright 2002, Elsevier.

### 2.3.1.2 Damage evolution model

A strain-based phenomenological ductile damage criterion was used to describe damage initiation, propagation, and fracture. The range of each stage was determined by two indicators,  $I_{ddi}$  and  $I_{df}$  in damage parameter ( $D$ ), Eq. 13. The indicators calculate the accumulation of damage throughout non-proportional loading paths and consider the stress state at each increment as stress triaxiality ( $\eta$ ) and normalized Lode angle parameter ( $\bar{\theta}$ ), Eq. 14-17. Note that the relation between damage initiation and fracture strains with loading condition was defined using the Bai-Wierzbicki (BW) model [28-30]. A more detailed description of the model can be found in the previous study by [1]. Parameters  $\sigma_{ddi}^c$ ,  $G_f$ ,  $C_i$ , and  $D_i$  are material constants. It is noted that a changeable cut-off value for damage was considered in this study as  $\eta_c < -\frac{3-\bar{\theta}}{3\sqrt{\bar{\theta}^2+3}} + 1/3$ , which proposed for a DP980 steel [2]. Therefore, no damage would accumulate in the case  $\eta < \eta_c$ .

$$D = \begin{cases} 0 & I_{ddi} < 1 \\ \frac{\sigma_{ddi}^c}{G_f} \int_{\varepsilon_{ddi}^p}^{\varepsilon^p} d\varepsilon^p & I_{ddi} \geq 1 \wedge I_{df} < 1 \\ 1 & I_{ddi} \geq 1 \wedge I_{df} \geq 1 \end{cases} \quad \text{Eq. 13}$$

$$I_{ddi} = \int_0^{\varepsilon^p} \frac{d\varepsilon^p}{\varepsilon_{ddi}^p(\eta, \bar{\theta})} \quad \text{Eq. 14}$$

Where  $\varepsilon_{ddi}^p(\eta, \bar{\theta}) = \begin{cases} +\infty & \eta \leq \eta_c \\ f_{ddi}(\eta, \bar{\theta}) & \eta > \eta_c \end{cases}$

$$f_{ddi}(\eta, \bar{\theta}) = (1/2 (C_1 e^{-C_2 \eta} + C_5 e^{-C_6 \eta}) - C_3 e^{-C_4 \eta}) \bar{\theta}^2 + 1/2 (C_1 e^{-C_2 \eta} - C_5 e^{-C_6 \eta}) \bar{\theta} + C_3 e^{-C_4 \eta} \quad \text{Eq. 15}$$

$$I_{df} = \int_{\varepsilon_{ddi}^p}^{\varepsilon^p} \frac{d\varepsilon^p}{\varepsilon_{df}^p(\eta, \bar{\theta}) - \varepsilon_{ddi}^p(\eta, \bar{\theta})} \quad \text{Eq. 16}$$

Where  $\varepsilon_{df}^p(\eta, \bar{\theta}) = \begin{cases} +\infty & \eta \leq \eta_c \\ f_{df}(\eta, \bar{\theta}) & \eta > \eta_c \end{cases}$

$$f_{df}(\eta, \bar{\theta}) = (1/2 (D_1 e^{-D_2 \eta} + D_5 e^{-D_6 \eta}) - D_3 e^{-D_4 \eta}) \bar{\theta}^2 + 1/2 (D_1 e^{-D_2 \eta} - D_5 e^{-D_6 \eta}) \bar{\theta} + D_3 e^{-D_4 \eta} \quad \text{Eq. 17}$$

### 2.3.1.3 Implementation of damage model in the plasticity model

The plasticity model was coupled with the damage model through a user-defined VUMAT subroutine to use in Abaqus finite element software, as described in the following. Note that the crack initiation and propagation were defined by element deletion.

In the finite element context, for the time  $n$  the current state variables are known, such as  $\varepsilon_n^p, \sigma_n, \alpha_n, \beta_n, \alpha_{*n}, \bar{\sigma}_n, D_n$ , etc. For further plastic deformation at time step  $n+1$ , the plastic corrector/radial return mapping method was employed. In this regard, Hook's law is written as

$$\boldsymbol{\sigma}_{n+1} = 2\mu\boldsymbol{\varepsilon}_{n+1}^e + \lambda \text{Tr}(\boldsymbol{\varepsilon}_{n+1}^e)\mathbf{I} \quad \text{Eq. 18}$$

where  $\mu$  and  $\lambda$  are shear and Lamé moduli, respectively. The elastic strain at this time is

$$\boldsymbol{\varepsilon}_{n+1}^e = \boldsymbol{\varepsilon}_n^e + \Delta\boldsymbol{\varepsilon}^e \quad \text{Eq. 19}$$

$$\Delta\boldsymbol{\varepsilon}^e = \Delta\boldsymbol{\varepsilon} - \Delta\boldsymbol{\varepsilon}^p \quad \text{Eq. 20}$$

so that

$$\boldsymbol{\sigma}_{n+1} = 2\mu(\boldsymbol{\varepsilon}_n^e + \Delta\boldsymbol{\varepsilon} - \Delta\boldsymbol{\varepsilon}^p) + \lambda \text{Tr}(\boldsymbol{\varepsilon}_n^e + \Delta\boldsymbol{\varepsilon} - \Delta\boldsymbol{\varepsilon}^p)\mathbf{I} \quad \text{Eq. 21}$$

since

$$\text{Tr}(\Delta\boldsymbol{\varepsilon}^p) = 0 \quad \text{Eq. 22}$$

the stress tensor could be written as [Elastic predictor]-[Plastic corrector], like below

$$\boldsymbol{\sigma}_{n+1} = [2\mu(\boldsymbol{\varepsilon}_n^e + \Delta\boldsymbol{\varepsilon}) + \lambda \text{Tr}(\boldsymbol{\varepsilon}_n^e + \Delta\boldsymbol{\varepsilon})\mathbf{I}] - [2\mu\Delta\boldsymbol{\varepsilon}^p] \quad \text{Eq. 23}$$

The elastic predictor or trial stress is

$$\boldsymbol{\sigma}_{n+1}^{\text{trial}} = 2\mu(\boldsymbol{\varepsilon}_n^e + \Delta\boldsymbol{\varepsilon}) + \lambda \text{Tr}(\boldsymbol{\varepsilon}_n^e + \Delta\boldsymbol{\varepsilon})\mathbf{I} \quad \text{Eq. 24}$$

The increment plastic strain tensor could be written according to the plastic multiplier and the plastic flow direction tensor, as

$$\Delta\boldsymbol{\varepsilon}^p = \Delta\gamma \mathbf{n}_{n+1} \quad \text{Eq. 25}$$

$$\mathbf{n}_{n+1} = \frac{\mathbf{s}_{n+1}^{\text{trial}} - \boldsymbol{\alpha}_{n+1}}{\|\mathbf{s}_{n+1}^{\text{trial}} - \boldsymbol{\alpha}_{n+1}\|} = \frac{\mathbf{s}_{n+1}^{\text{trial}} - \boldsymbol{\alpha}_n}{\|\mathbf{s}_{n+1}^{\text{trial}} - \boldsymbol{\alpha}_n\|} \quad \text{Eq. 26}$$

Thus, the stress tensor becomes

$$\boldsymbol{\sigma}_{n+1} = \boldsymbol{\sigma}_{n+1}^{\text{trial}} - 2\mu \mathbf{n}_{n+1} \Delta\gamma \quad \text{Eq. 27}$$

Then, the yielding possibility is checked considering the flow potential function as

$$\Phi_{n+1} = \bar{\sigma}_{n+1} - (1 - D_{n+1})\sigma_y = 0 \quad \text{Eq. 28}$$

According to the aforementioned models and considering the von Mises yielding criterion the description of each parameter would be

$$\bar{\sigma}_{n+1} = \sqrt{\frac{3}{2}} \|\mathbf{s}_{n+1}^{\text{trial}} - (1 - D_{n+1})\boldsymbol{\alpha}_{n+1} - 2\mu \mathbf{n}_{n+1} \Delta\gamma\| \quad \text{Eq. 29}$$

$$\boldsymbol{\alpha}_{n+1} = \boldsymbol{\alpha}_n + \Delta\boldsymbol{\beta} + \Delta\boldsymbol{\alpha}_* \quad \text{Eq. 30}$$

$$\Delta\boldsymbol{\beta} = k \left[ \frac{b}{Y} (\mathbf{s}_{n+1}^{\text{trial}} - (1 - D_{n+1})\boldsymbol{\alpha}_{n+1} - 2\mu \mathbf{n}_{n+1} \Delta\gamma) - \boldsymbol{\beta}_n \right] \Delta\gamma \quad \text{Eq. 31}$$

$$\Delta\boldsymbol{\alpha}_* = C \left[ \frac{B+R-Y}{Y} (\mathbf{s}_{n+1}^{\text{trial}} - (1 - D_{n+1})\boldsymbol{\alpha}_{n+1} - 2\mu \mathbf{n}_{n+1} \Delta\gamma) - \sqrt{\frac{B+R-Y}{\|\boldsymbol{\alpha}_{*n}\|}} \boldsymbol{\alpha}_{*n} \right] \Delta\gamma \quad \text{Eq. 32}$$

$$\Delta R = k(R_{\text{sat}} - R) \Delta\gamma \quad \text{Eq. 33}$$

Note that since the strength differential effect is weak for DP steels, especially DP980 [31], using von Mises yield surface model is sufficiently accurate. Calculating the damage parameter and assessing the initiation of ductile damage and fracture by using the indicators  $I_{ddi(n+1)}$  and  $I_{df(n+1)}$ , as

$$D_{n+1} = D_n + \left( \frac{\sigma_{di}^c}{G_f} \right) \Delta\gamma \quad \text{Eq. 34}$$

$$I_{ddi(n+1)} = I_{ddi(n)} + \frac{\Delta\gamma}{\varepsilon_{ddi(n+1)}^p} \quad \text{Eq. 35}$$

$$I_{df}(n+1) = I_{df}(n) + \frac{\Delta\gamma}{\varepsilon_{df}(n+1)^p - \varepsilon_{ddi}(n+1)^p} \quad \text{Eq. 36}$$

The flow potential function could be written based on  $\Delta\gamma$  with the form as

$$\Phi_{n+1} = \|A + B\Delta\gamma\| + C + D\Delta\gamma = aa + bb\Delta\gamma + cc + dd\Delta\gamma \quad \text{Eq. 37}$$

By assuming  $(\Delta\gamma)^2 \approx 0$  is negligible,

$$(\Delta\gamma)^2 \approx 0 \quad \text{Eq. 38}$$

the plastic multiplier is calculated as

$$\Delta\gamma = -\frac{aa+cc}{bb+dd} \quad \text{Eq. 39}$$

With the plastic corrector, deviatoric stress tensor  $\mathbf{s}$ , stress tensor  $\boldsymbol{\sigma}$ , and equivalent stress  $\bar{\sigma}$  can be updated backwardly for time  $n+1$ .

### 2.3.2 Simulation model

To study and analyze the deformation history and damage evolution of the experiments, parallel finite element models were employed using Abaqus2019/Explicit software. The details of the models are described below.

#### 2.3.2.1 Calibration of models

The constants of plasticity and damage models were calibrated reversely by comparison of flow curve and force-displacement curves between the simulations and experiments. Since for high strength DP steels, the fracture happens immediately after damage initiation [1, 30], the damage and fracture indicator were defined the same. The eight-node brick elements with reduced integration (C3D8R) and size of  $0.1 \times 0.1 \times 0.1 \text{ mm}^3$  were applied at the critical areas, where the deformation and damage concentrated.

#### 2.3.2.2 Shear-cutting and the subsequent hole expansion processes

The shear-cutting and the following hole expansion test were simulated as a one-stroke two-step model. In this model, the cutting punch, holder, die, and hole-expansion punch were designed as solid rigid parts, while the sheet was a deformable solid. In order to reduce the computational time and according to the symmetric axes, only 5° of set-up was studied. The C3D8R elements with a size of  $0.025 \times 0.025 \times 0.025 \text{ mm}^3$  were used in the critical areas to capture relatively accurate damage distribution at the shear-cut edges. However, for the simulation of wire-cut edges, the element size of  $0.1 \times 0.1 \times 0.1 \text{ mm}^3$  was used to decrease the running time. The set-up assembly and mesh pattern are depicted in Figure 4. The Coulomb friction coefficient of 0.1 [32, 33] was applied between the contact pairs which were defined by a node-to-surface algorithm. An optimal clamping force was chosen such that the blank was neither drawn in nor torn improperly during the forming processes.

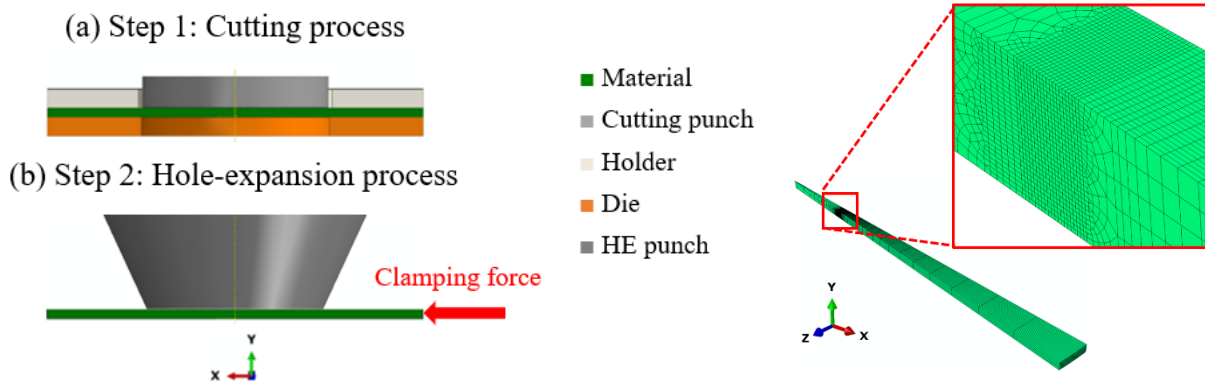


**Figure 4.** The assembly (left) and mesh pattern (right) of the created model.

### 3 Results and discussion

The capability of the proposed method was assessed for 3 DP steel sheets. At first, the model material parameters were calibrated for each material (section 3.1) and then the calibrated models were applied for the prediction of various shear-cutting processes (section 3.2) processes (section 3.2) and hole expansion tests (section 3.3).

#### 3.1 Materials behavior and calibration

The YU plasticity model was calibrated through monotonic and cyclic torsion loading conditions, Figure 5 and Table 3. The in-plane torsion test induced a shear stress state ( $\eta=0$ ) with no deformation localization. Thus, the whole flow curves up to fracture were considered for the calibration process. To investigate the advantages of the YU model, the same cyclic loading was also simulated using true stress-strain data of the monotonic loadings along with the default isotropic hardening in Abaqus. These results are shown in Figure 5 in black dashed lines. Figure 5 reveals the earlier yielding was successfully predicted using YU plasticity, while obviously isotropic hardening approach was unable to. Since fracture behavior occurs shortly after damage in many high-strength DP steels as indicated in Ref [1] and [30], using an uncoupled fracture model could work properly and even accurately. Therefore, the uncoupled version of the aforementioned damage model was employed. The calibrated parameters are listed in Table 3 and the calculated fracture strains are plotted in the space of stress triaxiality, normalized Lode angle parameter in Figure 6. The calibrated plasticity-damage model showed the accurate prediction of material response for different stress states, figure 7. The fracture locus of DP700/980 was significantly higher than others, which implies higher local deformation.

**Table 3.** Calibrated parameters for YU plasticity and the fracture model for the studied materials at reference stress rate ( $\dot{\epsilon}_0^P=0.001$  s<sup>-1</sup>) and temperature ( $T_0=298$  K).

	$Y$	$B$	$R_{sat}$	$c$	$K$	$b$	$D_1$	$D_2$	$D_3$	$D_4$	$D_5$	$D_6$
DP440/780	440	830	190	100	2.4	5	1.20	1.50	0.68	2.43	0.35	0.20
DP590/980	610	1150	157	85	1	5	1.00	2.60	0.41	1.70	0.25	0.00
DP700/980	705	1100	133	100	1	5	2.00	2.20	0.86	1.90	0.41	0.00



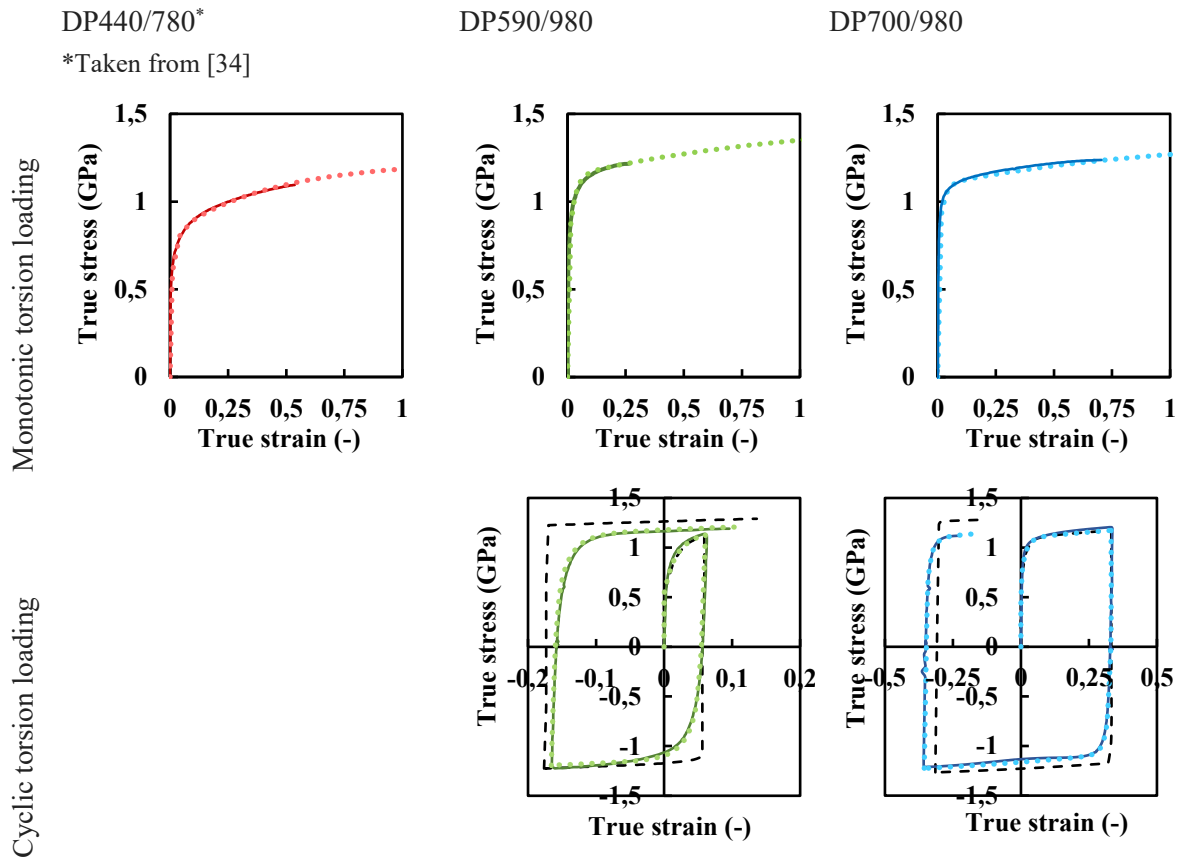


Figure 5. Comparison between the flow curves of experiments (solid lines), simulations with YU plasticity (dotted lines), and isotropic hardening (black dashed lines).

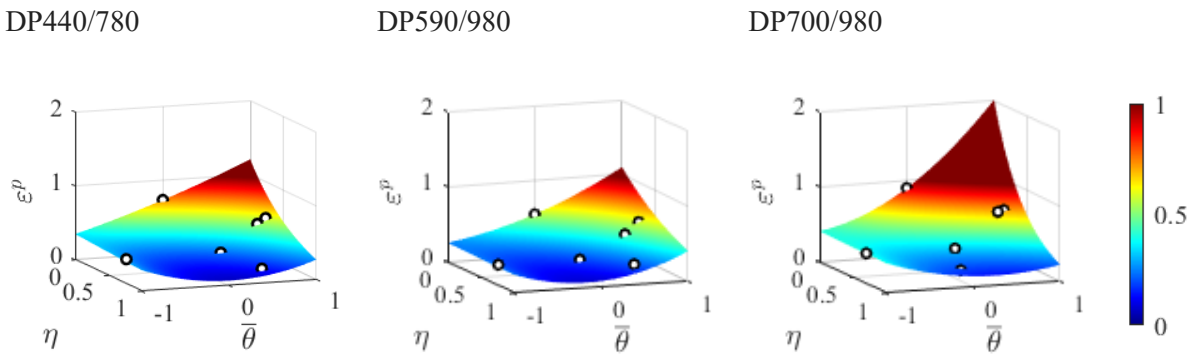
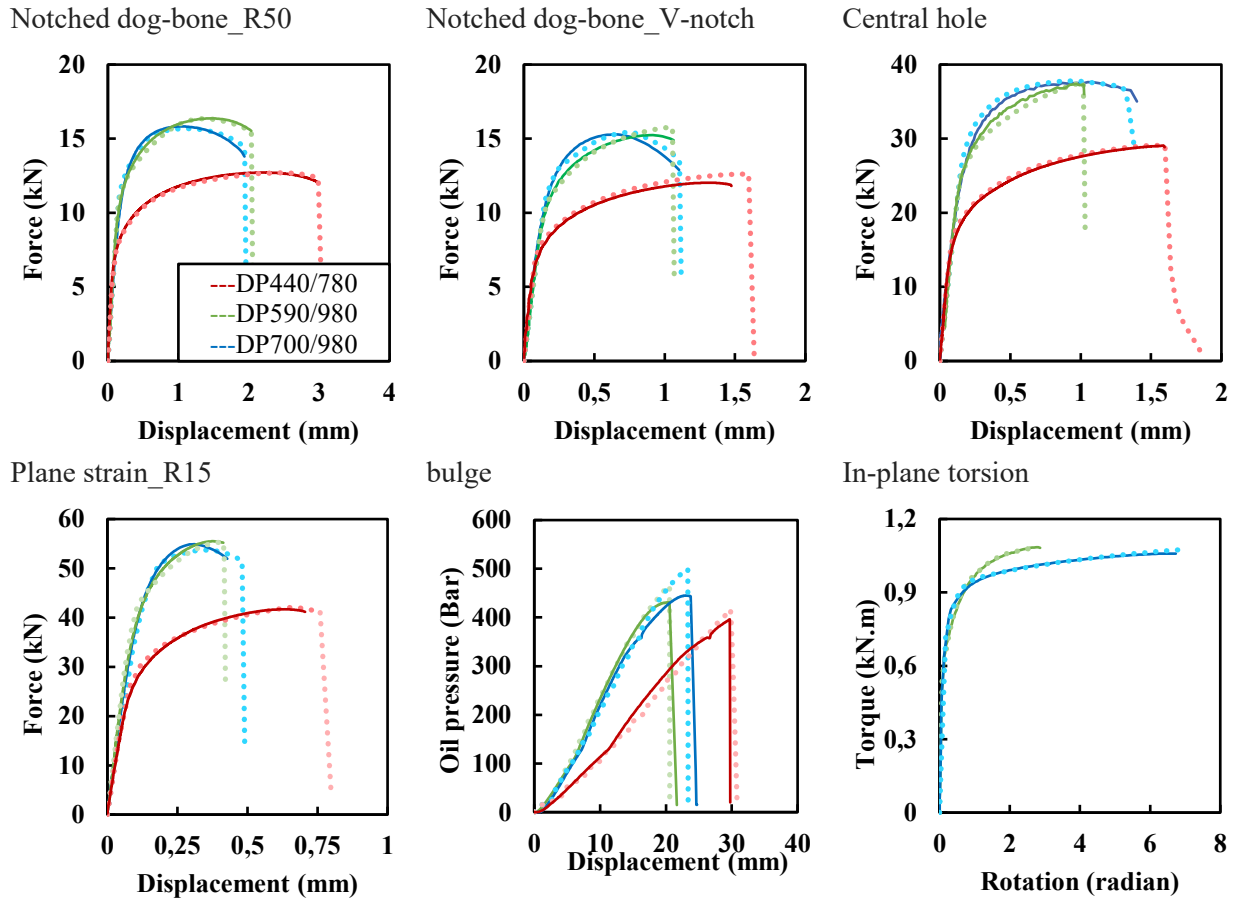


Figure 6. Ductile fracture loci of the investigated DP steels.



**Figure 7.** Responses of the materials through various testing techniques, experimental results (solid lines) and simulation results (dotted lines). The torsion test was not performed for DP440/780.

Accordingly, the thickness reduction, damage micro-mechanisms, and fracture surface of these specimens were observed through the SEM micrographs as each material endured necking differently, figure 8. The thickness measurement at the central part of the fracture site reveals that the thickness reduced from 1.5 mm to 1.10 mm and 1.22 mm for DP440/780 and DP590/980 by small localization and through-thickness shearing, and to 0.75 mm for DP700/980 by severe necking. In addition, distinguished damage micro-mechanisms were observed for each studied steel. Martensite cracking is the dominant failure mechanism in DP440/780 (mostly in the martensite bands) and DP590/980, while decohesion between ferrite and martensite interfaces is the main damage mechanism for DP700/980. These distinct damage behaviors were dictated by deformation distribution through the material and between the phases, as a result of microstructural features. Phase fractions, their distributions, and morphologies in Figure 1, as well as phase strength differences, which were estimated by the local carbon content in Figure 9, play the main roles. Therefore, it can be briefly concluded that the closer phase fractions, finer grain sizes, phase distribution consistency, and lower strength differences of individual phases led DP700/980 to accommodate the deformation more homogeneously and retard the damage initiation. It is worth mentioning, due to wide martensitic band structures, DP440/780 showed large scatter data for its local formability, which was even

more considerable in specific stress states. For example, Figure 10 displays the reproducibility of results for a plane-strain tensile test for the studied DP steels. The three repeats for DP440/780 fractured at a wide range of displacement, which made the numerical study of the failure behavior of this material difficult.

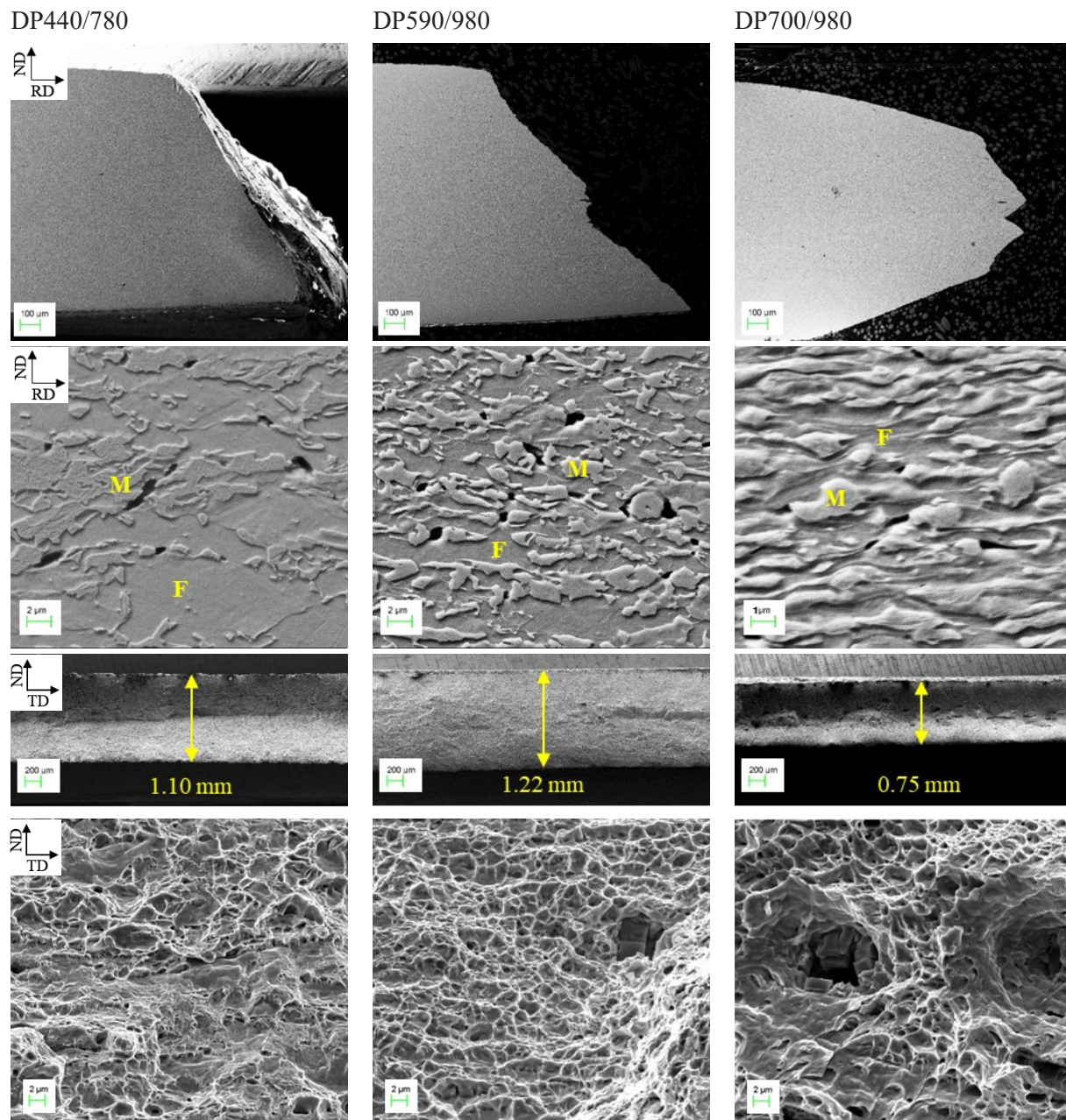


**Figure 8.** SEM micrographs from different views of the fracture site for uniaxial tensile tests.

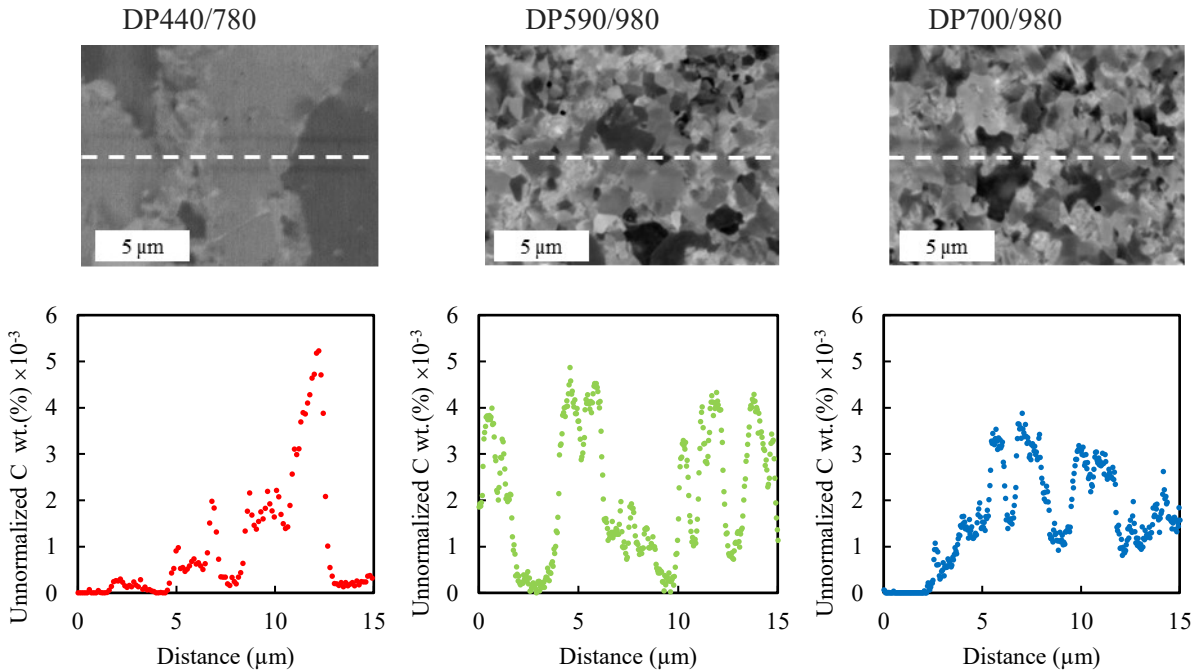


**Figure 9.** The chemical composition, initial microstructure, and phase fraction for the studied materials. The area with zero carbon content represents ferrite grains.

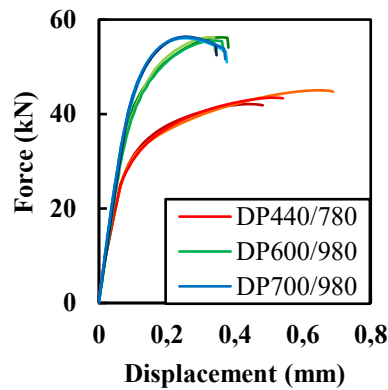


**Figure 10.** Range of scattering data of plane-strain with 7.5 mm grooves for different studied materials, which is very large for DP440/780.

### 3.2 Shear cutting

Shear-cutting induces severe hardening and some damage on the edge as well as the adjacent material, which could drastically reduce the edge formability. To describe accurately the shear-affected zone (SAZ) in simulations, the effects of strain rate and generated adiabatic heating were considered in both plasticity and fracture behaviors. The implementation of strain rate and temperature functions into plasticity was explained before, and the calibrated parameters were extracted from previous works for exactly the same

DP590/980 and DP700/980, Table 3. Although the punching speed was 1 mm/s, which is usually not considered a very fast condition, the simulations showed intermediate strain rates in the deformed zone, Figure 11. The strain rate increased gradually from 2 to 30 1/s before the crack appeared and afterwards rose to over 60 1/s. Consequently, the temperature increased locally up to 450 and 620 K before and right after the crack initiation. Since these loading conditions were different from the tests for calibration of fracture loci, the fracture parameters were recalibrated for shear-cutting using a reverse approach of fitting force-displacement curves. Fortunately, the stress state throughout this process evolves at  $\bar{\theta} \approx 0$  [33]. Therefore, only  $D_3$  and  $D_4$  were required to be adjusted, Table 4. The new loci represented higher fracture strains for an intermediate range of strain rates, Figure 12, as expected from previous reports [35, 36].

**Table 4.** Calibrated parameters for plasticity correction due to strain rate and plasticity, as well as fracture parameters for shear-cutting loading (as dynamic fracture parameters at  $\bar{\theta}=0$ ).

	$c_1^{\dot{\epsilon}^p}$	$c_2^{\dot{\epsilon}^p}$	$c_1^T$	$c_2^T$	$c_3^T$	$D_3^{cut}$	$D_4^{cut}$
DP590/980	0.01 <sup>†</sup>	1.092 <sup>‡,*</sup>	2.2 <sup>†</sup>	0.017 <sup>†</sup>	1.005 <sup>†</sup>	0.75	1.60
DP700/980	0.007 <sup>‡</sup>	1.064 <sup>‡,*</sup>	0.62 <sup>‡</sup>	0.005 <sup>‡</sup>	0.86 <sup>‡</sup>	1.19	1.30

\* In the current formulation with  $\dot{\epsilon}_0^p=0.001 \text{ s}^{-1}$  ( $c_2^{\dot{\epsilon}^p} = 1 - c_1^{\dot{\epsilon}^p} \cdot \ln \dot{\epsilon}_0^p$ ).

<sup>†</sup>Taken from [37], and <sup>‡</sup>taken from [1]

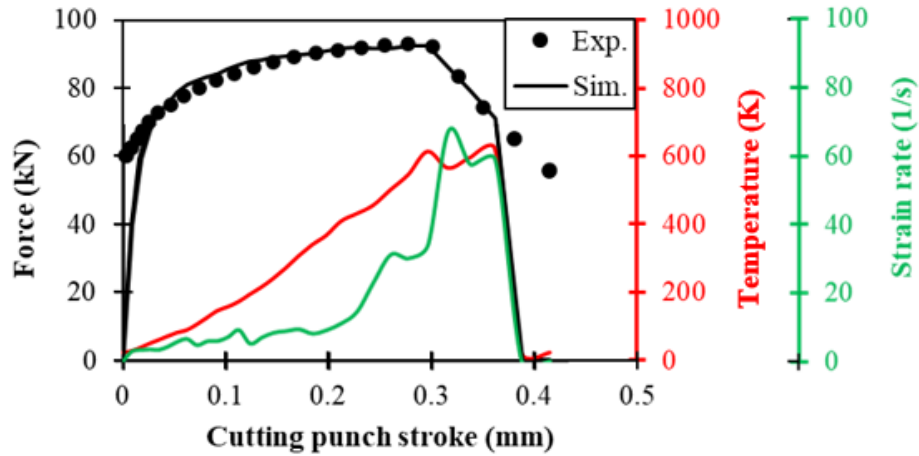


**Figure 11.** Comparison of force displacement between the experiment and simulation for  $\varnothing$  Cutting die of 30 mm and clearance of 13%. The maximum temperature and strain rate throughout the cutting were derived from the simulation.



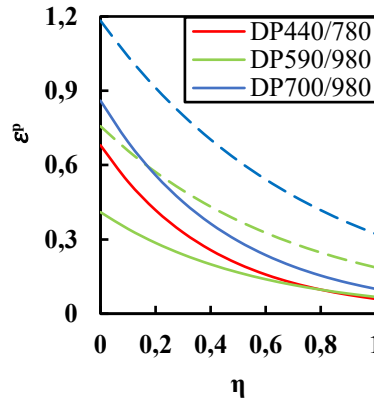


**Figure 12.** Comparison of the calibrated  $D_3$  and  $D_4$  for quasi-static tests (solid lines) and shear-cutting/intermediate speed tests (dashed lines).

The edge characteristics of different conditions for experimental tests are compared with the simulations in Figure 13. The darker figures with dot patterns show the experiment images with black-marked edges and the colorful patterns represent the simulated ones. The colors indicate the distribution of the fracture indicator. Due to the lack of experimental data, simulations were not performed for DP440/780. According to the results, the highest amount of damage concentrated at fracture and burr parts of the edge, because the final separations happened also there. The burr sizes are negligible for all cases. The SAZ size was smaller in smaller hole size as well as smaller clearance. Secondary burnishes were observed in the 10% clearance for all the studied steels. As the crack path was not wide enough to let the crack propagate easily, a second crack appeared to accomplish the cutting [18]. In this case, usually several microcracks form which create rougher surfaces than relatively larger clearances. Since the applied element size was not sufficiently fine, the simulation edges could not perfectly match the experiments. However, the accumulated hardening and damage play the main role in edge cracking during subsequent forming processes [38].

The size of SAZ was also experimentally investigated by measuring the size and distribution of formed microcracks in an area of  $300 \mu\text{m} \times 300 \mu\text{m}$  at the middle of the fracture zone which is marked in Figure 13 with a red square. The experimental void distribution is shown in Figure 14. The larger voids were discovered in lower clearances, which implies the difficulties that the main crack has faced with propagating. It therefore needed a secondary crack to occur. Besides cutting tool conditions, the damage behavior of materials is another contributing factor to the size of SAZ. Figure 14 displays the furthest voids from the cut edge were observed about 90, 75, and  $25 \mu\text{m}$  for DP440/780, DP590/980, and DP700/980, respectively, which could indicate the SAZ size for each material. Furthermore, the void sizes were significantly different for each material. The size of the largest observed void was about 4.2, 1.6, and  $0.65 \mu\text{m}$  for DP440/780, DP590/980, and DP700/980, respectively. Note that the microcracks around the inclusions were not considered. This trend is expected as each steel endured deformation and fracturing differently, as discussed in the previous section. Also, the numerical fracture distribution in Figure 13 illustrates a smaller SAZ for DP700/980.

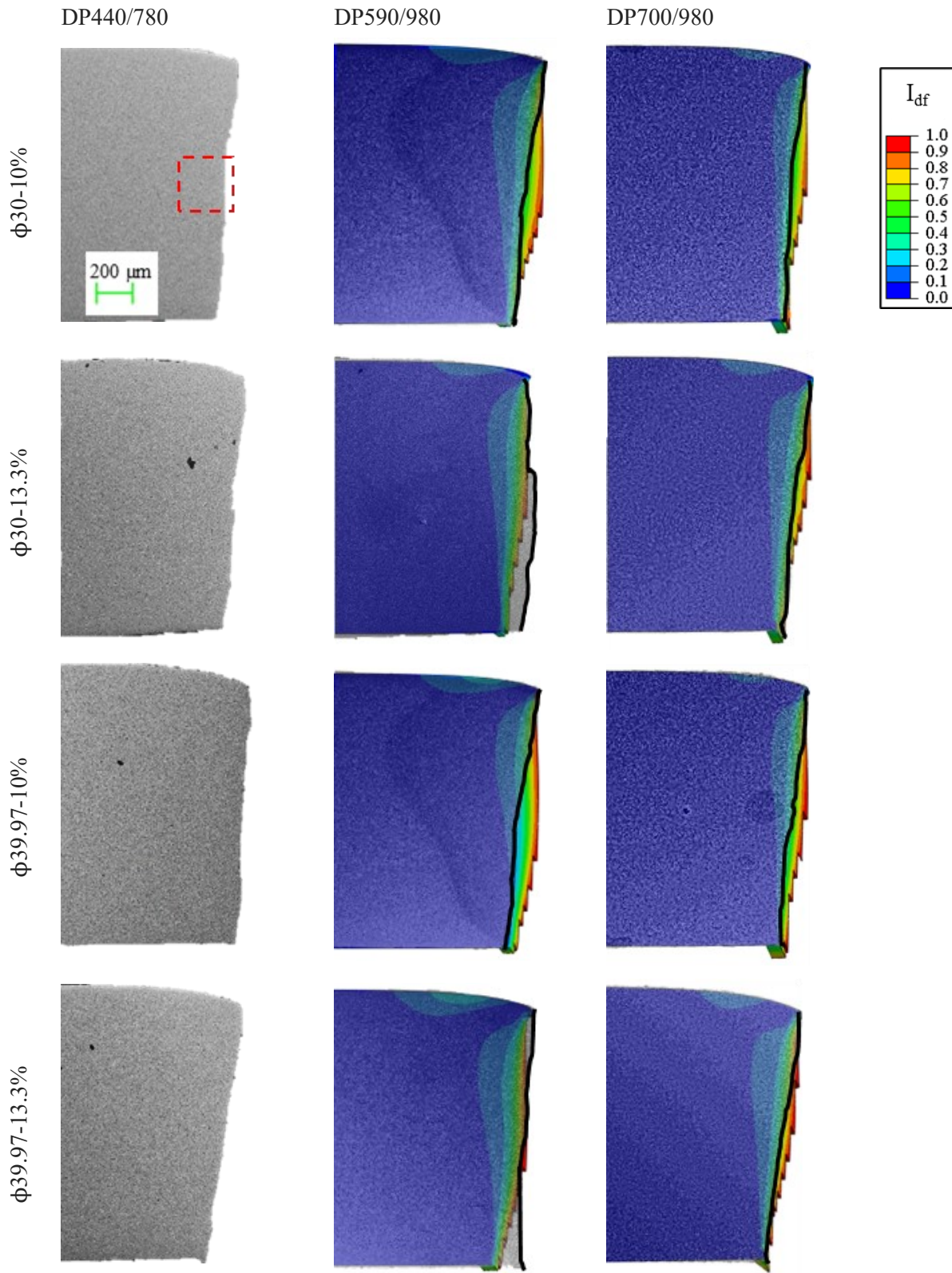


**Figure 13.** Comparison of the cut edge in simulations (colorful pattern of fracture indicator distribution) and experiments (grey background).



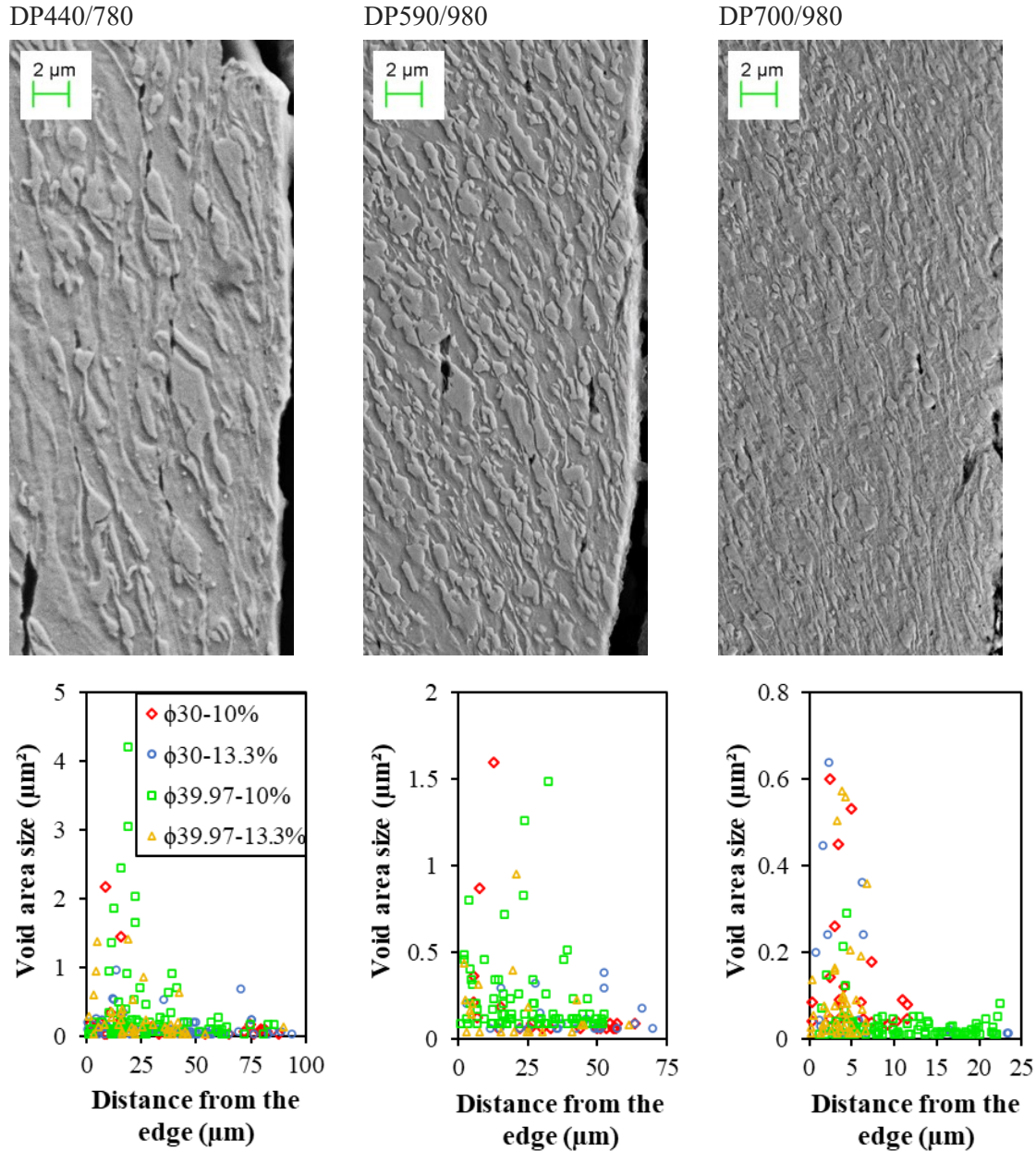


Figure 14. Microcrack formation at the shear cut edge for different cutting conditions.

### 3.3 Hole expansion tests

The hole expansion tests were also performed on both the wire-cut edges and shear-cut edges, by using conical as well as flat-bottom punches. This test is massively employed as a simulative test to quantify the edge crack sensitivity by offering the hole expansion ratio parameter. However, because of differing set-up and forming parameters, the standard HER needs to be reconsidered and it cannot be directly used in production procedures. For instance, according to the definition of hole expansion ratio, Eq. 40, decreasing the initial hole size could increase the HER, which does not necessarily imply that the forming limits are

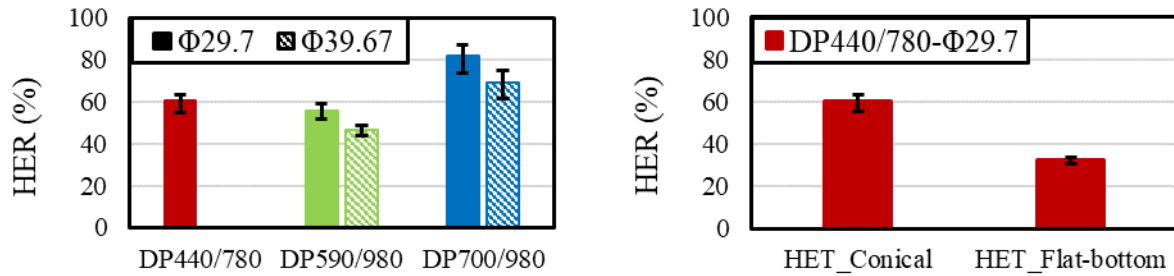
higher in the specific condition. Hence, the HER values are only comparable within one set of tool conditions.

$$HER = \frac{D_h - D_0}{D_0} \times 100 = \left( \frac{D_h}{D_0} - 1 \right) \times 100 \quad \text{Eq. 40}$$

The conventional HER was calculated for each case and plotted in Figures 15 and 16. The key findings are summarized as follows:

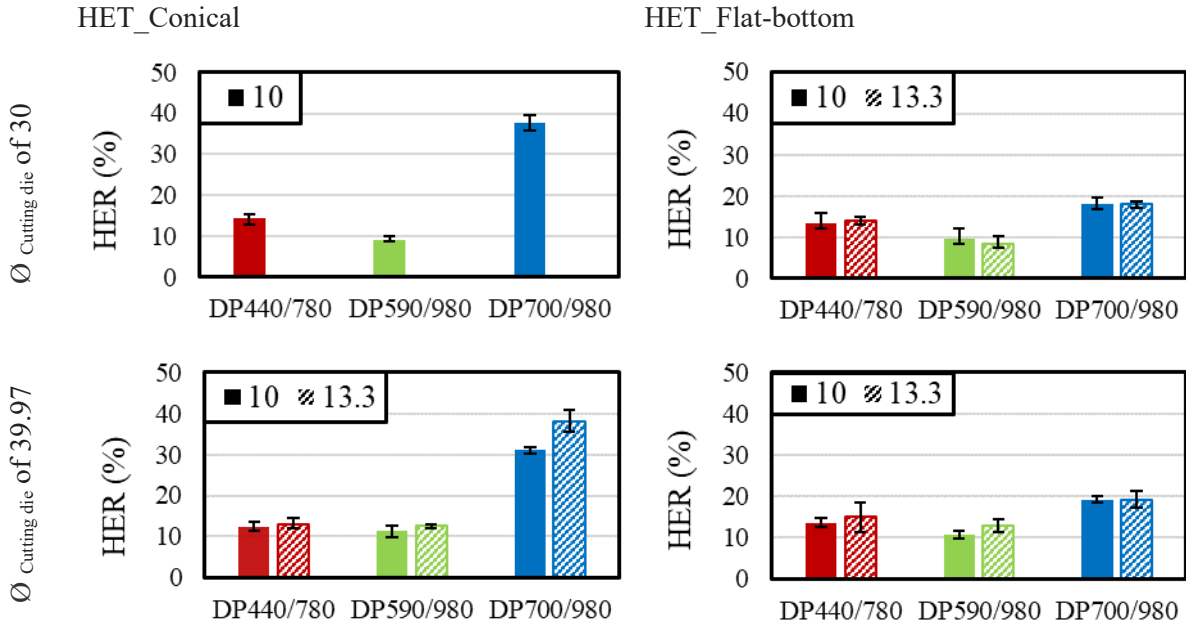
- DP700/980 represented notably higher HERs. HERs for DP440/780 are slightly higher than DP590/980. These responses were predictable based on the different damage behavior of the studied materials.
- The shear-cutting reduced the edge flangeability to even one-quarter in comparison to the wire-cutting technique.
- Applying the higher clearance (13.3%) might cause higher HER. Forming of the secondary burnished part and more microcracks in clearance of 10% led to a rougher surface and lower edge quality.
- The HE Flat-bottom punch could decrease HER significantly; and in the case of DP700/980, HER remained constant, regardless of edge condition.

These phenomena are discussed more elaborately below, assisted by simulation outcomes. Besides employing accurate material modeling and inputs, considering the loading history is crucial in the simulation of complex forming processes. This approach provides in-depth information on the failure happenings.



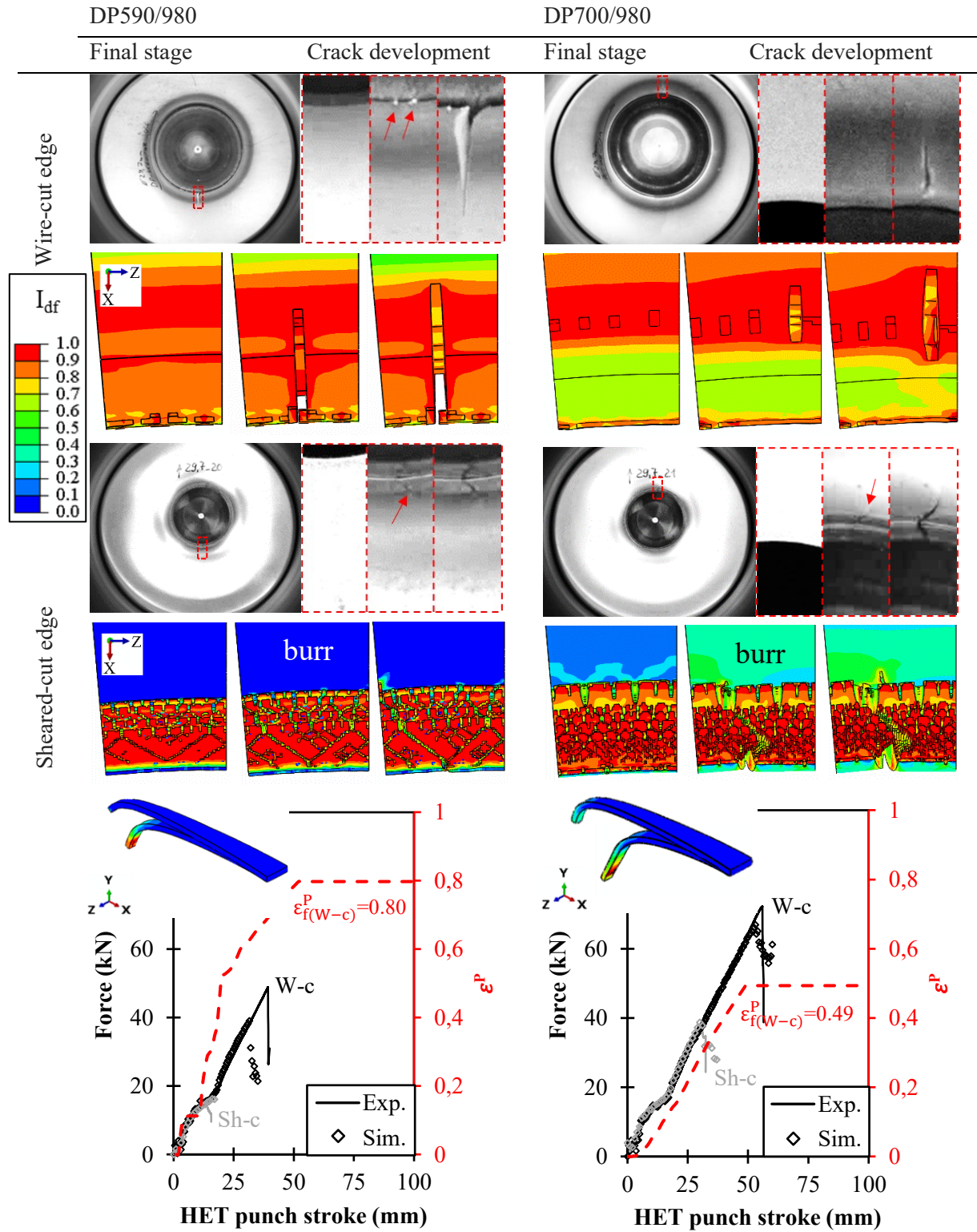
**Figure 15.** The hole expansion ratios of the wire-cut holes for different conditions; (left) for different materials with HET conical punch. (right) with a hole size of 29.7 with a HET flat-bottom punch.

Figure 17 shows the damage evolution during the hole expansion test with a conical punch for four specimens, a combination of two materials (DP590/980 and DP700/980) and two hole-manufacturing processes (wire-cutting or shear-cutting). The initial hole size was 29.7 mm for all the specimens in this figure. It demonstrates good agreement between the simulations and experiments in terms of the force-displacement response and crack initiation site. Since the shear-cut edges underwent higher prior damage, their HE forces dropped significantly earlier than the wire-cut edges. However, it was not the only effect of pre-damage. Figure 17 reveals the crack site also altered and edge cracking was promoted. In other words, for wire-cut edges during the hole expansion test, cracks were initiated for DP590/980 at the edge inner corner (next to the HET punch) and for DP700/980 a bit away from the edge. In contrast, it happened at the outer corner of sheared-cut edges for both materials, where the burr parts with higher residual damage were located.



**Figure 16.** Comparison of hole expansion ratios between different materials, cutting conditions, and hole expansion punches.

The crack initiation site could vary also for different initial hole sizes. Figure 18 shows the results for the wire-cut hole with an initial size of 39.67 mm. For DP700/980, the final crack formed by the initiation of two cracks, from the inner edge like DP590/980, and the other far from the edge. The comparison of force-displacement between different hole sizes, Figures 17 and 18, shows the failure happened earlier for the smaller hole size, although the measured HERs are higher for them in Figure 16. Nevertheless, the derived fracture strains from the first deleted elements were very close, which signifies the formability was not affected by the size of the hole. As suggested in the previous works [21 ,22], a larger strain gradient leads to a delay in localization and exceeds the forming limits. Therefore, the equivalent plastic strains and fracture indicators ( $Idf$ ) were plotted regarding the distance in the radial direction at the frame that a crack initiated, Figure 19. When the value of  $Idf$  reaches the threshold of one, the element is deleted. Surprisingly, the results reveal that the cracks initiated from the same distance from the manufactured edges. In other words, for DP590/980, the crack initiated from the edge likewise the smaller hole. For DP700/980, the failure initiated with a plane-strain necking far from the edge, which triggered the cracking similar to the smaller hole. However, in addition, some edge cracks appeared and were connected to the former one. To disclose the loading conditions of critical sites for each specimen, the stress states were extracted for different elements in terms of stress triaxiality and normalized Lode angle parameter. Also, the damage behavior of the studied materials for each element is displayed in Figure 20, with respect to fracture indicator evolution. It seems the stress state histories are approximately identical for both hole sizes, only proportionally shrank/extended regarding the failure time (= force drop displacement). The steep slope of damage evolution in DP590/980 versus DP700/980, recalls the significant difference in the levels of their fracture strains. Based on the extracted damage evolution, for DP590/980, the edge elements failed earlier than the ones at the contact site with the HET punch.



**Figure 17.** Comparison of damage evolution during hole expansion tests between wire-cut and sheared-cut edges. The initial hole size is 29.7 mm. Also, the plastic strain changes history for the critical elements throughout the HET are plotted.



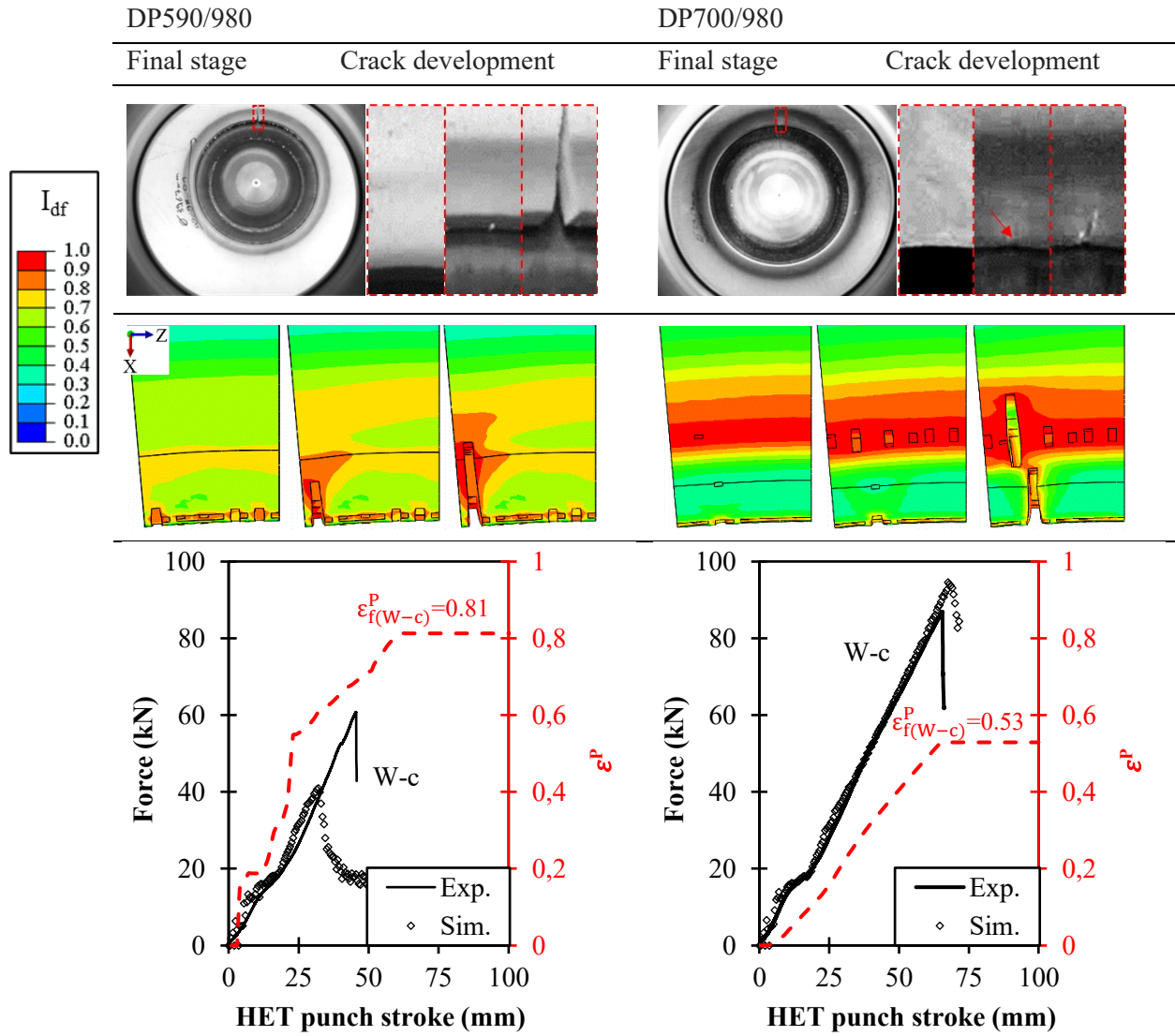


Figure 18. Crack evolution for wire-cut edges of hole size 39.67 mm.

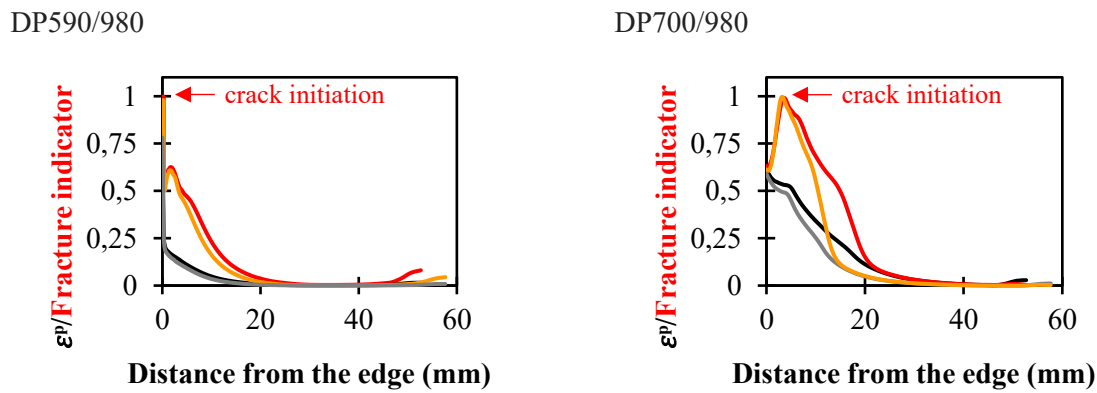
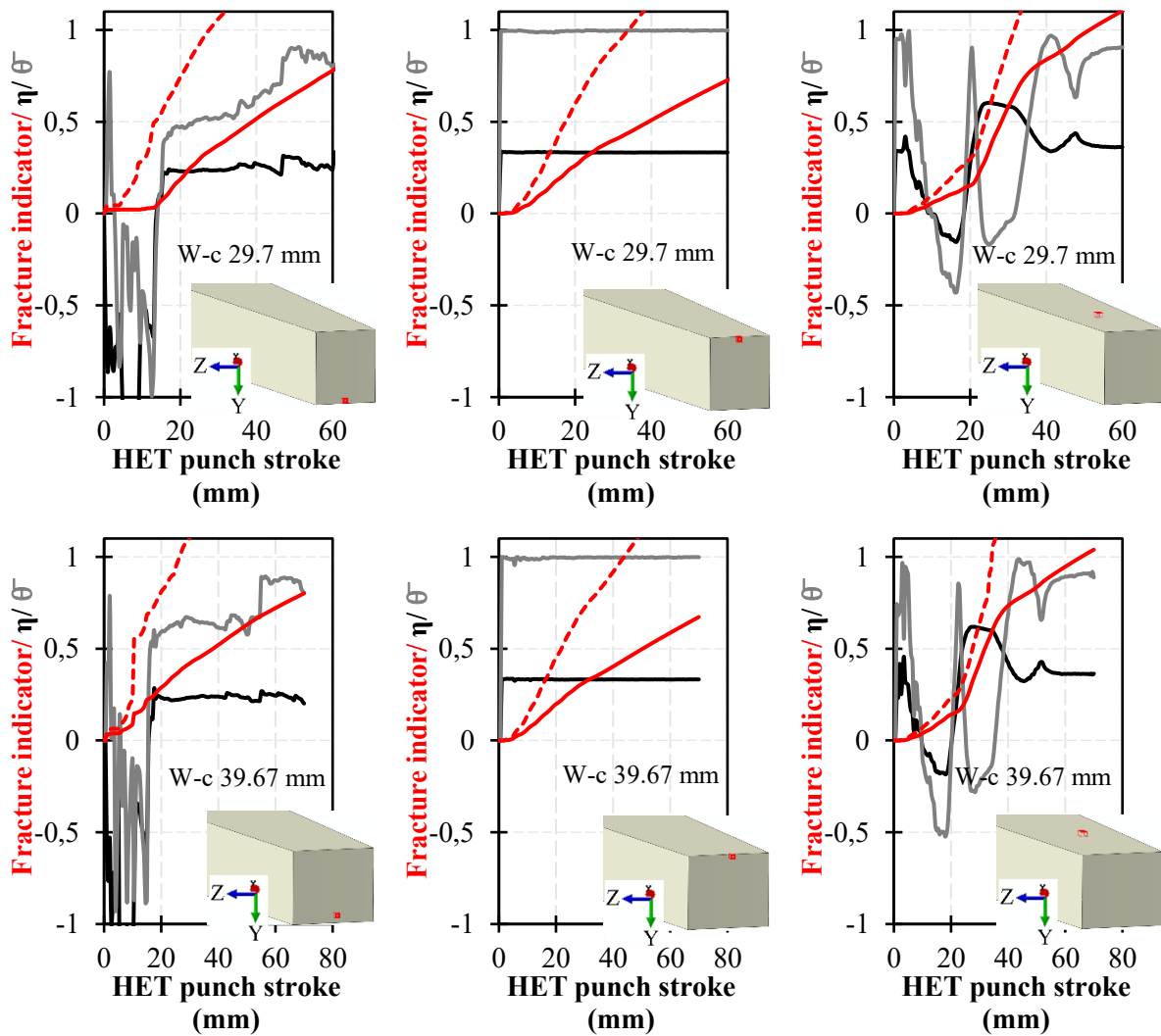
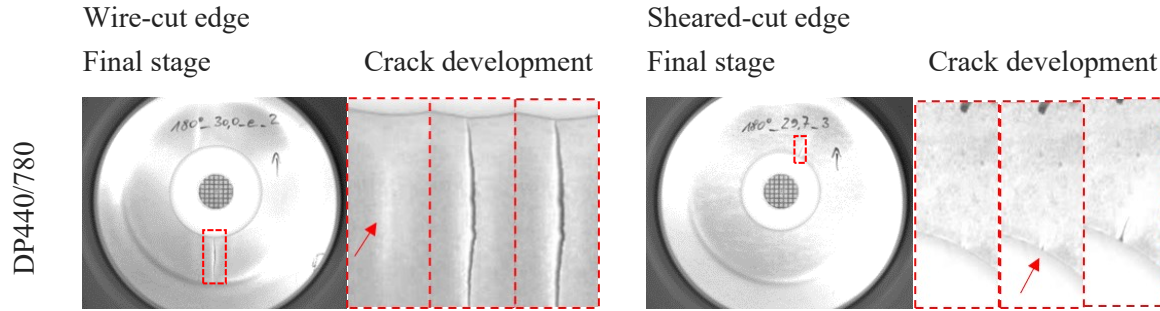


Figure 19. Gradients of strain and fracture indicator for wire-cut holes with different initial sizes, 29.7 mm (lighter colors) and 39.67 mm (darker colors).

Additionally, the shape of the HET punch diversifies damage evolution in the specimens. Although the HER values were strongly diminished in comparison to the results of the conical punch, the formability was only material dependent and remained constant, while only the employed stress states were different. As a reminder, HER values are not comparable for different HET setups. The comparison of crack initiation sites between the sheared-cut and wire-cut edges for DP440/980 shows two critical locations are prone to cracking. One is at the edge and the other one is in the middle of the punch contact area, Figure 21. In case the accumulated damage from the edge manufacturing step is high enough, the crack appears at the edge, which is counted as the edge cracking category. Otherwise, the crack initiates far from the edge. Therefore, edge cracking was observed for DP440/980 with the sheared-cut edge, while plane-strain localization occurred in the specimen with the wire-cut edge.



**Figure 20.** Comparison of stress state and damage evolution for the critical elements during conical HET for DP590/980 (red dashed line) and DP700/980 (red solid line) between the wire-cut holes with sizes of 29.7 mm (first row) and 39.67 mm (second row). Note that the stress states for the same elements but different materials are almost identical here.



**Figure 21.** Crack initiation and propagation during hole expansion of DP440/980 with the flat-bottom punch for wire-cut and sheared-cut holes with a size of 29.7 mm.

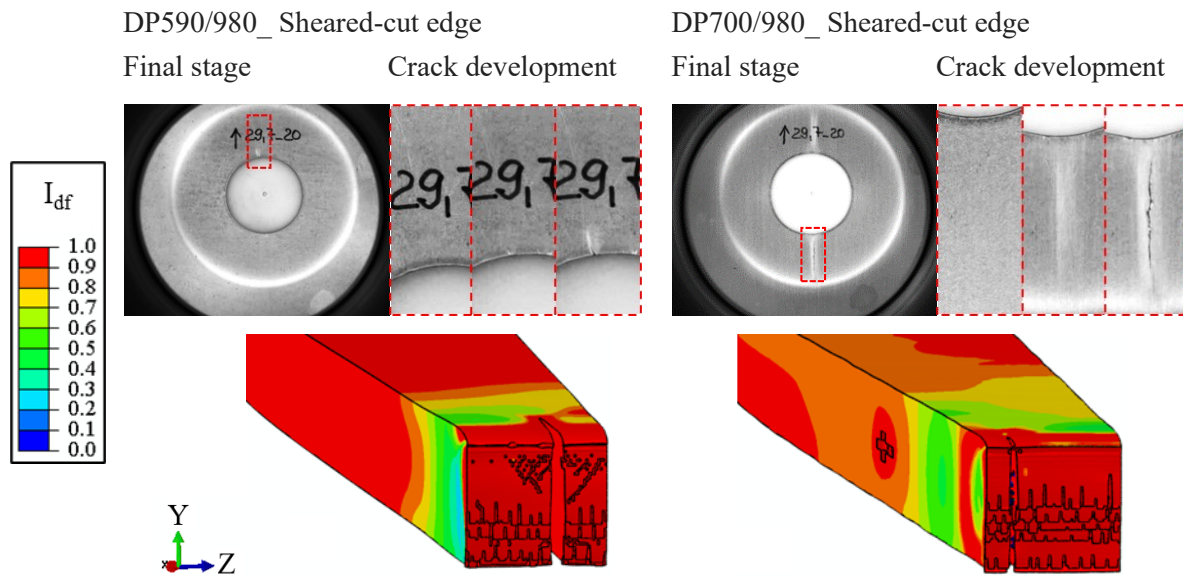


**Figure 22.** Crack initiation and propagation during hole expansion with the flat-bottom punch for sheared-cut holes with the size of 29.7 mm. The simulations are taken from the force drop frame.

Although the HER values for DP440/780 and DP590/980 were slightly different for different sheared-cut edge conditions with HET flat-bottom punches, they remained constant for DP700/980. In fact for this material, although some small cracks were observed at the edge, the main failure was not due to edge cracking, Figure 22. Therefore, the crack sensitivity was not influenced by the edge quality. Tracking the stress state and damage evolution for shear-cut edges during applying the HET flat-bottom punch, Figure 23, shows the uniaxial tension loading ( $\eta \approx 0.33$   $\bar{\Theta} \approx 1.00$ ) at the edge, and the stress state of  $\eta \approx 0.5$   $\bar{\Theta} \approx 0.5$  through the contact area with the punch. The results reveal that the deformation at the edge for DP590/980 is highly sensitive to cracking. Therefore, this material is more sensitive to the effects of edge quality. It should be mentioned, that despite the crack sites being predicted correctly for DP700/980 in the simulations with HET flat-bottom punch, the force drop displacements were quite late, and the predicted HERs were almost double the experimental results. This problem could be solved by defining a much lower fracture strain for  $\eta \approx 0.5$   $\bar{\Theta} \approx 0.5$  versus  $\eta \approx 0.33$   $\bar{\Theta} \approx 1.00$ . Unfortunately, it is not feasible considering the equation of



fracture strains and experimental results for the calibration. In brief, edge manufacturing and further edge forming do not change the intrinsic formability of materials. Only the accumulated damage should be considered throughout the entire production process, which could be easier and more accurate with a proper computer-aided method. Since some DP steels could show high local formability which is not obvious from the experimental assessment of their global formability.

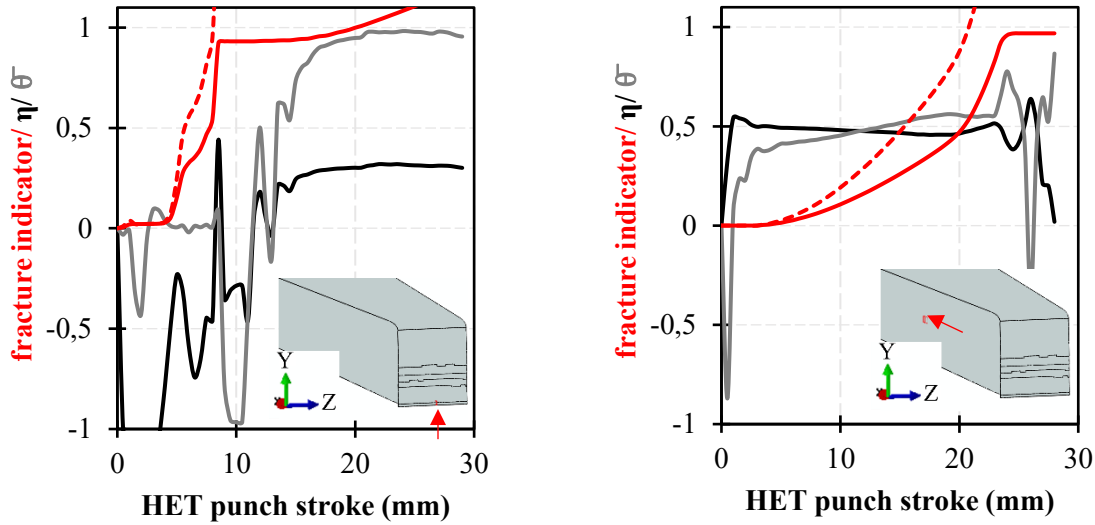


**Figure 23.** Comparison of stress state and damage evolution during flat-bottom HET for the critical elements between DP590/980 (red dashed line) and DP700/980 (red solid line) for the sheared-cut holes with a size of 29.7 mm. Note that the stress states for the same elements but different materials are almost identical here.

## Conclusion

- This study introduces a groundbreaking approach to investigating edge cracking in multi-step forming processes, addressing a gap in traditional experimental methods like HET, which have proven unreliable for evaluating edge crack sensitivity in manufacturing. By employing finite element methods in computer-aided engineering, this research provides a powerful tool for accurately predicting mechanical and failure behaviors of the materials throughout the complex forming processes. The novelty lies in the incorporation of precise material models, such as the YU isotropic-kinematic hardening model coupled with the BW fracture model, which are essential for designing complex forming processes. Additionally, the influence of strain rate, adiabatic heating, and the Bauschinger effect were taken into the account. According to the results, the following conclusions can be drawn:
- 
- The microstructural features impose the deformation distribution throughout the material and facilitate/retard the failure. In brief, a material with more homogenous microstructural and micro-mechanical characteristics represents higher local formability limits. In this work, the void sizes and their distribution throughout the SAZ area as well as the standard HER illustrated approved the important role of microstructure on the damage behavior.

- The YU isotropic-kinematic hardening model coupled with the BW fracture model is a promising approach for designing a complex multi-step forming process. However, it requires cyclic loading for calibration of the YU model and at least 6 different stress states for calibration of BW. The suggested testing techniques in this work satisfied all the requirements.
- In case of rapid fracture after damage initiation, like for studied DP steels, the uncoupled fracture version could still show high accuracy.
- The effects of strain rate and induced adiabatic heating were also considered. Although the speed of the cutting process was quite low (1 mm/s), high strain rates of up to 60 mm/s were observed in the deformed zone, which generated temperatures up to 650 °C at the end. Therefore, using the fracture loci for quasi-static conditions was not feasible, and a second fracture locus was proposed through the shear-cutting process.
- Failure through HE tests is affected by the setup design besides the edge quality.
- Cracking happens when the accumulated damage reaches its threshold, whether at the edge or far from it. Therefore, a comprehensive tool, like the computer-aided method, is required to consider the evolution of the whole component throughout the entire process.

### Declaration of competing interest

The authors declare that they have no known competing financial interests or personal relationships that could have appeared to influence the work reported in this paper.

### CRedit authorship contribution statement

**Niloufar Habibi:** Writing – original draft, Methodology, Data curation, Investigation, Software. **Thorsten Beier:** Resource, Investigation. **Junhe Lian:** Writing – Review & Editing. **Berk Tekkaya:** Writing – Review & Editing. **Markus Koenemann:** Supervision. **Sebastian Muenstermann:** Supervision, Funding acquisition, Writing – Review & Editing.

### Acknowledgement

The authors gratefully acknowledge Dr. Heinrich Traphöner from TU Dortmund for performing in-plane torsion tests. Thanks to Barbara Hoppe for her support in the material modeling script. In addition, the simulations were performed with computing resources granted by RWTH Aachen University under project <rwth0459> and <rwth1234>. Open Access funding enabled and organized by Projekt DEAL.

### References

- [1] W. Liu, J. Lian, S. Münstermann, C. Zeng, X. Fang, *Int. J. Mech. Sci.* **2020**, 176, 105534.
- [2] N. Park, H. Huh, S.J. Lim, Y. Lou, Y.S. Kang, M.H. Seo, *Int. J. Plast.* **2017**, 96, 1.
- [3] C.C. Tasan, M. Diehl, D. Yan, M. Bechtold, F. Roters, L. Schemmann, C. Zheng, N. Peranio, D. Ponge, M. Koyama, *Annu. Rev. Mater. Res.* **2015** 45, 391.
- [4] D. Raabe, B. Sun, A. Da Kwiatkowski Silva, B. Gault, H.-W. Yen, K. Sedighiani, P. Thoudde Sukumar, I.R. Souza Filho, S. Katnagallu, E. Jägle, *Metall. Mater. Trans. A* **2020**, 51, 5517–5586.
- [5] D. Casellas, A. Lara, D. Frómeta, D. Gutiérrez, S. Molas, L. Pérez, J. Rehrl, C. Suppan, *Metall. Mater. Trans. A* **2017**, 48, 86–94.

- [6] S. Heibel, T. Dettinger, W. Nester, T. Clausmeyer, A.E. Tekkaya, *Materials* **2018**, 11, 761.
- [7] M. Schneider, A. Geffert, I. Peshekhodov, A. Bouguecha, B.-A. Behrens, *Mater. Werkstofftech.* **2015**, 46, 1196–1217.
- [8] N. Pathak, C. Butcher, M.J. Worswick, E. Bellhouse, J. Gao, *Materials* **2017**, 10, 346.
- [9] X. Hu, X. Sun, K. Raghavan, R.J. Comstock, Y. Ren, *Mater. Sci. Eng. A* **2020**, 780, 139176.
- [10] N. Habibi, S. Mathi, T. Beier, M. Könemann, S. Münstermann, *Crystals* **2022**, 12, 845.
- [11] W. Cho, B.-S. Jeong, K. Jeong, S.-H. Lee, H. Kim, J. Lee, S.-I. Kim, H.N. Han, *J. Mater. Res. Technol.* **2023**.
- [12] N. Habibi, N. Vajragupta, S. Münstermann, *Crystals* **2021**, 11, 805.
- [13] S. Park, J. Jung, W. Cho, B.-S. Jeong, H. Na, S.-I. Kim, M.-G. Lee, H.N. Han, *Int. J. Plast.* **2021**, 136, 102900.
- [14] K. Wang, M. Luo, T. Wierzbicki, *Int. J. Fract.* **2014**, 187, 245–268.
- [15] A. Ishiwatari, U. Masaki, T. Inazumi, *JFE Tech. Rep.* **2013**, 18, 96–102.
- [16] X.H. Hu, X. Sun, S.F. Golovashchenko, *Finite Elem. Anal. Des.* **2016**, 109, 1–13.
- [17] P. Larour, J. Hinterdorfer, L. Wagner, J. Freudenthaler, A. Grünsteidl, M. Kerschbaum, *AHSS Automot. Grades* **2022**, 1.
- [18] X. Wu, H. Bahmanpour, K. Schmid, *J. Mater. Process. Technol.* **2012**, 212, 1209–1224.
- [19] S. Han, Y. Chang, C.Y. Wang, H. Dong, *J. Mater. Process. Technol.* **2022**, 299, 117377.
- [20] S.K. Paul, *Materialia* **2020**, 9, 100566.
- [21] C. Krempaszky, P. Larour, J. Freudenthaler, E. Werner, *Towards More Efficient Hole Expansion Testing* **2014**.
- [22] E. Iizuka, M. Urabe, Y. Yamasaki, Y. Hiramoto, *AHSS Automot. Grades* **2017**, 1.
- [23] Q. Yin, A.E. Tekkaya, H. Traphöner, *CIRP Ann.* **2015**, 64, 261–264.
- [24] W.S. Farren, G.I. Taylor, *Proc. R. Soc. Lond. A* **1925**, 107, 422–451.
- [25] ISO 16630, *Metallic Materials—Sheet and Strip—Hole Expanding Test* **2017**, ISO-International Organization for Standardization Geneva.
- [26] G.I. Taylor, H. Quinney, *Proc. R. Soc. Lond. A* **1934**, 143, 307–326.
- [27] F. Yoshida, T. Uemori, *Int. J. Plast.* **2002**, 18, 661–686.
- [28] Y. Bai, T. Wierzbicki, *Int. J. Plast.* **2008**, 24, 1071–1096.
- [29] J. Lian, M. Sharaf, F. Archie, S. Münstermann, *Int. J. Damage Mech.* **2013**, 22, 188–218.
- [30] F. Pütz, F. Shen, M. Könemann, S. Münstermann, *Int. J. Fract.* **2020**, 226, 1–15.
- [31] Y. Hou, J. Min, N. Guo, J. Lin, J.E. Carsley, T.B. Stoughton, H. Traphöner, T. Clausmeyer, A.E. Tekkaya, *J. Mater. Process. Technol.* **2021**, 287, 116314.
- [32] K. Wang, L. Greve, T. Wierzbicki, *Int. J. Solids Struct.* **2015**, 71, 206–218.
- [33] N. Habibi, M. Zhou, J. Lian, M. Koenemann, S. Muenstermann, *J. Mater. Process. Technol.* **2023**, 316, 117965.
- [34] F. Kolpak, H. Traphöner, O. Hering, A.E. Tekkaya, *CIRP Ann.* **2021**, 70, 247–250.

- [35] S. Chandran, W. Liu, J. Lian, S. Münstermann, P. Verleysen, *Eur. J. Mech. A Solids* **2022**, 92, 104446.
- [36] I. Pätzold, J. Stahl, R. Golle, W. Volk, *J. Mater. Process. Technol.* **2023**, 313, 117872.
- [37] M.J. Könemann, *Toughness of Cold Formable Steel Sheet*, In Fakultät für Georessourcen und Materialtechnik der Rheinisch-Westfälischen Technischen Hochschule Aachen **2021**, vol. Dr.-Ing. Aachen: RWTH Aachen. <https://doi.org/10.18154/RWTH-2020-12086>.
- [38] N. Habibi, T. Beier, H. Richter, M. Könemann, S. Münstermann, *AHSS Automot. Grades* **2019**, 1.

---

## **Chapter V: Numerical quantification of damage accumulation resulting from blanking in multi-phase steel**

---

**Niloufar Habibi, Felix Pütz, Markus Könemann, Viktoria Brinnel, Sebastian Münstermann, Martin Feistle and Wolfram Volk**

IOP Conf. Series: Materials Science and Engineering 2018, 418 (012058)

<https://doi.org/10.1088/1757-899X/418/1/012058>

### **Highlights:**

- Edge crack sensitivity is studied through Edge-Fracture-Tensile-Test.
- Edge-Fracture-Tensile-Test contains one milled-edge and one shear-cut edge.
- Unlike standard tensile test, cracking initiates from the shear-cut edge instead of the center.
- A phenomenological coupled damage model is successfully used for edge cracking prediction.

## Numerical quantification of damage accumulation resulting from blanking in multi-phase steel

N Habibi<sup>1</sup>, F Pütz<sup>1</sup>, M Könemann<sup>1</sup>, V Brinnel<sup>1</sup>, S Münstermann<sup>1</sup>, M Feistle<sup>2</sup> and W Volk<sup>2</sup>

<sup>1</sup> Steel Institute, RWTH-Aachen University, Germany

<sup>2</sup> Institute of Metal Forming and Casting, Technische Universität München, Germany

niloufar.habibi@iehk.rwth-aachen.de

**Abstract.** The high potentials of utilizing high strength steels in the automotive industry have been proved. However, there are still some unsolved challenges. Forming of a component that has been produced by blanking is one of these. Blanking is commonly used in sheet metal forming as the initial cutting process. Yet, it introduces damage into the blanked edges that in subsequent forming steps may lead to crack formation. This problem arises in particular in modern multi-phase steels and can currently not be avoided thoroughly due to a lack of understanding of the relevant influences. In the present work, the effects of the blanking process on an HCT980XD sheet were therefore numerically investigated. To achieve this, the *Edge-Fracture-Tensile-Test* method was simulated. By using this method, a conventional uniaxial tensile specimen is manufactured with one milled side and one blanked side. This allows to highlight the effect of blanking in a subsequent tensile test. In order to investigate the damage process, the coupled Modified-Bai-Wierzbicki model was applied to simulate first the blanking process and then the tensile test. The results revealed that during the blanking process, the failure initiated from the surface elements near the punch and propagated through the thickness. Meanwhile, another crack initiated from the opposite side of the sheet. The elements of these cracks experienced near pure-shear condition at both damage initiation and fracture moments. At the end of this step, the remaining damage, which is considered as the predamage of the next step, was higher in the middle of thickness. During the subsequent uniaxial tension, the crack in the specimen initiated at a shear cut edge and crossed the width. The possible detailed resolution of loading paths and crack formation shows that the damage mechanics simulation provides researchers with a powerful tool for assessing limit states in forming processes.

### 1. Introduction

High Strength Steel (HSS) sheets are widely used in automotive industries. They mostly undergo several complicated forming processes to obtain their final shape. Blanking is a common forming process which is used for the initial cutting. This process imposes some adverse effects on the shear cut edge, which become profound during the subsequent forming processes. Some materials like multi-phase steels are more sensitive to edge properties and blanking may result in formation of premature cracks in their edge [1]. These induce component failure during the forming process ahead of the expected forming limits, which are determined by the conventional methods.

Prediction of forming limits especially by using computer-aided engineering method is highly beneficial for increasing productivity by reducing cost and effort of production design and improving its accuracy. There are few experimental testing techniques, which have been so far proposed to measure edge crack sensitivity. The most common one is the Hole Expansion Test (HET) which has been widely used for HSS

sheets [2-4]. However, only a few numerical studies have been conducted on the edge crack sensitivity through HET [5], especially by considering the cutting impacts [6-9]. Sartkulvanich et al. [7] illustrated how metal flow, strains and stresses in cutting affect edge cracking through the following stretch flanging by using 2D finite element method and a simple uncoupled damage model. However the simulation and experimental results showed good agreement with each other, applying 3D model along with a simple uncoupled damage model (critical plastic strain at fracture) can describe the localized edge cracking more precisely. Hu et al [8] predicted the effect of cut conditions on hole expansion ratio of an aluminum alloy using 3D finite element method. The results showed that by increasing the clearance, accuracy of the predictions decreased. They also predicted tensile stretchability for the same material by implementing Rice-Tracey uncoupled damage model [9]. They showed that the prediction was not accurate for clearance more than 10%.

Recently a promising experimental method has been developed by the Chair of Metal Forming and Casting of the Technical University of Munich, called *Edge-Fracture-Tensile-Test* (EFTT). In this method, influences of the blanking process on the formability of the shear cut edge are investigated by manufacturing a conventional uniaxial tensile specimen which contains a milled side and an edge cut side. Figure 1 illustrates the manufacturing steps of an EFTT specimen. This testing technique represents several advantages, for instance providing a frictionless medium, avoiding any strain gradients ahead of local necking, offering a convenient study on the shear cut edge, and showing a high reproducibility [10, 11]. These characteristics make this method a favorable model for numerical investigations, however no attempts have been made in this regard yet. Hence, the objective of the present work is to study EFTT process numerically and assess the accuracy of results by comparing with the experiments.

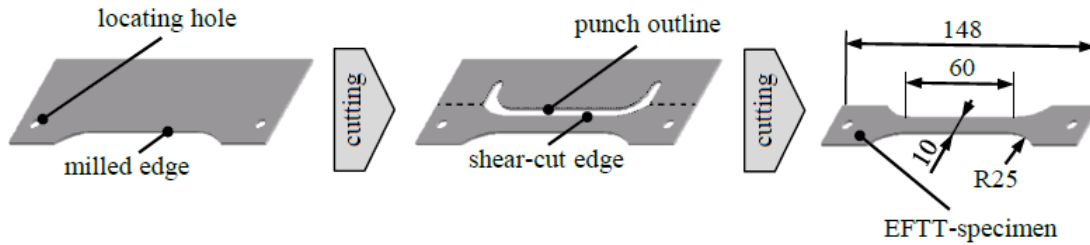


**Figure 1.** Manufacturing process of a blanked EFTT specimen with a closed cutting lines [12].

## 2. Methods

### 2.1 Plasticity model

In order to describe the material's behavior in the simulations, a plasticity-damage model was employed based on a combined experimental and numerical approach. In this regard, the Modified-Bai-Wierzbicki (MBW) damage mechanics model, presented by Wu et al. [13], was applied and the damage parameters for different stress states were determined. In this plasticity model, equation (1), damage appears as strain-softening in the material behavior.

$$\Phi = \sigma_e - (1 - D)\sigma_{yld} \leq 0 \quad (1)$$



Herein,  $\Phi$  is flow potential,  $\sigma_e$  is equivalent stress,  $\sigma_{yld}$  is yield stress, and  $D$  is ductile damage variable. According to the damage model, equation (2), the initial material is assumed to be defect-free and only strain-hardening contributes to the deformation. The damage initiates when equivalent plastic strain,  $\bar{\epsilon}^p$ , reaches a threshold value,  $\bar{\epsilon}^i$  as defined in equation (3). Afterwards, the damage evolves until the fracture occurs at equivalent plastic strain of  $\bar{\epsilon}^f$ , which is fulfilled by equation (4). It is worth mentioning that the damage model is defined in terms of stress-triaxiality,  $\eta$ , and normalized Lode angle parameter,  $\bar{\theta}$ , to describe stress state of the material during the deformation. Note that all  $C_i$  and  $D_i$  parameters are materials' constants.

$$D = \begin{cases} 0, & \bar{\epsilon}^p \leq \bar{\epsilon}^i \\ \frac{\sigma_{y,i}}{G_f} \int_{\bar{\epsilon}^i}^{\bar{\epsilon}^p} d\bar{\epsilon}^p & \bar{\epsilon}^i < \bar{\epsilon}^p < \bar{\epsilon}^f \\ D_{crit} & \bar{\epsilon}^f < \bar{\epsilon}^p \end{cases} \quad (2)$$

$$\bar{\epsilon}^i = (C_1 e^{-C_2 \eta} - C_3 e^{-C_4 \eta}) \bar{\theta}^2 + C_3 e^{-C_4 \eta} \quad (3)$$

$$\int_{\bar{\epsilon}^i}^{\bar{\epsilon}^f} \frac{dD}{(D_1 e^{-D_2 \eta} - D_3 e^{-D_4 \eta}) \bar{\theta}^2 + D_3 e^{-D_4 \eta}} = 1 \quad (4)$$

## 2.2 Material and parameter identification

Dual-phase HCT980XD steel sheets, DP1000 according to DIN EN 10346, were received with the thickness of 1.5 mm. Its mechanical properties were evaluated through different uniaxial loading conditions along with ARAMIS digital image correlation (DIC) analysis. The hardening parameters were calculated directly by fitting Hollomon model (equation (5)) on the homogenous plastic part of the flow curve, which was extracted from the results of uniaxial tensile tests. The damage parameters were calibrated using an inverse strategy, i.e. parameters were determined by minimizing the difference between experimental and simulation results, here particularly the results of force displacement were considered. Since MBW parameters are non-unique, a wide range of stress states should be examined to calculate the parameters properly. Therefore, notched dog bone, plane-strain, central hole, and shear specimens were tested along with the parallel numerical simulations using finite-element software Abaqus/Explicit 2017, figure 2 and 3. In all the simulations, eight-node reduced-integration solid elements of type C3D8R were employed. In order to minimize the computational time, a mesh size of 0.1 mm was applied only on those regions of samples which are exposed higher plastic straining. The material parameters are summarized in table 1.

**Table 1.** Mechanical properties of the investigated material.

Parameter	$E$ (GPa)		$\nu$	$R_{p0.2}$ (MPa)		$k$ (MPa)		$n_H$	
Value	210		0.3	693		1476		0.10	
Regime	Elastic			Plastic					
Identification	Direct								
Parameter	$C_1$	$C_2$	$C_3$	$C_4$	$G_f$	$D_1$	$D_2$	$D_3$	$D_4$
Value	0.4	1	0.1	1.5	6500	0.15	1.5	0.08	1.5
Regime	Damage initiation				Damage propagation	Fracture			
Identification	Inverse								

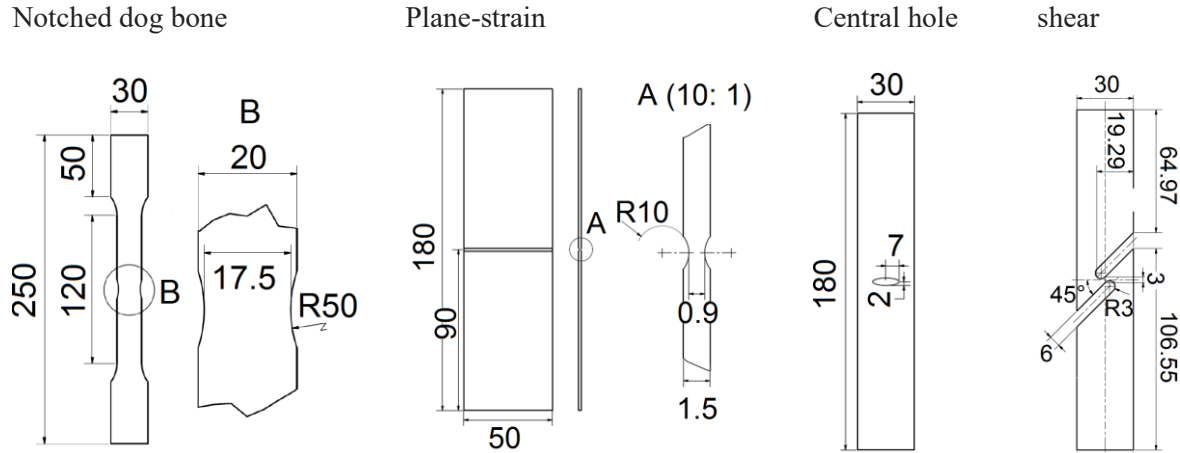


**Figure 2.** The geometries of different specimens (all dimensions are in mm).

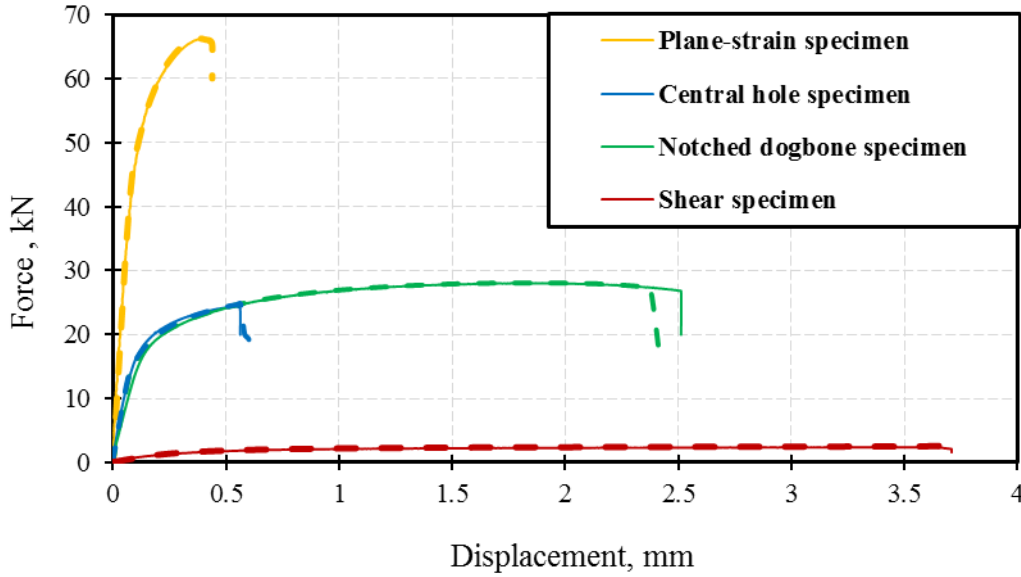


**Figure 3.** The force-displacement curves of experiments (solid lines) and simulations (dashed lines).

$$\sigma_e = k \cdot (\bar{\varepsilon}^p)^{n_H} \quad (5)$$

### 2.3 Simulation of Edge-Fracture-Tensile-Test

The numerical simulations of a two-stage *Edge-Fracture-Tensile-Test* were performed for a set-up with sharp cutting edges tool (edge radii of 0.05 mm) and a die clearance of 15%. In order to reduce the computation time, only half of the symmetric model was modeled, figure 4. In the blanking process, the die, punch, and blank holder were considered as discrete rigid parts, and the sheet was modeled as a deformable homogenous solid. Friction between the tools and the sheet was considered as the Coulomb model with a coefficient of 0.1 [9]. The contact pairs were defined as a surface-to-surface algorithm. However, the contacts between new surfaces which are created during blanking process and the tool were

defined as a node-to-surface algorithm. Since the applied damage model is a local model and influenced by the mesh size, mesh size of 0.1 mm was used in the critical regions of the sheet like the models which were used for the parameter calibration. In order to apply homogenous force on the sheet during the blanking process, finer elements were defined in the contact regions of the tool. An optimal clamping force was chosen such that the blank was neither drew in nor torn improperly during the blanking process. For the second stage, the tensile test on the produced sample, the unnecessary parts of the sheet were deleted and uniaxial tension was quasi-statically employed on the gauge length to assess the effect of the blanked edge on the formability of the material.

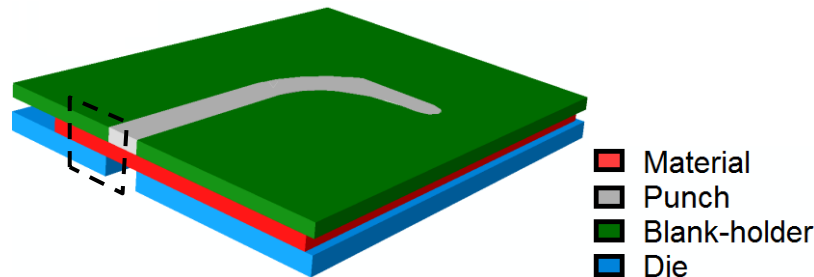


**Figure 4.** The assembly model of half Edge-fracture-tensile test for the blanking stage.

#### 2.4 EFTT process: Blanking stage

Blanking is the first stage of EFTT process. Through this stage, the blanked edge of the tensile specimen is manufactured. The gradual formation of the blanked edge is shown in figure 5, in terms of stress-triaxiality and Normalized Lode-angle parameter, i.e. the stress-state. Moreover, the geometrical features of the edge, which are created during the blanking process, are shown in figure 6. By penetration of the punch through the material, an elastic deformation began and turned into a plastic deformation. When the equivalent plastic strain reached the critical value, damage occurred. Up to this moment, the imposed elements experienced shear stress-state, since both  $\eta$  and  $\bar{\eta}$  are about 0, figure 5(a). The stress-state remained in near shear mode while the damage propagated through the material and accumulated, figure 5(b). Up to a crack initiated, the upper area was exposed bending effects. This area is called rollover [14].

The crack initiated from the element in adjacent to the punch and grew towards the direction of cutting, figure 5(c). Meanwhile, a second crack initiated from the other side of the thickness and grew upwards, figure 5(d). The formation of the second crack prevented the burr surface from expanding. The stress-state from crack initiation until the entire separation changed from pure-shear mode to plane-strain state [14]. The new surface which was created under pure shearing is called clean-shear. The rest of new surface is called fracture surface.

#### 2.5 EFTT process: Tension stage

The manufactured EFTT specimen undergoes uniaxial tensile test in the second stage. The specimen is expected to fail earlier than a uniaxial tensile specimen which is manufactured by milling process in both sides [12]. Results of the simulation are compared with experimental data in figures 7 and 8, which imply that the simulation approach was quite reliable.

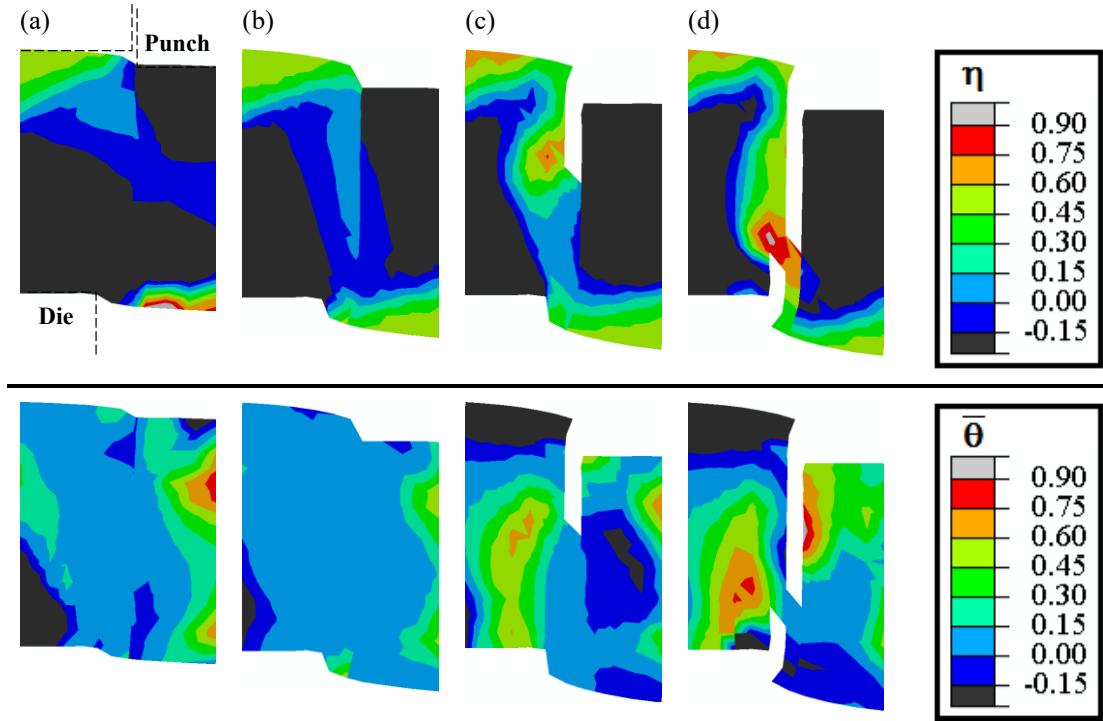


**Figure 5.** The stress state, in terms of stress-triaxiality and normalized Lode angle parameter, in different steps of blanking process (the figures were captured from the view, which was shown in figure 4 by a black dashed rectangular). The frames before the damage initiation, the crack initiation, the second crack initiation, and the material's final separation are shown in (a) to (d), respectively.

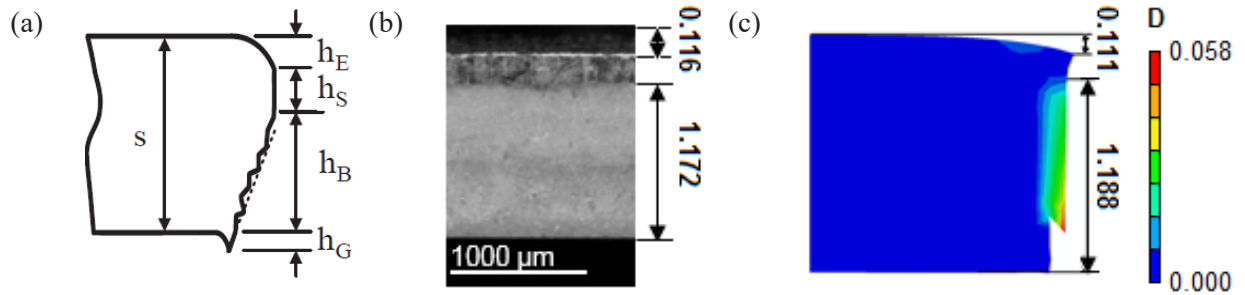


**Figure 6.** The blanked surface characteristics (a)  $h_E$ ,  $h_S$ ,  $h_B$ ,  $h_G$  represent height of rollover, cleanshear, fracture, and burr parts, respectively [14].  $S$  is the initial thickness of sheet; (b) the experimental data which was measured with accuracy of  $1.0 \mu\text{m}$  [10]; and (c) the simulation results in terms of damage parameter (all dimensions are in mm).

The effect of predamage is obvious in figure 8, which shows that damage initiated from the blanked edge. First, the crack propagated a little bit diagonally, then soon it grew perpendicularly to the loading direction and crossed the specimen. The same trend can be seen in the experiments as well. The experimental values of  $\epsilon_1$  which were taken by DIC are slightly higher than the simulation's values, as the DIC method is less

sensitive and accurate in comparison to the simulations. In brief, the location and moment of fracture are predicted precisely by this method. Figure 9 illustrates that the damage and fracture initiated from the part of thickness which underwent the highest residual damage from the cutting process, i.e. the transition part of fracture to burr. Multiple cracks initiated along the shear cut edge during the *Edge-Fracture-Tensile-Test*.

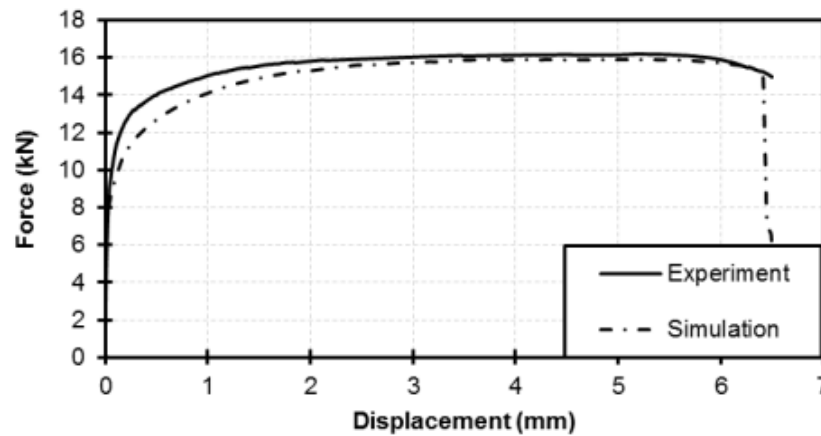


**Figure 7.** The comparison between *Edge-Fracture-Tensile-Test* results for experiment and simulation.

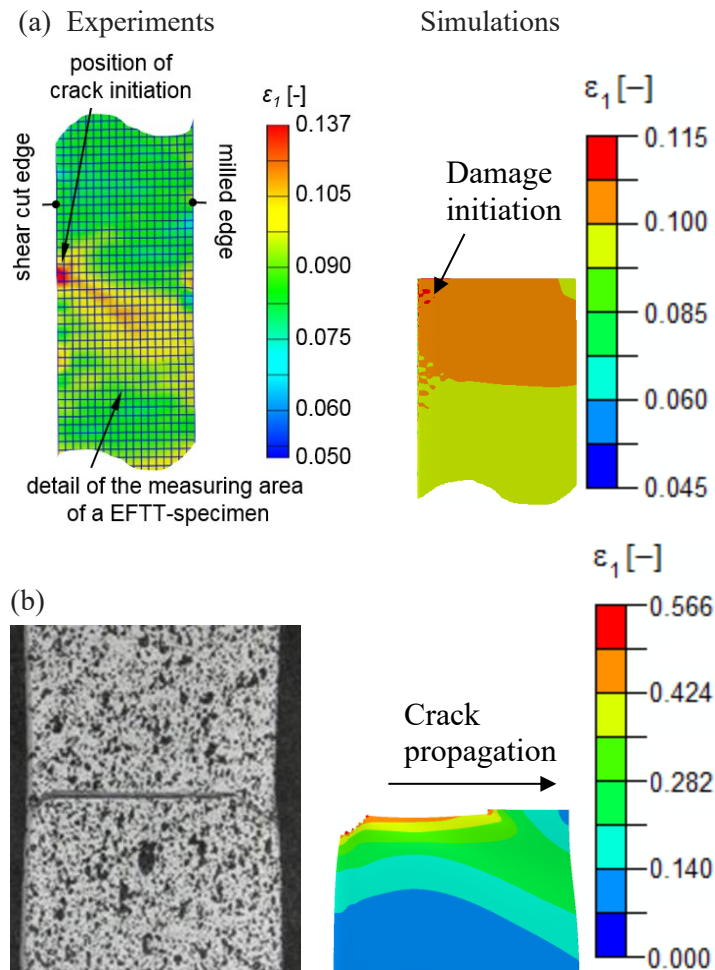


**Figure 8.** The comparison between experimental and simulation results of (a) damage initiation, and (b) fracture.

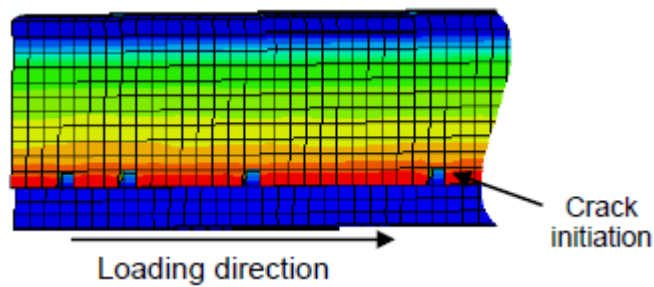


**Figure 9.** The view of EFTT specimen along the cut edge implies that the cracks initiated at the transition part from the fracture to the burr during the subsequent tensile test.

### 3. Conclusion

The presented study introduces a promising numerical tool for assessing the influences of the blanking process on formability of a component through *Edge-Fracture-Tensile-Test*. The important findings of this work are summarized below.

- The simulation of the blanking process by using MBW plasticity model provided detailed information of material's stress-state during the whole process. It showed that the damage and fracture initiated in the near shear state and changed gradually to the plane-strain mode until ultimate separation happened.
- The geometry features of the blanked edge, including rollover, clean-shear, fracture, and burr, were properly calculated by the simulation.
- The simulation of the subsequent uniaxial tensile test was able to predict the force displacement curve and the damage behavior of the EFTT specimen in terms of location and moment of the damage.
- This numerical method along with MBW model could acquaint researchers with sound data of edge crack sensitivity which is one of the serious challenges of producing complicated components from HSSs.

### Acknowledgement

The authors would like to thank Dr. Bo Wu from IWM institute of RWTH-Aachen University for his kind contribution.

### Reference

- [1] Naserlahkami S, Golovashchenko S, Pan K, Brown L and Gugnani B 2016 SAE Int. 2016-01-0358
- [2] Hasegawa K, Kawamura K, Urabe T and Hosoya Y 2004 ISIJ Int. 44 603
- [3] Casellas D, Lara A, Frómeta D, Gutiérrez D, Molas S, Pérez L, Rehrl J and Suppan C 2017 Metall. Mater. Trans. A 48 86
- [4] Karelova A, Krempaszky C, Werner E, Tsiouridis P, Hebseberger T and Pichler A 2009 Steel Res. Int. 80 71
- [5] Wang K, Luo M and Wierzbicki T 2014 Int. J. Fracture 187 245
- [6] Wang K, Greve L and Wierzbicki T 2015 Int. J. Solids. Struct. 71 206

- [7] Sartkulvanich P, Kroenauer B, Golle R, Konieczny A, Altan T 2010 CIRP Annals – Manufact. Tech. 59 279
- [8] Hu X, Sun X and Golovashchenko S 2016 FE Anal.Des. 109 1
- [9] Hu X, Sun X and Golovashchenko S 2014 Comput. Mater. Sci. 85 409
- [10] Feistle M, Golle R and Volk W 2016 Procedia CIRP 41 1078
- [11] Feistle M, Krinninger M, Paetzold I, Stahl J, Golle R and Volk W 2017 J. Phys.: Conf. Ser.(Munich) vol 896 (IOP Science) p 012106
- [12] Feistle M, Krinninger M, Pätzold I and Volk W 2015 Edge-fracture-tensile-test 60 Excellenct Invention in Metal Forming ed Tekkaya A et al (Berlin, Heidelberg: Springer Berlin Heidelberg) pp 193-198
- [13] Wu B, Li X, Di Y, Brinnel V, Lian J and Münstermann S 2017 Fatigue Fract. Eng. Mate. Struct. 40 2152
- [14] N N 1994 Quality of cut faces of (sheet) metal parts after cutting, blanking, trimming or piercing, shearing form of sheared edge and characteristic values Association of Engineers (Berlin: Beuth Verlag GmbH) VDI 2906-2
- [15] Gutknecht F, Steinbach F, Hammer T, Clausmeyer T, Volk W and Tekkaya A E 2016 Procedia S truct. Integ. 2 1700



---

## **Chapter VI: Deformation and damage assessments of two DP1000 steels using a micromechanical modelling method**

---

**Niloufar Habibi, Napat Vajragupta and Sebastian Münstermann**

Crystals 2021, 11(7), 805

<https://doi.org/10.3390/cryst11070805>

### **Highlights:**

- Local deformation and damage evolution of two DP1000 steels were investigated using a micromechanical modelling approach.
- Representative microstructural and micro-mechanical features of individual phases were driven from SEM, EBSD, and nano-indentation tests.
- A crystal plasticity parameter calibration procedure for each material was developed and the maximum shear stress criterion was employed as damage initiation definition.
- More homogenous microstructural and micromechanical properties led the material to endure more deformation and damage later.
- The results showed good agreement with the edge crack sensitivity of the studied materials.

## Deformation and damage assessments of two DP1000 steels using a micromechanical modelling method

Niloufar Habibi<sup>1</sup>, Napat Vajragupta<sup>2</sup> and Sebastian Münstermann<sup>1</sup>

<sup>1</sup> Integrity of Materials and Structures, Steel Institute, RWTH Aachen University, Intzestr. 1, 52072 Aachen, Germany; niloufar.habibi@iehk.rwth-aachen.de; sebastian.muenstermann@iehk.rwth-aachen.de

<sup>2</sup> Interdisciplinary Center for Advanced Materials Simulation (ICAMS), Ruhr-Universität Bochum, Universitätsstr. 150, 44801, Bochum, Germany; napat.vajragupta@rub.de

\*niloufar.habibi@iehk.rwth-aachen.de

**Abstract:** Damage characterization and micromechanical modelling in dual-phase (DP) steels have recently drawn attention, since any changes in the alloying elements or process route strongly influence the microstructural features, deformation behavior of the phases, and damage to the micro-mechanisms, and subsequently the particular mechanical properties of the material. This approach can be used to establish microstructure–properties relationships. For instance, the effects of local damage from shear cutting on edge crack sensitivity in the following deformation process can be studied. This work evaluated the deformation and damage behaviors of two DP1000 steels using a microstructure-based approach to estimate the edge cracking resistance. Phase fraction, grain size, phase distribution, and texture were analyzed using electron backscatter diffraction and secondary electron detectors of a scanning electron microscope and employed in 3D representative volume elements. The deformation behavior of the ferrite phase was defined using a crystal plasticity model, which was calibrated through nanoindentation tests. Various loading conditions, including uniaxial tension, equi-biaxial tension, plane strain tension, and shearing, along with the maximum shear stress criterion were applied to investigate the damage initiation and describe the edge cracking sensitivity of the studied steels. The results revealed that a homogenous microstructure leads to homogenous stress–strain partitioning, delayed damage initiation, and high edge cracking resistance.

**Keywords:** micromechanical modelling; representative volume element; dual-phase steel; damage; edge cracking

### 1. Introduction

Dual-phase steels (DP steels) have been progressively used in automotive structural applications, since they exhibit a good combination of strength and formability. These outstanding properties originate from the microstructure, where hard martensite islands are dispersed within a soft ferritic matrix. Nevertheless, their sensitivity to edge cracking still remains a challenge and hinders their wide application in complex parts [1–4].

Edge cracking appears mostly in advanced high-strength steels during the forming processes as premature cracks initiated at blanked, pierced, or trimmed edges, which cannot be predicted by conventional forming limit strains. During these processes, the sheared edge and shear-affected zone are exposed to severe plastic deformation, leading to damage onset [5–7]. Therefore, a thorough understanding of the effects of microstructural features on local mechanical and damage behaviors are highly required. However, this could be very complicated for multiphase materials, of which complex microstructures with particular characteristics can be produced by altering the chemical composition and manufacturing process. Phase

fractions, phase distributions, grain sizes, and mechanical properties of individual phases strongly influence the strain localization process and general damage behavior of the material [8–11]. Although several studies have been carried out to investigate the microstructural deformation and fracture micromechanisms in DP steels [12–15], only few of them correlated the findings with edge crack sensitivity [16,17], especially by using micromechanical modelling [18].

Therefore, the present work aimed to bridge the microstructural features of DP steels to the macroscale mechanical and damage responses of the materials, in order to estimate their edge formability potential. For this purpose, representative volume elements (RVEs) were generated according to the microstructural characteristics, which were obtained by the electron backscatter diffraction (EBSD) method, and the micromechanical behavior of the individual phases assessed by applying the nanoindentation technique along with crystal plasticity (CP) modelling. Finally, damage initiation was predicted through various strain paths, which can happen during shear cutting and hole expansion processes. Herein, the maximum shear stress fracture criterion was used for damage prediction.

## 2. Materials and Methods

This section describes the geometrical algorithm needed for generating a 3D representative synthetic microstructure in detail, and a method for providing the appropriate microstructural and micromechanical properties as the algorithm inputs.

### 2.1. 3D Artificial Microstructure Modelling Method

In order to construct representative microstructure models for multiphase crystalline materials, a Laguerre–Voronoi tessellation technique was implemented using the power diagram module in the software Voro++ [19,20]. In this technique, a domain was partitioned into convex polygonal regions according to distances between defined seed points and their individual assigned weights. The weights determine the influence of each point on the region of its adjacent points [21], so that they help to properly reconstruct the grain size distribution. Therefore, it was crucial to define the proper number of seed points, their site in the domain, and their weights to create a representative volume element (RVE).

Here, a box was assumed as the spatial domain that defined the RVE structure. The number of required points was defined equal to the number of material grains that were able to occupy the volume of the box. In this regard, the phase fraction, grain size distribution of each phase, and phase distribution were taken into account. Phase fraction and grain size were derived from real microstructural data. The grain size distribution was expressed by a log-normal probability density function (PDF) [22], Equation (1),

$$f(x) = \frac{1}{x\sigma\sqrt{2\pi}} \exp\left[-\frac{(\ln x - \mu)^2}{2\sigma^2}\right] \quad (1)$$

where  $x$  is the measured sample value. The mean and the standard deviation parameters of the corresponding normal distribution of  $\ln x$  are showed by  $\mu$  and  $\sigma$ , respectively.

Afterwards, the number of grains at a specific grain size for the defined RVE size was calculated using the cumulative distribution function (CDF) based on the parameters obtained from the PDF. However, to ensure that no free space might be left by directly using these data, a modification was employed on the data to attain proper input data. In this regard, the classical theory of geometry, close-packing of equal spheres in

a face-centered cubic (FCC) structure, was applied. In this theory, the densest packing density in a three-dimensional space is 0.74. Therefore, instead of assuming a grain with a diameter of  $x_i$  occupied the volume of  $x_i^3$ , it occupied  $\sqrt{2}x_i^3$ , which is the volume of the FCC structure. Hence, the total volume occupied within the spheres is 0.74 times the size of the RVE. However, a promising strategy of characterizing microstructural features based on neural networks, using experimental data as training data, is being developed by Pütz et al. [23] and Henrich et al. [24].

The distribution of phases was assumed homogenized by applying the random sequential addition algorithm (RSA) [25,26] in 3D space. To reduce computational time, the RVE size was minimized by applying the periodic Voronoi tessellation, which is copying the original germs around the RVE. In order to employ the finite element method (FEM), RVEs were created in Abaqus/2017 along with the required Python scripts. Although, they were meshed elements, using a 3D finite element mesh generator Gmsh 4.2.2. with tetrahedra. The maximum length between two nodes were defined as 1  $\mu\text{m}$ , and the size of the elements could be reduced regarding the size of the created grains. Note that each element represented only one grain. Moreover, the periodic boundary conditions were applied to the constructed RVE using a node-coupling method [27,28] (Figure 1). In this figure, the red system is independent, and the deformation gradient was prescribed, whereas the blue system is dependent and follows the applied deformation. According to an elaborate study on the deformation behavior of the materials, different loading conditions were applied, such as uniaxial tension, biaxial tension, plane strain tension, and shear.

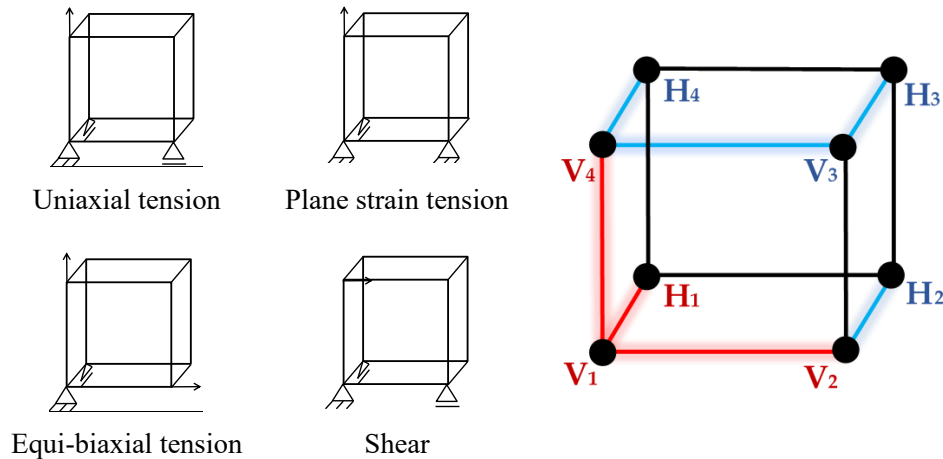


**Figure 1.** Scheme of the applied periodic boundary conditions.

Moreover, in polycrystalline materials, effects of grain orientation and strain hardening are crucial. In this order, the texture features of the materials were also considered. Thus, the orientation distribution function (ODF) was applied to describe the grain orientation distribution using Euler angles,  $\varphi = \{\varphi_1, \Phi, \varphi_2\}$ . The extracted texture was mapped to the RVEs by performing an iterative process of random assignment of crystallographic orientations to the grains to achieve the desired ODF by minimizing the quantitative differences between the inverse pole figures (IPFs) of the experimental and assigned data. The used MTEX MATLAB scripts for this analysis were taken from References [29,30].

## 2.2. Material Characterization as Input Data

Two different DP1000 grade steels with a thickness of 1.5 mm were investigated. Their chemical compositions are given in Table 1. The phase fractions were determined by analyzing several scanning electron microscopy photos. The grain size and crystallographic texture were characterized using the electron backscatter diffraction (EBSD) method. The analysis was operated on an area of  $100 \times 100 \mu\text{m}^2$ , at 15 kV, and using a step size of 50 nm.

**Table 1.** Chemical composition of the studied DP1000 steels (wt.%).

Materials	C	Mn	Si	Al	Ti	S	P	Fe
CR590Y980T-DP	0.043	1.807	0.301	0.037	0.048	0.007	0.012	Bal.
CR700Y980T-DP	0.080	2.813	0.293	0.291	0.075	0.002	0.011	Bal.

Since the selected materials were multiphase steels, the hardening behavior of each phase was determined considering the effect of the grain orientation for the ferrite phase and random texture for the martensite phase. Thus, for the ferrite phase, crystal plasticity (CP), modelling a phenomenological constitutive law [31], was used, which is briefly introduced here. This type of model mostly adopts a critical resolved shear stress as a state variable for each slip system. Therefore, the shear rate,  $\dot{\gamma}$ , is formulated as a function of the resolved shear stress,  $\tau$ , and the critical resolved shear stress,  $\tau_c$ . Prominent formulations along these lines were suggested by Rice et al. [32] for metallic crystals. In this framework, the kinetic law on a slip system is as in Equation (2),

$$\dot{\gamma}^\alpha = \dot{\gamma}^0 \left| \frac{\tau^\alpha}{\tau_c^\alpha} \right|^{\frac{1}{m}} \text{sgn}(\tau^\alpha) \quad (2)$$

where  $\dot{\gamma}^\alpha$  is the shear rate on slip system  $\alpha$  subjected to the resolved shear stress  $\tau^\alpha$  at a slip resistance of  $\tau_c^\alpha$ ; and  $\dot{\gamma}^0$  and  $m$  are material constants, which describe the reference shear rate and the rate sensitivity of the slip, respectively. The influence of any set of slip system, index  $\beta$ , on the hardening behavior of a (fixed) slip system  $\alpha$  is given as Equation (3),

$$\tau_c^\alpha = \sum_{\beta=1}^n h_{\alpha\beta} |\dot{\gamma}^\beta| \quad (3)$$

where  $h_{\alpha\beta}$  is referred to as the hardening matrix in Equation (4).

$$h_{\alpha\beta} = q_{\alpha\beta} \left[ h_0 \left( 1 - \frac{\tau_c^\beta}{\tau_s} \right)^a \right] \quad (4)$$

Here,  $h_0$ ,  $a$ , and  $\tau_s$  are the slip-hardening parameters, which are considered to be identical for all slip systems as a result of the underlying characteristic dislocation reactions. The parameter  $q_{\alpha\beta}$  is related to latent hardening, which is assumed to be 1.0 for coplanar slip systems  $\alpha$  and  $\beta$  [31,33]. These parameters were calibrated through nanoindentation tests of the ferrite grains and corresponding parallel simulations, by getting the best fit of the load–displacement responses of the material.

The nanoindentation tests were carried out on three relatively large grains on the materials with different grain orientations. For this purpose, a cube-corner indenter tip was chosen for the tests. Each grain underwent three loading rates of 0.1 nm/s, 1 nm/s, and 10 nm/s to reach a 100 nm depth and unloaded with

the same speed as the loading. A parallel simulation of nanoindentation was modelled using Abaqus/2017 (Figure 2). The indenter was defined as a discrete rigid of 3  $\mu\text{m}$  in length. A large deformable cube was created to represent a single grain, which meshed with the C3D8 (8-node linear brick) element type with minimum size of 30 nm at the critical area. A frictional coefficient of 0.1 was applied between the contact surfaces using the Coulomb friction model.

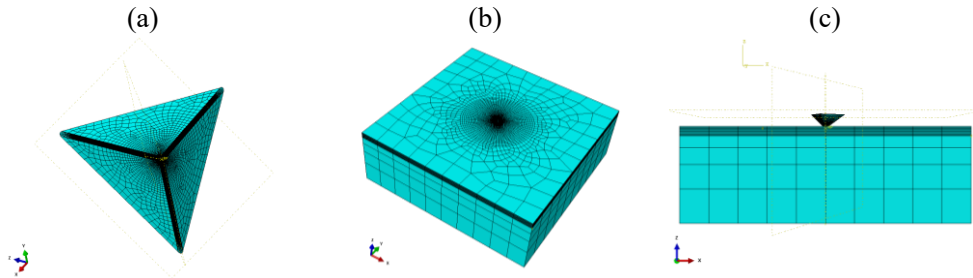


**Figure 2.** 3D nanoindentation model: (a) indenter, (b) grain, and (c) assembly.

Since the martensite grains in the studied materials were very fine, applying nanoindentation tests was impossible. Therefore, the flow curve of this phase was derived by subtracting the flow curve of a fully ferritic RVE under uniaxial tension from the extrapolated flow curve of a conventional uniaxial tensile test of the material. The extrapolation was done using the Hollomon–Voce hardening law [34]. In contrast to the ferrite phase, the deformation behavior of the martensite was considered independent from texture, i.e., isotropic elasticity and J2 plasticity laws were applied.

Moreover, the capability of the micromechanical model in prediction of local damage and edge crack sensitivity was assessed. Thus, the maximum shear stress damage criterion (Tresca) was calibrated for crack initiation in martensite grains at strain of 0.05 [35]. Hence, the damage initiation of the RVEs for different loading conditions were predicted and compared qualitatively to the experimental hole expansion ratio (HER) of the materials. The hole expansion tests were performed with 50° conical punch on shear-cut (with 10% die clearance) and wire-cut holes.

### 3. Results and Discussion

The deformation and damage behavior of the studied DP steels were evaluated using the mentioned micromechanical modelling method. The results are displayed and discussed in the following sections. First, the microstructural and micromechanical features of the materials, which were applied to synthesize the representative volume elements, are shown. Then, the responses of each RVE through different loading conditions are compared and explained.

#### 3.1. Synthesis of the 3D Representative Volume Elements

For generating a microstructural model that can represent the mechanical behavior of materials accurately, defining precise microstructural features, such as the phase fraction, grain size distribution, and texture, are required. Employing the proper mechanical properties in each phase is also vital for a rational study.

### 3.1.1. Phase Fraction

As expected, the studied dual-phase steels had a ferritic–martensitic microstructure (Figure 3). By analysis of several high-magnification SEM images using Digimizer version 5.6.0 by MedCalc Software Ltd [36], the fraction of each phase was revealed. CR590Y980T-DP contained 65% ferrite and 35% martensite, and CR700Y980T-DP had 55% ferrite and 45% martensite. Although an EBSD study was carried out in this work, it was not properly capable to distinguish similar crystal structures of the body-centered cubic (BCC) ferrite and body-centered tetragonal (BCT) martensite, especially for these fine microstructures [9].

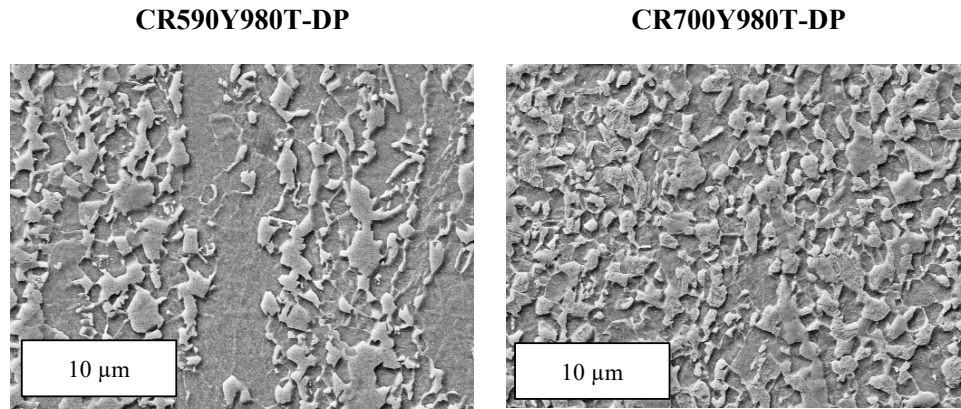


**Figure 3.** The initial microstructure of the studied materials shown in the plane of RD-TD, RD↑ ND→. The brighter and darker grains display the martensite and ferrite phases, respectively.

### 3.1.2. Grain Size Distribution

The grain sizes and their distributions were derived from EBSD images by distinguishing image quality (IQ) values. As shown in Figure 4, the grain sizes of CR590Y980T-DP were clearly coarser than in the other material. The average and maximum grain sizes of the ferrite grains for CR590Y980T-DP were 2.90 and 14.05  $\mu\text{m}$ , while for CR700Y980T-DP, they were 1.76 and 4.53  $\mu\text{m}$ , respectively. The average and maximum grain sizes of the martensite grains for CR590Y980T-DP were 0.69 and 2.34  $\mu\text{m}$ , while for CR700Y980T-DP, they were 0.55 and 2.09  $\mu\text{m}$ , respectively.

To construct the grains of the RVEs in a reasonable size range, as explained in detail in the previous section, the statistical frequency of a specific grain size was estimated based on the EBSD data. The log-normal distribution function parameters, mean, and standard deviation of the characterized microstructures were calculated by MATLAB software, (Figure 5). Then, the number of grains in each grain size was determined according to the phase fraction and size of the RVE box of  $10\ \mu\text{m} \times 10\ \mu\text{m} \times 10\ \mu\text{m}$  (Figure 6). As expected, the number of ferrite grains is lower in CR590Y980T-DP than the other material, 42 grains versus 84 grains, since their grain sizes were also larger, although its ferrite fraction was smaller. The number of martensite grains was also lower for CR590Y980T-DP, as their grain sizes were lower, and also its martensite fraction was lower than the other. In brief, the fine microstructure of CR700Y980T-DP led to create 3.5 times more grains than CR590Y980T-DP. In Figure 6, note that the ferrite grains are represented in different colors, as different crystallographic orientations were required to assign them (which is described later), whereas the



martensite grains are only shown in one color, since no texture characteristics were considered for this phase.

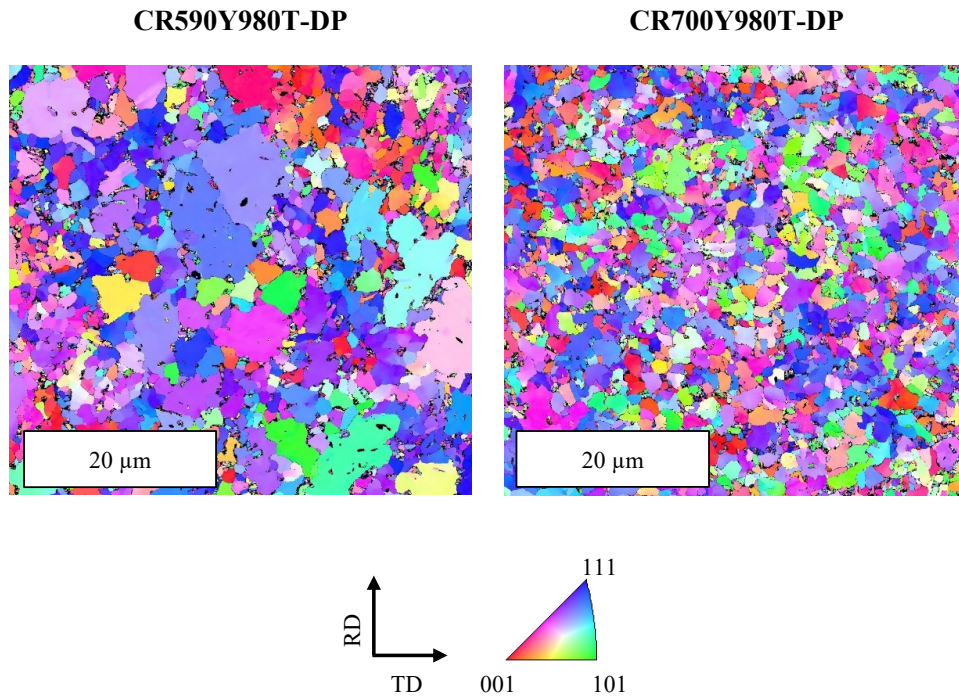


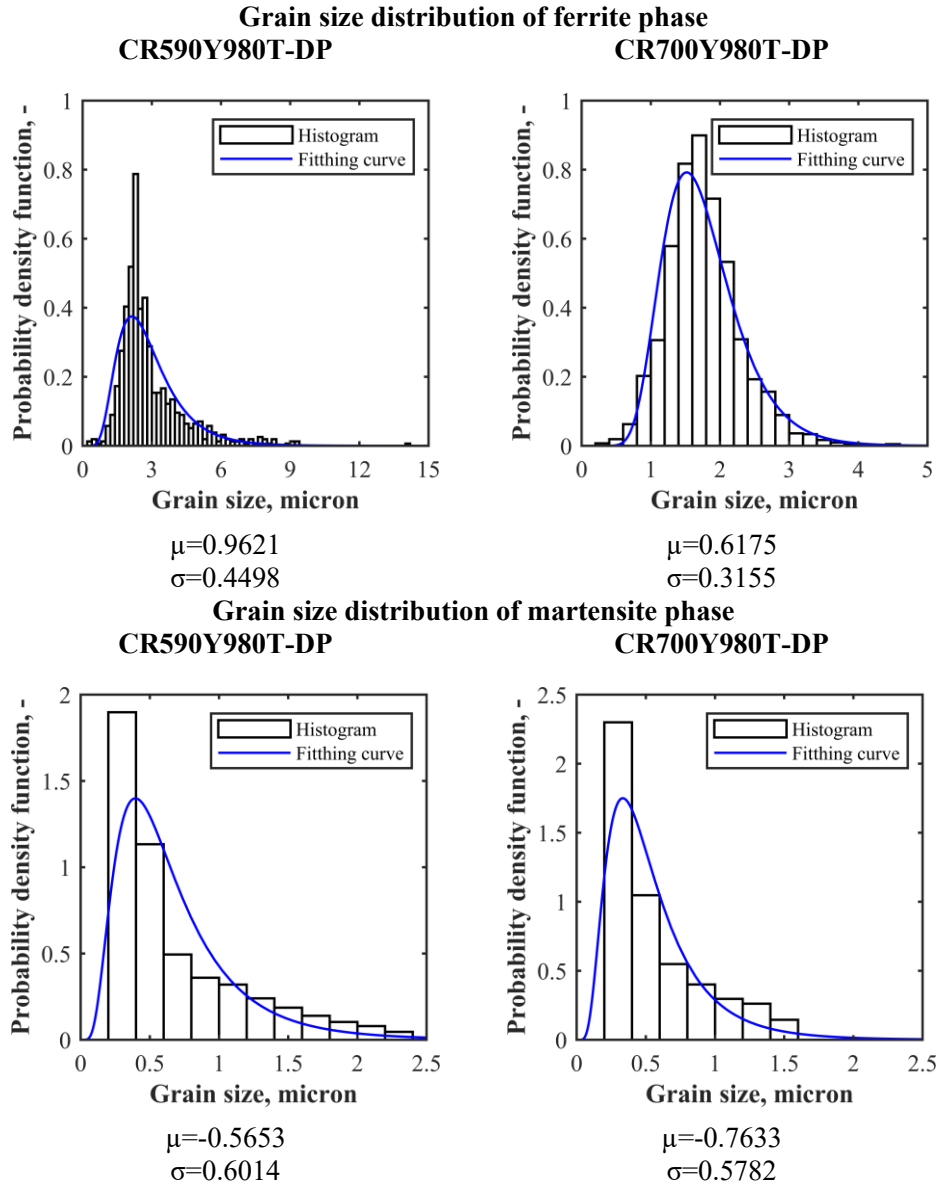
**Figure 4.** EBSD orientation maps for the studies materials on the RD-TD plane, IPF ND.

The grain size of the synthesized RVE might be a little bit different from the input data, as the procedure for generating the RVEs is based on randomly placing the seeds. To ensure that the differences were negligible, the grain size distribution of the RVEs for each phase and each material is plotted in Figure 7, as the output histogram. It reveals that for the ferrite phase, the number and range size of the created grains had good agreement with the EBSD data, while for martensite grains, the mean values were higher than the input data. This can happen in this method of RVE generation, since the grains grew and filled the space between spheres, which could cause those grains to grow larger than the assigned weights [22]. Here, this occurrence was observed mostly in martensite grains, as the smaller grains were placed later. Note that the mean sizes of the martensite grains were smaller than the ferrite grains in the studied materials. However, the results were acceptable so far, since the mean size of the martensite grains for CR700Y980T-DP was still higher than CR590Y980T-DP. In addition, for each phase, the mechanical properties' sensitivity to grain size was not considered here; also, the martensite grains usually gathered and formed martensite islands.

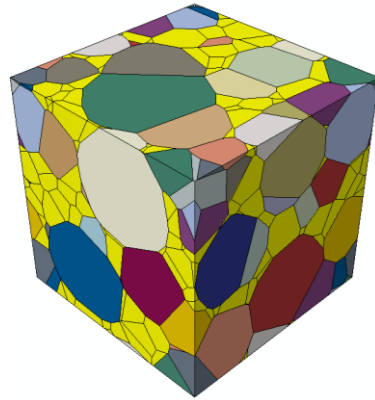
### 3.1.3. Texture

In the present work, only the effects of ferrite grain texture on the RVE behavior were considered. This assumption was reasonable for the studied steels, as their fine, well-dispersed martensite islands represented a random texture. The crystallographic orientation distributions of the as-received materials and synthesized RVEs are illustrated in Figure 8, in terms of IPFs, which represents acceptable agreement between the data.

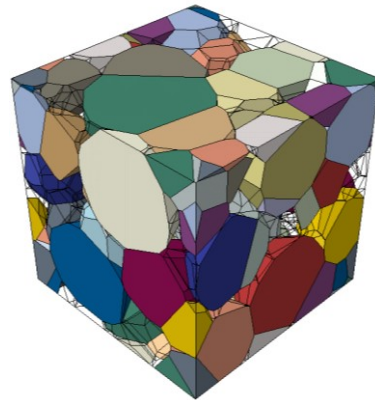
A relatively higher intensity was observed for the  $\{111\}$  fiber texture, although the overall texture has no significant preferential orientation.



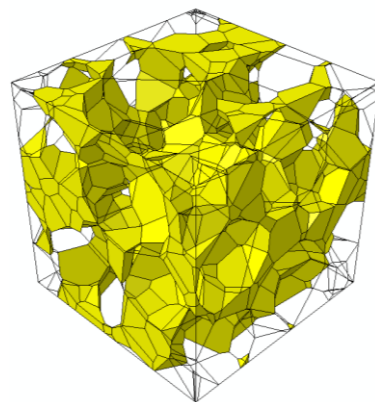
**Figure 5.** Grain size distribution of the ferrite and martensite phases in the studied steels. Parameters of the log-normal distribution function of each histogram were obtained by the best fitting of the curve.

**CR590Y980T-DP**

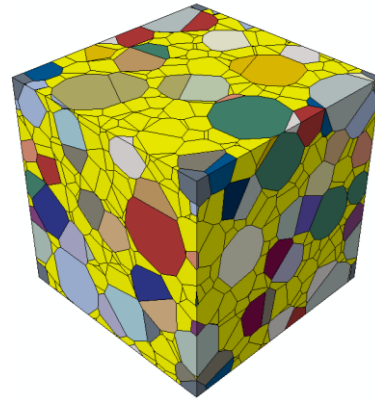
Number of total grains = 272



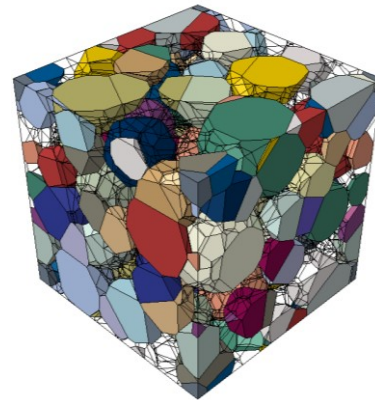
Number of ferrite grains = 42



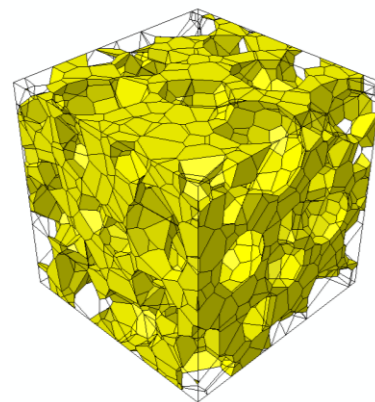
Number of martensite grains = 230

**CR700Y980T-DP**

Number of total grains = 962



Number of ferrite grains = 84



Number of martensite grains = 878

**Figure 6.** The generated RVEs (with sizes of  $10\ \mu\text{m} \times 10\ \mu\text{m} \times 10\ \mu\text{m}$ ) for each investigated steel. The grains and number of grains for each phase are shown.

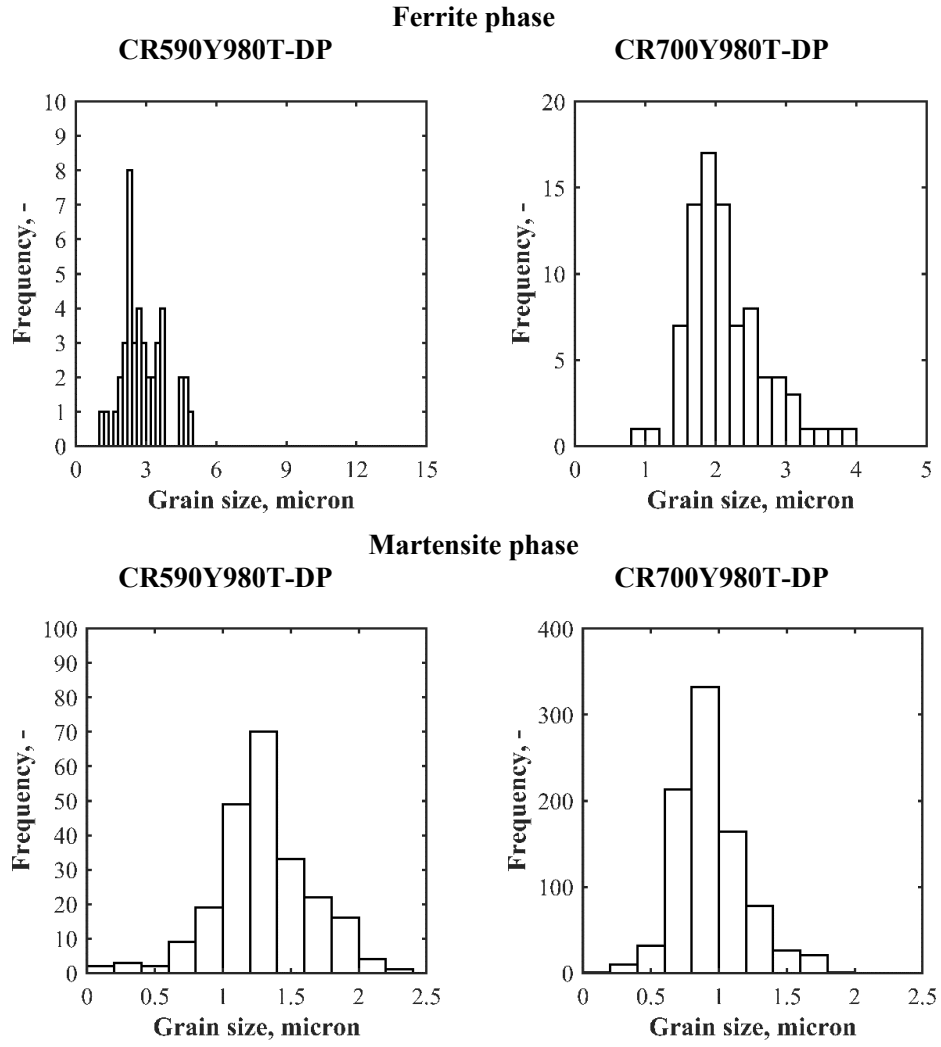


**Figure 7.** Grain size distribution of the ferrite and martensite phases in the generated RVEs.

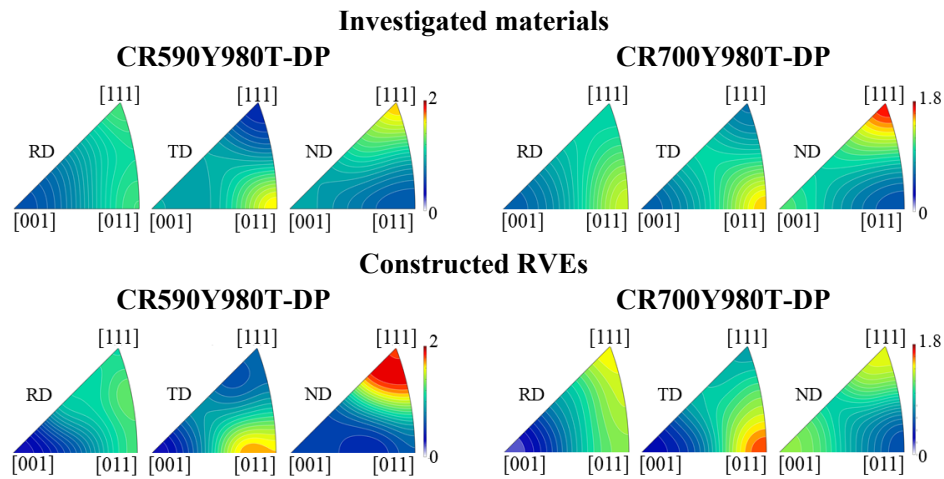


**Figure 8.** Crystallographic orientation distribution of the investigated materials in terms of IPFs.

### 3.1.4. Micromechanical Properties of an Individual Phase

The deformation behavior of the ferrite grains in RVEs were defined using the aforementioned crystal plasticity model for BCC. The parameters were calibrated by performing nanoindentation tests on a single grain and parallel corresponding FEM simulations. The grains with different crystallographic orientations were examined to investigate the effects of grain orientation on their deformation response. The detailed crystallographic information of the tested grains is listed in Table 2. The load–displacement curves and hardness values were extracted from the nanoindentation tests at different loading rates, as seen in Figures 9 and 10, which indicate that the rate and orientation dependencies of the tested grains were low. However, these results could be the consequence of the fine grain size of the studied materials and the applied testing technique. Average hardness values of 2.3 and 2.9 GPa, and a load of 210  $\mu\text{N}$  and 255  $\mu\text{N}$  at 100 nm were measured for CR590Y980T-DP and CR700Y980T-DP, respectively, which noticeably displayed the higher strength of the ferrite phase for CR700Y980T-DP.

**Table 2.** Grain ID and orientation of the test areas.

Materials	Grain ID	Average Orientation		
		$\phi 1$	$\Phi$	$\phi 2$
CR590Y980T-DP	1522 ( $\{111\}$ )	204.2	114.7	39.1
	1355 ( $\{100\}$ )	148.9	69.3	20.0
	1351 ( $\{110\}$ )	176.1	135.5	355.1
CR700Y980T-DP	3198 ( $\{111\}$ )	19.864	50.998	311.74
	1441 ( $\{100\}$ )	155.55	35.663	222.51
	2744 ( $\{110\}$ )	336.4	89.4	54.2

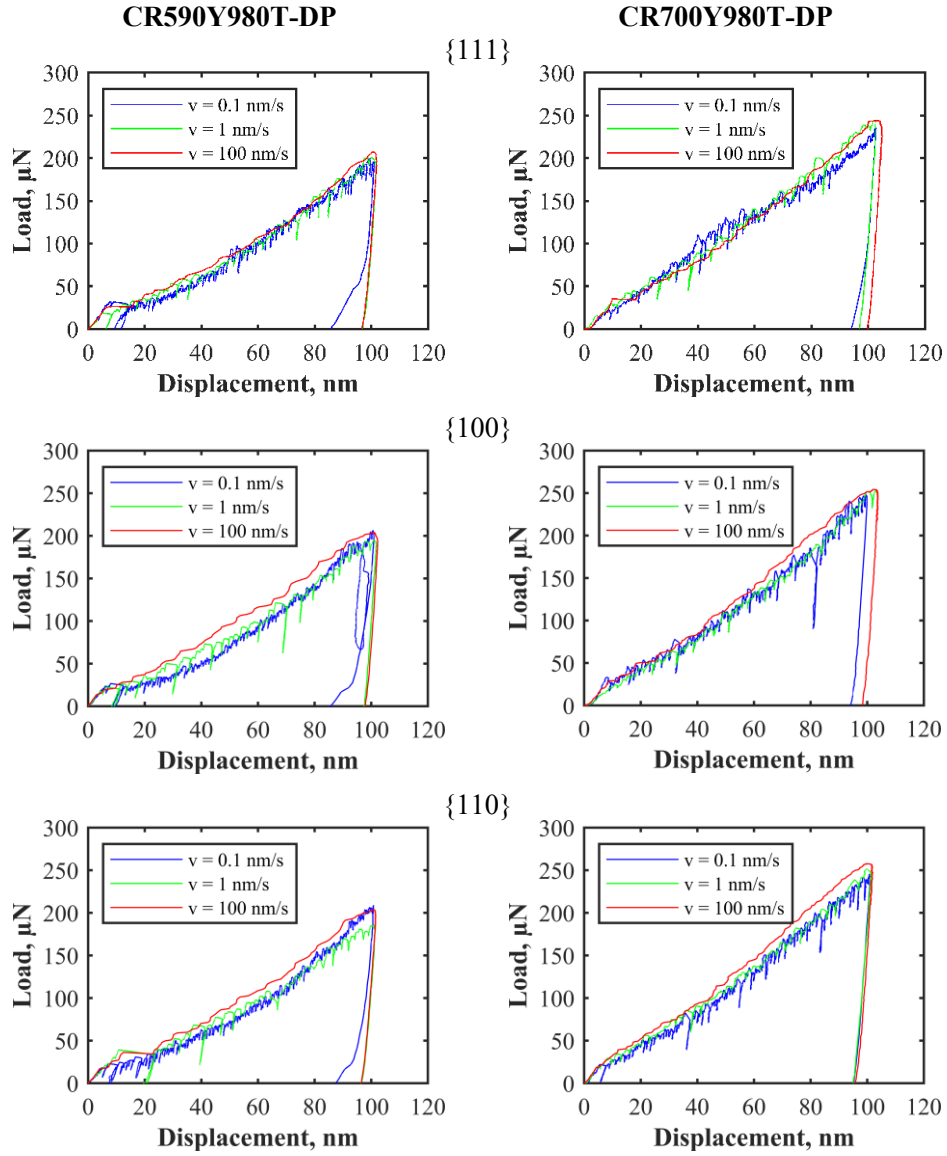


Figure 9. Load–displacement curves of the nanoindentation tests at different grains with different loading rates.

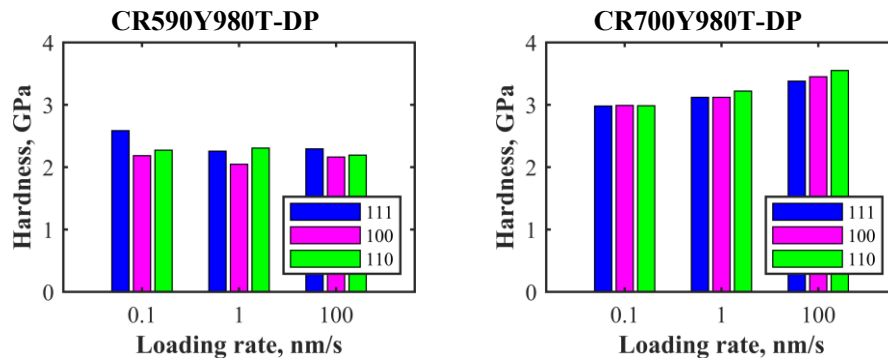
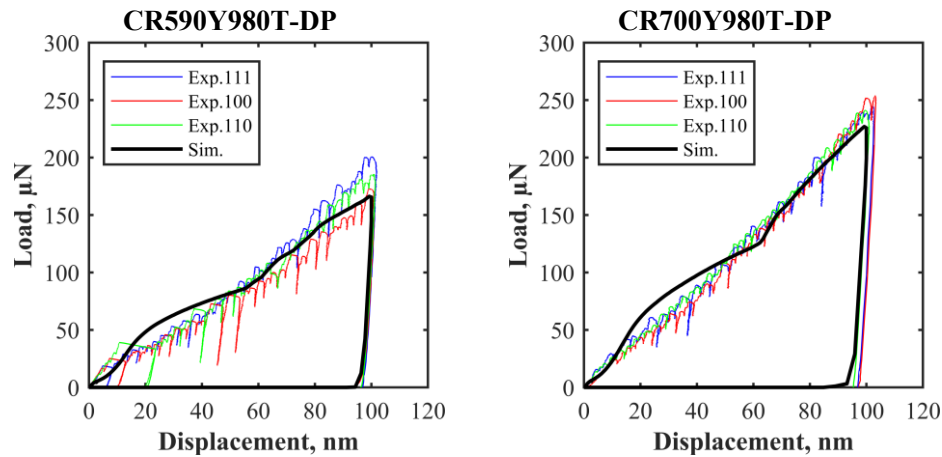


Figure 10. The hardness of ferrite grains with different orientations and different loading rates.

The CP parameters were calibrated for the studied steels, by reaching the best fit of the simulated load–displacement curve on the experimental results (Figure 11). The calibrated parameters are listed in Table 3. The number of dislocation slip systems was assumed to be 24, since the slip systems of  $\{110\} \langle 111 \rangle$  and  $\{112\} \langle 111 \rangle$  are activated at room temperature for BCC. It is worth mentioning, as the nanoindentation tests and the corresponding simulations were not sensitive to loading rate and grain orientation, only one load–displacement curve was available for simultaneous calibration of several CP parameters, which caused the set of parameters for the proper fitting to become non-unique. However, only one set of parameters, as seen in Table 3, could satisfy the assumption of soft ferrite and harder martensite phases; i.e., the flow curve of ferrite should be lower than the tested material. The stress–strain flow curve of the ferrite phase was derived by applying the calibrated CP parameters into uniaxial tension of a single-phase RVE with random texture.



**Figure 11.** The deformation behavior of the calibrated CPFEM ferrite under nanoindentation test shows good agreement with the experimental results.

**Table 3.** Calibrated crystal plasticity parameters of the investigated materials.

Materials	$c_{11}^1$	$c_{12}^1$	$c_{44}^1$	$\dot{\gamma}^0^1, 1/s$	$\tau_0, \text{MPa}$	$\tau_s, \text{MPa}$	$m^1$	$h_0, \text{MPa}$	$a$
CR590Y980T-DP	230.1d5	134.6d5	116.6d5	0.001	100	400	0.05	1000	4
CR700Y980T-DP	230.1d5	134.6d5	116.6d5	0.001	200	400	0.05	1000	4

<sup>1</sup> The parameters were taken from Reference [37].

Since the martensite grains were very fine, using nanoindentation tests was impossible for these microstructural constituents. Therefore, the mechanical properties of the martensite grains were calculated by subtracting the flow curve of the ferrite phase from the flow curve of the DP steel, based on the fraction of each phase. The flow curves of the ferrite and martensite phases are plotted in Figure 12. Note that a large range of strain is always required to apply in FEM simulations for elaborated studies; however, a maximum strain of only 0.12, through homogeneous deformation of the tensile tests, was achievable for



the studied materials. Thus, the Hollomon–Voce hardening law was calibrated for the quasi-static uniaxial tensile test and extrapolated to the large strains in the DP steels' flow curves (Table 4). As mentioned before, the effects of texture on deformation were not considered for the martensite phase, hence only isotropic elasticity and J2 plasticity laws were employed to describe the mechanical properties of martensite.

Figure 12 shows that the stress–strain behaviors of the materials were in the same range for low strains, such as 0.1, but they vary at larger strains. The level of the flow curves for ferrite in CR590Y980T-DP was lower than in CR700Y980T-DP, especially the yield stress. In contrast, for the martensite phase, the level of the flow curve in CR590Y980T-DP was significantly higher than in CR700Y980T-DP. For instance, the initial yield stresses for the ferrite phases were 301 and 601 MPa and for the martensite phases were 922 and 793 MPa, respectively, for steels CR590Y980T-DP and CR700Y980T-DP. In brief, the flow curves of the different phases are so close for CR700Y980T-DP, whereas in CR590Y980T-DP the flow curves of the phases are quite different. These differences are also visible in the hardness results (Figure 13). The macro Vickers hardness of CR590Y980T-DP was higher than the other materials, 3.4 versus 3.2 GPa, while the hardness of the ferrite phase for CR590Y980T-DP was much lower. Thus, a harder martensite phase could be expected for CR590Y980T-DP. To sum up, the strength levels of ferrite and martensite were closer in CR700Y980T-DP than in CR590Y980T-DP.

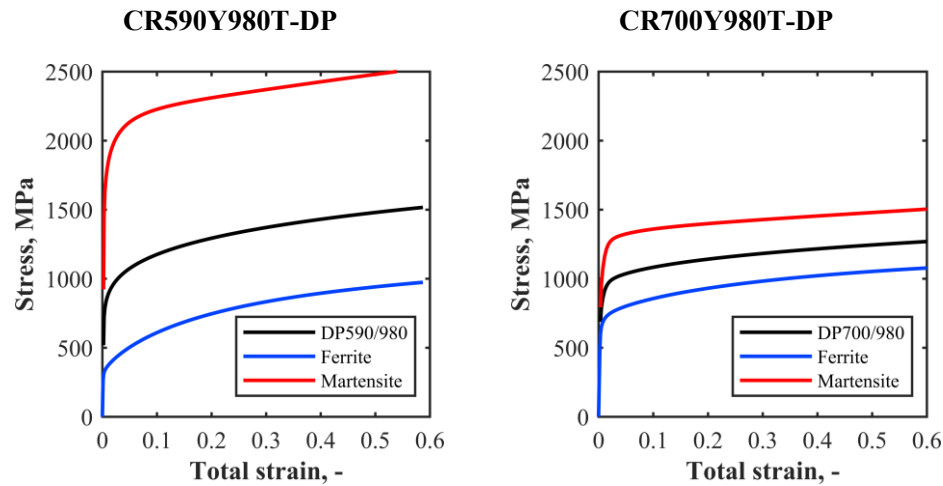
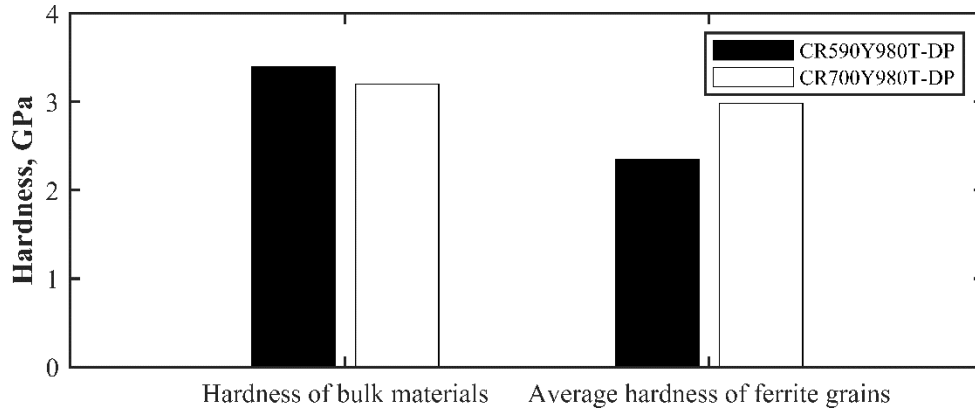


Figure 12. The stress–strain flow curve of the materials and their individual phases.

Table 4. Fitted parameters of the Hollomon–Voce hardening law.

Materials	Hollomon–Voce Hardening Law
CR590Y980T-DP	$1121.5 (\varepsilon_p)^{0.2} + 525.4$
CR700Y980T-DP	$474.7 (\varepsilon_p)^{0.4} + 189.9 \exp(-177.2\varepsilon_p) + 861.1$



**Figure 13.** The comparison of hardness of the DP steels and their ferrite grains.

The meshed RVEs are displayed in Figure 14. Since CR700Y980T-DP contained finer grains, the number of total elements was higher than the RVE of the other material, 101,799 versus 42,487 elements.

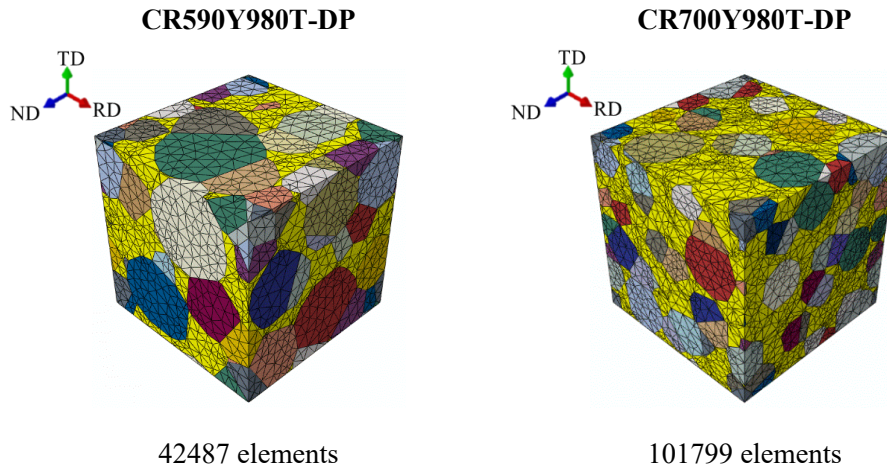


**Figure 14.** The meshing patterns of the different RVEs.

### 3.2. Deformation and Damage Assessments

The RVEs were constructed to study the grain-scale deformation and damage behaviors of the studied DP1000 steels under different loading conditions. This knowledge is vital in the material selection process, since some mechanical properties at the macroscopic scale are mainly dependent on the material microstructural features, such as the hole expansion ratio, which still remains a challenge in DP steels. Figures 15 and 16 illustrate the responses of the materials through different loading paths, uniaxial tension, equi-biaxial tension, plane strain tension, and pure shear. All the images were taken at an equivalent strain of 0.1 for the RVE boxes. The results show that although martensite represented higher level of stress, the contribution towards plastic deformation was mostly made by ferrite, since it is the softer phase, as also observed by Liu et al. [38]. A strong heterogeneous stress distribution was observed in CR590Y980T-DP, while the deformation partitioned very homogeneously in CR700Y980T-DP. This tendency was predictable in consideration of the more homogeneous and consistent microstructural and micromechanical features

that were represented by CR700Y980T-DP, in terms of the phase fraction, grain size, texture, and mechanical properties of the different phases. Moreover, grain orientation influenced the different deformation contribution of each ferrite grain under different loading conditions. It is worth mentioning that the RVE of CR590Y980T-DP was strongly deformed under the shear condition, while no significant difference was seen for CR700Y980T-DP in comparison to the other loading paths.

Moreover, damage behavior of the RVEs were studied under various loading conditions, to compare the sensitivity of the materials through complicated local deformation, to estimate their capability of edge crack resistance. Note that an edge can experience severe shearing and uniaxial tension stress state at the cutting stage [5], and mixed uniaxial tension, plane strain, and biaxial tension during hole expansion tests [39]. The maximum shear stress at initiation of martensite cracking was obtained 1067 and 662 MPa for CR590Y980T-DP and CR700Y980T-DP, respectively. These values were derived from the calculated flow curve of martensite, Figure 12, at a plastic strain of 0.05, which assume martensite cracking initiates [35]. Based on the Tresca yield criterion, the maximum shear stress is half of the equivalent stress in uniaxial tensile test. The equivalent strain of the RVE box was calculated at the damage initiation moment (Figure 17). The results show that damage initiated in CR590Y980T-DP much earlier than that of CR700Y980T-DP, i.e., it is more sensitive to deformation. Therefore, it can be expected that CR590Y980T-DP is more prone to edge cracking and its HER is lower than CR700Y980T-DP, which was totally proved by the experimental results of hole expansion tests, Figure 18, where the HER of CR700Y980T-DP was 1.5 times that of CR590Y980T-DP. In brief, a lower strength differential between ferrite and martensite causes homogenous deformation and delays local damage initiation, which leads to higher edge crack resistance and a higher hole expansion ratio. This conclusion is supported by findings of other researchers from the microstructural analysis of other DP steels [16–18].

According to the RVE results (Figure 19), the ferrite–martensite interfaces represent the potential sites for damage initiation for both materials. However, the microstructural studies close to fracture site in uniaxial tensile specimens, Figure 20, reveal that the dominant damage micromechanism for CR590Y980T-DP was martensite cracking, while for CR700Y980T-DP, it was decohesion of the ferrite–martensite interfaces. It has been reported that fine microstructure in DP steels usually leads to a decohesion micromechanism, whereas coarser microstructure causes martensite cracking [37]. In fact, in both cases, the microcrack nucleates at the interfaces of the ferrite and martensite, and only its propagation path is different [40], which can also influence the multi-stage deformation processes, such as hole manufacturing and the subsequent hole expansion process. Nevertheless, damage propagation was not studied, as more factors should be considered in this regard, such as misorientation of neighbor grains. Marteau et al. [41] showed that the local microstructural neighborhood plays a more crucial role in strain heterogeneity rather than the specific grain orientation, shape, or size.

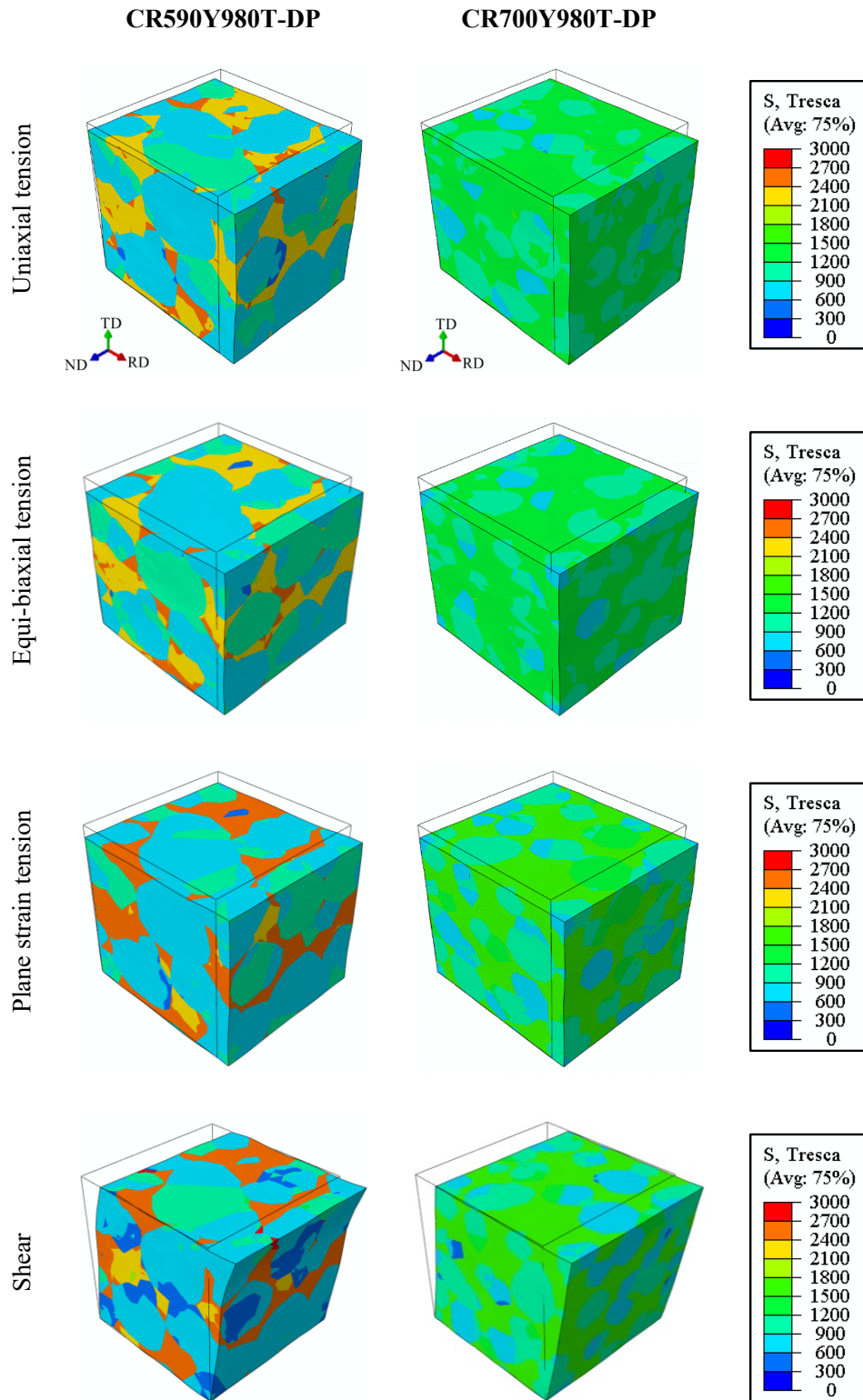


**Figure 15.** The responses of RVEs under different loading conditions, at an equivalent strain of 0.1 for the RVE box.

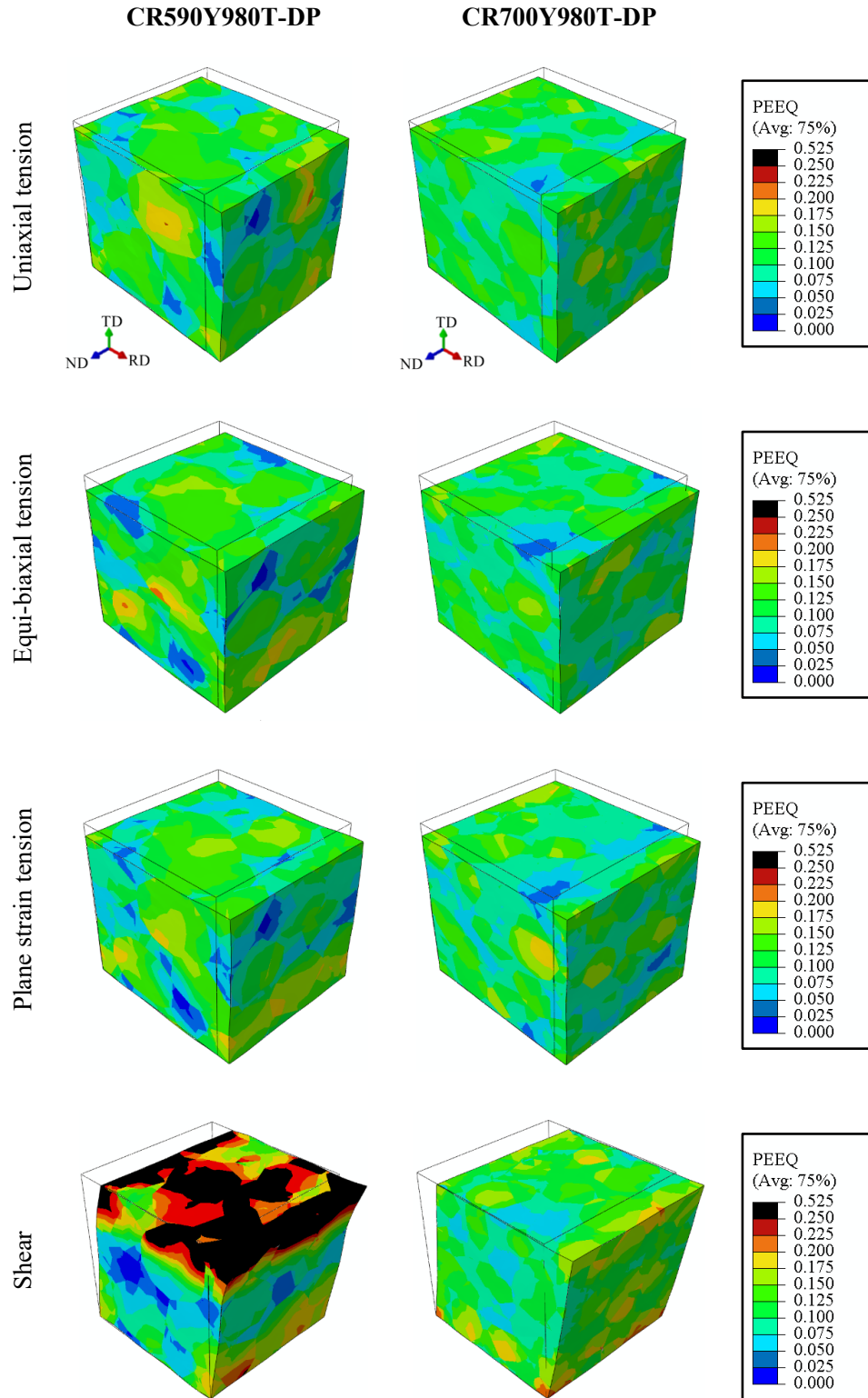


**Figure 16.** Strain partitioning of RVEs under different loading conditions, at an equivalent strain of 0.1 for the RVE box. “PEEQ” stands for equivalent plastic strain.

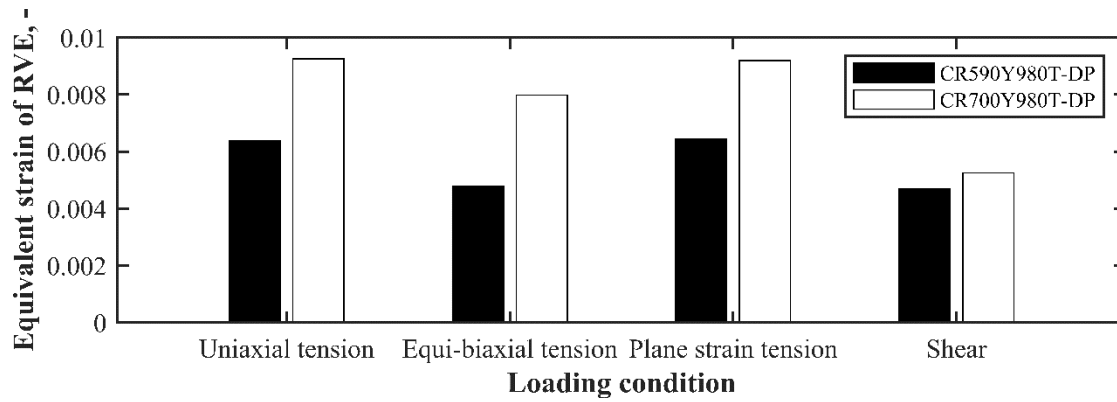


**Figure 17.** The predicted damage initiation of the RVEs at different loading conditions.

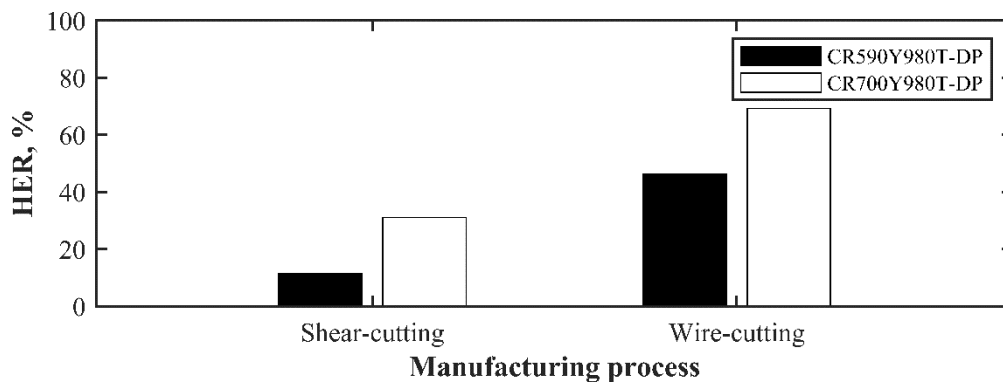


**Figure 18.** Comparison of hole expansion ratio and edge crack sensitivity of the studied materials.

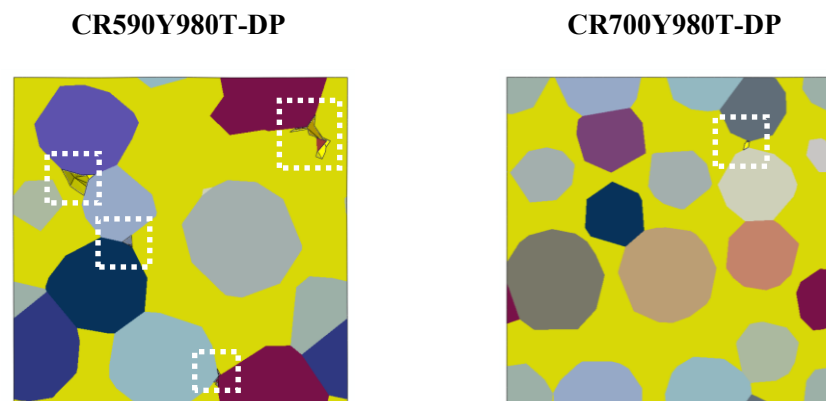


**Figure 19.** Some damage initiation sites are marked in cross-sections of the RVEs, which indicate damage initiates at the interfaces of the ferrite–martensite. The distribution of the phases is showed here. Martensite islands are shown in yellow, and the other colors illustrate the ferrite phases with different crystallographic orientations. The crack initiation was displayed by deletion of elements with the critical maximum shear stress.

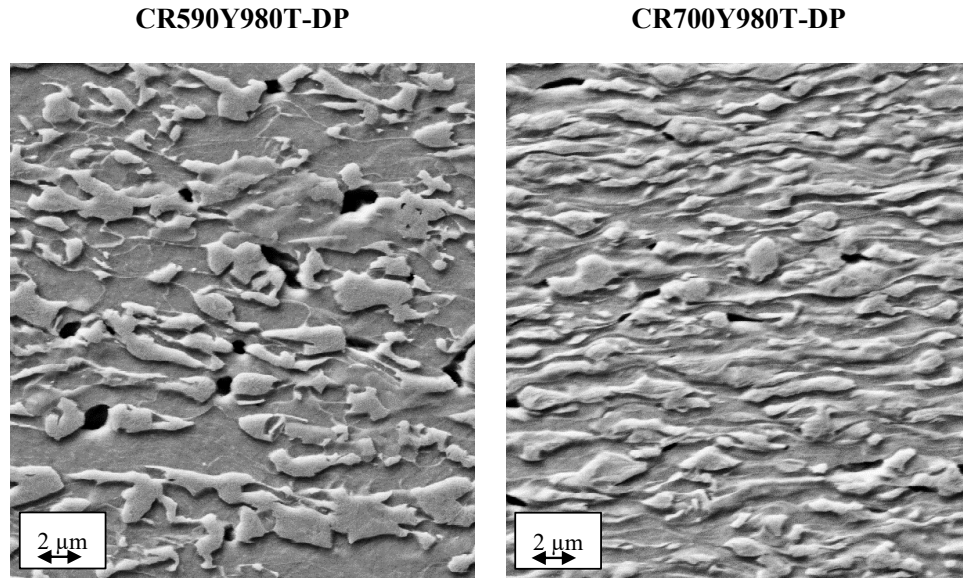


**Figure 20.** Martensite cracking and ferrite–martensite decohesion are observed in SEM images as the dominant damage micromechanisms in CR590Y980-DP and CR700Y980-DP, respectively.

#### 4. Conclusions

Microstructure-based models of two DP1000 steels were generated using representative element methods according to the actual microstructural and micromechanical features of the materials. Damage initiation at the RVEs were evaluated for different loading conditions by using the maximum shear stress criterion to consider crack initiation in martensite. The results showed that when the microstructural and micromechanical properties of the ferrite and martensite were more similar, damage was triggered later; i.e., this material represented a higher local formability prior to damage initiation. Therefore, it is expected that edge crack sensitivity reduces and HER increases.

**Author Contributions:** Conceptualization, N.H. and S.M.; methodology, N.H. and S.M.; software, N.H. and N.V.; validation, N.H.; formal analysis, N.H.; investigation, N.H.; writing—original draft preparation, N.H.; writing—review and editing, N.H., N.V. and S.M.; funding acquisition, S.M. All authors have read and agreed to the published version of the manuscript.

**Funding:** The funding of this research was provided by Deutsche Forschungsgemeinschaft (DFG, German Research Foundation)—Project number 278868966—TRR 188.

**Acknowledgments:** The authors would like to acknowledge Wenqi Liu and Junhe Lian from Aalto University for their support in the nanoindentation tests, and Seyed Amirhossein Motaman from RWTH Aachen University for his support in the texture analysis. In addition, the simulations were performed with computing resources granted by RWTH Aachen University under project <rwth0459>.

**Conflicts of Interest:** The authors declare no conflict of interest. The funders had no role in the design of the study; in the collection, analyses, or interpretation of data; in the writing of the manuscript, or in the decision to publish the results.



## References

1. Casellas, D.; Lara, A.; Frómeta, D.; Gutiérrez, D.; Molas, S.; Pérez, L.; Rehrl, J.; Suppan, C. Fracture toughness to understand stretch-flangeability and edge cracking resistance in AHSS. *Metall. Mater. Trans. A* 2017, 48, 86–94.
2. Wu, X.; Bahmanpour, H.; Schmid, K. Characterization of mechanically sheared edges of dual phase steels. *J. Mater. Process. Technol.* 2012, 212, 1209–1224.
3. Thakur, A.K.; Kumar, R.R.; Bansal, G.; Verma, R.K.; Tarafder, S.; Sivaprasad, S.; Mandal, G.K. Processing-microstructure-property correlation for producing stretch-flangeable grade dual-phase steel. *J. Mater. Eng. Perform.* 2021, 30, 4300–4317.
4. Habibi, N.; Pütz, F.; Könnemann, M.; Brinnel, V.; Münstermann, S.; Feistle, M.; Volk, W. Numerical quantification of damage accumulation resulting from blanking in multi-phase steel. *IOP Conf. Ser. Mater. Sci. Eng.* 2018, 418, 012058.
5. Habibi, N.; Beier, T.; Richter, H.; Könnemann, M.; Münstermann, S. The effects of shear affected zone on edge crack sensitivity in dual-phase steels. *IOP Conf. Ser. Mater. Sci. Eng.* 2019, 651, 012073.
6. Butcher, C.; Anderson, D.; Worswick, M. Predicting failure during sheared edge stretching using a damage-based model for the shear-affected zone. *SAE Int. J. Mater. Manuf.* 2013, 6, 304–312.
7. Levy, B.; Gibbs, M.; Van Tyne, C. Failure during sheared edge stretching of dual-phase steels. *Metall. Mater. Trans. A* 2013, 44, 3635–3648.
8. Choi, S.-H.; Kim, E.-Y.; Woo, W.; Han, S.; Kwak, J. The effect of crystallographic orientation on the micromechanical deformation and failure behaviors of DP980 steel during uniaxial tension. *Int. J. Plast.* 2013, 45, 85–102.
9. Tasan, C.C.; Diehl, M.; Yan, D.; Bechtold, M.; Roters, F.; Schemmann, L.; Zheng, C.; Peranio, N.; Ponge, D.; Koyama, M. An overview of dual-phase steels: Advances in microstructure-oriented processing and micromechanically guided design. *Annu. Rev. Mater. Res.* 2015, 45, 391–431.
10. Pütz, F.; Shen, F.; Könnemann, M.; Münstermann, S. The differences of damage initiation and accumulation of DP steels: A numerical and experimental analysis. *Int. J. Fract.* 2020, 226, 1–15.
11. Ghadbeigi, H.; Pinna, C.; Celotto, S. Failure mechanisms in DP600 steel: Initiation, evolution and fracture. *Mater. Sci. Eng. A* 2013, 588, 420–431.
12. Kusche, C.F.; Pütz, F.; Münstermann, S.; Al-Samman, T.; Korte-Kerzel, S. On the effect of strain and triaxiality on void evolution in a heterogeneous microstructure—A statistical and single void study of damage in DP800 steel. *Mater. Sci. Eng. A* 2021, 799, 140332.
13. Ramazani, A.; Schwedt, A.; Aretz, A.; Prah, U.; Bleck, W. Characterization and modelling of failure initiation in DP steel. *Comput. Mater. Sci.* 2013, 75, 35–44.
14. Uthaisangsuk, V.; Prah, U.; Bleck, W. Modelling of damage and failure in multiphase high strength DP and TRIP steels. *Eng. Fract. Mech.* 2011, 78, 469–486.
15. Vajragupta, N.; Maassen, S.; Clausmeyer, T.; Brands, D.; Schröder, J.; Hartmaier, A. Micromechanical modeling of dp600 steel: From microstructure to the sheet metal forming process. *Procedia Manuf.* 2020, 47, 1540–1547.
16. Pathak, N.; Butcher, C.; Worswick, M.J.; Bellhouse, E.; Gao, J. Damage evolution in complex-phase and dual-phase steels during edge stretching. *Materials* 2017, 10, 346.
17. Fang, X.; Fan, Z.; Ralph, B.; Evans, P.; Underhill, R. Effects of tempering temperature on tensile and hole expansion properties of a C–Mn steel. *J. Mater. Process. Technol.* 2003, 132, 215–218.

18. Hu, X.; Sun, X.; Raghavan, K.; Comstock, R.; Ren, Y. Linking constituent phase properties to ductility and edge stretchability of two DP 980 steels. *Mater. Sci. Eng. A* 2020, 780, 139176.
19. Aurenhammer, F.; Klein, R. Voronoi Diagrams. *Handb. Comput. Geom.* 2000, 5, 201–290.
20. Bargmann, S.; Klusemann, B.; Markmann, J.; Schnabel, J.E.; Schneider, K.; Soyarslan, C.; Wilmers, J. Generation of 3D representative volume elements for heterogeneous materials: A review. *Prog. Mater. Sci.* 2018, 96, 322–384.
21. Imai, H.; Iri, M.; Murota, K. Voronoi diagram in the Laguerre geometry and its applications. *SIAM J. Comput.* 1985, 14, 93–105.
22. Vajragupta, N.; Wechsuwanmanee, P.; Lian, J.; Sharaf, M.; Münstermann, S.; Ma, A.; Hartmaier, A.; Bleck, W. The modeling scheme to evaluate the influence of microstructure features on microcrack formation of DP-steel: The artificial microstructure model and its application to predict the strain hardening behavior. *Comput. Mater. Sci.* 2014, 94, 198–213.
23. Pütz, F.; Henrich, M.; Fehlemann, N.; Roth, A.; Münstermann, S. Generating input data for microstructure modelling: A deep learning approach using generative adversarial networks. *Materials* 2020, 13, 4236.
24. Henrich, M.; Pütz, F.; Münstermann, S. A novel approach to discrete representative volume element automation and generation-DRAGen. *Materials* 2020, 13, 1887.
25. Tarjus, G.; Schaaf, P.; Talbot, J. Random sequential addition: A distribution function approach. *J. Stat. Phys.* 1991, 63, 167–202.
26. Torquato, S. Optimal design of heterogeneous materials. *Annu. Rev. Mater. Res.* 2010, 40, 101–129.
27. Smit, R.J.; Brekelmans, W.M.; Meijer, H.E. Prediction of the mechanical behavior of nonlinear heterogeneous systems by multi-level finite element modeling. *Comput. Methods Appl. Mech. Eng.* 1998, 155, 181–192.
28. Wu, W.; Owino, J.; Al-Ostaz, A.; Cai, L. Applying periodic boundary conditions in finite element analysis. In *Proceedings of the SIMULIA Community Conference in Providence, Rhode Island, RI, USA, 20–22 May 2014*; pp. 707–719.
29. Motaman, S.A.H.; Roters, F.; Haase, C. Anisotropic polycrystal plasticity due to microstructural heterogeneity: A multi-scale experimental and numerical study on additively manufactured metallic materials. *Acta Mater.* 2020, 185, 340–369.
30. Motaman, S.A.H.; Haase, C. The microstructural effects on the mechanical response of polycrystals: A comparative experimental-numerical study on conventionally and additively manufactured metallic materials. *Int. J. Plast.* 2021, 140, 102941.
31. Roters, F.; Eisenlohr, P.; Hantcherli, L.; Tjahjanto, D.D.; Bieler, T.R.; Raabe, D. Overview of constitutive laws, kinematics, homogenization and multiscale methods in crystal plasticity finite-element modeling: Theory, experiments, applications. *Acta Mater.* 2010, 58, 1152–1211.
32. Rice, J.R. Inelastic constitutive relations for solids: An internal-variable theory and its application to metal plasticity. *J. Mech. Phys. Solids* 1971, 19, 433–455.
33. Tasan, C.C.; Diehl, M.; Yan, D.; Zambaldi, C.; Shanthraj, P.; Roters, F.; Raabe, D. Integrated experimental–simulation analysis of stress and strain partitioning in multiphase alloys. *Acta Mater.* 2014, 81, 386–400.
34. Sung, J.H.; Kim, J.H.; Wagoner, R. A plastic constitutive equation incorporating strain, strain-rate, and temperature. *Int. J. Plast.* 2010, 26, 1746–1771.

- 
35. Steinbrunner, D.L.; Matlock, D.; Krauss, G. Void formation during tensile testing of dual phase steels. *Metall. Trans. A* 1988, 19, 579–589.
  36. Digimizer, image analysis software; MedCalc Software Ltd, Ostend, Belgium. Available online: <https://www.digimizer.com> (Accessed on 23.03.2021 ).
  37. Tasan, C.C.; Hoefnagels, J.P.; Diehl, M.; Yan, D.; Roters, F.; Raabe, D. Strain localization and damage in dual phase steels investigated by coupled in-situ deformation experiments and crystal plasticity simulations. *Int. J. Plast.* 2014, 63, 198–210.
  38. Liu, W.; Lian, J.; Aravas, N.; Münstermann, S. A strategy for synthetic microstructure generation and crystal plasticity parameter calibration of fine-grain-structured dual-phase steel. *Int. J. Plast.* 2020, 126, 102614.
  39. Paul, S.K. A critical review on hole expansion ratio. *Materialia* 2020, 9, 100566.
  40. Alharbi, K.; Ghadbeigi, H.; Efthymiadis, P.; Zanganeh, M.; Celotto, S.; Dashwood, R.; Pinna, C. Damage in dual phase steel DP1000 investigated using digital image correlation and microstructure simulation. *Model. Simul. Mater. Sci. Eng.* 2015, 23, 085005.
  41. Marteau, J.; Haddadi, H.; Bouvier, S. Investigation of strain heterogeneities between grains in ferritic and ferritic-martensitic steels. *Exp. Mech.* 2013, 53, 427–439.

---

## Chapter VII: Summary, discussion, and outlook

---

The present work aims to provide a comprehensive understanding of one of the underlying challenges in widespread use of advanced high strength steels, called “edge cracking”. Since the current computational power facilitates elaborate investigations in the continuum framework, a cross-scale modelling approach was developed to integrate microstructural features with their mechanical response in-process or even in-service behaviors. This chapter will reveal the connections and interactions between different chapters, discuss the results, and propose possible outlooks.

### 7.1 Macro-scale investigation

In industrial manufacturing, the production of a final product often involves a series of complex forming steps. These steps are designed to shape the raw material into the desired configuration. Among these forming processes, several initial operations are commonly applied to sheet metals, including blanking, punching, trimming, and piercing, which all can be classified as shear-cutting processes. Afterwards, the sheared cut parts are subjected to various additional forming processes to achieve the final shapes. As reviewed in Chapter 1, shear-cutting induces significant hardening and damage at the edges. Since AHSSs represent low local formability, they are more sensitive to cracking, especially at the edge, through further deformation. Numerical investigations could disclose detailed information about edge cracking. However, accurate plasticity and damage definitions are required for the materials. In this regard, in Chapter 2, first the loading modes that a DP sheet undergoes throughout a shear-cutting and the following hole expansion were extracted from simulations using FE Abaqus software. The simulations exhibited various stress states during these processes, which imply the plasticity and damage models should cover a wide range of loading paths and consider both  $\bar{\theta}$  and  $\eta$  for describing employed stress states. The results revealed that during the shear-cutting process, the critical elements endured a loading path with constant  $\bar{\theta}=0$  and increasing  $\eta$ . This signifies the fact that the accurate phenomenological fracture model should be calibrated by experimental tests with  $\bar{\theta}=0$ , like pure shear or plane-strain loading conditions. During the subsequent hole expansion, the cracking initiated at the edge. However, it could propagate in two directions, one along the cut-edge and the other one orthogonal to the cut-edge. The material underwent uniaxial tension loading mode for the former, while biaxial to plane-strain tension stress states for the latter.

According to the obtained information and necessity of designing a wise and sensible numerical approach, a series of fundamental tests were considered with a locally proportional loading history, including various notched/central tensile tests, plane-strain tensile tests, bulge tests with equi-biaxial tension mode, and in-plane torsion tests with pure-shear loading condition, Chapter 3. Although these tests were performed on two dual phase steels from the same grade of DP1000 (DP600/980 vs. DP700/980), their responses were noticeably different. Note that the first number stands for the yield stress and the second one shows their ultimate tensile strength. DP600/980 represented lower yield stress and longer total elongation in standard uniaxial tension tests, whereas DP700/980 showed higher yield stress with smaller total elongation. The measured local strains by DIC method also revealed that DP600/980 could withstand small localization

with considerably lower fracture strains than DP700/980. It is worth mentioning, for lower stress triaxiality loading, like torsion tests, the differences were more (major strain of 0.465 vs. 0.75 at fracture) than the higher stress triaxiality mode, like plane-strain tensions (major strain of 0.147 vs. 0.142 at fracture).

The results provided the crucial experimental data for the reliable parameter calibration of the macro-scale model in Chapter 4. In this chapter, several shear-cutting and hole expansion test set-ups were applied to study on edge cracking for the mentioned DP1000 steels, plus a DP800 (DP440/780) which also showed negligible necking. HER was measured for each condition as quantified laboratory assessment of edge crack sensitivity. Corresponding numerical simulations were performed to gain deeper insight into the materials responses. For this purpose, a two-surface kinematic-isotropic YU hardening model along with a coupled phenomenological MBW damage model was implemented. However, regarding close occurrence of damage and fracture for high strength DP steels, the uncoupled version of the damage model was used. The hardening model was calibrated through cyclic torsion tests and the fracture criterion was calibrated using the experimental tests from Chapter 4. It is worth mentioning that the constant parameters in the models were calibrated by iterative reverse fitting of force-displacement strategy. Nevertheless, the effects of strain rate and temperature on plasticity and damage were considered, which proved vital for the shear-cutting process. Despite the cutting speed was counted as quasi-static (1 mm/s), the simulation findings showed the strain rate could rise up to 60 1/s for critical elements and the consequent adiabatic heating could increase the temperature to 650 °C before complete separation. Note that, since the experimental tests were performed for room temperature quasi-static conditions, the strain rate and temperature correction functions for plasticity were derived from the literature for the similar materials. However for the fracture model, it was recalibrated for shear-cutting. Since it was explained in Chapter 2 that applied stress states for this process showed  $\bar{\theta}=0$ , the 6-parameter BW fracture model could be simplified and only 2 parameters were required to be recalibrated. The deformed elements experienced mostly shearing before crack initiation, and afterwards by cracking and dropping in the force,  $\eta$  increased to plane-strain mode. The results showed the shear affected zone was strongly influenced by the level of fracture strains. The materials with higher forming limits exhibited smaller SAZ. Furthermore, the SAZ size was smaller in smaller hole size as well as smaller clearance. Besides the accumulated damage during shear-cutting, hole expansion tests applied further damage on the specimens, which was more considerable at two parts, one at the edge and the other one at the contact site of HE-punch and sheet. Throughout the HET, the edge mostly experienced uniaxial tension ( $\eta \approx 0.33$ ,  $\bar{\theta} \approx 1.00$ ), while the contact site tolerated the stress state of  $\eta \approx 0.5$ ,  $\bar{\theta} \approx 0.5$ . In case  $\text{damage}_{\text{edge}}^{\text{cutting}} + \text{damage}_{\text{edge}}^{\text{HET}} > \text{damage}_{\text{contact\_site}}^{\text{HET}}$  edge cracking happened, otherwise the damage initiated far from the edge at the contact site, i.e., no edge cracking. Moreover, HER was not a proper tool for assessing edge cracking and could not be directly used in design of a forming process, as the initial hole and shape of HE-punch had strong influence on the HER value.

Hence, the potential of another technique for evaluating edge crack sensitivity was briefly studied in Chapter 5, Edge-Fracture-Tensile-Test (EFTT). The specimen geometry of this test was similar to the standard uniaxial tensile test; however, one side was manufactured by milling and the other side by shear-cutting. This method could be a promising tool to compare the edge crack sensitivity of different materials

with different manufactured edges. Yet, only the stress state for the whole specimen was uniaxial tension, which does not often happen at the industrial level. Nevertheless, computer aided engineering along with proper materials input and modelling, as shown throughout this thesis, could successfully predict all the forming cases, in addition to substantial reduction in cost, effort, and time.

The macro-scale investigation in this work underscored that while manufacturing and forming processes were integral in successfully creating components, the intrinsic properties of the materials, particularly the damage behavior, played the key role. Various imaginary but probable fracture loci were constructed in Chapter 2. The different responses through the shear-cutting and following HET were significant. In brief, the material with lower fracture strains experienced early damage and rapid crack propagation. While the material with higher fracture limits tolerated the deformation more with appearance of necking, and after crack initiation, it did not fail quickly. Mechanical responses of the materials were dictated by their microstructural features, which are also studied in the present work and will shortly be reviewed and discussed in the following.

## 7.2 Meso-scale investigation

Edge cracking is controlled by local formability of materials, which is directly imposed by their microstructural features, such as grain size, morphology, texture, etc. However, study on microstructural characteristics could be complicated when the material contains a complex multi-phase structure. Therefore, three high strength dual phase steels were selected for this study, DP440/780, DP600/980, and DP700/980. The volume fraction, distribution, morphology and grain size of each ferrite and martensite phases were derived by SEM and EBSD analyses, Chapter 3 and 4. DP440/780 contained 65/35% ferrite/martensite with the coarse ferrite grains and large martensite banding structure, DP600/980 represented also 65/35% ferrite/martensite with the coarse ferrite grains but more homogeneous phase distribution, and DP700/980 contained 55/45% ferrite/martensite with the fine ferrite grains and totally random phase distribution. Their mechanical strength was estimated according to carbon content using EPMA method. The carbon content of martensite was  $C_{DP440/780} > C_{DP600/980} > C_{DP700/980}$ . Note that the potential of carbon solid solution in ferritic phase is negligible for all steels. Furthermore, the nano-indentation technique and Vickers micro-hardness tests were applied on the ferrite grains and base materials, respectively, to measure their strength. Therefore, the strength differential between ferrite and martensite phases were  $SD_{DP700/980}^{f/m} < SD_{DP600/980}^{f/m} < SD_{DP440/780}^{f/m}$ . Their distinguished microstructural features led into distinctive damage micro-mechanisms. Thus, the fracture site at various loading conditions were studied. The dominant damage mechanism for DP440/780 was martensite cracking at large martensite bands, for DP600/980 was also martensite cracking which connected each other through shear bands which originated inside of the large ferrite grains, and for DP700/980 was ferrite-martensite interface decohesion. Also, the sizes of created micro-cracks were significantly different,  $Void\_size_{DP440/780} > Void\_size_{DP600/980} > Void\_size_{DP700/980}$ .

To investigate the materials behavior under different stress states, representative volume elements with periodic geometries and boundary conditions were generated based on experimental data. A phenomenological CP model was used to describe the mechanical behavior of ferrite phases in this scale,

and J2 plasticity model was applied for martensitic phases. Note that the CP model was calibrated using reverse fitting of force-displacement of nano-indentation tests. Various loading conditions were applied on the RVE, including uniaxial tension, plane-strain, equi-biaxial tension, and pure shear. The Tresca maximum shear stress fracture model was utilized to determine the damage initiation. It was calibrated based on martensite flow curve, as cracking was assumed to happen at first at martensite phase with significantly higher stress level. The results displayed that the deformation distributed more uniformly in DP700/980 with more homogenous microstructure than DP600/980. As the mechanical properties in ferrite and martensite phases were closer in DP700/980, the strain could be accommodated fairly between different phases and cracking could be delayed, than DP600/980. Since martensite banding structures completely controlled the mechanical properties of DP440/780 and made the experimental data quite scattered, the numerical study at meso-level was not considered for it here.

### 7.3 Multi-scale integration

The comprehensive multi-scale analysis conducted in this research provides valuable insights into the behavior of materials under applied deformation. The findings suggest that a more uniform distribution of deformation across the microstructure heightens capacity to withstand external stresses. Therefore, the onset of damage is delayed, i.e. local fracture strains increase.

This fascinating phenomenon contributes significantly to enhancing the local formability of the material, thereby playing a key role in mitigating the occurrence of edge cracking.

### 7.4 Outlook

The current work presents a commendable strategy for material design and selection by addressing issues related to low edge crack sensitivity and providing a reliable tool for edge crack prediction. However, some improvement could be helpful and even necessary for complex microstructures.

- The macro-scale model needs
  - Incorporating strain rates and temperature effects: The current macro-scale model should integrate the effects of strain rates and temperature on damage and fracture limits, particularly concerning high-speed forming processes. Materials undergoing such processes often exhibit varying behaviors influenced by strain rates and temperature. Accurate representation of these parameters is critical for a more realistic predictive model.
  - Non-local damage model: Using A non-local version of the damage model could enhance the simulation accuracy. Especially, the prediction of the edge quality made by shear cutting requires considering both the edge roughness (shape) as well as the damage level and distribution. Both parameters could be influenced by element size and type.
- The meso-scale model needs
  - Grain size effects: Expanding the meso-scale model to include grain size effects is essential. Different grain sizes can significantly alter the material's mechanical properties,



deformation behavior, damage initiation sites, and damage growth path. Accurate prediction of these effects is imperative for comprehensive material analysis.

- Grain boundaries: considering the effect of grain boundaries in polycrystal RVEs is essential for capturing the realistic behavior of the material. This involves understanding how the interactions at grain boundaries affect phenomena such as deformation, damage accumulation, and failure.
- Misorientation between adjacent grains: Incorporating the misorientation between neighboring grains into the meso-scale model will contribute to a more precise prediction of deformation distribution and damage initiation. Grain misorientation plays a crucial role in dictating material behavior under stress.
- Considering various damage micro-mechanisms: Complex materials experience different damage micro-mechanisms, which could initiate simultaneously or at different stages of deformation development. Understanding and accurately representing these mechanisms are essential for both initiation and propagation of damage within the material.
- RVE boundary conditions: Applying the exact boundary conditions of shear-cutting and subsequent forming processes on RVE could mirror the real happenings in the meso-scale.

Moreover, this study is restricted to the studied materials or similar ones. For other materials, the following improvement might be needed.

- Extension of the macro-scale model with
  - Anisotropy mechanical behavior: Sheet materials often exhibit anisotropic behavior, which significantly affects their response to external forces. Extending the macro-scale model to accommodate such behaviors would broaden its applicability to diverse materials.
  - A stress state dependent plasticity model: A model that accounts for stress state dependence would significantly enhance the predictive capability of the macro-scale model, particularly under varying stress conditions.
- Extension of the meso-scale model with
  - Shape-factor and morphology: Incorporating shape-factor and morphology effects is vital to represent accurate material behavior, especially in complex geometries like martensite band structures.
  - Temperature and strain rate effects: For sensitive materials the CP parameters should be temperature and strain rate dependent.